Calcium aluminate blended cements incorporating engineered residues

Jennifer Astoveza

Calcium Aluminate Blended Cements Incorporating Engineered Residues

Jennifer ASTOVEZA

Main supervisors:
Prof. dr. ir. Y. Pontikes
Prof. dr. ir. A. Lecomte

Chairman:
Prof. R. Puers

Reporters:
Prof. S.A.B. Lopez
Dr. ir. V. Baroghel-Bouny

Other members of the jury:
Prof. dr. ir. R. Trauchessec *(co-supervisor)*
Dr. ir. R. Soth *(co-supervisor)*
Dr. ir. R. Snellings
Prof. J. Elsen

Dissertation presented in partial fulfilment of the requirements for the degree of Doctor of Engineering Science (PhD): Materials Engineering

June 2022

École Doctorale Chimie – Mécanique – Matériaux – Physique

Thèse

Docteur de l'Université de Lorraine Mention :
« Mécanique des matériaux »

Ciments composés à base d'aluminate de calcium incorporant des résidus traités valorisables

Par: Jennifer ASTOVEZA

Thèse soutenue publiquement le 15 juin 2022 à Louvain, Belgique
devant le jury suivant :

Directeurs de thèse:
Yiannis Pontikes – *Professeur des universités*
André Lecomte – *Professeur des universités*

Examinateurs:

Romain Trauchessec – *Maître de conférences (co-directeur)*
Ratana Soth – *Docteur (co-directeur)*
Jan Elsen – *Professeur des universités (président du jury)*
Ruben Snellings – *Docteur*

Rapporteures:
Susan Andrea Bernal Lopez – *Professeure des universités*

Véronique Baroghel-Bouny – *Docteur HDR*

Invité:
Robert Puers – *Professeur des universités*

This manuscript is presented in partial fulfilment of the requirements for a dual PhD from the Faculty of Engineering Science of KU Leuven, and the Institut Jean Lamour of the Université de Lorraine.

This work was funded by the SOCRATES Project under the European Union Framework Program for Research and Innovation Horizon 2020 Grant Agreement No.721385 (EU MSCA-ETN SOCRATES).

Uitgegeven in eigen beheer, Jennifer Astoveza, 1 Rue Le Chatelier, Vaulx-Milieu 38090 (France)

ISBN 9789464447224

Acknowledgements

This work would not have been possible without the contribution of the following people/organizations:

- the team behind the SOCRATES Project for the conception and funding of this research
- Imerys, KU Leuven and Université de Lorraine for the warm accommodation and support
- my thesis advisers, Prof. Yiannis Pontikes, Prof. André Lecomte, Prof. Romain Trauchessec, and Dr. Ratana Soth for their relentless supervision, and for always believing in my abilities especially whenever I am overwhelmed with self-doubt
- The members of the jury: Prof. Robert Puers, Prof. Jan Elsen, Dr. Véronique Baroghel-Bouny, Prof. Susan Andrea Bernal Lopez and Dr. Ruben Snellings for their constructive review
- Dr. Chris Parr and Dr. Christoph Wöhrmeyer of Imerys for offering me the opportunity to join their team, while providing continuous support for the completion of my thesis

I would also like to acknowledge several colleagues for their direct contribution to the experimental works and data analyses, namely:

- Dr. Jeroen Soete of KU Leuven for his assistance in tomography and for performing the analysis on cylindrical volumes in section 3.2.2
- Dr. Arne Peys and Christina Siakati of KU Leuven for fitting the Mössbauer spectra of the raw materials (section 2.2.5) and the hydrated binary blends (section 3.4.3) using Model 1
- Sébastien Diliberto of Institut Jean-Lamour for performing the Mössbauer spectroscopy and for fitting the spectra in section 3.4.3 using Model 2
- Sylvie Migot-Choux and Mélanie Emo of Institut Jean-Lamour for performing with us the TEM and STEM, respectively
- Dr. Tobias Hertel of KU Leuven for his assistance in ATR-FTIR
- Dr. Bruno Espinosa of Imerys for the encouragement and for sharing his insights on the fate of Fe during hydration
- my supportive friends and colleagues at Imerys, KU Leuven and Université de Lorraine for the training and insightful exchanges

Lastly, I would like to express my gratitude to my friends, my second parents (Michèle & Daniel, Maria & Guido, Zuri & Gonza) and my family (Nordin, Moises, Everlyn, Glaiza and Maycee). Thank you for choosing to be part of my life, and for embracing my best and worst.

Abstract

The pressure to decarbonize the cement industry in light of sustainability goals has been motivating the search for new types of supplementary cementitious materials (SCM) in the recent decades. Industrial residues, which otherwise end up in landfills or find low added-value applications, are of particular interest in near-zero-waste process schemes.

This thesis explored the potential for valorization of pre-treated residues as SCM in calcium aluminate cement (CAC)-calcium sulfate hemihydrate (HH) system. These residues included non-ferrous metallurgy (NFM) slags, municipal solid waste incinerator (MSWI) bottom ashes, jarosite and paper-fabrication residues. Using isothermal calorimetry and mechanical strength test, a screening test was first established to compare their early-age and the long-term reactivity. The highly-amorphous NFM slags exhibited superior reactivity showing evidence of long-term (> 28 days) contribution to the mechanical strength of mortars at 30 wt% replacement level. However, the slags' slow hydration kinetics in the first days of hydration could be an issue for CAC systems, given that their applications greatly rely on their rapid-hardening property. Moreover, the amorphous nature of the NFM slags and the dominance of iron (Fe) in their composition, set them apart from traditional SCM's. As of this writing, there are only limited publications discussing the hydration mechanism of Fe in CAC-based binders.

In order to overcome the slow kinetics of the slag hydration, the influence of three factors, including: (1) the proportion of sulfates by varying the CAC/HH ratio; (2) the addition of lime-rich paper residue at 5 wt% as activator; and (3) the incorporation of 30 wt% PC in ternary CAC-HH-PC systems, were investigated. For all these formulations, the early hydration reactions were characterized using isothermal calorimetry on paste samples. The dimensional stability and mechanical strength were followed using standard mortars up to 1 year curing period. Furthermore, a methodology to estimate the slag hydration degree using a non-destructive technique based on X-ray Computed Tomography (XCT) combined with volume analysis was developed in this study. Several techniques were used to follow the phase assemblage evolution, including: X-ray diffraction (XRD), thermogravimetric analysis (TGA), attenuated total reflection-Fourier transform infrared spectroscopy (ATR-FTIR). Lastly, transmission electron microscopy (TEM), scanning transmission electron microscopy (STEM) and Mössbauer spectroscopy were also performed in order to gain a better understanding of the fate of Fe, the main component of the slag, during hydration.

High early strengths (>20 MPa) were obtained for all formulations at 30 wt% slag-binder replacement level. The increased proportion of sulfates (CAC/HH ratio = 1.6) improved the mechanical strength due to the more extensive ettringite formation. The addition of PC and paper residue also improved the strengths at early ages. The slag addition improved the dimensional stability of mortars by diluting the binder, consequently mitigating the excessive expansion in the ternary systems. The XCT results showed that about 50 % of the slag has reacted after more than 180 days of curing. This was in agreement with the estimations obtained from Mössbauer spectroscopy, based on the relative amounts of absorption areas of the newly-formed Fe species during the hydration. While the proportion of sulfates did not have a clear influence on the slag's dissolution rate based on the XCT results, the addition of PC and paper residue appeared to have accelerated it in the first 28 days. At longer term however, the reaction degree remained relatively comparable to those obtained for the binary CAC-HH systems. Using the ATR-FTIR spectra, a hypothetical peak displacement of the Si-O asymmetric stretching band of the slag at around 930 cm^{-1} was proposed, supporting this reactivity.

As to the fate of Fe, TEM showed evidence of uptake in hydrated phases grouped into two compositional clusters when plotted on a Ca-Si-Al ternary diagram. These included: (1) an Al-rich intermixed phase for the binary systems; and (2) an amorphous phase mainly containing Ca, Si and Al for the ternary systems. After longer curing periods (>180 days), STEM revealed the formation of an unidentified nano-crystalline phase richer in Fe with a distinct rod/needle-like morphology and a d-spacing of approximately 7.2 Å. The evolution of the Mössbauer spectra could suggest Fe oxidation from the 2+ to 3+ state during slag hydration. This was accompanied by a shift from tetrahedral to octahedral coordination as a new Fe-containing hydrated phase is formed. There was no substantial evidence of Fe uptake in the more abundant hydrated phases, such as in ettringite or monosulfoaluminates, contrary to the models obtained from thermodynamic simulations and synthetic systems.

To conclude, the overall properties of the blends containing the industrial residues support their potential for valorization as SCM in CAC-based systems. However, it will be critical to continue this investigation to clearly identify the Fe-bearing hydrated phase/s and to, ultimately, utilize the understanding of the hydration mechanism in improving the blends' performance.

Samenvatting

De druk om de cementindustrie koolstofarm te maken in het licht van duurzaamheidsdoelstellingen heeft de afgelopen decennia de zoektocht naar nieuwesupplementaire cementerende materialen. (SCM) gemotiveerd. Industriële residuen, die anders op stortplaatsen terechtkomen of enkel toepassingen kennen met een lage toegevoegde waarde, zijn van bijzonder belang in bijna-nul-afvalprocesschema's.

Dit proefschrift onderzocht het potentieel voor valorisatie van behandelde residuen als SCM in calciumaluminaatcement (CAC)-calciumsulfaat hemihydraat (HH) systeem. Deze residuen omvatten non-ferrometallurgie (NFM) slakken, bodemas van de gemeentelijke afvalverbrandingsoven (AEC), jarosiet en papierfabricageresiduen. Met behulp van isotherme calorimetrie en mechanische sterktetest werd eerst een screeningstest uitgevoerdom hun reactiviteit op jonge en oude leeftijd te vergelijken. De zeer amorfe NFM-slakken vertoonden een superieure reactiviteit, waaruit blijkt dat ze op lange termijn (> 28 dagen) bijdragen aan de mechanische sterkte van mortels bij een vervangingsniveau van 30 gew.%. De langzame hydratatiekinetiek van de slakken in de eerste dagen van hydratatie kan echter een probleem zijn voor CAC-systemen, aangezien hun toepassingen sterk afhankelijk zijn van hun snelle uithardingseigenschappen. Bovendien onderscheiden de amorfe aard van de NFM-slakken en de dominantie van ijzer (Fe) in hun samenstelling ze van traditionele SCM's. Op het moment van schrijven zijn er slechts beperkte publicaties die het hydratatiemechanisme van Fe in op CAC gebaseerde bindmiddelen bespreken.

Om de langzame kinetiek van de hydratatie van de slak te overwinnen zijn drie factoren onderzocht, waaronder: (1) het gehalte aan sulfaten door de CAC/HH-verhouding te variëren; (2) de toevoeging van 5 gew.% kalkrijk papierresidu als activator; en (3) de opname van 30 gew.% PC in ternaire CAC-HH-PC-systemen. Voor alle formuleringen werden de vroege hydratatiereacties gekarakteriseerd met behulp van isotherme calorimetrie op pastamonsters. De maatvastheid en mechanische sterkte van standaardmortels werd gemonitord over een uithardingsperiode van 1 jaar. Verder werd in deze studie een methodologie ontwikkeld om de hydratatiegraad van de slak te schatten met behulp van een niet-destructieve techniek op basis van X-stralen computertomografie (XCT) in combinatie met volume-analyse. Verschillende technieken werden gebruikt om de evolutie van de fase-assemblage te volgen, waaronder: röntgendiffractie (XRD), thermogravimetrische analyse (TGA), verzwakte totale reflectie-Fourier-transformatie infraroodspectroscopie (ATR-FTIR). Ten slotte werden ook transmissie-elektronenmicroscopie (TEM), scanning transmissie-elektronenmicroscopie (STEM) en Mössbauer-spectroscopie uitgevoerd om een beter begrip te verwervenover het lot van Fe, het hoofdbestanddeel van de slak, gedurende de hydratatie.

Voor alle formuleringen met een vervangingsniveau van 30 gew.% NFM slak werd een hoge vroege sterkte bekomen. Het verhoogde gehalte aan sulfaten (CAC/HH-verhouding = 1,6) verbeterde de mechanische sterkte door een verhoogde ettringiet vorming. De toevoeging van PC en papierresten verbeterde ook de sterkte op jonge leeftijd. De toevoeging van slakken verbeterde de maatvastheid van mortels door het bindmiddel te verdunnen, waardoor de overmatige uitzetting in de ternaire systemen werd verminderd. De XCT-resultaten toonden aan dat ongeveer 50 gew.% van de slak reageerde na meer dan 180 dagen.. Dit was in overeenstemming met de schattingen verkregen met Mössbauer-spectroscopie, gebaseerd op de relatieve hoeveelheden absorptiegebieden van de nieuw gevormde Fe-soorten tijdens de hydratatie. Hoewel het gehalte aan sulfaten geen duidelijke invloed had op de oplossnelheid van de slak op basis van de XCT-resultaten, leek de toevoeging van PC en papierresten dit in de eerste 28 dagen te hebben versneld. Op langere termijn bleef de reactiegraad echter relatief vergelijkbaar met die verkregen voor de binaire CAC-HH-systemen. Met behulp van de ATR-FTIR-spectra werd een hypothetische piekverplaatsing van de Si-O asymmetrische rekband van de slak bij ongeveer 930 cm^{-1} waargenomen, wat deze reactiviteit ondersteunt.

Wat het lot van Fe betreft, leverde TEM bewijs aan voor de opname in gehydrateerde fasen gegroepeerd in twee samenstellingsclusters op een Ca-Si-Al ternair diagram. Deze omvatten: (1) een Al-rijke vermengde fase voor de binaire systemen; en (2) een amorfe fase die voornamelijk Ca, Si en Al bevat voor de ternaire systemen. Na langere uithardingsperioden (>180 dagen), onthulde STEM de vorming van een niet-geïdentificeerde nanokristallijne fase rijker aan Fe met een duidelijke staaf/naaldachtige morfologie en een d-afstand van ongeveer 7,2 Å. De evolutie van de Mössbauer-spectra zou kunnen wijzen op de oxidatie status van Fe (van 2+ naar 3+) tijdens de hydratatie van de slak. Dit ging gepaard met een verschuiving van tetraëdrische naar octaëdrische coördinatie als een nieuwe Fe-bevattende gehydrateerde fase werdgevormd. Er was geen substantieel bewijs van Fe-opname in de meer overvloedige gehydrateerde fasen, zoals in ettringiet of monosulfoaluminaten, in tegenstelling tot de modellen verkregen uit thermodynamische simulaties en synthetische systemen.

Globaal gezien, de resultaten in dit werk ondersteunen het valorisatiepotentieel van industiële residuen als SCM in op CAC gebaseerde systemen. Het zal echter van cruciaal belang zijn om dit onderzoek voort te zetten om de Fe-dragende gehydrateerde fase(s) duidelijk te identificeren en om uiteindelijk het begrip van het hydratatiemechanisme te gebruiken bij het verbeteren van de prestaties van de mengsels.

Résumé

Au vu des objectifs de durabilité visant à décarboner l'industrie du ciment, les liants alternatifs ont fait l'objet d'une attention considérable à l'échelle mondiale au cours des dernières décennies. Ces liants sont basés sur l'utilisation de sous-produits industriels comme substituts aux ciments, ou comme granulats ou encore comme composants de matériaux de construction, à performances équivalentes.

Dans le cadre de cette thèse, des résidus traités valorisables sont évalués comme addition cimentaire notamment dans des mélanges binaires (ciment alumineux CAC - hémihydrate HH). Trois des sous-produits ont fait l'objet d'une évaluation plus approfondie : i) un laitier riche en fer provenant d'une usine pilote de plomb-zinc sous forme granulée (trempe) ii) un résidu de jarosite ; iii) un résidu du recyclage du papier. Pour identifier et sélectionner ces résidus, il a été réalisé un test de conductimétrie pour mesurer la cinétique de dissolution; des mesures de flux de chaleur pour apprécier les réactions au jeune âge; et une mesure de résistance mécanique sur mortiers standards pour caractériser la réactivité à long terme. Sur la base de leurs caractéristiques générales et d'essais préliminaires, le laitier amorphe riche en fer a été retenu pour l'étude détaillée de la réactivité. Les mortiers standards incorporant les laitiers ont présenté une réactivité supérieure montrant d'une contribution positive à long terme (> 28 jours) à la résistance mécanique. Cependant, il existe actuellement peu de publications sur le mécanisme d'hydratation du fer dans les liants à base de CAC.

Afin d'augmenter la cinétique d'hydratation du laitier, l'influence de trois facteurs principaux, dont : (1) l'ajout de résidu de papier riche en chaux comme activateur ; (2) la proportion de sulfates; et (3) l'ajout de ciment Portland (PC), ont été évalués. Plusieurs techniques ont été utilisées pour caractériser les propriétés des mélanges entre 1 jour et 1 an : la résistance mécanique et la stabilité dimensionnelle ont été suivies en utilisant des éprouvettes de mortier. Le degré d'hydratation du laitier a été quantifié à l'aide de la microscopie électronique à balayage (MEB), de la tomographie par rayons X (XCT) et de la spectroscopie Mössbauer. L'assemblage des phases en fonction de la proportion de CAC a été simulé à l'aide de la modélisation thermodynamique et plusieurs techniques, notamment la calorimétrie isotherme, la diffraction des rayons X (DRX), l'analyse thermogravimétrique (ATG) et la spectroscopie infrarouge à transformée de Fourier (IRTF) ont été utilisées pour suivre expérimentalement l'évolution des assemblages. Le mécanisme d'hydratation du fer contenu dans le laitier a été décrit à partir des résultats de la spectroscopie

Mössbauer, de la microscopie électronique à transmission (MET) et de la microscopie électronique à transmission à balayage (METB).

La caractérisation approfondie des propriétés physiques et chimiques des ciments composés incorporant des résidus a démontré leur potentiel de valorisation dans cette application. Des mortiers de haute résistance et stables dimensionnellement ont été obtenus en incorporant 30% d'un laitier amorphe riche en fer dans des liants binaires CAC-HH et ternaires CAC-HH-PC. La méthodologie basée sur la tomographie a permis de montrer qu'environ 50 % du laitier était dissout au-delà de 180 jours. Ce résultat a été confirmé par spectroscopie Mössbauer, qui a montré également que l'hydratation du laitier s'accompagnait de l'oxydation du fer 2+ à 3+, et de la formation de nouveaux hydrates contenant du fer. À l'aide de la microscopie électronique (MET et METB), le fer a été détecté au jeune âge dans des phases complexes formées de gels amorphes riches en aluminium. Le fer a également été détecté à des proportions plus élevées à plus long terme, au sein d'une phase nanocristalline non identifiée. Dans les systèmes ternaires, cette phase était également associée à du calcium, du silicium et une petite quantité de magnésium.

En ce qui concerne l'augmentation de la cinétique d'hydratation du laitier, les résultats ont montré qu'il n'y avait pas de différences substantielles entre les systèmes à faible et à haute teneur en sulfate étudiés. Au contraire, l'ajout de ciment Portland et de résidus du recyclage du papier ont montré une augmentation du degré d'hydratation, toutefois cantonnée au jeune âge (< 28 jours). Cet effet pourrait résulter de la présence accrue d'ions Ca^{2+} dans le système, ainsi que de l'augmentation de l'alcalinité favorisant la dissolution du laitier.

Pour conclure, l'étude a bien montré la réactivité de plusieurs résidus industriels traités valorisables et son impact positif sur les propriétés des ciments composés à base de CAC. Néanmoins, il reste encore des questions importantes en suspens, tant pour expliquer les mécanismes fondamentaux de l'hydratation que pour tester la durabilité de ces liants. Ainsi, les travaux futurs sur l'ajout de laitier devraient se concentrer sur des analyses complémentaires pour identifier la phase nanocristalline contenant du fer et son éventuelle évolution.

Ciments composés à base d'aluminate de calcium incorporant des résidus traités valorisables

Jennifer ASTOVEZA

Introduction

Le projet européen MSCA-ETN SOCRATES a pour objectif de promouvoir l'économie circulaire en créant des procédés de valorisation des résidus industriels qui génèrent le moins possible de nouveaux déchets. Comme le montre la **Figure 1**, la technologie SOCRATES vise tout d'abord à récupérer et à concentrer les métaux nobles et les éléments critiques issus des résidus, ainsi qu'à retirer et à confiner les composants toxiques. La fraction minérale restante, qui représente plus de 80-90% du volume total, est ensuite valorisée comme précurseur de géopolymères, comme catalyseurs ou bien comme addition cimentaire. C'est cette dernière voie de valorisation qui est étudiée dans le cadre de cette thèse. Les additions prétraitées devant être ajoutées au ciment sont appelées résidus traités valorisables ou encore « sous-produits SOCRATES ».

Figure 1 *Schéma simplifié du projet SOCRATES axé sur les travaux de l'auteure: valorisation des résidus comme additions cimentaires dans les ciments composés.*

En général, l'utilisation de sous-produits comme substituts aux ciments, ou comme granulats ou encore comme composants de matériaux de construction, à performances équivalentes, a pour objectif d'en retirer des avantages économiques et environnementaux [1,2]. Si les résidus du projet SOCRATES s'avéraient être des matériaux qui satisfont ces critères, alors les retombées de ce projet de valorisation constitueraient une avancée substantielle, compte tenu de l'impact environnemental général des matériaux de construction visés [3]:

- ≈ 8 % du CO_2 anthropique mondial est attribué à la fabrication du ciment;
- ≈ 30 milliards de tonnes de béton sont produites chaque année dans le monde;
- Une augmentation de ≈ 25-50 % de la demande mondiale de béton est prévu d'ici à 2050.

Au vu de ces chiffres, on comprend pourquoi les liants alternatifs ont fait l'objet d'une attention considérable à l'échelle mondiale au cours des dernières décennies. Néanmoins, pour contrôler le comportement physique et chimique des liants incorporant des additions, il reste de nombreux défis de recherche à relever, non seulement selon le type de résidu utilisé mais aussi selon le type de liant visé. Dans la littérature, la majorité des travaux de recherche sont axés sur l'ajout d'additions traditionnelles (i.e. laitiers de hauts-fourneaux, cendres volantes, calcaire, etc.) dans des liants majoritairement composés de ciment Portland [4,5].

Les résidus du projet SOCRATES ont des propriétés chimiques différentes de celles des additions traditionnelles. En effet, ces dernières sont principalement constitués de CaO, SiO_2 et Al_2O_3, alors que les laitiers issus des métaux non-ferreux (cuivre, zinc…) et les résidus de jarosite du projet SOCRATES sont beaucoup plus riches en fer ou en sulfates, respectivement. Les différences chimiques entre les résidus du projet SOCRATES, les additions traditionnelles et les ciments Portland (PC) ou Alumineux (CAC) sont illustrées dans le diagramme de composition de la **Figure 2**.

Parmi les résidus du projet, les laitiers issus des métaux non-ferreux sont riches en fer et présentent un intérêt particulier en tant qu'addition au ciment car leur nature hautement amorphe est généralement reconnue comme un critère déterminant de la réactivité de ce type de produits [10]. De plus, ces laitiers ont subi un prétraitement à haute température de sorte que les métaux lourds et les composants toxiques y ont été pratiquement éliminés. Cependant, à la connaissance de l'auteure, il n'y a pas eu jusqu'à présent d'études traitant de la réactivité et du mécanisme d'hydratation des

laitiers riches en oxyde de fer (FeO-Fe_2O_3) dans les systèmes à base de ciment d'aluminate de calcium (CAC).

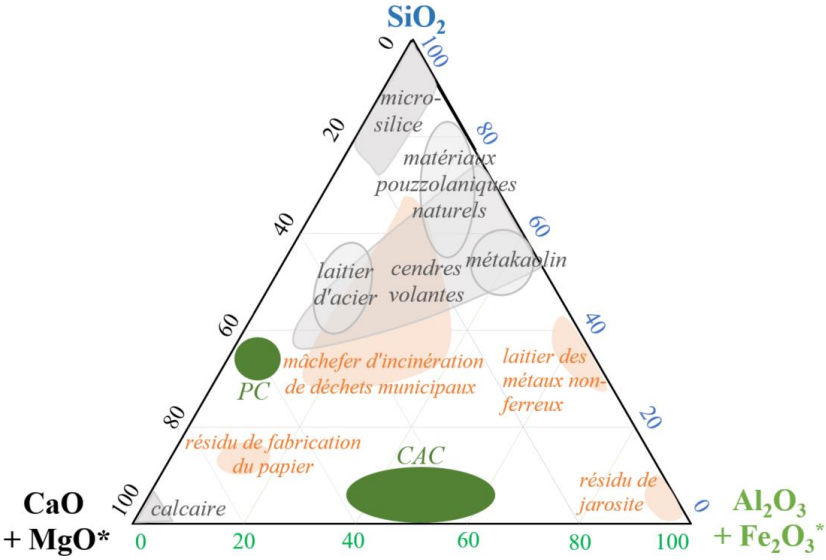

Figure 2 *Compositions chimiques de certains résidus de SOCRATES (orange) ; additions traditionnelles (gris) et ciments (vert). Les composants *MgO et *Fe_2O_3 sont exclusivement pris en compte pour les résidus SOCRATES (orange). Les données ont été rassemblées pour créer une version modifiée des diagrammes ternaires rapportés dans [6–9].*

CAC est un terme générique adopté pour les ciments à haute teneur en alumine (typiquement entre 40 % et 80 % d'Al_2O_3) avec l'aluminate monocalcique (CA) comme composant principal [11]. Dans l'industrie du bâtiment, les CAC sont généralement associés en proportions variables au ciment Portland et au sulfate de calcium (liants ternaires). Ils sont utilisés dans des applications spéciales telles que les enduits de réagréage ou enduits de lissage, les liants pour matériaux réfractaires ou les applications en environnements agressifs. D'un point de vue environnemental, une analyse du cycle de vie appliquée aux chapes autonivelantes [12] a montré que l'empreinte carbone est plus faible pour les liants ternaires à base de CAC que pour les liants riches en ciment Portland, tout en maintenant le même niveau de performances. À ce jour, il existe peu d'articles scientifiques dédiés à l'ajout d'additions issues de résidus industriels dans les liants à base de CAC. Les travaux de recherche publiés se limitent aux additions traditionnelles, principalement les laitiers de hauts-fourneaux et les cendres volantes [13–16].

L'un des objectifs du projet SOCRATES est de tester cette solution, en étudiant notamment, sur le plan fondamental et appliqué, les mécanismes d'hydratation propres à ces systèmes. La connaissance approfondie de

l'influence de divers paramètres (formules, minéralogie, etc.) sur les performances de ces liants composés constitue une étape clé qui servira par la suite à évaluer le potentiel de valorisation d'autres résidus SOCRATES en tant qu'additions dans ce type de ciment à applications spéciales.

Objectifs et Problématique

Deux objectifs principaux ont été définis dans le cadre du projet SOCRATES :

1. Évaluer la réactivité des sous-produits SOCRATES dans les systèmes à base de CAC ;
2. Proposer des techniques d'activation de ces sous-produits afin d'améliorer la cinétique de leur réaction, et les performances associées.

Guidée par ces objectifs, une méthodologie a été mise en place afin de repérer le résidu ayant le potentiel de valorisation le plus élevé. L'évolution des propriétés physiques et chimiques du résidu sélectionné au cours de l'hydratation a ensuite été étudiée en détail.

L'une des difficultés de la recherche est liée à la complexité des systèmes. En effet, l'hydratation des liants ternaires (ciment alumineux - ciment Portland - hémihydrate HH) engendre des réactions complexes souvent difficiles à dissocier car elles se produisent simultanément. De plus, l'origine variée des résidus du projet SOCRATES peut engendrer des compositions irrégulières et des chimies très différentes, de sorte qu'une comparaison directe de leur réactivité n'est pas toujours applicable, même à volume égal de substitution. Enfin, l'abondance du fer et le caractère amorphe de certains résidus, notamment les laitiers issus de métaux non-ferreux, nécessitent des techniques de caractérisation complémentaires aux méthodes plus conventionnelles utilisées pour l'étude des ciments. Étant donné que cette étude implique l'utilisation de matières premières réelles plutôt que des produits purs de synthèse, il faut aussi s'attendre à ce que certaines propriétés ne puissent pas être directement reliées à une réaction unique. En revanche, l'avantage d'utiliser des résidus industriels est de pouvoir analyser leur comportement dans des systèmes complexes, de sorte que, le cas échéant, une perspective industrielle puisse être directement proposée pour ces liants plus écologiques.

Matériaux et Méthodologie

Six sous-produits SOCRATES ont été étudiés : un laitier riche en fer provenant d'une usine pilote de plomb-zinc, disponible sous forme granulée (trempe) et sous forme refroidie à l'air ; les « fumées » d'un laitier de fayalite (produit prétraité) ; une cendre d'incinération de déchets municipaux ; un résidu de jarosite ; un résidu du recyclage du papier. Sur la base de leurs caractéristiques générales et d'essais préliminaires, trois d'entre eux ont fait l'objet d'une évaluation plus approfondie. Ces trois résidus sont représentés **Figure 3**.

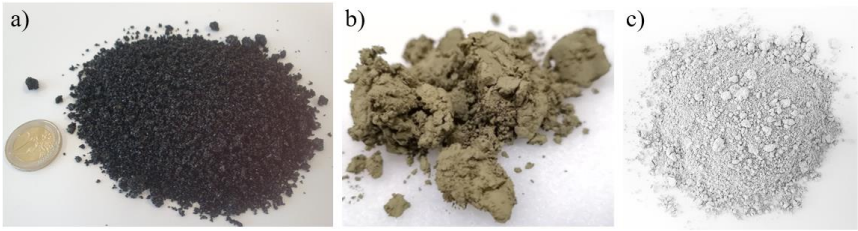

Figure 3 *Les principaux sous-produits SOCRATES évalués dans cette étude, notamment : le laitier riche en fer granulé (a) ; le résidu jarosite (b) ; et les résidus du recyclage du papier (c)*

Pour identifier et sélectionner ces résidus, il a été réalisé : i) un test de conductimétrie pour mesurer la cinétique de dissolution ; ii) des mesures de flux de chaleur pour apprécier les réactions au jeune âge ; iii) une mesure de résistance mécanique sur mortiers standards pour caractériser la réactivité à long terme. En utilisant la fluorescence X (FX) et l'analyse par diffraction des rayons X (DRX) couplée à l'analyse Rietveld, on montre que le laitier granulé de fayalite est composé de 46 % de FeO. La fraction amorphe représente 92 % du produit, les 8 % restant étant de la wüstite. Ce résidu amorphe riche en fer a été retenu pour l'étude détaillée de la réactivité. Les résidus de jarosite et ceux issus du recyclage du papier sont principalement composés de sulfates (51 %) et de chaux (68 %), respectivement. Ils ont été étudiés en tant que sources de sulfates ou de chaux dans des études distinctes.

Les principales formules incorporant le laitier de fayalite sont présentées dans le **Tableau 1**. Les formules A et B correspondent à un ajout du laitier dans des mélanges binaires CAC-HH, tandis que pour les liants A-PC et B-PC, l'ajout est réalisé dans des mélanges ternaires CAC-HH-PC. L'utilisation de deux rapports CAC/HH - 4,5 (formules A) et 1,6 (formules B) – est destinée à étudier la réactivité dans des mélanges respectivement à faible et à forte teneur en sulfate de calcium. De plus, pour chaque mélange, deux formules de référence ont été utilisées, l'une avec des composants cimentaires purs (CAC, HH et PC), l'autre où l'addition (le

laitier) est remplacée par un volume égal de quartz broyé. Les pâtes de ciment ont été préparées avec un rapport eau/liant (e/l) de 0,65 et stockées sous enveloppes hermétiques à 20°C. Les mortiers standards ont un rapport e/l de 0,5 et ils ont été conservés sous eau à 20°C.

Tableau 1 *Composition de liants incorporant le laitier riche en fer granulé*

code	*(en % massiques)*	laitier	CAC	HH	PC	somme liant	CAC/HH
A	4.5CAC-HH	30	57	13	0	100	4.5
B	1.6CAC-HH	30	43	27	0	100	1.6
A-PC	4.5CAC-HH-30PC	30	33	7	30	100	4.5
B-PC	1.6CAC-HH-30PC	30	25	15	30	100	1.6

formulations de référence :

REF_{ciment} *(référence ciment) pas d'ajout de sous-produits ni de quartz*

REF_{quartz} *(référence quartz) laitier remplacé par un volume égal de quartz*

Plusieurs techniques ont été utilisées pour caractériser les propriétés des mélanges (entre 1 jour et 1 an), et certaines ont été spécifiquement adaptées aux propriétés particulières du laitier et à sa teneur élevée en fer (i.e. densité élevée, masse atomique élevée, effet Mössbauer important) :

- la résistance mécanique et la stabilité dimensionnelle ont été suivies en utilisant des éprouvettes de mortier;
- le degré d'hydratation du laitier a été quantifié à l'aide de la microscopie électronique à balayage (MEB), de la tomographie par rayons X (XCT) et de la spectroscopie Mössbauer;
- l'assemblage des phases en fonction de la proportion de CAC a été simulé à l'aide de la modélisation thermodynamique et plusieurs techniques, notamment la calorimétrie isotherme, la diffraction des rayons X (DRX), l'analyse thermogravimétrique (ATG) et la spectroscopie infrarouge à transformée de Fourier (IRTF) ont été utilisées pour suivre expérimentalement l'évolution des assemblages;
- le mécanisme d'hydratation du fer contenu dans le laitier a été décrit à partir des résultats de la spectroscopie Mössbauer, de la microscopie électronique à transmission (MET) et de la microscopie électronique à transmission à balayage (METB).

Résultats et Discussion

Pour un taux de remplacement massique de 30 % de laitier issu de métaux non-ferreux, l'indice d'activité (IA) déduit de la résistance mécanique sur mortiers a montré une bonne contribution à long terme (> 28 jours, IA ≈ 1). Pour cette raison, la suite de l'étude a été faite avec un taux d'incorporation du laitier de 30 % dans les liants binaires CAC-HH et ternaires CAC-HH-PC.

Propriétés physiques

Les mortiers incorporant le laitier issu de métaux non-ferreux granulé et 1,3 % d'acide citrique (**Figure 4**) ont atteint des valeurs de résistance à la compression élevées, de l'ordre de 20 MPa à 1 jour et de 40 MPa à 28 jours. La faible quantité d'acide citrique, initialement ajouté pour retarder la prise, a également contribué à améliorer les propriétés au jeune âge. D'une manière générale, des résistances à la compression plus élevées ont été obtenues dans les systèmes à haute teneur en sulfate, grâce à la formation plus importante d'ettringite. Mais le caractère expansif de l'ettringite s'est avéré problématique, notamment dans la formule de référence du système ternaire (avec ciment Portland) où une expansion excessive a finalement conduit à des macro-fissures (**Figure 5**) et à une perte de résistance des mortiers. L'ajout du laitier dans les systèmes binaires et ternaires a limité cette expansion. Cette addition améliore donc la stabilité dimensionnelle du liant (**Figure 5**). Cet effet est probablement gouverné par un effet de dilution au jeune âge (facteur physique), et par la nature de phases hydratées formées à plus long terme (contribution chimique du laitier).

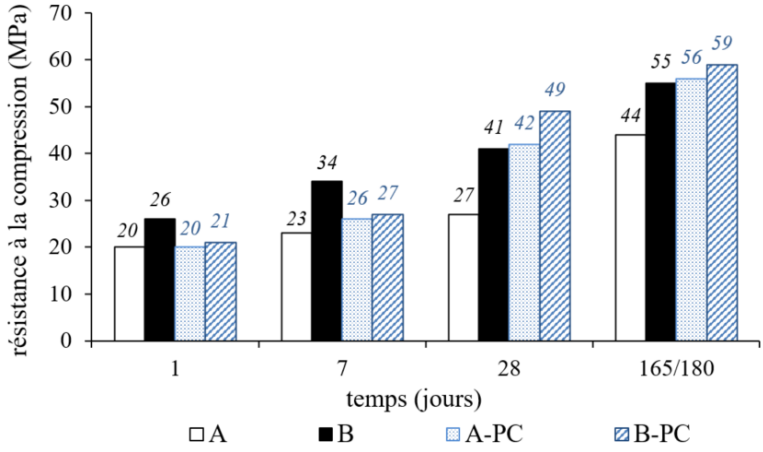

Figure 4 *Résistance à la compression des mortiers incorporant le laitier*

Figure 5 *Photos des mortiers B et B-PC après 45 jours de conservation sous eau*

Quantification du degré d'hydratation du laitier

Une méthodologie pour estimer le degré d'hydratation du laitier a été développée par analyse des images issues de la tomographie à rayons X (XCT). Les principales étapes déployées sont illustrées à la **Figure 6**. Cette technique a pu être utilisée car les propriétés du laitier (quantité et densité du fer) et de la matrice cimentaire sont très contrastées. Les résultats ont été comparés à ceux obtenus par spectroscopie Mössbauer (**Figure 7**). Cette dernière technique est basée sur l'évolution de l'absorption des rayons gamma par le fer lorsque l'environnement chimique et le degré d'oxydation sont modifiés par l'hydratation du laitier.

L'estimation du degré d'hydratation du laitier à l'aide de la spectroscopie Mössbauer et de la tomographie ont mis en évidence une cinétique plus rapide de l'hydratation du laitier en présence de ciment Portland. Cependant, à long terme, le taux d'hydratation des différentes formules converge vers 50 %. Les valeurs généralement plus faibles obtenues à partir de la tomographie sont probablement liées à deux facteurs : i) l'hypothèse selon laquelle le laitier est complètement non réactif au cours des 24 premières heures d'hydratation ; ii) le réglage de la résolution (voxel à 2,15 µm) qui exclut la contribution des particules de laitier les plus fines.

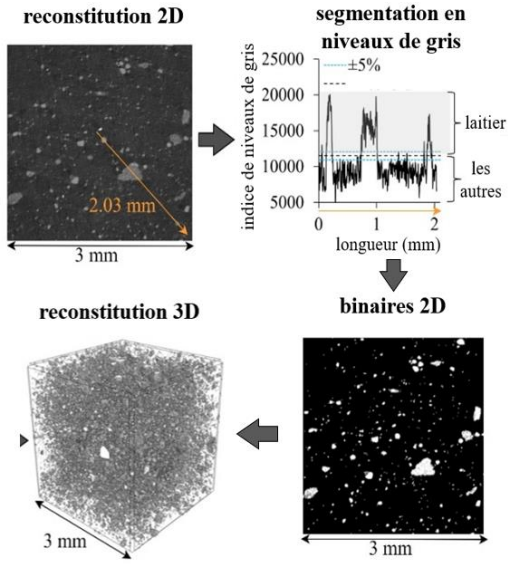

Figure 6 *Principales étapes de l'estimation du degré d'hydratation du laitier à l'aide de XCT, notamment : (1) reconstruction 2D des scans ; (2) segmentation de seuil pour distinguer les particules du laitier ; (3) création d'images binaires 2D sur la base de l'étape précédente ; (4) modélisation des volumes 3D à partir desquels le degré d'hydratation a été estimé.*

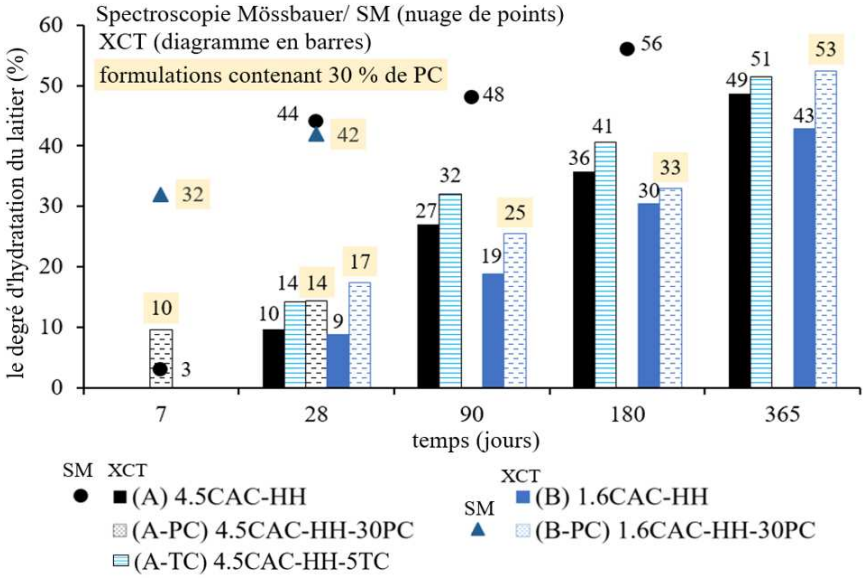

Figure 7 *Degré d'hydratation du laitier estimé à l'aide de la XCT et la spectroscopie Mössbauer*

Évolution de l'assemblage des phases

La nature et la quantité d'hydrates formés pour plusieurs formules contenant du laitier ont été prédites à l'aide d'une modélisation thermodynamique (logiciel GEMS) et comparées à celles observées expérimentalement à l'aide de la diffraction des rayons X, des analyses thermogravimétriques et de la spectroscopie infrarouge. Lors de la modélisation, il a été supposé que le taux d'hydratation du laitier était de 50 %. Un résumé des résultats est présenté dans le **Tableau 2.**

Tableau 2 *Résumé des assemblages de phases obtenus à partir de la modélisation thermodynamique et des résultats expérimentaux (> 165 jours d'hydratation). Le monosulfoaluminate est abrégé en Ms.*

	modélisation thermodynamique		**résultats expérimentaux**	
composants:	principal	mineur	principal	mineur
A	ettringite, hydrogrenat	gibbsite, strätlingite	Ms	ettringite, gibbsite, strätlingite
B	ettringite	hydrogrenat, gibbsite	ettringite, gibbsite	Ms, strätlingite
A-PC	strätlingite, Ms	hydrogrenat, C-S-H	strätlingite, Ms	C-S-H
B-PC	Ms, C-S-H	strätlingite, ettringite, hydrogrenat	ettringite	strätlingite, C-S-H, Ms

Les résultats expérimentaux sont généralement en accord avec les modélisations, notamment sur la nature des phases formées. Les principales différences portent sur les proportions respectives. Elles ont été attribuées à la cinétique d'hydratation, non prise en compte lors de la simulation. Par exemple, la présence d'une forte proportion d'ettringite est expérimentalement observée au jeune âge dans les systèmes à haute teneur en sulfates, tandis que le laitier et le ciment portland présentent une cinétique d'hydratation plus lente par rapport au CAC et à l'hémihydrate. L'ettringite formée étant relativement stable dans le temps, sa présence modifie la proportion des ions disponibles pour l'hydratation par rapport au système initial. C'est également la raison principale proposée pour expliquer pourquoi l'hydrogrenat et le monosulfoaluminate contenant du fer, prédit dans les modèles, n'ont pas été détectés expérimentalement, du moins en quantités significatives. Le faible degré de cristallinité de ces phases peut également expliquer la difficulté de quantifier la proportion réelle des divers hydrates.

Par rapport aux formules de référence, l'évolution au cours du temps de l'assemblage des phases déterminée expérimentalement montre que l'influence du laitier se manifeste principalement sur les silicates (i.e.

strätlingite, gehlénite, C-S-H) où des changements majeurs ont été observés. Le composant cristallisé du laitier, la wüstite, est également apparu non réactif, démontrant que seule la fraction vitrifiée du laitier se dissolvait de manière significative tout au long de la période de durcissement d'un an. De plus, la réactivité du laitier a pu être démontrée à partir des spectres IRTF sur la base du déplacement du pic de la bande asymétrique Si-O du laitier à environ 930 cm^{-1}. Cependant, la complexité des systèmes étudiés et la difficulté de caractériser les phases amorphes en utilisant les techniques de caractérisation de l'hydratation du ciment n'ont pas permis d'identifier de manière concluante la nature de la phase hydratée contenant du fer.

Mécanisme de l'hydratation du fer

Le fer initialement contenu dans le laitier a été détecté à l'aide de la microscopie électronique (MET et METB) principalement dans des phases de gel amorphe (**Figure 8**). Ces gels sont plus riches en Al dans les systèmes binaires, tandis que les proportions de Ca et de Si sont plus élevées dans les systèmes ternaires (**Figure 9**). Cette différence est liée à la contribution du ciment Portland dans ces derniers. Les images MET de certaines des phases observées dans les pâtes contenant du laitier sont présentées à la **Figure 8**. Dans ces images, la morphologie distincte de chaque phase est bien visible.

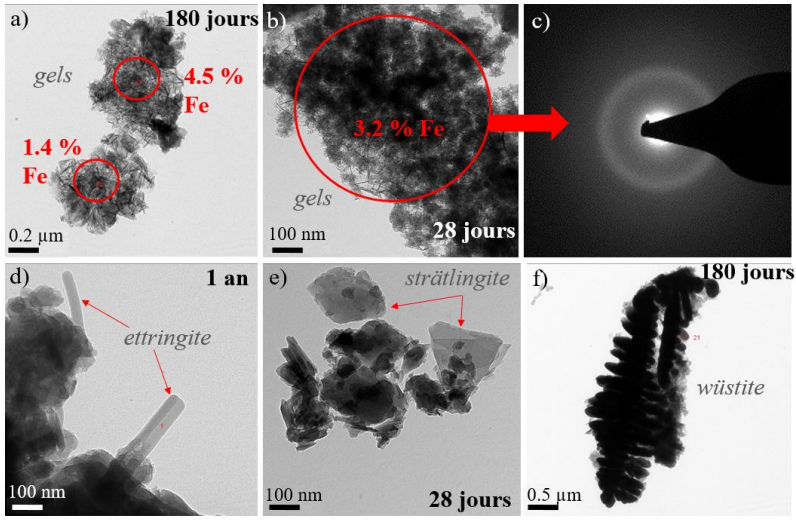

Figure 8 *Images MET de certaines phases observées dans les pâtes contenant du laitier, notamment : gels contenant du fer (a-b) avec leur diffractogramme (c) ; ettringite (d) ; strätlingite (e) et wüstite (f)*

À plus longs termes, les résultats obtenus par microscopie électronique ont montré que la composition des gels tend à se déplacer, dans le diagramme

ternaire, vers celle d'hydrates à plus faible teneur en calcium. Après une période de durcissement plus longue (> 180 jours), les cartographies obtenues par METB ont révélé la formation d'une phase nanocristalline riche en fer dans le système binaire. Cette phase non identifiée présentait une morphologie en forme de tige/aiguille (**Figure 9**) avec un espacement inter couches atomiques d'environ 7,2 Å, estimé à partir de son diagramme de diffraction électronique. Sur la base de ces caractéristiques et de la composition chimique (EDS), les phases pouvant correspondre seraient l'hydroxyde de fer-aluminium et l'hydroxyde doubles lamellaires (LDL) contenant du fer. Cette dernière structure pourrait expliquer davantage la quantité relativement importante de Mg détectée dans cette phase. Malheureusement, les techniques mises en œuvre n'ont pas permis de révéler avec certitude l'identité de cette phase hydratée riche en fer. Des techniques ou des méthodologies complémentaires sont nécessaires pour l'identifier avec certitude. Néanmoins, la possibilité que cet hydrate se transforme à termes en hydrogrenat ou en monosulfoaluminate contenant du fer, comme suggéré par les modèles thermodynamiques, doit également être envisagée.

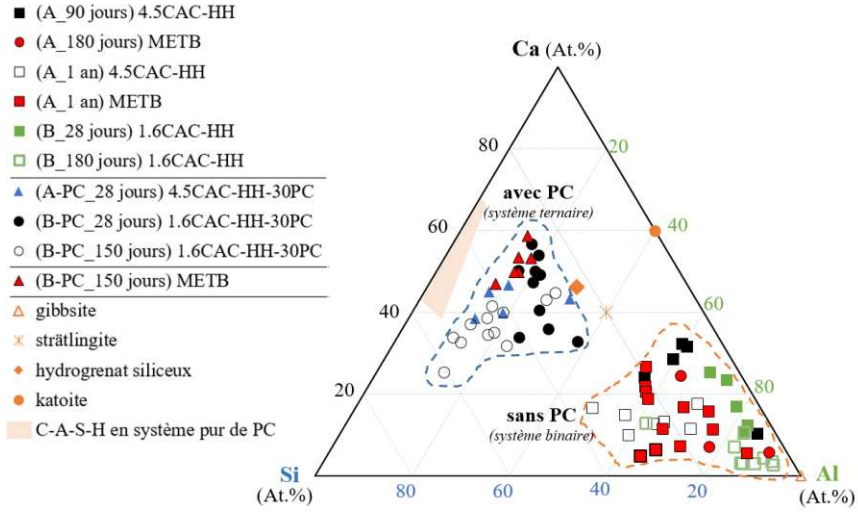

Figure 9 *Diagramme ternaire de composition atomique (At.%) de gels d'hydrates avec 1-12% de fer obtenu à partir d'analyses MET et METB à dispersion d'énergie (EDS). Des points de référence pour la gibbsite, la strätlingite, la katoite, l'hydrogrenat siliceux et le C-A-S-H ont été ajoutés à partir des données de la littérature [17]*

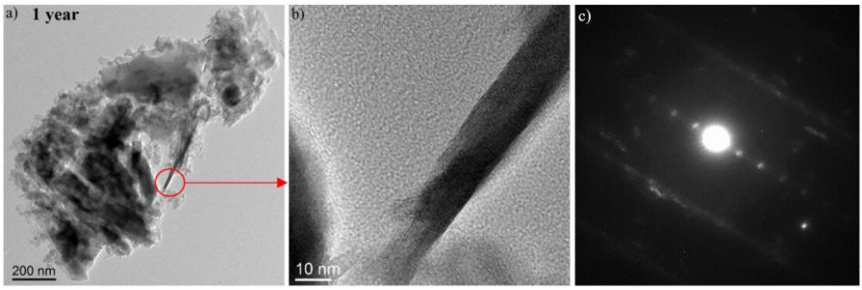

Figure 10 *Images MET (a-b) et diffractogramme (c) mettant en évidence les caractéristiques de la phase nanocristalline non identifiée contenant du fer détectée après 1 an d'hydratation dans le système binaire*

D'autre part, l'évolution des spectres Mössbauer lors de l'hydratation a mis en évidence la transformation de l'environnement atomique du fer, principal composant du laitier. Deux modèles indépendants de décomposition des spectres ont suggéré que l'hydratation du laitier s'accompagnait d'une oxydation du fer de l'état 2+ à 3+ et d'un changement de coordination tétraédrique à octaédrique avec des atomes d'oxygène. Les paramètres Mössbauer utilisés pour les nouvelles phases formées sont similaires à ceux rapportés pour les gels de ferrihydrite et les monosulfoaluminates contenant du fer. L'un des modèles a également indiqué un composant supplémentaire de Fe (II) ayant une coordination de 4 à 5, phase hydratée jamais signalée pour des ciments jusqu'à présent.

Les autres sous-produits SOCRATES

Le potentiel de valorisation du résidu de jarosite en tant que source de sulfate et du résidu du recyclage du papier en tant qu'activateur minéral dans les systèmes binaires CAC-HH ont également été explorés.

Les résultats ont montré que lorsque le résidu de jarosite remplace la source de sulfate de calcium (jusqu'à 50 % en masse), la résistance à la compression est maintenue à 26 MPa après 1 jour et 60 MPa après 28 jours d'hydratation. Ces performances sont obtenues malgré la faible quantité de soufre soluble dans le résidu de jarosite mesuré à partir du test de conductivité. Cependant, compte tenu de la nature de ce résidu, des analyses rigoureuses de toxicité et de lixiviabilité restent indispensables pour identifier les opérations de prétraitement nécessaires.

D'autre part, l'ajout de 5 % de résidus provenant du recyclage du papier a été ajouté pour induire la dissolution du laitier. Cette addition, riche en chaux, a été accompagnée de 1,3 % d'acide citrique pour le contrôle de la prise. Ce résidu a significativement augmenté la résistance mécanique du mélange (différence de > 10 MPa) alors que seule une augmentation minimale (2-5 %) du degré d'hydratation du laitier a été estimée à l'aide de

la tomographie. L'ajout du résidu du recyclage du papier a semblé avoir un impact sur le pH et la composition de la solution interstitielle ce qui a favorisé la formation de phases AFm.

Conclusion et perspectives

La caractérisation approfondie des propriétés physiques et chimiques des ciments à base d'aluminates de calcium (CAC) incorporant des résidus du projet européen SOCRATES a démontré le potentiel de valorisation de ces produits dans ce type de liant. Des mortiers de haute résistance et stables dimensionnellement ont été obtenus en incorporant 30% d'un laitier amorphe riche en fer dans des liants binaires CAC-HH et ternaires CAC-HH-PC. La méthodologie développée (tomographie, etc.) a permis de montrer qu'environ 50 % du laitier était dissout au-delà de 180 jours. Ce résultat a été confirmé par spectroscopie Mössbauer, qui a montré également que l'hydratation du laitier s'accompagnait de l'oxydation du fer 2+ à 3+, et de la formation de nouveaux hydrates contenant du fer. À l'aide de la microscopie électronique (MET et METB), le fer a été détecté au jeune âge dans des phases complexes formées de gels amorphes riches en aluminium. Le fer a également été détecté à des proportions plus élevées à plus long terme, au sein une phase nanocristalline non identifiée. Dans les systèmes ternaires, cette phase était également associée à du calcium, du silicium et une petite quantité de magnésium.

L'effet du ciment portland, des sulfates et des résidus du recyclage du papier sur la réactivité du laitier ont également été explorés dans cette étude. Les résultats ont montré qu'il n'y avait pas de différences substantielles dans le degré d'hydratation du laitier entre les systèmes à faible et à haute teneur en sulfate étudiés. Au contraire, l'ajout de ciment portland et de résidus du recyclage du papier ont montré une augmentation du degré d'hydratation, toutefois cantonnée au jeune âge (< 28 jours). Cet effet pourrait résulter de la présence accrue d'ions Ca^{2+} dans le système, ainsi que de l'augmentation de l'alcalinité favorisant la dissolution du laitier.

Pour conclure, il reste encore des questions importantes en suspens, tant pour expliquer les mécanismes fondamentaux de l'hydratation que pour tester la durabilité de ces liants. Ainsi, les travaux futurs devraient se concentrer sur des analyses complémentaires pour identifier la phase nanocristalline contenant du fer. Elles pourraient utiliser des techniques de caractérisation supplémentaires, ou bien reproduire les systèmes de manière synthétique (phases pures) pour limiter notamment le problème de l'interférence des phases à échelle nanométrique. De plus, la méthodologie par tomographie et les modèles utilisés pour la spectroscopie

Mössbauer pourraient être encore améliorés afin d'affiner les résultats et leur interprétation.

L'étude a bien montré la réactivité du laitier et son impact positif sur les propriétés. Cependant, avant d'envisager la commercialisation de ce liant, il faudrait encore optimiser les proportions de CAC, HH, PC et laitier, voire aussi augmenter la réactivité du laitier au jeune âge (broyage, composition, trempe) et enfin évaluer la durabilité de ce nouveau liant alumineux.

Enfin, optimiser les proportions de CAC, HH, PC et laitier ; augmenter davantage la réactivité du laitier surtout au jeune âge ; et l'évaluation de la durabilité, sont des étapes essentielles pour augmenter le potentiel de commercialisation de ce liant.

Bibliographie

[1] United Nations Environement Program (UNEP), Buildings and climate change: Summary for decision-makers, 2009, www.unep.fr/scp/sun.

[2] K.L. Scrivener, V.M. John, E.M. Gartner, Eco-efficient cements: Potential economically viable solutions for a low-CO2 cement-based materials industry, Cement and Concrete Research 114 (2018) 2–26.

[3] P.J.M. Monteiro, S.A. Miller, A. Horvath, Towards sustainable concrete, Nature materials 16 (2017) 698–699.

[4] A. Vollpracht, B. Lothenbach, R. Snellings, J. Haufe, The pore solution of blended cements: a review, Mater Struct 49 (2016) 3341–3367.

[5] S. Samad, A. Shah, M.C. Limbachiya, Strength development characteristics of concrete produced with blended cement using ground granulated blast furnace slag (GGBS) under various curing conditions, Sādhanā 42 (2017) 1203–1213.

[6] SOCRATES EU MSCA-ETN, Project proposal: Innovative training networks (ITN) call: H2020-MSCA-ITN-2016, Part B, 2016, https://etn-socrates.eu/.

[7] J.E. Rossen, Composition and morphology of C-A-S-H in pastes of alite and cement blended with supplementary cementitious materials, Lausanne, EPFL, 2014.

[8] R. Snellings, G. Mertens, J. Elsen, Supplementary Cementitious Materials, Reviews in Mineralogy and Geochemistry 74 (2012) 211–278.

[9] D. Marchon, S. Kawashima, H. Bessaies-Bey, S. Mantellato, S. Ng, Hydration and rheology control of concrete for digital fabrication: Potential admixtures and cement chemistry, Cement and Concrete Research 112 (2018) 96–110.

[10] W. Chen, H.J.H. Brouwers, The reaction of slag in cement, theory and computer modelling: Materials Science, 2006.

[11] M.F. Zawrah, A.B. Shehata, E.A. Kishar, R.N. Yamani, Synthesis, hydration and sintering of calcium aluminate nanopowder for advanced applications, Comptes Rendus Chimie 14 (2011) 611–618.

[12] E. Henry-Lanier, B. Espinosa, C. Eychenne-Baron, Environmental footprint of calcium aluminate cement (CAC), in: C.H. Fentiman, R.J. Mangabhai, K. Scrivener (Eds.), Calcium aluminates: Proceedings of the international conference 2014, Palais des Papes, Avignon, France, 18-21 May 2014 / edited by Charles Fentiman, Raman Mangabhai and Karen Scrivener, IHS, Bracknell, Berkshire, 2014, pp. 3–16.

[13] A.M. Dunster, F. Moulinier, K.C. Quillin, G.J. Osborne, Durability of concrete made with calcium aluminate cement and ground granulated blastfurnace slag in sulfate and marine environments, in: C. Fentiman, R. Mangabhai, K. Scrivener (Eds.), Calcium Aluminate Cements Proceedings of the centenary conference 2008, 2008.

[14] S. Kucharczyk, J. Deja, M. Zajac, Effect of Slag Reactivity Influenced by Alumina Content on Hydration of Composite Cements, ACT 14 (2016) 535–547.

[15] L. Fernández-Carrasco, E. Vázquez, Reactions of fly ash with calcium aluminate cement and calcium sulphate, Fuel 88 (2009) 1533–1538.

[16] A.J. Majumdar, R.N. Edmonds, B. Singh, Hydration of Secar 71 aluminous cement in presence of granulated blast furnace slag, Cement and Concrete Research 20 (1990) 7–14.

[17] I. Garcia-Lodeiro, A. Palomo, A. Fernández-Jiménez, D.E. Macphee, Compatibility studies between N-A-S-H and C-A-S-H gels. Study in the ternary diagram Na2O–CaO–Al2O3–SiO2–H2O, Cement and Concrete Research 41 (2011) 923–931.

Table of Contents

List of Figures

List of Tables

Glossary

Cement shorthand notations for oxides:

H: H_2O C: CaO A: Al_2O_3 S: SiO_2 F: Fe_2O_3 $: SO_3 c: CO_2 T: TiO_2

Abbreviations of main anhydrous and hydrated phases:

CA	$CaAl_2O_4$	Monocalcium aluminate
C_3S	$Ca_3S_iO_5$	Alite
C_2S	Ca_2SiO_4	Belite
C_4AF	$Ca_4Al_2Fe_2O_{10}$	Tetracalcium aluminoferrite (ferrite)
C_2AS	$Ca_2Al_2SiO_7$	Gehlenite (Geh)
Cc	$CaCO_3$	Calcite
$C\$H_{0.5}$	$CaSO_4 \cdot 0.5H_2O$	Calcium sulfate hemihydrate
$C\$H_2$	$CaSO_4 \cdot 2H_2O$	Gypsum (Gyp)
$C_6A\$_3H_{32}$	$Ca_6Al_2(SO_4)_3(OH)_{12} \cdot 26(H_2O)$	Ettringite (Ett)
$C_4A\$H_{12}$	$Ca_4Al_2(SO_4)(OH)_{12} \cdot 6(H_2O)$	Monosulfoaluminate (Ms)
C_2ASH_8	$Ca_2Al_2SiO_2(OH)_{10} \cdot 3(H_2O)$	Strätlingite (Str)
C_3AH_6	$Ca_3Al_2(OH)_{12}$	Hydrogarnet (Hdg)
AH_3	$2 \cdot Al(OH)_3$	Gibbsite (Gib)
	FeO	Wüstite (Wue)

Materials:

CAC	Calcium aluminate cement, Ciment Fondu® or Secar 51®
PC	Ordinary Portand cement, Milke® Premium
HH	Calcium sulfate β-hemihydrate, Prestia Selecta®
C$	Calcium sulfate
(quartz) filler	Fine sand, Millisil E400®
NFM slags	Non-ferrous metallurgy slags
slag	Granulated iron-rich slag (Chapters 3and 4)
paper residue	Residue from paper recycling, Top-Crete®
SCM	Supplementary cementitious materials
binder	Cement (CAC, PC) + HH + SCM or filler

IP	Inorganic polymer

Techniques:

PSD	Particle size distribution
SSA	Specific surface area
XRF	X-ray fluorescence
XRD	X-ray diffraction
TGA	Thermogravimetric analysis
ATR-	Attenuated total reflection-
FTIR	Fourier transform infrared spectroscopy
XCT	X-ray computed tomography
SEM	Scanning electron microscopy
(S)TEM	(Scanning) Transmission electron microscopy
MS	Mössbauer spectroscopy
XANES	X-ray absorption near edge structure
NMR	Nuclear magnetic resonace spectroscopy
XAS	X-ray absorption spectroscopy

Other abbreviations:

wt%	weight percent
at%	atomic percent
vol%	volume percent
w/b	water to binder ratio
SAI	strength activity index
VOI	volume of interest in XCT
BSE	backscaterred electron in SEM or TEM
EDS	energy-dispersive (detector) in SEM or TEM
primary axis	located on the vertical left
secondary axis	located on the vertical right

Introduction

Circular economy is one of the fundamental building blocks of the European Union's (EU) agenda towards sustainable growth enacted by the 2021 European Green Deal [1]. This concept revolves around regenerative resource cycles with a focus on minimization of waste through process optimization, materials substitution and recycling. As a consequence, research and development of sustainable processes and products is instigated as a critical prerequisite towards achieving EU's climate neutrality targets by 2050.

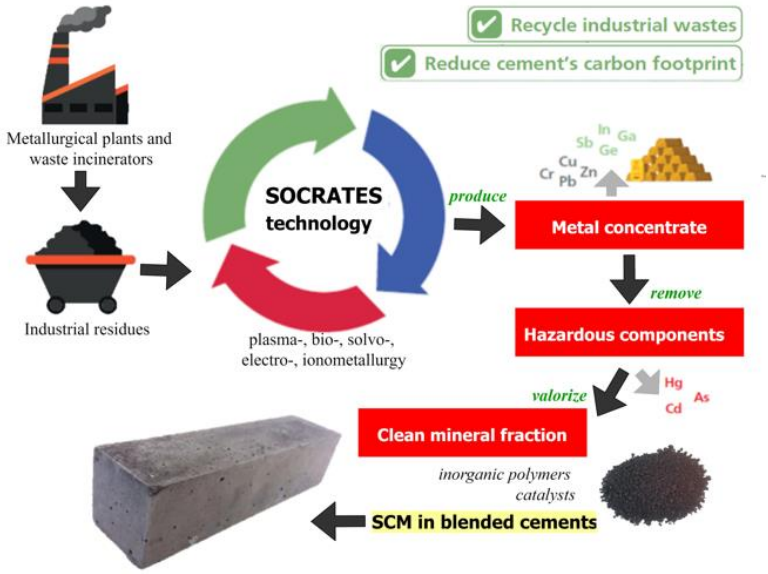

Figure 2 *Simplified flow sheet of the SOCRATES Project with emphasis on the work of the author: residual matrix valorization as supplementary cementitious materials (SCM) in blended cements*

The EU MSCA-ETN SOCRATES[1] project promotes circular economy through valorization of industrial by-products including (but not limited to) non-ferrous metallurgy (NFM) slags, municipal solid waste incinerator (MSWI) bottom ash, jarosite and paper residue, in various applications. A general flow sheet of this project is shown in **Figure 2**. Initially, precious metals and critical elements are extracted for further refining while toxic components are removed for containment. The remaining clean mineral

[1] Marie Skłodowska-Curie Actions (MSCA) – European Training Network (ETN) for the sustainable, zero-waste valorization of critical-metal-containing industrial process residues under the EU Framework Program for Research and Innovation Horizon 2020 Grant Agreement No.721385

fraction, comprising at least 80-90 % of the total volume, is then valorized as precursor for inorganic polymers, as catalysts, or as supplementary cementitious materials (SCM) in blended cements [2]. The lattermost encompasses the research work presented in this thesis manuscript. Having undergone pre-processing prior to the addition in the dry-mix, these materials are generally referred to as "engineered residues" or "SOCRATES residues/by-products".

Generally, when by-products are adapted as substitutes to cements, as aggregates, or as precursors for other construction materials, environmental and economic benefits are envisioned while maintaining acceptable product performance [3,4]. If the SOCRATES residues prove to be viable candidates, the impact of this valorization path would be substantial, considering the following figures [5]:

- ≈ 8 % of the global anthropogenic CO_2 is attributed to cement manufacturing
- ≈ 30 billion metric tons of concrete is produced globally per year
- ≈ 25-50 % of projected global increase in demand for concrete in 2050

With these, it is easy to comprehend how sustainable binders have received significant attention in Europe in the recent decades. Nonetheless, there remain plenty of research gaps to be addressed not only in terms of the variety of residues and cement systems investigated, but also in understanding the properties and hydration mechanism of these binders. Majority of the previous research works are focused on the addition of the more traditional SCM (i.e., GGBFS[2], coal combustion fly ash, and limestone) in ordinary Portland cement (PC)-dominated binders [6,7].

Studies on the more conventional systems consistently support the "filler effect" mechanism, suggesting that the SCM promote a more extensive hydration by acting as an inert filler in the early hours. This was due to the enhanced nucleation and growth when the SCM added is finer than the cement component; and to the higher effective water to cement ratio as less proportion of cement is added in the blend [8,9]. In the early stage of hydration, this effect is said to be mainly physical in nature considering the often lower dissolution rate of SCM relative to the cement component. At long term however, ions released from the dissolving SCM could chemically alter the hydration mechanism. For instance, siliceous SCM such as fly ashes contribute silica for the formation of strätlingite, C_2ASH_8. In addition, the dissolution of lime and alkali from the SCM could also

[2] ground granulated blast furnace slag (GGBFS)

modify the pH of the pore solution, thereby modifying the solubility of the phases during hydration [6,9].

Industrial Residues as SCM

The incorporation of various types of traditional SCM in cement-based construction materials have long been widely adopted on a commercial scale [4]. However, their limited and often localized availability remains to be an important challenge in boosting their market share. This is further threatened by the sustainability-motivated decline in the numbers of carbon-intensive energy and iron manufacturing plants where most of the traditional SCM are generated [10]. This opens the opportunity for exploring alternative sources of SCM with the general preconditions being that these sources should be relatively clean (depleted of metals and toxic components), sustainable (low environmental footprint), of lower or comparable-cost, and of substantial high volume. Although these main conditions are aligned with those envisioned for the pre-treated SOCRATES residues, it is obviously still critical to assess their reactivity and performance in the binders.

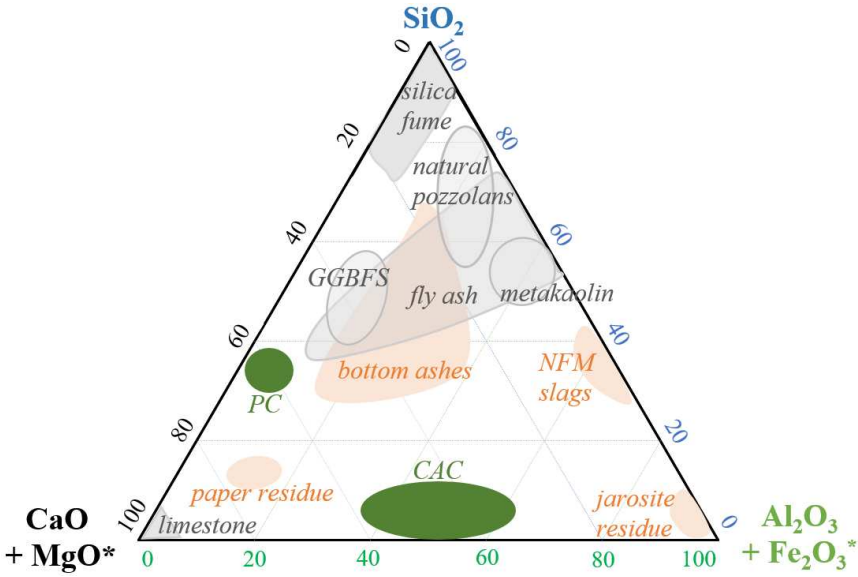

Figure 3 *Chemical compatibility of some of the SOCRATES residues (orange); traditional SCM (gray) and cements (green). The *MgO and *Fe2O3 components are exclusively accounted for the SOCRATES residues. Data were collated to create a modified version of the ternary diagrams reported in [2,11–13].*

The chemistry, crystal structure and other properties of the SOCRATES residues could be very different compared to those of the traditional SCM.

For instance, whereas the latter consist mainly of CaO, SiO_2 and Al_2O_3, NFM slags and jarosite residue are much richer in iron and sulfates, respectively. The difference in the chemistry among the SOCRATES residues, traditional SCM and cements is depicted in a ternary diagram in **Figure 3**. Although this diagram is already valuable in grouping the different resources, there is more information not disclosed. For instance, the phase where iron partitions in the NFM slag and jarosite is amorphous versus crystalline, and predominantly Fe^{2+} versus Fe^{3+}.

Although MSWI bottom ashes could have major (>70 wt%) proportion of CaO, SiO_2 and Al_2O_3, they typically have a much lower degree of vitrification as opposed to fly ashes or the GGBFS. Apart from the difference in chemistry and oxidation state of certain metals (that might affect the glass forming ability), this is also due to the lower firing temperature they have been exposed to (where only partial vitrification occurred) as well as due to the slower cooling rate afterwards. On the other hand, the substitution level with the commercially-marketed paper residue [14] remains limited due to its relatively high free lime content.

Overall, the NFM slags are of particular interest as SCM among the SOCRATES residues. This is mainly because of their expected highly amorphous nature which is often linked to their reactivity [15]. In addition, these slags have undergone high temperature pre-treatment such that the heavy metals and toxic components are substantially depleted. However, there have been no foregoing studies, to the best of the author's knowledge, discussing the reactivity and the hydration mechanism of iron (Fe)-rich slags in calcium aluminate cement (CAC)-based systems.

With this general perspective, the work defined in the context of the SOCRATES project targets a missed opportunity not only in the application stand point, but also in the fundamental understanding of the fate of Fe during CAC hydration. The need for a thorough investigation on the influence several properties to the performance of the binders will be critical in assessing the valorization of the rest of the SOCRATES residues as SCM in this particular cement system.

Calcium aluminate blended cements

CAC is a collective term adopted for high-alumina cements (typically between 40 wt% and 80 wt% Al_2O_3) with monocalcium aluminate (CA) as the principal component [16]. They are used in special applications such as self levelling underlayment (SLU), refractory, and in aggressive environments (**Figure 4**). These applications are driven by the unique properties of CAC, such as of rapid strength development at a wide

temperature range, and resistance to high temperature and chemically aggressive conditions [17].

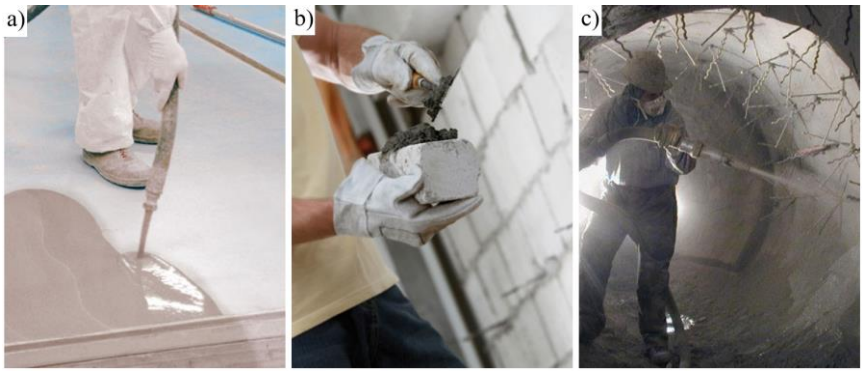

Figure 4 *Some applications of CAC-based binders: (a) self-levelling underlayment, (b) tile adhesive, (c) refractory lining [18]*

In the building chemistry industry, CAC is typically combined with PC and calcium sulfate in different proportions. Binders dominated by CAC take advantage of the fast setting, rapid hardening, shrinkage compensation, and self-drying capacity[3] related to ettringite formation. These binders could display substantial expansion while maintaining high mechanical strength and durability [9]. On the other hand, PC-rich systems are less expensive and more suitable for high volume applications. In these systems, the minor proportion of CAC and calcium sulfate is primarily responsible for the quick setting and relatively high early strength property of the binder [19]. Whereas, the PC component hydrating at a slower rate is known to contribute to the long term strength properties [20].

There are relatively few scientific papers in the open literature on the addition of SCM in CAC-based blends. Even the existing works are limited to the traditional SCM such as GGBFS and fly ashes [21–23]. In terms of sustainability, a Life Cycle Assessment (LCA) comparing SLU blends [24] has previously estimated a lower carbon footprint for CAC-rich ternary binders (containing CAC, PC and calcium sulfate) versus a PC-rich blend while maintaining a comparable applicative performance. In the end, despite the significantly lower scale of annual production estimated for CAC at 2 million tons versus that for PC at 4 giga tons [25], the niche market of CAC should be regarded as a supplemental opportunity for sustainable binders rather than a direct competitor of PC.

[3] The ability of the binder to fully consume the mix water for hydration

Research aims and outline

Two main objectives were laid out in the context of the SOCRATES project, as follows:

1. To evaluate the reactivity of the SOCRATES by-products in CAC-based systems
2. To propose activation techniques for these by-products in order to improve their reactivity, and the performance of the binder

Guided by these objectives, various reactivity tests were established serving as a screening test in order to determine which among the residues has the highest potential for valorization in this application. The evolution of the physical and chemical properties of the selected residue during hydration was subsequently investigated in greater detail.

The challenge of this research work lies in the complexity of the system. The hydration of the ternary CAC, PC and calcium sulfate hemihydrate (HH) binders involves complex reactions often difficult to distinguish as they occur simultaneously. Furthermore, the diverse origin of the SOCRATES residues cannot permit a comparison of the reactivity at equal volume substitution. In addition, the abundance of Fe and the amorphous nature of some of the residues, particularly the NFM slags, require complementary characterization techniques in addition to the more conventional options widely employed in cement systems (i.e., XRD and TGA). Since this investigation involves the use of raw materials rather than synthetic components, it is expected that certain properties could not be directly linked to a single reaction. Nonetheless, the interest is directed towards demonstrating the behavior of raw materials in real complex systems closer to the industrial setting.

The thesis is organized into four chapters, as follows:

Chapter 1 begins with a discussion on the SOCRATES project to provide a general outlook on the unit processes and industrial flow sheets where the residues are generated. The properties and hydration reactions of binary (CAC-calcium sulfate) and ternary (CAC-PC-calcium sulfate) binders are then discussed based on literature reports. The state-of-the-art in SCM addition in these cement systems is also described. Finally, relevant studies on the fate of Fe based on the evolution of its speciation during hydration are collated towards the end of the chapter.

The first half of ***Chapter 2*** provides details on the materials and methods of the study. The properties of the SOCRATES residues, based on their origin, are highlighted. The characterization techniques employed throughout the study are discussed in detail along with the protocols of the tests. The second half of the chapter is dedicated to a screening test to

compare the reactivity of the residues. It ends with a short case study evaluating the use of jarosite as a possible sulfate source in the binary CAC-HH blend. This chapter aims to address the first objective on the list by demonstrating the superior reactivity of one of the Fe-rich NFM slags among the residues tested. This selection narrowed down the focus of the last two chapters of the manuscript.

The reactivity of the Fe-rich slag in the binary (CAC-HH) and ternary (CAC-HH-PC) systems are presented in ***Chapters 3*** and ***4***, respectively. A rapid non-destructive technique for quantifying the degree of slag hydration using tomography is demonstrated in these chapters. The physical properties (strength, setting time, and dimensional stability) of the binders are evaluated using standard mortar samples. The phase assemblage evolution is followed from the early hours (isothermal calorimetry) up to 1 year of curing (XRD, TGA, FTIR) using paste samples. The results were compared to models obtained from (GEMS) thermodynamic simulation. Finally, the fate of Fe during hydration is described at the end of both chapters using advanced microscopy and spectroscopy techniques. The second objective of the research is addressed by examining the potential role as activators of the PC (in the ternary system), sulfates (by varying the CAC/HH ratio), and lime (in the form of the paper residue).

Chapter 1
State-of-the-art

Contents

Introduction

This chapter provides a wider outlook on the SOCRATES Project; calcium aluminate blended cements; supplementary cementitious materials (SCM) in calcium aluminate cement (CAC)-based systems; and the reactivity of non-ferrous metallurgy (NFM) slags. It is essential to begin the discussion with the origin of the SOCRATES residues in order to understand their properties. This also helps assess the environmental impact of their valorization as SCM in blended cements. This discussion is followed by the state-of-the-art on the properties and hydration mechanism of CAC-based blends in pure CAC, binary CAC-calcium sulfate (C$) and ternary CAC-C$-Portland cement (PC) systems.

Moreover, an overview of the incorporation of traditional SCM and industrial by-products (bottom ash, jarosite and NFM slags) in cements is provided highlighting the need for the latter alternative materials and the state-of-the-art in this application. The discussion in this particular section is modified from the author's publication attached in Appendix A. Finally, a brief literature review on the reactivity of Fe-rich NFM slags in cement and inorganic polymer (IP) systems is provided at the end of the chapter. Among the SOCRATES residues, the NFM slags are of particular interest considering their relatively low heavy metals content and their amorphous nature. Both of these are generally considered as favorable properties of SCM and will be elaborated in more detail in this section. The discussion on the fate of Fe during hydration will provide a critical background for the interpretation of results in Chapters 3 and 4 which are dedicated to the addition of NFM slags in CAC-based binders.

1.1. The SOCRATES Project

While promoting circular economy through valorization of industrial residues, the SOCRATES project also aims to develop alternative sources of critical and economically-important metals [26] such as indium, germanium, gallium and antimony. As illustrated in **Figure 1.1**, the recovery of these metals from industrial residues extracted from landfills or directly from primary (ores) and secondary (recycled) metal production flow lies within the scope of the project. Through technospheric mining, whereby minerals are recovered from alternative stocks often considered as wastes, the project aims to close the loop towards circular economy.

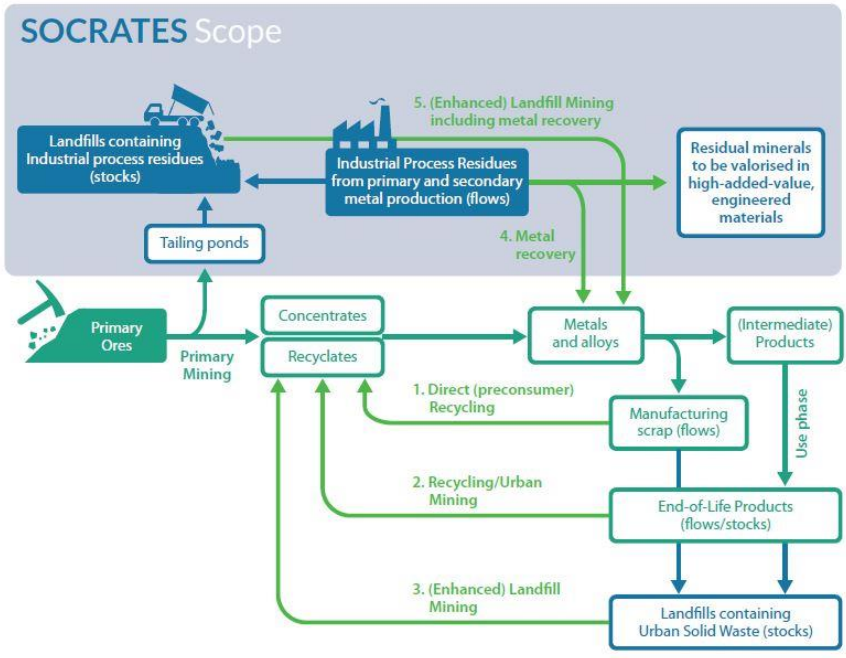

Figure 1.1 *The scope of the SOCRATES project (top part) presented in a generalized life cycle flow sheet for metals and alloys [2]*

It has been reported that there are between 150,000 and 500,000 landfills throughout EU which could be a potential source of secondary raw materials and energy [27]. The benefits from their extraction do not only range from economic (minimizing the landfill remediation cost) and ecologic (land reclamation and health hazards from associated pollution) aspects but could also trigger novel technologies to facilitate the metal extraction [28]. Case in point, a wide range of metallurgical processes including plasma-, bio-, solvo-, electro- and ionometallurgy are explored in the SOCRATES project both in extracting valuable metals and in

removing the hazardous components of the residues [29–33]. Some of the industrial by-products investigated include: NFM slags, MSWI bottom ashes, jarosite and paper-fabrication residues. Most of which have been left in stockpiles or landfills for a long period of time for the lack of suitable application and some due to their toxic components.

The NFM slags in this study are coming from secondary copper and lead-zinc smelting processes typically operated at 1200-1300°C in reducing environment. They are generally dominated by FeO and SiO_2, and contain moderate amounts of Al_2O_3 and CaO. The degree of vitrification is determined by the cooling rate following the tapping[4]. Granulation is often performed by quenching in water to yield higher glass fraction as opposed to air-cooling conditions. When slowly-cooled, the mineralogy is often dominated by fayalite (Fe_2SiO_4) along with other olivine and spinel group phases. Compared to ferrous metallurgy slags, NFM slags are typically richer in trace elements (i.e., Cu, Cr, Mn, Pb and Zn) that may pose challenge to their reuse in construction applications. Case in point, heavy metals have been reported to retard the precipitation of portlandite with the reduction of pH resulting from the hydrolysis of metal ions [34].

One of the promising technologies to refine NFM slags, particularly fayalitic copper slags, in the project is the submerged plasma fuming process (**Figure 1.2**). It aims to recover Pb and Zn, and remove other volatile components (i.e., Cl, F, Ge) using an energy-dense reducing gas made from a combination of heated compressed air and natural gas. The volatile components are precipitated in a post combustion duct and recovered in the form of oxide dusts [35]. The resulting slag, being generally metal-depleted, is being marketed since 2018 as a clean synthetic mineral for sustainable building applications [36].

Another clean (metal-depleted) commercialized by-product assessed in this project is the paper residue. It is derived from the de-inking sludge during the recycling of paper wastes in a fluidized-bed incinerator. This process is designed for waste-to-energy applications, such that approximately 7 GWh of electricity (or equivalent to the estimated annual energy requirement of 151,000 households) is generated annually from the incineration of 140,000 tons of paper pulp residue in this process alone [37]. The remaining lime-rich residue after the combustion is marketed as a green binder displaying pozzolanic activity that can be applied in dosages up to 20 wt% [14].

[4] removal of slag by allowing it to flow in a tap hole at the lower region of a blast furnace

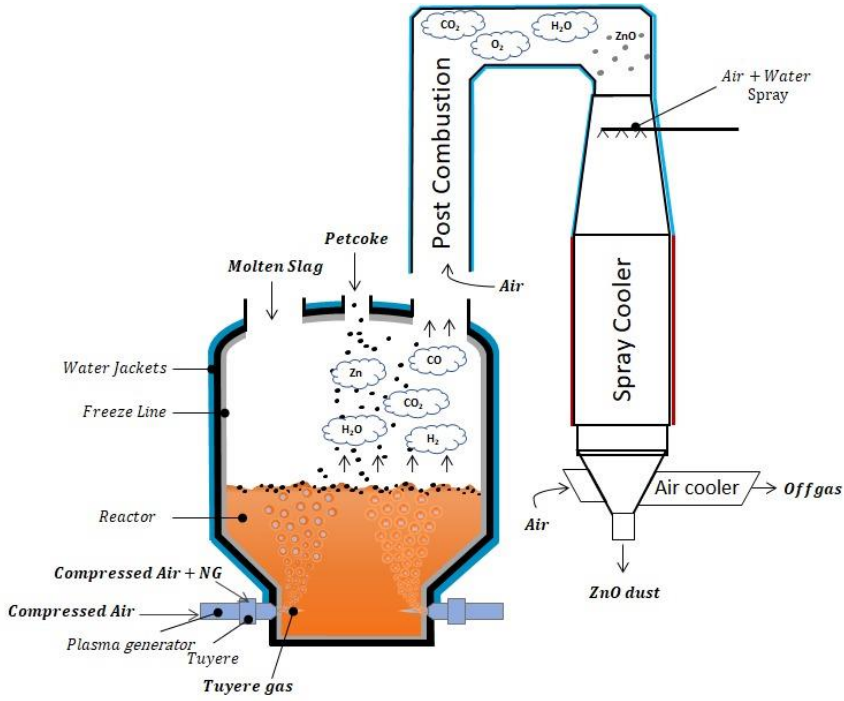

Figure 1.2 *Submerged plasma-driven slag fuming process [35]*

The other SOCRATES by-products, MSWI bottom ash and jarosite residue, generally require further pre-treatment to better adapt their properties according to their intended application. For the latter, this step is often critical to reduce its toxic and heavy metals components. Jarosite ($NaFe_3(SO_4)_2(OH)_6$), in general, is a family of iron-hydroxysulphate minerals formed when iron sulfides are oxidized in ore deposits [38]. Residues of jarosite could be formed as by-products of zinc hydrometallurgy, often classified as hazardous waste due to their heavy metals (Pb and Zn) content [39]. In the SOCRATES project, the elemental sulphur-rich waste stream from direct zinc sulphide leaching and the jarosite-rich precipitates from the other direct leaching reactors are filtered together creating "jarosite residue" as it is labelled in this study. While the majority of these residues are currently contained in landfills, pilot scale pyrometallurgical trials have been initiated to recover the metals and produce a cleaner slag more suitable for construction applications [40].

On the other hand, the MSWI bottom ash investigated is heterogeneous, with inclusions of plastics, stones, bricks, glass, metals and other unburnt materials. Without prior assortment (i.e., sieving and magnetic separation) to remove these unburnt fraction, the irregularly-shaped particles when used as SCM could increase its water absorption capacity and

consequently reduce its strength [41]. In addition, thermal treatment might even be necessary in some cases (i.e., high metallic aluminum and bottle glass in fines fraction) to vitrify the bottom ash and obtain a denser microstructure [42].

After pre-treatment, three valorization pathways are explored for the metal-depleted by-products of the SOCRATES project, namely: as heterogeneous catalysts; (2) as precursors to inorganic polymers (IP); and (3) as SCM in CAC-based binders. These applications are directed towards high-value, high-volume valorization relative to the more conventional utilization in sandblasting and in aggregates replacement. Unlike the latter applications, the reactivity of the residues will be critical in their role as catalysts and binders.

For catalysis, the residual matrix in the SOCRATES flow sheet could be interesting for specific reactions[5] due to their high FeO and CaO contents [2,43]. They could serve as cheaper alternatives for precursors although the influence of the impurities on the catalytic performance must be rigorously investigated to corroborate this application. On the other hand, utilization as precursors to construction materials offers the high volume valorization especially in the case of IP where the viability of complete substitution of aluminosilicates[6] with similar NFM slags has been previously demonstrated [44–46]. In these systems, the slags are mixed with alkali silicates or hydroxides to form a 3D-connected Si-O networks. The abundance of Fe in the glass component of the NFM slags favors its dissolution in the alkaline medium and could be a favorable criterium towards Fe's participation in the polymerization process [34,47]. Similar to CAC, the durability and environmental advantages of IP binders relative to PC has been driving its demand in niche markets [48,49].

The third valorization pathway, for which this PhD work is dedicated, revolves around the incorporation of the by-products as SCM in CAC-based binders. As previously highlighted in the introduction, this valorization potential not only aims to recycle the industrial by-products but also to reduce the carbon footprint of cement. The specialized market of CAC dedicated to fast repair, aggressive environment, and high temperature applications is a supplemental opportunity to those of the PC systems. The limited work in the open literature concerning the addition of similar industrial by-products in CAC systems also supports the novelty of this study. As an SCM, it will be critical to assess the chemical reactivity

[5] in particular: selective catalytic reduction of NO_x with NH_3 ; propane dehydrogenation to propylene and propylene epoxidation

[6] kaolinite, fly ash and blast furnace slags more conventionally used as precursors to IP

of the by-products and to perform a screening test to narrow down the selection. Based on this selection, the physical properties and the hydration mechanism of the by-product with the highest potential are explored in more details aided by advanced characterization techniques.

1.2. Calcium aluminate blended cements

Cements based on calcium aluminates marked more than a century of full commercialization since Jules Bied's patent for the manufacture of CAC in 1908. His process is based on the fusion of low-silica aluminous and ferruginous raw materials, mainly bauxite, with limestone. Initially, the demand for this special type of cement has been driven by the durability issues encountered with PC, particularly in sulfate-rich environment. An even greater volume demand for CAC was realized in 1916 during the First World War as its rapid hardening properties made it suitable for construction of gun emplacements [50]. Rigorous tests and studies that followed led to the production of various CAC products that we now know today.

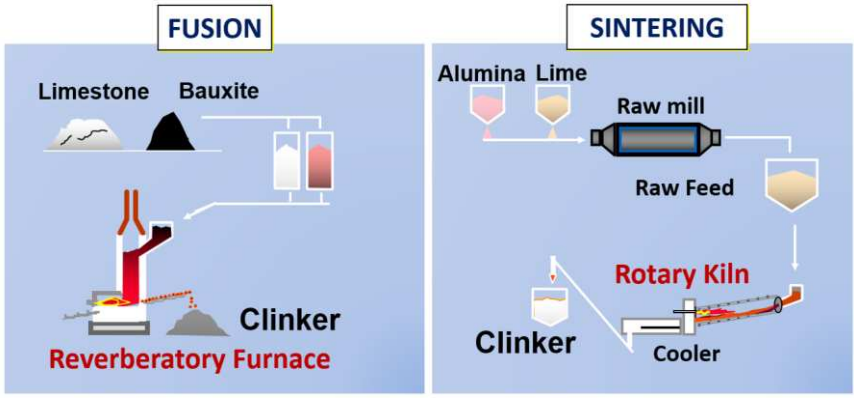

Figure 1.3 *Two manufacturing processes for CAC production [18]*

There are two manufacturing processes for CAC production, namely: fusion and sintering (**Figure 1.3**). Fusion is operated at temperatures above 1400°C in a reverberatory furnace using limestone and bauxite as the main raw components. This process yields the more traditional CAC products (i.e., Ciment Fondu®, Secar 51®) at the lower alumina range, typically below 52 wt%, and could be darker in color due to the higher Fe content. On the contrary, the white varieties of CAC (i.e., Secar 71®), richer in alumina, are produced from the sintering of alumina and lime at temperatures above 1500 °C in rotary kilns. The latter is primarily used for

refractory and decorative usage, while the former is more adapted for higher volume construction purposes [18,19].

CAC is generally dominated[7] by monocalcium aluminate (CA) and could alternatively contain significant proportions of calcium di-aluminate (CA_2) and mayenite ($C_{12}A_7$) as the "active phases". Moderate amounts of gehlenite (C_2AS) and ferrite phase (C_4AF) are typically present and the rest is principally balanced by smaller percentages (<5 wt%) of belite (C_2S), perovskite (CT), and spinel ($MgAl_2O_4$).

1.2.1. Pure CAC systems

CAC hydration is highly dependent on temperature, in contrary to that of the PC for which hydrates formed are said to be generally similar at a broader temperature range [51]. This temperature dependence defines whether the hydrates formed are metastable (CAH_{10}, C_2AH_8) or stable (C_3AH_6). The metastable hydrates form, according to reactions given in **Equation 1.1 and 1.2**, at lower temperature [52]. On the other hand, stable hydrogarnet, C_3AH_6, is formed at elevated temperature as represented in **Equation 1.3**. In real systems however, the presence of impurities that can act as nucleation sites, and the kinetic effects can influence the formation of the hydrate phases therefore shifting the below indicated temperatures of formation [19].

$$CA + 10H \rightarrow CAH_{10} \qquad <15°C \qquad \textit{Equation 1.1}$$

$$2CA + 11H \rightarrow C_2AH_8 + AH_3 \qquad 27\text{-}50°C \qquad \textit{Equation 1.2}$$

$$3CA + 12H \rightarrow C_3AH_6 + 2AH_3 \qquad >50°C \qquad \textit{Equation 1.3}$$

The above reactions occur in the solution following a dissolution-precipitation mechanism [53]. Ca^{2+} and $Al(OH)_4^-$ ions are released as the main component of CAC, CA, dissolves in contact with water. A layer of $Ca[Al(OH)_4]_2$ is generated around the surface layer of CA as the ions are hydrated until supersaturation where the hydroxylated phase dissolves again to form calcium aluminate hydrates, as those presented in the above equations. In these reactions, the AH_3 formed can take an amorphous or crystalline form (i.e., gibbsite, bayerite or nordstrandite). Setting is triggered by the consumption of one of the reactants or by the limited space for hydrate precipitation [9]. Other possible reactions during the hydration of pure CAC systems originate from the hydration of the minor components (< 10 wt% in total), such as alite (C_3S), belite (C_2S), tricalcium

[7] approximately <60 wt% CA for fused CAC and 60-70 wt% CA for sintered CAC

aluminate (C_3A), ferrite (C_4AF) phase, and calcium carbonate (Cc)[8], listed in **Equation 1.4 to 1.10** [19,54].

$$C_3S + (y + 1.3)H \rightarrow C_{1.7}SH_y + 1.3CH \quad \textit{Equation 1.4}$$

$$C_3S + AH_3 + 6H \rightarrow C_2ASH_8 + CH \quad \textit{Equation 1.5}$$

$$C_2S + (y + 0.3)H \rightarrow C_{1.7}SH_y + 0.3CH \quad \textit{Equation 1.6}$$

$$2C_3A + 21H \rightarrow C_4AH_{13} + C_2AH_8 \quad \textit{Equation 1.7}$$

$$C_3A + Cc + 11H \rightarrow C_4AcH_{11} \quad \textit{Equation 1.8}$$

$$C_3A + 0.5Cc + 0.5CH + 11.5H \rightarrow C_4Ac_{0.5}H_{12} \quad \textit{Equation 1.9}$$

$$C_4AF + 32H \rightarrow C_4(A,F)H_{13} + 2C_2(A,F)H_8 + (A,F)H_3 \quad \textit{Equation 1.10}$$

where y=H_2O/Si; and (A,F) signifies Al_2O_3-Fe_2O_3 substitution

Aside from the difference in the principal active phase compared to PC, the pore water pH of pure CAC systems is 11.4-12.5, which is typically much lower compared to the 12.6-14 for the PC system [55]. This lower pH is considered as an advantage for certain applications such as in engineered barrier systems for containing high-level radioactive waste where a clay layer of bentonite is often integrated. This clay layer is reported to be altered in contact with hyper-alkaline solutions leading to the reduction in its swelling ability [56]. In this application, CAC-based blends can be an ideal alternative as structural cast concrete, grouting, sealing of plugs and lining of tunnels [57–59].

However, the main challenge limiting the direct application of pure CAC is the inevitable phenomenon called conversion. It is well-known to be an unfavorable, but manageable, phenomenon in pure CAC binder where the metastable hydrates are converted to stable hydrates **(Equation 1.11 and 1.12)**. These reactions are triggered by the nucleation of C_3AH_6 and could take only a few minutes to occur at elevated temperatures, i.e., 80°C, or several years below 30°C [51,60]. Since these hydrates exhibit differences not only in morphology (**Figure 1.4**) but more importantly in density and solubility, the dimensional stability and hence the mechanical strength of hardened binder is compromised when conversion occurs [61]. In the early 70's, the collapse of reinforced concrete beams in three different buildings in the UK, for which conversion was associated, triggered the restriction for the use of pure CAC binder in construction applications [62–64].

[8] originating either as a component of the raw cement; or produced as a carbonation product of C and CH with the CO_2 gas from the atmosphere during curing/sample preparation

$$3CAH_{10} \rightarrow C_3AH_6 + 2AH_3 + 18H \qquad \textit{Equation 1.11}$$

$$3C_2AH_8 \rightarrow 2C_3AH_6 + AH_3 + 9H \qquad \textit{Equation 1.12}$$

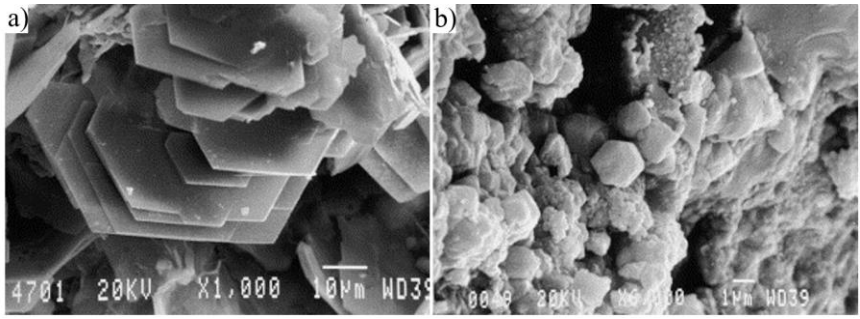

Figure 1.4 *SEM images of the hexagonal CAH_{10} (a) and cubic C_3AH6 (b) [65]*

In order to mitigate the conversion phenomenon, the hydrate phase assemblage can be altered by the addition of: (1) SCM, (2) sulfate carrier or (3) by introducing PC in the system. The incorporation of the more conventional SCM, including GGBFS, microsilica and metakaolin, have been widely investigated in the past [22,66–68] despite these studies being limited to siliceous mineral additives. These previous works have demonstrated that the addition of SCM could reduce the conversion by favoring the formation of strätlingite (C_2ASH_8) over that of the metastable aluminate hydrates. In addition, SCM could also increase the capillary water absorption by altering the pore structure. They can contribute to the long term mechanical strength hence improving the overall stability of the CAC binders, according to these studies.

On the other hand, the addition of sulfates in the system is another approach with the same goal of shifting the hydrate phase assemblage to avoid conversion. An ettringite-binder system is created with the addition of sulfate-containing substances (i.e., gypsum, anhydrite, hemihydrate or mixes thereof) with the main reaction presented in **Equation 1.13**. The self-drying capacity, high early strength, and expansive properties of CAC-based binders particularly in self-levelling mortars are linked to this main hydration reaction [69].

$$3CA + 3C\$ + 38H \rightarrow C_6A\$_3H_{32} + 2AH_3 \qquad \textit{Equation 1.13}$$

In a similar manner, the addition of PC further increases the complexity of the system by modifying the hydrate phase assemblage. In these (CAC-C$-PC) ternary systems, ettringite ($C_6A\$_3H_{32}$) and C-S-H are formed in the early stages of hydration but the assemblage changes with the depletion of the sulfate source [70]. The corresponding reactions depending on the proportion of the components are elaborated in more detail in section 1.2.3.

Despite this major setback in the utilization of pure CAC systems, it is clear that there are several solutions currently available which have been widely demonstrated to mitigate the conversion phenomenon. The interest in CAC binders continue to grow with recent advances directed towards amorphous calcium aluminate cements (ACA) having mayenite, $C_{12}A_7$, as the main reactive phase instead of CA. These latest variants were reported to have lower carbon footprint and display faster hydration kinetics compared to the more conventional CAC based on CA [71,72].

1.2.2. Binary CAC-C$ systems

During the first hours of hydration, the amount of sulfates added influences the phase assemblage, setting time, rheology, and porosity distribution [19]. When designing the formulations, the CA/C$ molar ratio is important in determining the main hydration reactions. In lower sulfate systems (CA/C$ > 2), the formation of ettringite ($C_6A\$_3H_{32}$) and aluminum hydroxide (AH_3) according to **Equation 1.13** is the dominant reaction during the early ages of hydration. The minor components of CAC could also contribute to ettringite formation according to **Equation 1.14 and 1.15**.

$$C_3A + 3C\$H_x + (32 - 3x)H \rightarrow C_6A\$_3H_{32} \quad \textit{Equation 1.14}$$

$$3C_4AF + 12C\$H_x + (134 - 12x)H \rightarrow 4C_6(A,F)\$_3H_{32} + 2(A,F)H_3 \quad \textit{Equation 1.15}$$

When the sulfates are depleted, ettringite transforms into calcium monosulfoaluminate ($C_4A\$H_{12}$) as it reacts with the remaining CA and C_3A from CAC [63] (**Equation 1.16 and 1.17**). The presence of calcium carbonate could also contribute to the consumption of ettringite, leading to the precipitation of monocarboaluminate (C_4AcH_{11}) or hemicarboaluminate ($C_4Ac_{0.5}H_{12}$) according to **Equation 1.18 and 1.19**, respectively.

$$6CA + C_6A\$_3H_{32} + 16H \rightarrow 3C_4A\$H_{12} + 16H + 4AH_3 \quad \textit{Equation 1.16}$$

$$2C_3A + C_6A\$_3H_{32} + 4H \rightarrow 3C_4A\$H_{12} \quad \textit{Equation 1.17}$$

$$C_6A\$_3H_{32} + 2C_3A + 3Cc + 7H \rightarrow 3C_4AcH_{11} + 3C\$H_2 \quad \textit{Equation 1.18}$$

$$C_6A\$_3H_{32} + 2C_3A + 1.5Cc + 10H \rightarrow 3C_4Ac_{0.5}H_{12} + 3C\$H_2 \quad \textit{Equation 1.19}$$

In high sulfate systems (CAC/C$ < 2), the ettringite formed in the early hours of hydration remains stable overtime. However, the excessive

gypsum allows the formation of secondary ettringite at later ages as the less reactive components of CAC (i.e., C_4AF) hydrate. Over-expansion leading to disintegration of mortar samples has been previously reported in such high sulfate formulations, associated to the crystallization pressure of ettringite forming at later ages [73].

Early hours' hydration reactions characterized using ex-situ isothermal calorimetry [9] revealed two main hydration peaks for the majority of CA/HH ratios investigated (**Figure 1.5**). Using in-situ XRD, these peaks were determined to correspond to: (1) the rapid dissolution of HH leading to gypsum formation; and (2) the massive precipitation of ettringite, likely[9] accompanied by aluminum hydroxide. In the low sulfate system with CA/HH molar ratio of 4 (80CA-20HH), a third peak was exclusively observed attributed to the monosulfoaluminate formation as the sulfates were depleted, simultaneous to the continuous dissolution of CA.

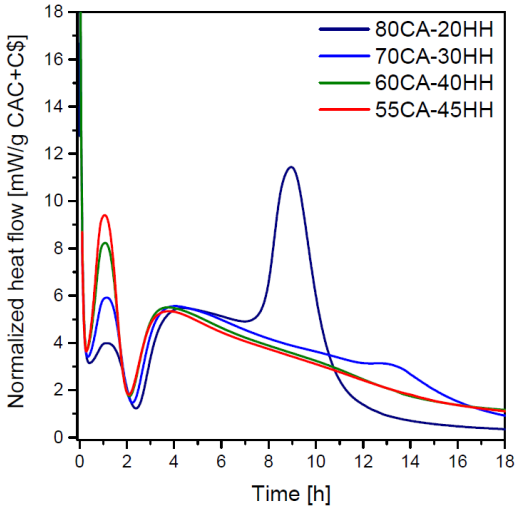

Figure 1.5 *Heat flow curves of formulations with different proportion of CA and HH measured per 10 g of paste samples with 0.4 water to binder (w/b) ratio at 20°C using ex-situ isothermal calorimeter [9]*

This observed influence of the sulfate amount to the phase assemblage during the first hours of hydration, was also reflected at long term through the thermodynamic modelling of a similar binary system (CA-anhydrite) in Saout *et al.,* 2018 [74] in **Figure 1.6**. In this model, the highest water demand coincides with the maximum volume of ettringite formed due to the high amount of bound water in its structure. This yields the aforementioned self-drying capacity of ettringite which is a valuable

[9] the amorphous nature of AH_3 in this formulation hindered its detection using XRD

property in self-levelling concrete applications. It shortens the waiting time by eradicating the need to completely evaporate the excess mix water prior to flooring installation [75].

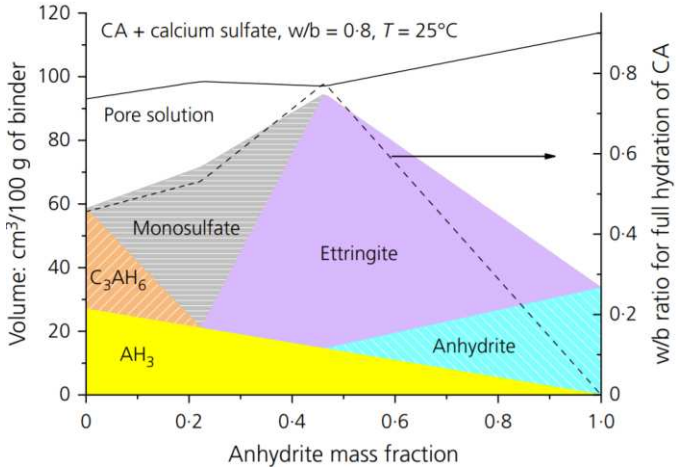

Figure 1.6 *Phase assemblage evolution of CA-C$ (anhydrite) paste derived using thermodynamic modelling at 25°C and 0.8 w/b ratio. The volume of phases are presented on the primary y-axis; while the w/b ratio needed for the full hydration of CA is on the secondary axis [74].*

In terms of the mechanical strength, maximizing the formation of stable ettringite is often targeted to formulate high strength binders [76]. Compared to the typical hexagonal platelets of monosulfoaluminates (**Figure 1.7** a), ettringite is often characterized as having a needle-like morphology (**Figure 1.7** b). Han *et al.,* 2021 [77] reported that these relatively[10] low-density needles of ettringite are able to fill up macropores during hydration, contributing to the compressive strength of the binder. However, the crystal growth pressure accompanying ettringite formation is also reported to cause expansion strains during the early hours of hydration by enlarging the distances between the anhydrous cement particles [79].

[10] ettringite has the lowest (true) density at 1.78 g/cm^3 among the other common hydrate phases in these systems such as monosulfoaluminates (2.01 g/cm^3); gibbsite (2.42 g/cm^3) and strätlingite (1.94 g/cm^3) [78]

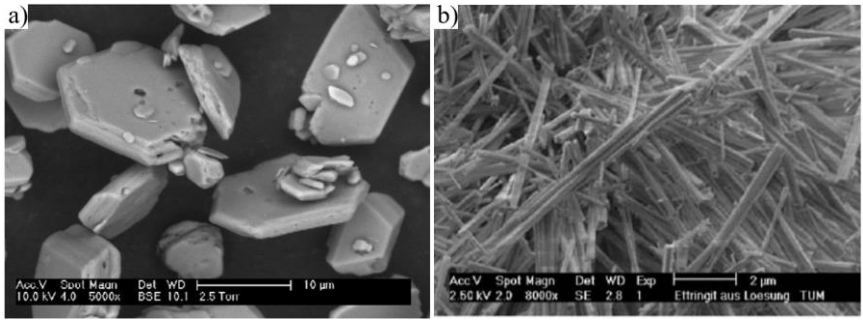

Figure 1.7 *SEM micrograph of: (a)synthesized monosulfoaluminate [80] and (b) ettringite [81].*

Other than the sulfate's influence to the phase assemblage, it also plays a crucial role in controlling the setting time of the dry mix. The typical sulfate carriers (gypsum, anhydrite and HH) readily hydrate and set into calcium sulfate dihydrate in contact with water leading to an accelerated rate of expansion and hardening [79]. For this reason, set retarders (i.e., citric acid, tartaric acid) are often introduced as admixtures in order to counteract the influence of sulfates. Nguyen *et al.,*2019 [82] reported that at a significant dosage of 2 wt%, citric acid does not only retard hydration but could also contribute to the conversion of ettringite to monosulfoaluminate; and influence the mechanical strength of mortars. This was associated to the formation of citrate ligand around ettringite crystals that temporarily inhibits its precipitation, consequently favoring monosulfoaluminate formation [83]. Nonetheless, citric acid is more typically used in smaller amounts (0.1-0.5 wt%) only to control the setting. No evident influence to the phase assemblage or to the mechanical strength should be expected at this dosage [82].

1.2.3. Ternary CAC-PC-C$ systems

Previous studies [84–87] in ternary CAC-PC-C$ binders have hypothesized the governing hydration mechanism in these system. Bizzozero and Scrivener (2014) enumerated the hydration reactions and discussed their kinetics by following the phase assemblage evolution over time in a CAC-rich system [85]. Their study demonstrated the formation of ettringite and AH_3, principally in the early hydration days in a similar manner as in the binary CAC-C$ systems according to **Equation 1.13**. PC could further contribute to this initial ettringite formation by providing additional Ca^{2+} ions in the form of portlandite (CH) in a reaction described in **Equation 1.20**. C-S-H is formed as the main hydration product in PC-rich systems (>80 wt% PC) along with other minor components (i.e., hydrogarnet, strätlingite, monocarboaluminates). This is better

demonstrated in the thermodynamic models of a PC-rich (a) and a CAC-rich (b) ternary systems by Qoku (2017) in **Figure 1.8**.

$$3CA + 9C\$H_X + 6CH + (90 - 9x)H \rightarrow 3C_6A\$_3H_{32} \qquad \textit{Equation 1.20}$$

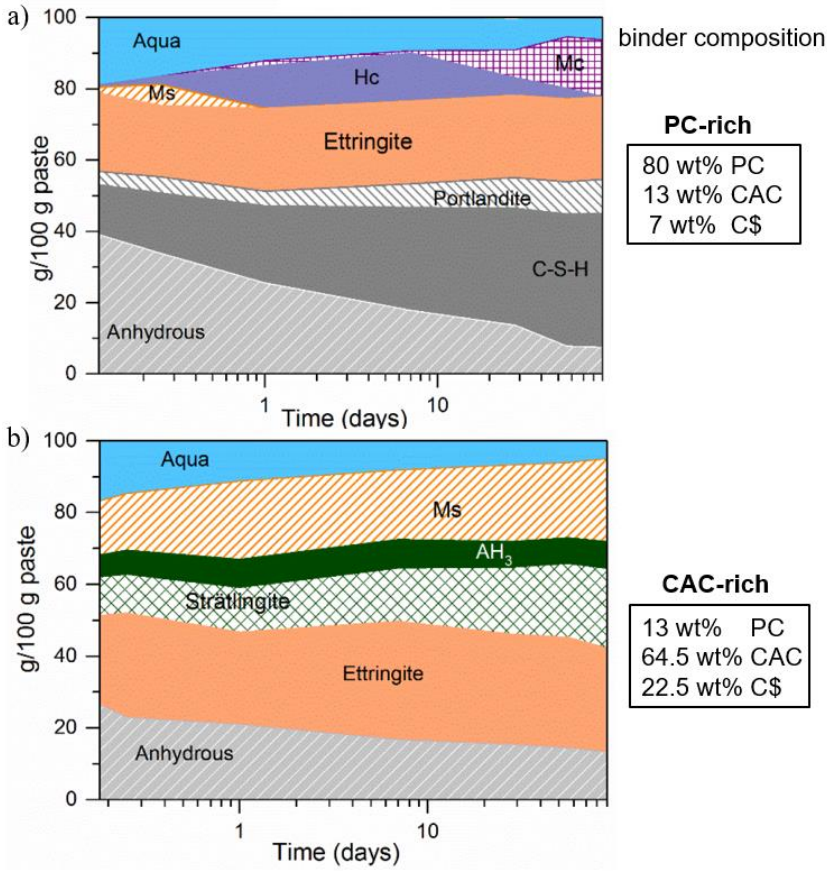

Figure 1.8 *Phase assemblage evolution of: (a) a PC-rich ternary system; and (b) a CAC-rich ternary system, simulated using GEMS thermodynamic modelling at 20°C and 1 bar pressure. Phases were abbreviated as follows: (Ms) monosulfoaluminate; (Hc) hemicarboaluminate; (Mc) monocarboaluminate [19]*

In both the (80 wt%) PC- and (65 wt%) CAC-rich formulations modelled in **Figure 1.8**, ettringite was predicted to form in a significant quantity and remained stable throughout the simulated 90 days of hydration. C-S-H and CH, the main hydration products in pure PC systems, were only present in the PC-rich system. Instead, the silicates from the minor PC added were predicted to be incorporated in strätlingite for the CAC-rich formulation. Furthermore, these models illustrate that CH and AH_3 do not co-exist

thermodynamically; and that the formation of Hc and Mc were likely associated to the PC, typically containing a small amount (< 2 wt%) of calcite. The only significant discrepancy that the author noted between the modelled and the experimental phase assemblages were linked to the kinetic effect. In the thermodynamic models, the components were predicted to dissolve and diffuse uniformly while this may not be exactly the case in the real system [19].

Torréns-Martin *et al.,* 2013 [86] and Nehring *et al.,* 2018 [87] both highlighted the significance of CAC/C$ and PC/CAC ratio to the kinetics of hydration. They explained that in CAC-rich systems with sufficient[11] C$, ettringite layer could form around the anhydrous grains provisionally delaying the silicates (mainly C_3S and C_2S) hydration as it retards the diffusion of ions by creating a temporary barrier. This mechanism was referred as "ettringite barrier layer formation" and was attributed to the observed delay in PC hydration. Using isothermal calorimetry, Torréns-Martin *et al.,* 2013 [86] associated this mechanism to the observed temporary (3-6 hours) halt in the increase of the cumulative heat release curve of a similar ternary binder. When the barrier layer is broken with the continuous dissolution of ions, the cumulative heat release continued to increase again [86]. In terms of mechanical performance, Bizzozero and Scrivener (2014) supported that PC is less reactive in the early hydration and only contributes to the long term (>28 days) strength of mortars [85].

Despite the numerous studies relating to this ternary binder system, the previous investigations were mostly limited to PC-rich formulations, where PC takes 70-85 wt% of the binder in the dry mix. While these blends are more representative of the industrial high volume applications considering the lower cost of PC, the adaptability of CAC-dominated blends in specialized applications along with its conceivable environmental advantage remains indispensable. Case in point, the maximization of the self-drying capacity of CAC in flooring applications can be used as a criterion to optimize the CAC/PC ratio when designing the dry-mix formulations [88]. In terms of sustainability, a Life Cycle Analysis Assessment (LCA) report comparing blends for SLU flooring mortars [24] had previously estimated a lower carbon footprint for a CAC-dominated ternary binder compared to an equivalent volume of a PC-rich ternary blend. Both displayed comparable applicative performance, notably in terms of mechanical strength.

In CAC-based blends, PC is also added at lower proportions (10-30 wt%) to improve the reactivity of GGBFS [19,89] not only by increasing the pH

[11] at the amount where ettringite formation is favored over that of Ms

of the pore solution, but also by contributing ions (Ca^{2+}, $Al(OH)_4^-$ and SO_4^{2-}) that can participate during hydrate formation. Thermodynamic modelling estimates pH values above 12 in pore solution of pure PC hydration [90]; whereas a pH less than 12 is expected for CAC-rich systems even reaching 10.5 with excess C$ [9]. This advantage is further supported by the improved stability of ettringite formed at pH 12 reported in Van-Rompaey, 2006 [91].

1.3. Supplementary Cementitious Materials

Green cements or eco-efficient cements [4] are produced using alternative materials or energy sources with lower environmental footprint for a performance-comparable product. Among other major considerations in assessing the viability of replacement, the cost and the technical performance of the derived formulations are standing out. The substituting material is referred to as a "filler" when its contribution to the properties of the blend and the hydration reactions, if any, are purely physical in nature. On the other hand, the term SCM is used for materials exhibiting hydraulic or pozzolanic properties during hydration [12].

1.3.1. Traditional SCM

Snellings *et al.,* 2012 [12] provided a comprehensive review covering both natural and artificial SCM. The natural SCM are extracted raw from the nature, either of volcanic or sedimentary origin, among which pyroclastic materials, pumices, zeolitic tuffs, and naturally burned clays are included. On the other hand, artificial SCM refer to thermally-treated materials typically generated as by-products of industrial processes. These could range from slags, incineration ashes, burned residues, silica fumes to waste glass. Among these numerous types of SCM, only three materials are considered to take a major role as SCM in the market over the past 25 years [4], briefly described in this reference as follows:

- **GGBFS.** A by-product of ferrous smelting having a global generation of above 300 Mt annually. Historically, metal-depleted ferrous slag were naturally cooled at ambient temperature and once hardened, were sold as aggregates employing minimal comminution. With extensive research supporting the latent hydraulicity of GGBFS and demonstrating its potential as SCM, granulation was integrated in the operation to make this by-product marketable.

- **Fly ash.** A by-product of coal combustion for electricity generation. Despite its threefold annual production compared to GGBFS at 900 Mt, the heterogeneity of this material has kept its valorization as SCM limited. Moreover, as a direct output of coal combustion known to have a primary contribution to the anthropogenic CO_2 emissions, the reallocation of fly ash' environmental loads is under scrutiny [92].
- **Limestone.** Formerly having a limited application as a filler, the reported reactivity of this abundant natural SCM in the past decades has expanded its application in the cement industry. In the recent years, keen efforts have been dedicated to the development and commercialization of a PC-based binder with substantial limestone and calcined clay substitution, claiming a promising impact on reducing the carbon footprint in the building sector [93,94].

The contribution of SCM during the first hours of hydration is said to be limited to physical effect, given that their dissolution is often significantly slower than the cement component in the blend [8]. This "filler effect" mechanism introduced earlier in the discussion is commonly demonstrated using heat flow curves from isothermal calorimetry, as presented in **Figure 1.9** [95]. It shows that the 40 wt% replacement of PC with either slag or fly ash enhanced the intensity of the main hydration peak, creating a sharper acceleration slope and a prolonged deceleration period. As explained earlier, this was attributed to the higher effective water to cement ratio and the additional nucleation sites particularly for fine SCM [9]. The use of quartz as a relatively "inert" filler reference illustrates that SCM displayed no significant chemical reactivity during the first 35 h of hydration.

At longer hydration period, a reactive SCM is expected to influence the mechanical strength evolution of the binder [96]. One of the methods used to estimate the reactivity of slags is the hydraulic efficiency index, h, under the French standard NF P 18 – 506 (1992)[12]. This value is calculated as the ratio of the compressive strength of a (PC) mortar with 50 wt% SCM to cement substitution, to that of a pure PC-binder mortar. The typical values for GGBFS ranges from 0.6 to 0.85, after 28 days of hydration [97].

[12] equivalent to the ASTM C 989 for GGBFS

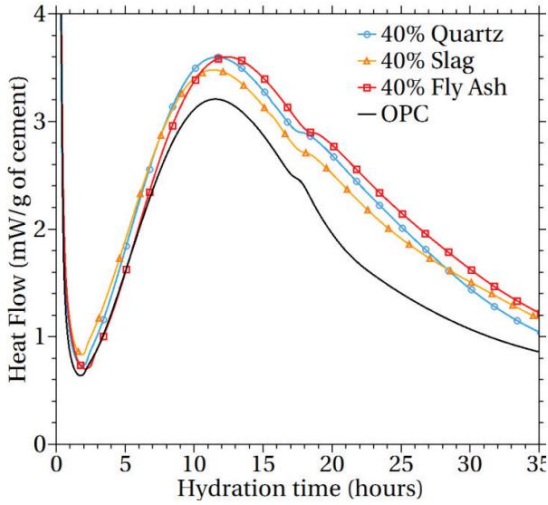

Figure 1.9 *Heat flow curves of a pure PC system and blends with 40 wt% replacement with SCM, calculated per gram of cement [95].*

High level of substitution with SCM typically results in strength reduction, especially in the early days of hydration when the SCM has not yet reacted extensively. This is better illustrated in **Figure 1.10** b where the compressive strengths of PC-based mortars decrease in function of the replacement level with GGBFS and fly ash. On the contrary, it can be seen that the addition of very fine silica fume has an inverse effect, mainly attributed to the higher packing density[13] obtained from this binder formulation [96].

A systematic investigation was performed in Lothenbach *et al.,* 2011 [8] connecting the properties of traditional SCM to the physical and chemical properties of PC-based binders. In that study, the changes in pore solution due to the SCM dissolution were linked to the mechanism of hydrate formation and subsequently to the volume, porosity and durability of the systems. It was highlighted that despite the reduced early strength at higher replacement levels, the addition of SCM could ultimately contribute to the durability aspects including: better control of alkali-silica reaction[14]; increased chloride penetration resistance; sulfate resistance; or lower heat of hydration.

[13] pertains to the ability of the SCM to fill up the voids of the binder, associated to its PSD and the morphology of the particles

[14] deleterious expansion in concrete attributed to the formation of hygroscopic sodium silicate gels from the reaction of highly alkaline cement paste, siliceous aggregates and water

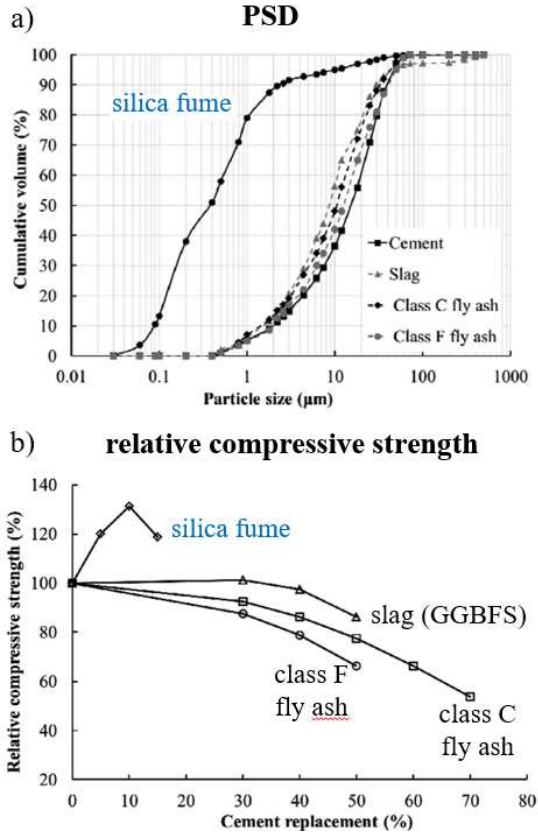

Figure 1.10 *(a) Particle size distribution of several SCM compared to that of a PC; and (b) the compressive strengths in function of cement replacement level, relative to a pure PC binder [96].*

1.3.2. Non-conventional SCM

Despite recognizing numerous types of traditional SCM and their growing application on a commercial scale, their limited and often localized availability further triggered by the declining numbers of carbon-intensive energy and steel manufacturing plants poses a critical challenge for a full shift towards blended cements. To answer this demand for alternative sources, the promising approach of the Enhanced Landfill Mining (ELFM) concept [98] opens new pathways for potential types of novel SCM. Landfill mining is a form of secondary mining whereby valuable materials, such as high-value metal components, are extracted from ancillary sources, particularly pre-existing landfills [99]. It is a long-existing concept elicited by the diminishing supply of high grade ores, newly-developed metal extraction technology and the increasing cost of land use.

With an integrated sustainability target, the concept of ELFM conveys a more rigorous approach on energy flow, social and ecological considerations in landfill mining while placing the concept of circular economy [100] in the limelight. ELFM offers a promising solution in parallel with direct recycling of scraps and urban mining of end-of-life products [27]. Prior to the utilization of the landfilled by-products, pre-treatment is often necessary to recover their valuable components and to better adapt their properties as SCM – a concept aligned with the framework of the SOCRATES project. Additionally, the pre-treatment step provides a margin to engineer the by-products in order to induce or increase their reactivity as SCM and to remove their heavy metals and hazardous components making them more suitable for building applications. This makes the remaining residues good candidates as mineral additives: clean (metal-depleted), low-cost and high volume materials. To have a substantial impact in reducing the carbon footprint by replacing cements, these residues must effectively contribute to the application-based performance of the binder thereby providing a direct reduction to the clinker factor [4].

Some of the properties of the by-products investigated in the SOCRATES project can differ substantially from those of the aforementioned traditional SCM. The typical composition of similar by-products published in literature [101–105] is presented in **Table 1.1**.

Table 1.1 *Chemical composition of by-products, similar to those of the SOCRATES', published in literature [101–105]. Significant percentage falls under "others" for MSWI bottom ash and jarosite residue related to their high loss on ignition. While "–" indicates values below detection limit.*

	NFM slags			MSWI	jarosite
in wt%	copper slag	zinc slag	lead slag	bottom ash	residue
CaO	5.2	14.5	10.5	38.1	6.9
SiO_2	41	19.8	24.4	15.8	6.8
Al_2O_3	3.8	–	3.4	0.9	6.8
FeO or Fe_2O_3	44.8	37.2	46.8	4.2	32.1
MgO	1.2	–	1.3	3.5	1.9
K_2O	–	–	0.5	7.3	0.7
Na_2O	–	–	4.1	0.2	0.6
SO_3	1.1	4.4	6.6	1.5	–
TiO_2	–	–	0.2	0.3	–
PbO	–	1.5	1.4	–	2
ZnO	–	14.2		–	9.2
others	3	8.4	0.7	28.2	33.2
Sum	100	100	100	100	100

Whereas the traditional SCM are typically aluminosilicates in composition, NFM slags and jarosite residue are Fe-rich given their production process described in section 1.1. Furthermore, the Fe component in the NFM slags principally has 2+ oxidation state considering the reducing atmosphere in smelting furnaces as opposed to the 3+ state in cements [106]. On the other hand, MSWI bottom ashes usually have a lower degree of vitrification as opposed to fly ashes considering the cooling rates during their generation. The chemical composition and the degree of vitrification are only two of the many factors [107,108] considered to define the reactivity of residues and consequently their potential for valorization as SCM.

A more detailed state-of-the-art review on the use of NFM slags, MSWI bottom ashes and jarosite residues has been co-published by the author in a conference article attached in Appendix A. The paper discusses the use of these by-products as non-conventional SCM highlighting the advances and opportunities in this valorization pathway both in the industrial and the laboratory scale. Based on this review, their commercialization is still widely limited to low-value applications particularly as aggregates in concrete. Their generally lower reactivity, inhomogeneity, undesirable components (i.e., heavy metals and glass) and other factors (i.e., availability of local supply) are among the biggest challenges. In addition, the annual global production of NFM slags (30-40 Mt [103]), MSWI bottom ashes (26 Mt [109]); and jarosite residues (6-7 Mt [110]) are significantly lower than the traditional SCM, often limiting their use to niche applications.

The review paper (Appendix A) also highlights the lack of publications in the open literature dealing with the incorporation of these by-products in specialized cement binders, such as in CAC systems. Oftentimes, the previous studies evaluate their potential in pure PC or PC-rich systems. Among the by-products discussed, the NFM slags could have the highest potential as SCM considering their reported contribution to the mechanical performance of the binders [28,101,111]; their relatively higher production volume [112]; and the availability of pre-treatment installations to generate a metal-depleted supply ideal for the construction market [35].

The second part of the paper presents the result of an LCA and exergy[15] analysis on the use of NFM slag as a substitute to PC. The case study demonstrated 26 % decrease in the exergy cost (in MW) mainly related to the lower material circulation in the rotary kiln; and the 32 % lower Global Warming Potential (in kg CO_2) with the 30 wt% substitution of PC with

[15] measure of work needed to perform a process or produce a material

the slag. These sustainability measures further support the interest in the valorization potential, particularly, of NFM slags as SCM. In this regard, it will be crucial to understand the fundamentals of the slag's reactivity during hydration that could influence the physical and chemical properties of these binders.

1.4. The role of Fe in inorganic polymers and cement binders

1.4.1. Fe speciation in slag-containing inorganic polymers

While the typical Fe in a conventional slag-containing cement systems are mostly in their elemental form (for GGBFS) or in the 3+ oxidation state (for C_4AF) [113][16], those in the NFM slags are dominantly in the 2+ state given the reducing atmosphere in the furnace during their generation [114]. The presence of several oxidation states (2+, 3+) and coordination numbers (4, 5, 6) adds to the complexity of the hydration reactions of these NFM slags [115]. In the recent years, publications investigating the Fe speciation in NFM slags as binder precursors have been widely directed towards IP [47,114–118].

Using Mössbauer spectroscopy, Onisei *et al.,* 2018 [114] provided insights on the atomistic structure of an industrially-quenched (80 wt% amorphous) fayalite slag before and after polymerization. Three main Fe components were derived from the deconvolution of the Mössbauer spectra of the raw slag, namely: (1) Fe^{2+} in fayalite; (2) Fe^{2+} in a hercynite ($FeAl_2O_4$)-like phase; and (3) Fe^{2+} in the glass state. During the polymerization, the Fe^{2+} component in the crystalline fraction only reacted to a very low extent. On the other hand, those in the glass state were predominantly converted into Fe^{3+} in an amorphous ferrifayalite-like phase most likely having a 5-fold O-coordination [114]. These results were consistent with subsequent works on synthetic slags in Peys *et al.,* 2019 [116] further suggesting the presence of an additional Fe^{3+} species as a minor component (15 % absorption area) of the amorphous raw slag; and a new Fe^{2+} site in a distorted octahedra as a reaction product. No new crystalline phase was detected through XRD leaving a question as to the identity of this new product formed despite its seeming resemblance to the structure of fayalite minerals. Nonetheless, both studies demonstrated the role of the newly-formed Fe^{3+} component as network former in the glassy silicate IP network. Peys *et al.,* 2019 [116] further elaborated that the observed oxidation commences between 3 h to 6 h after mixing and progresses

[16] The study only took the Fe speciation of the non-amorphous fraction in consideration

significantly within the first 24 h. This timeline was consistent with the onset of the polymerization exotherm in the calorimetry performed in the same study [116]. Peys *et al.,* 2019 [115] considered $O_2 + 4\ e^- \Rightarrow 2\ O^{2-}$ and $Fe^{2+} \Rightarrow Fe^{3+} + e^-$ as possible half reactions governing this oxidation, the result of their study on polymerization under N_2 atmosphere revealed oxygen imbalance in the system. Nonetheless, the study demonstrated that the observed oxidation was only driven by the atmospheric conditions during the later stages (>28 days), and not during the first (3) days after mixing [115].

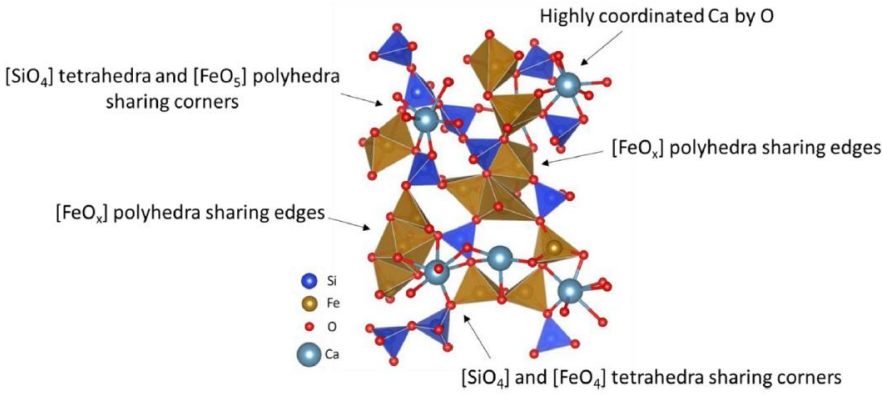

Figure 1.11 *The structure of a synthetic NFM slag proposed in Siakati et al., 2020 [119] simulated based on MD simulations and PDF studies. The slag has a molar composition of 0.33CaO:0.67FeO-SiO₂ following (CaO+FeO)/SiO₂ = 1. The [FeOₓ] (where x = 5 or 6) and [SiO₄] tetrahedra were represented in yellow and dark blue planes, respectively*

Using experimentally-obtained pair distribution functions (PDF) [120] in conjunction with molecular dynamic (MD) simulations, Siakati *et al*., 2020 [119] proposed the glassy structure of a synthetic NFM slag graphically represented in **Figure 1.11**. In this structure, Fe is mainly present in tetrahedral (4-fold coordination) and pyramidal (5 or 6-fold coordination) configurations. The randomly distributed Fe atoms tend to exhibit the lower coordination with O when more Si atoms are present in the neighboring environment, and the higher coordination with more Ca and Fe atoms around [119]. Knowledge on the atomistic structure of the slag is not only important in controlling its polymerization or hydration reactions, but can also be decisive in optimizing the physical properties of the binder, such as: its density and color [121]; and its setting and chemical shrinkage [115,122].

1.4.2. Fe speciation in cementitious binders

Fe in conventional cementitious systems can be contributed by the slag (GGBFS), the clinker and the aggregates. The identification of Fe-bearing phases using the classical (i.e., XRD and TGA) or even with the more advanced techniques (i.e., X-ray absorption near edge structure (XANES) spectroscopy) is made complicated by its poorly-defined coordination geometry in glasses [123]. A recent investigation, Mancini *et al*., 2021 [124], discussed the evolution of Fe speciation in slag cements under different curing conditions using synchroton-based techniques: XANES and micro-XRF. The results demonstrated the oxidation of Fe^{2+} (mainly in the form of C_4AF) from the anhydrous blend to Fe^{3+} during hydration. The most common[17] Fe-containing hydration product was siliceous hydrogarnet, $(CaO)_3(Al,Fe)_2O_3(SiO_2)_{0.84}(H_2O)_{4.32}$, generally consistent with the prediction based on thermodynamic modelling. It was explained however that some of the small differences between the experimental and the modelled phase assemblage were attributed to the kinetic effect and the heterogeneity of the samples. Moreover, the corrosion (accompanied by oxidation) of free Fe from the slag was characterized, revealing the formation of several possible hydration products (i.e., $Fe(OH)_2$, FeOOH, FeO, Fe_2O_3) determined by the abundance of O_2 in the environment. They also found that the oxidation was accelerated by the presence of chloride ions in seawater, and was hindered by high pH in cement pore solutions [124]. Considering the significant difference in the volume of free Fe and its corrosion products [125,126], the reaction mechanism could be critical in maintaining the dimensional stability of these binders.

Several other studies [106,113,127–134] on cement systems have previously described the fate Fe from C_4AF during hydration. Rose *et al*., 2006 [127] emphasized that controlling the C_4AF hydration could be beneficial given its metal sorption capabilities; while Tao *et al*., 2021 [128] reiterated its contribution to the wear and sulfate resistance of special application cements. Changes in the coordination structure (bond type, bond strength, polarity, etc.) are reported to be directly related to the reactivity of C_4AF [128]. This property could differentiate the reactivity rate among crystals with varying extent of Fe-Al substitution. By complementing Mössbauer spectroscopy and XRD results with atomistic simulations[18], Tao *et al*., 2021 [128] ranked the reactivity of cations in the laboratory synthesized C_4AF crystals from highest to lowest, as follows:

[17] except for the supersulphated slag cement (84.5 wt% slag, 15 wt% anhydrite and 0.5 wt% KOH) due to the lower amount of Ca versus CEM II and III samples investigated in their study

[18] quantum-mechanical simulation based on density functional theory

Ca > Al > Fe ions, implying that lower Fe-Al substitution begets higher reactivity. They also concluded that tetrahedral coordination for both Al and Fe ions are more easily broken (more reactive) as opposed to octahedral coordination.

Using Mössbauer spectroscopy, the distorted octahedral and tetrahedral sites occupied by Fe^{3+} in C_4AF were discerned, and the evolution of the spectra revealed the incorporation of Fe in several hydrate phases [129,130,135]. **Figure 1.12** shows the evolution over time of the Mössbauer spectrum of a pure PC sample (a) and the corresponding deconvoluted models (b) [129]. The model supports the presence of two Fe components from C_4AF in the raw PC, decreasing in intensity over time as a third doublet forms towards 14 days of hydration.

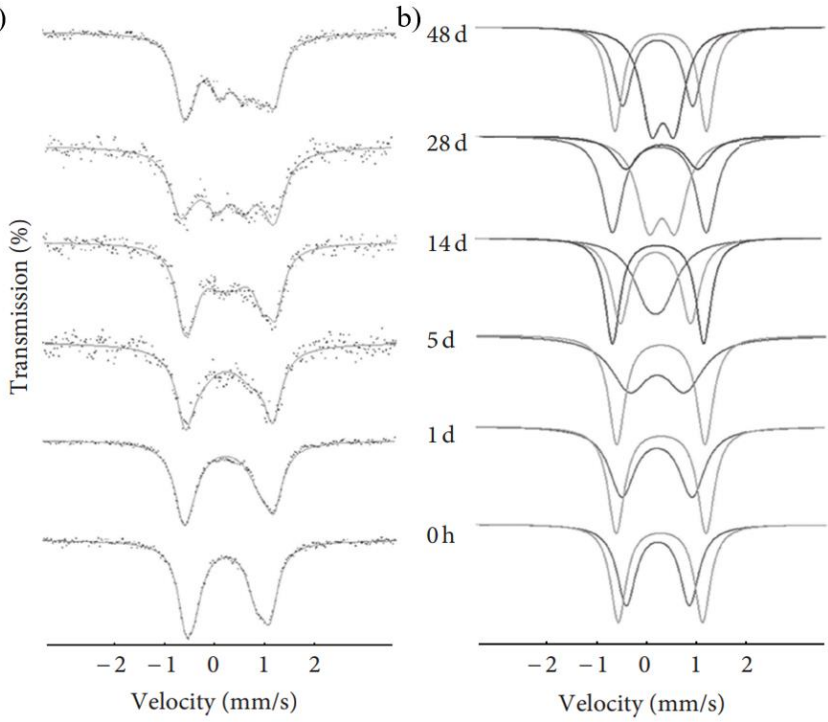

Figure 1.12 *(a) Evolution of the Mössbauer spectrum of a pure PC hydrated up to 48 days; and (b) its corresponding deconvoluted model with each doublet representing an Fe component [129].*

Aside from the aforementioned siliceous hydrogarnet, Fe uptake was similarly observed in ettringite [131,136], monosulfate or monocarbonate [127,132], and C-S-H [113,133], depending on the type and the abundance of ions in the pore solution. In most of these phases, Fe-Al solid solution was identified as the principal mechanism of incorporation. However,

these studies reported varying results regarding the formation of Fe hydroxide from the hydration of C_4AF. While some [127,128,132,134] supported the formation of amorphous Fe hydroxide phases (i.e., similar to goethite and lepidocrocite), others [135,136] did not observe substantial evidence of their presence. This could be explained by kinetic effects and compositional variations creating a different environment during hydration [124,132].

1.4.3. Other techniques to characterize and quantify the reactivity of slags

Fourier transform infrared spectroscopy (FTIR)

FTIR has been widely used together with Mössbauer spectroscopy in the previously-cited investigations. It proves to be a practical complementary technique with numerous advantages, including: (1) rapid results, obtained after a few minutes; (2) only a few milligrams of sample needed; (3) no need for specific sample preparation; (4) distinct peaks identified for certain cement phases such as for portlandite; (5) proven applications in IP, cements and coatings [137]. Using the Attenuated Total Reflection (ATR) mode, FTIR has effectively demonstrated the reactivity of highly amorphous Fe-rich slags characterized by a peak shift towards higher wavenumbers of the Si-O stretching absorbance band (700-1200 cm^{-1}) and towards lower wavenumbers of the Si-O rocking band (400-500 cm^{-1}) after 28 days of polymerization [114,116,117]. An illustration of this shift is presented in **Figure 1.13**. In a wide variety of materials, this phenomenon has been associated to the changes in the Si-O-T (where T could be Al, Fe or Si) distances [138]. The incorporation of Fe^{3+} in the silicate networks is reported to change the Si-O-Si linkages in the activating solution of IP systems [116]. An idea on the degree of slag reactivity, relative to its glass fraction, may also be derived in function of this peak shift, as shown in **Figure 1.13**.

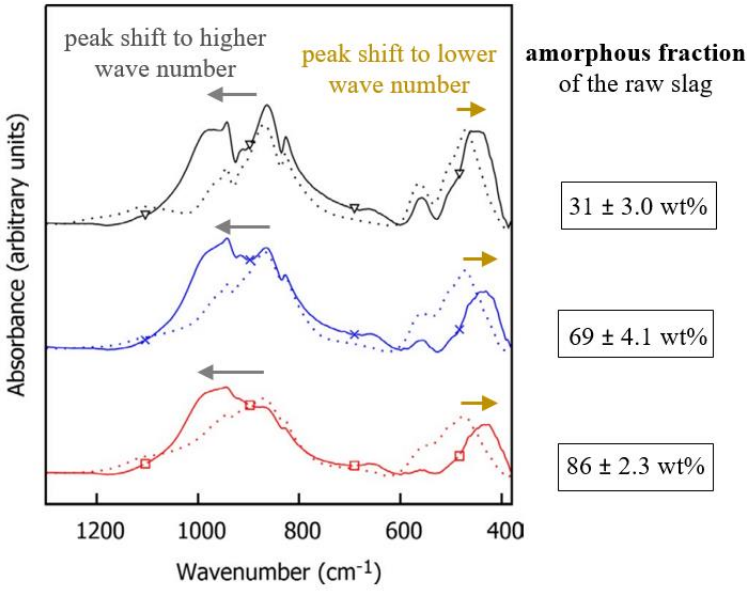

Figure 1.13 *ATR-FTIR spectra of three synthetic Fe-rich (65-68 wt% FeO) slags before (dotted lines) and after (solid lines) 28 days of polymerization modified from Siakati et al., 2020 [117].*

Selective dissolution

In a recent publication, Hallet *et al*., 2022 [139] adapted the ethylene diamine tetra acetic acid (EDTA)-triethanolamine (TEA)-NaOH selective dissolution test originally intended for fly ashes [140], to quantify the degree of NFM slag reaction in PC-based blended cements. They determined that almost 25 % of the slag has completely dissolved after 150 days of hydration and that the kinetics were comparable regardless of the slag-PC substitution level (30 wt%, 50 wt% or 70 wt%) [139]. On the other hand, a procedure using methanol-salicylic acid has been proposed for GGBFS-CAC systems in Nakagawa *et al*., 1990 [141]. However, there has been no methodology previously published for Fe-rich NFM slag in CAC-rich binder, to the best of the author's knowledge.

Scanning Electron Microscopy (SEM)

Vayghan *et al*., 2021 [142] estimated the degree of slag hydration using image analysis on the back scattered electron (BSE) micrographs of SEM. This study on another fayalitic NFM slag in PC system (at 30 wt% replacement level) estimated that 30 % of the slag has reacted after 90 days of hydration. The methodology presented addressed the challenges encountered in the more traditional techniques when dealing with the highly amorphous slags (i.e., XRD with Rietveld refinement quantification

[143]). It also took advantage of the wide compositional and density difference between the Fe-rich slag and the cement matrix.

X-ray Computed Tomography (XCT)

Finally, another recently-published image-based quantification technique for slag reactivity in a PC-based cement system utilizes XCT [144]. Collated figures taken from this study showing the main steps of image analysis, in order to produce a 3D segmented render of the hardened paste sample is shown in **Figure 1.14**.

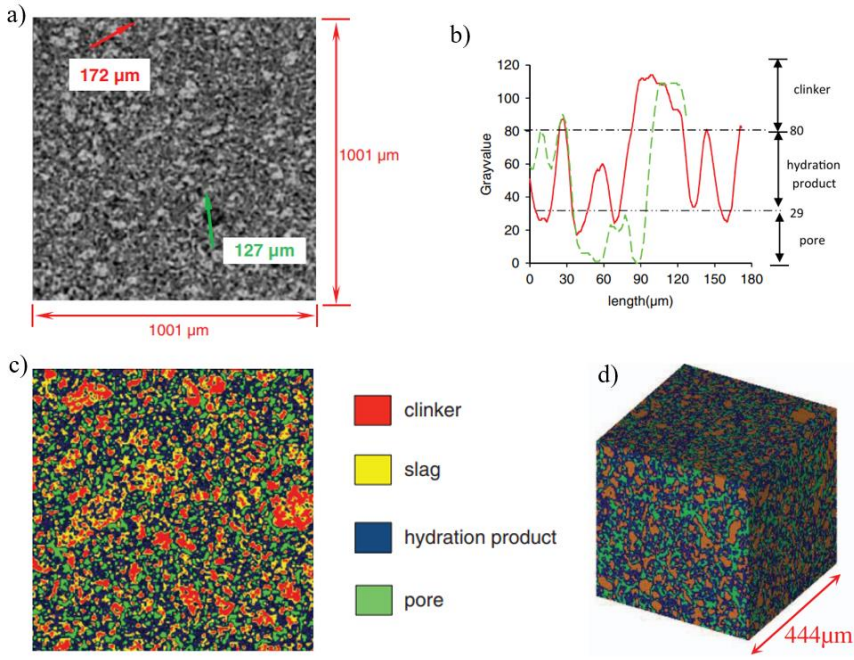

Figure 1.14 *Figures collated from the quantification of GGBFS hydration degree using XCT in Wu et al., 2020 [144]. The reconstructed 2D image after the scan is shown in (a). The grayscale threshold segmentation of the pixels under the green and red arrows in (a) is illustrated in (b). The 2D (c) and 3D (d) renders after segmentation are also presented.*

The refined methodology introduced in Wu *et al.,* 2020 [144] differentiated GGBFS particles from the rest of the matrix through grayscale threshold segmentation. Grayscale indices were assigned to a pre-defined voxel according to the composition and density of phases, in a similar manner to the aforementioned SEM-BSE technique but with the transmission of X-rays instead [144]. This technique provides a rapid, non-destructive alternative to SEM-BSE, eliminating the tedious sample preparation steps including hydration stoppage and surface polishing. The results of the study estimated that 56 wt% of the GGBFS was hydrated

after 28 days in a paste sample with 50 wt% PC replacement level at 0.5 w/b ratio. This methodology has not been previously adapted for cement systems incorporating NFM slags, to the best of the author's knowledge. Considering the significant compositional and density difference attributed to the Fe component of these slags, XCT is clearly a promising technique to estimate the hydration degree.

Conclusion

The SOCRATES project offers potential types of novel SCM in the form of pre-treated industrial by-products, including: NFM slags, MSWI bottom ashes, jarosite and paper residue. After the pre-extraction of valuable components and the removal of heavy metals (i.e., fuming process for NFM slags), the incorporation of the residual matrix in CAC-based binders is evaluated in this study.

CAC is typically blended with calcium sulfate (C$) and PC in rapid-repair building applications. The hydration products greatly depend upon the ratio of these components in the mix. In general, the complete hydration of a binary CAC-C$ system leads to an ettringite-rich binder given that sufficient amount of sulfate is present. Whereas, the formation of monosulfoaluminates is favored in low calcium sulfate systems. The phase assemblage becomes more complex with the addition of PC where other hydrates could form in greater proportions, such as C-S-H, hydrogarnet, strätlingite, and monocarboaluminates. No previous study has been published on the incorporation of residues similar to those of the SOCRATES' in these blended systems.

Among the residues investigated, the NFM slags are of particular interest given their generally metal-depleted and amorphous nature. Previous studies cited in this chapter, have demonstrated the reactivity of similar Fe-rich slags in IP systems and of C_4AF in cement systems. Using Mössbauer spectroscopy, these studies consistently suggest the presence of several oxidations states (2+, 3+) and coordination numbers (4, 5, 6) of Fe in both systems. During polymerization or hydration, the oxidation process of Fe^{2+} to Fe^{3+} was discerned from the deconvolution of the Mössbauer spectra. Fe uptake has been observed in several hydrate phases including siliceous hydrogarnet, ettringite, monosulfate or monocarboaluminate, C-S-H and even in several forms of Fe hydroxides.

Several techniques and methodologies have been employed to characterize and even quantify slag reactivity. ATR-FTIR has been used in conjunction with Mössbauer spectroscopy to indicate reactivity through distinctive peak-shifts in the Si-O absorbance bands of Fe-rich slags. While the degree of slag reaction in PC systems has been recently quantified using an adapted EDTA-TEA-NaOH selective dissolution test. Finally, image analyses from SEM-BSE micrographs and XCT 3D volumes also demonstrated promising alternatives to quantify the degree of slag reaction.

In the end, the challenge of this research work lies in the complexity of the system. Reactions arising from the hydration of the ternary CAC, PC and

C$ binders are expectedly difficult to distinguish, as they occur simultaneously. This is further aggravated by the heterogeneous compositions of the SOCRATES residues considering their diverse origins. A screening test that allows comparison of the by-products' reactivity at equal volume substitution, must be established to define a blend with the highest potential valorization in cement applications. The influence of the SCM addition to the physical and chemical properties of CAC-based blends must be followed from the early hours up to longer curing ages. The abundance of Fe and the amorphous nature of some of the residues, particularly the NFM slags, would require more advanced characterization techniques such as TEM, FTIR and Mössbauer spectroscopy, to complement the techniques more commonly employed in cement systems (i.e., XRD, TGA). An adaptation of the recently-published hydration degree estimation based on XCT and image analysis is also interesting to develop, considering the distinct properties of the slag (i.e., high density, Fe-rich composition) relative to the cement components; and the fast, non-destructive nature of the test.

Chapter 2

Materials, methods and residue selection

Contents

2.1. Materials and formulation

2.1.1. The Socrates residues

Six by-products from the SOCRATES Project were investigated in this study. A single batch of 10-20 kg of each material was received in buckets originating from several industrial partners all around Europe. The materials were homogenized and sampled to obtain a representative 3kg portion. The samples were then oven-dried for 48 hours at 100°C prior to grinding using a laboratory ball mill (if needed) until a comparable particle size distribution (PSD) and/or specific surface area (SSA) as the reference calcium aluminate cement (CAC) is obtained. A screening test was performed as a preliminary step in order to determine which among these by-products had the highest potential for valorization as supplementary cementitious material (SCM) in a CAC blended formulation and therefore will be the focus of the more extensive investigation that follows. These by-products include:

Granulated Fe-rich slag (slag)

A by-product of a pilot-scale thermal treatment of residues from lead-zinc metallurgy. The granulation process using water jets resulted to its glassy structure. This was performed for the ease in handling and for the increased reactivity when used in cementitious applications. Its dark color is a manifestation of its high Fe content. Unless otherwise specified, the general term "slag" pertains to this material for most part of this manuscript.

Figure 2.1 *Picture of the granulated Fe-rich slag as received*

Slowly-cooled Fe-rich slag

A by-product originating from the same process as the granulated Fe-rich slag but instead undergone air-cooling at an ambient temperature.

Figure 2.2 *Picture of the slowly-cooled Fe-rich slag sample as received*

Fumed fayalite slag (Koranel®)

A commercial product from Metallo marketed as clean synthetic mineral for building applications. It is a granulated Fe-silicate originating from secondary copper smelting where the slag is further subjected to a submerged plasma zinc fuming process for Zn and Pb recovery. In effect, the final granulated slag is expected to only have trace amounts of heavy metals making it an ideal mineral additive for construction applications.

Figure 2.3 *Picture of the fumed fayalite slag sample as received*

Municipal solid-waste incinerator (MSWI) bottom ash

One of the principal residues produced from the incineration of municipal waste. It consists of the coarser and denser fraction of the ashes typically extracted from the bottom of the furnace. Often positioned in the lower extremities, a portion of these materials could remain unburnt. Consequently, the composition could be widely heterogeneous as observed from the received materials where broken glasses and small fragments of plastic wastes are still identifiable.

Figure 2.4 *Picture of the MSWI bottom ash sample as received*

Jarosite residue

Dried filter cake coming from a combined stream of a direct zinc sulphide leaching stage and direct leaching reactors. This residue is often contained in specially constructed tailing ponds or industrial landfills depending on the levels of hazardous components.

Figure 2.5 *Picture of the jarosite residue sample as received*

Paper residue (Top-Crete®)

A commercial product from CDEM Minerals BV marketed as a green binder for concrete and cement industry. This white fine powder is produced in a fluidized-bed incinerator that dehydrates de-inking sludge formed from the recycling of paper wastes.

Figure 2.6 *Picture of the paper residue sample as received*

2.1.2. Cements

Three types of cements were used in this study, namely:

Ciment Fondu® and Secar 51® (CAC)
Two different varieties of calcium aluminate cement produced by Imerys Aluminates through a fusion process. Throughout this study, this component will be mostly abbreviated to "CAC".

Ordinary Portland cement, Milke® Premium (PC)
A CEM I 52.5 R type ordinary Portland cement manufactured by Heidelberg Cement.

2.1.3. Other blend components

Calcium sulfate β-hemihydrate, Prestia Selecta (HH)
Mineral additive manufactured by Lafarge, used as the primary sulfate carrier in the blends. Throughout this study, this component is mostly abbreviated as "HH".

Millisil E400® (quartz filler)
Fine sand filler manufactured by Sibelco. In this study, it was used to substitute SCM in mortars with the goal of accounting for filler effect.

Citric acid
Reagent grade admixture from Sigma-Aldrich, in granules/crystal form, added to the dry-mix blends primarily as a set retarder.

2.1.4. Dry mix formulations

EN 196-1 standard mortars were prepared based on several dry-mix formulations for various case studies involved this research. These mortars were used in monitoring the physical properties (mechanical strength and dimensional stability) of the blends. Their corresponding paste mixtures, maintaining the same proportions of the binder components, were used for further characterization (i.e., mineralogy, tomography, thermogravimetry, and spectroscopy). The water to binder (w/b) ratio was kept constant at 0.5 for all the mortars and 0.65 for all the paste samples. The higher amount of water used for the latter was directed towards compensating for the water-curing condition followed only for the mortar samples. Further details on these curing conditions will be given in the succeeding sections.

In this study "reference" formulations refer to the samples where:

- **reference filler**: the SOCRATES residue component of the binder was replaced by an equivalent volume of the quartz filler; or
- **reference cement**: the binder consists solely of cements (CAC, PC) and additives (HH, citric acid) preserving the same ratio of the components as with the SCM-containing formulation

The first case was more often used for the mortars in this study in order to distinguish any possible contribution to the physical properties of an SCM as an inert filler. On the other hand, the second case was mostly used for the pastes where the chemical reactivity is being investigated.

A screening test is presented at the end of this chapter (section 2.3) with the binder compositions detailed in **Table 2.1** to compare the reactivity of the SOCRATES residues in a CAC-based system. In this test, the variety of CAC used was Secar 51®. It is notable that the substitution by equal volume resulted in varying weight percent composition of each SCM.

Table 2.1 *Binder composition for the screening test where Fe-rich slag is abbreviated as FS. Values are expressed in wt% except for the CAC/HH ratio*

(in wt%)	SCM/filler	CAC	HH	total binder	CAC/HH ratio
reference	0	82	18	100	4.5
quartz filler	24	62	14	100	4.5
granulated FS	30	57	13	100	4.5
slowly-cooled FS	29	58	13	100	4.5
fumed fayalite slag	29	58	13	100	4.5
bottom ash	24	62	14	100	4.5

In another case study under the screening test, the use of the jarosite residue as a possible substitute to HH was explored. The binder composition used is shown in **Table 2.2**. In this test, the variety of CAC used is Ciment Fondu®.

Table 2.2 *Binder composition for the case study on jarosite use as a sulfate source in CAC- blended cement. Values are expressed in wt%*

code	*(in wt%)*	jarosite	CAC	HH	total binder
no jarosite	reference	0	67	33	100
20JAR	20% substitution	7	67	26	100
50JAR	50% substitution	17	67	17	100
100JAR	100% substitution	33	67	0	100

Chapters 3 and 4 focused on the incorporation of the granulated Fe-rich slag in CAC-HH binary and CAC-HH-PC ternary systems. The binder formulations are detailed in **Table 2.3**.

Table 2.3 *Composition of binders incorporating the granulated Fe-rich slag where certain components are represented as follows: (TC) TopCrete® paper residue and (PC) Portland cement. (CAC) Secar 51®*

code	*(in wt%)*	slag	CAC	HH	TC	PC	total binder	CAC/HH ratio
A	4.5CAC-HH	30	57	13	0	0	100	4.5
B	1.6CAC-HH	30	43	27	0	0	100	1.6
A-TC	4.5CAC-HH-5TC	29	54	12	5	0	100	4.5
A-PC	4.5CAC-HH-30PC	30	33	7	0	30	100	4.5
B-PC	1.6CAC-HH-30PC	30	25	15	0	30	100	1.6

reference formulations:

REF_{cement} *(reference cement) no SCM nor quartz filler added*

REF_{filler} *(reference filler) slag replaced by equal volume of quartz*

A shortened version of the sample name is provided in the first column. Throughout this study, the full sample name and their shortened code may be used interchangeably or together to occasionally recall the composition of the binders. The reference formulations in this case are distinguished either as reference cement or reference filler specified in the table above.

In all the binder formulations presented, a replacement level of 30 wt% for most of the SCM was selected with the goal of ensuring that the performance of the binders will not be significantly reduced at short term by the substitution compared to the reference formulation. As already mentioned in the literature review (section 1.3-1.4), these industrial residues tend to be less reactive than the other blend components (CAC, HH and PC). On the other hand, the risk of not being able to detect any impact of the substitution makes it unpractical to go below the 30 wt% level. Moreover, two CAC/HH ratios were set at 1.6 (high calcium sulfate system) and 4.5 (low calcium sulfate system) with the goal of representing the impact of sulfate proportion in the systems and its possible influence on the reactivity of the slag. In the end, it is important to mention that the selection of the binder compositions for this study was based on the results of literature references and guided by unpublished internal laboratory tests.

2.2. Methods

2.2.1. Basic characterization of raw materials

The chemical composition of the raw materials presented in **Table 2.4** was measured using semi-quantitative Bruker S4 Pioneer X-ray fluorescence (XRF).

Table 2.4 *Chemical analysis of raw materials obtained using XRF where Fe-rich slag is abbreviated as FS. Other components not specified primarily pertain to the oxides of Zn, Cu, Cr, P and Pb (more details in Table 2.5)*

(in wt%)	CaO	Al_2O_3	SiO_2	FeO/Fe_2O_3	SO_3	MgO	K_2O	Na_2O	others
granulated FS	12.5	4.8	25.9	46.0	0.7	2.2	0.6	4.0	3.3
slowly-cooled FS	17.6	6.0	31.1	33.4	0.7	3.0	0.5	4.8	2.9
fumed fayalite slag	4.2	10.3	30.6	42.4	0.8	1.3	0.2	2.1	8.1
bottom ash	18.3	11.4	42.9	9.9	2.9	2.3	1.3	5.6	5.4
jarosite residue	4.3	1.0	6.4	22.0	51.2	0.5	0.3	4.8	9.4
paper residue	68.1	11.0	15.2	1.1	0.4	0.5	0.4	0.5	3.0
Secar 51®	37.7	52.3	4.9	1.8	0.2	0.4	0.0	0.0	2.7
Ciment Fondu®	37.8	40.3	4.2	14.6	0.1	0.4	0.1	0.1	2.5
PC	67.1	3.9	20.9	1.4	4.3	0.7	0.8	0.3	0.6
HH	41.7	0.1	0.8	0.1	56.5	0.1	0.0	0.0	0.7
quartz filler	0.0	0.0	99.8	0.0	0.0	0.0	0.0	0.0	0.2

High Fe content is apparent for most of the SOCRATES residues except for the siliceous bottom ash and the lime-rich paper residue. The difference in the Fe content of the CAC used is also significant with a higher contribution measured for Ciment Fondu® as opposed to the Secar 51® having higher alumina content instead. The relevance of this difference is further elaborated during the characterization of the hydrated binders in the preceding sections. Although Fe oxide is expressed as Fe_2O_3 in XRD for most of the materials, the oxidation state Fe^{2+} specifically for the slags is more sensible given the reducing environment in the furnace during their production as previously discussed in the preceding chapter. More advanced characterization to better delineate the Fe speciation in the slag is presented in section 2.2.5.

The components labelled as “others” in **Table 2.4** is the summation of Zn, Cu, Cr, P and Pb oxides. Among the SOCRATES residues, this value for the fumed fayalite slag, bottom ash and the jarosite residue is strikingly elevated with details shown in **Table 2.5** posting an initial concern on their direct addition as SCM in the dry mix. Concerns on the effect to the hydration reactions and on the leachability of the heavy metals and toxic components, already introduced in the preceding section, have to be addressed. Despite this initial observation, however, it has to be reiterated that most of these materials from the SOCRATES project will still undergo pre-treatment process to reduce these minor components that are not ideal for cementitious applications.

Table 2.5 *Minor components of some of the raw materials not detailed in Table 2.4*

(in wt%)	ZnO	CuO	Cr_2O_3	P_2O_5	PbO	others
fumed fayalite slag	2.3	0.5	1.6	1.6	0.0	2.1
bottom ash	0.5	0.4	0.1	1.5	0.1	2.8
jarosite residue	3.3	0.1	0.0	0.1	4.4	1.6

In addition, the mineralogy of the raw materials was determined using the D8 Advance X-ray Diffractometer (XRD) from Bruker coupled with LynxEye detetor. CuK_α (1.54 Å) radiation was used with a step size of 0.02° and a counting time of 1.84 seconds per step at 2θ range 5-80°. DiffracEVA and TOPAS software were used for the phase identification and quantification. The amorphous content of the slag samples was determined by applying the method described in Środoń *et al.,* 2001 [145] where 10 wt% of analytical grade zincite is added as an internal standard during sample preparation. The XRD diffractograms and phase quantification are detailed in Appendix B. Generally, both the granulated Fe-rich slag and the fumed fayalite slag exhibited high amorphous content (>90 wt%). The slowly cooled Fe-rich slag yielded a much lower amorphous content (13 wt%), balanced by fayalite and spinel in the crystalline fraction. On the contrary, the other residues (bottom ash, jarosite and paper residue) were dominated by several crystalline phases.

The density of the raw materials shown in **Table 2.6** was obtained through helium displacement using the Micrometrics AccuPyc II 1340 pycnometer system. Particle size distribution (PSD) presented along was determined using the Malvern Mastersizer 3000 laser diffraction system. Specific surface area (SSA) was quantified using both a semi-automatic Blaine Air Permeability Apparatus and the Micrometrics BET Tristar 3000.

Table 2.6 *Density, particle size distribution and specific surface area of the raw materials*

	density	PSD			SSA	
(in wt%)	g/cm³	d10	d50	d90	Blaine (cm²/g)	BET (m²/g)
granulated FS	3.67	1.1	7.9	50.5	4370	1.352
slowly-cooled FS	3.47	0.9	17.5	84.6	3200	1.216
fumed fayalite slag	3.50	1.6	13.7	61.5	3460	1.363
bottom ash	2.70	0.9	11.2	53.3	6160	3.865
jarosite residue	2.91	0.6	5.4	104.0	5253	4.706
paper residue	2.80	0.6	4.0	38.7	7730	8.133
Secar 51®	3.02	1.1	11.6	52.3	4270	1.019
Ciment Fondu®	3.23	1.6	16.4	75.8	3300	0.876
PC	3.17	0.9	8.5	25.3	3412	0.992
HH	2.64	0.6	3.7	22.7	7580	3.519
quartz filler	2.66	1.2	12.4	40.6	4580	1.118

The goal of the grinding step during the sample preparation was to obtain a comparable PSD and SSA between the SOCRATES residues and the components of the blends to be substituted (CAC, PC and HH). Although the PSD plot of the raw materials presented in Appendix C could support that the curves relatively fall within a comparable range, it can be seen in **Table 2.6** that the bottom ash, jarosite and the paper residue have significantly higher SSA. This is significantly related to the previously-discussed difference in mineralogy of the materials and should be considered during the screening test in section 2.3.

2.2.2. Physical properties

Standard mortars (4 x 4 x 16 cm^3) were prepared according the norm EN 196-1 using a w/b of 0.5. These samples were used in monitoring the physical properties of the formulations including setting time, mechanical strength and dimensional variation.

Setting time

Initial and final setting times were determined using the Vicatronic Automatic Vicat Machine at 20°C (AFNOR room) without submersion to water during curing. 1.3g of citric acid (0.3 wt% of the binder) was added to formulations B, A-TC, A-PC and B-PC (refer to **Table 2.3**) to retard the setting and therefore provide sufficient time for placing the freshly-mixed blends in the moulds. Such low amount of citric acid (0.1-0.5 wt%) is not expected to influence the phase assemblage evolution nor the strength development of the mortars in ettringite-based binders according to Nguyen *et al.,* 2019 [82].

Mechanical strength

Compressive and flexural strengths were measured using the 3R Syntris and the 3R RP 10/300 ELC press respectively, following the EN 196-1 standard. After demoulding, the mortars were cured under water at 20° C. Each data point taken for a specific curing age represents the average value from three mortar samples for flexural strength or six half samples for the compressive strength with the standard deviation shown as error bars.

In parallel, the water-curing condition after extraction from the moulds was substituted by air-curing conditions at 20°C and 65% relative humidity for some of the slag-incorporating blends and their respective references in order to investigate the effect of the curing condition to the mechanical strength of the mortars. The results presented in Appendix D support the advantage of following the water-curing procedure in discerning the possible contribution of the slag to the long term (>28 days) strength development of the mortars.

In this study, two criteria were used to evaluate the strength development of the mortars calculated according to **Equation 2.1 and 2.2**. SAI_{cement} refers to the ratio of the mechanical strength of an SCM-containing mortar to that obtained from its reference cement mortar. On the other hand, SAI_{filler} is the ratio of the mechanical strength of the slag-containing mortar to that obtained from its reference filler mortar. The evolution of these indices over the curing period was used as a preliminary indication of slag reactivity in Chapters 3 and 4.

$$SAI_{cement} = \frac{f_{SCM}}{f_{cement}} \qquad \textit{Equation 2.1}$$

$$SAI_{filler} = \frac{f_{slag}}{f_{filler}} \qquad \textit{Equation 2.2}$$

where: SAI is strength activity index of the SCM-containing mortars; and ƒ is mechanical (compressive or flexural) strength of mortars with subscripts SCM (slag or filler), cement (reference formulation with no SCM), slag (granulated Fe-rich slag) and (quartz) filler.

Dimensional variation

Considering the expansive nature of ettringite binders, the dimensional stability of the mortars was monitored during curing. Two methods were used, described as follows:

a. Using 4 x 4 x 16 cm^3 standard mortars cured under water:

Figure 2.7 *Standard mortar mounted in an extensometer*

Length variation was followed with the aid of gauge studs cast into the opposite ends of the mortars. At different curing ages, the same mortars were taken out of the water bath to record the length using a digital length comparator apparatus (extensometer, see **Figure 2.7**)

with a resolution of 0.001 mm. The mortar's dimensions after the demoulding at 24 h were considered as the reference (zero change) point for the measurements.

b. Using the Walter+Bai shrinkage test in air-curing condition:

The SWG H-400 device type was used to measure the length variation of a triangular mortar sample with 7 x 7 x 7 cm^3 base and 40 cm maximum length. Measurements were continuously recorded in-situ, a few minutes after mixing, through displacement transducers positioned at the opposite ends of the freshly-casted blends. In some cases, the monitoring of the length could continue after extracting (between 24 and 48 hours) the solidified samples using extensometers similar to method (a).

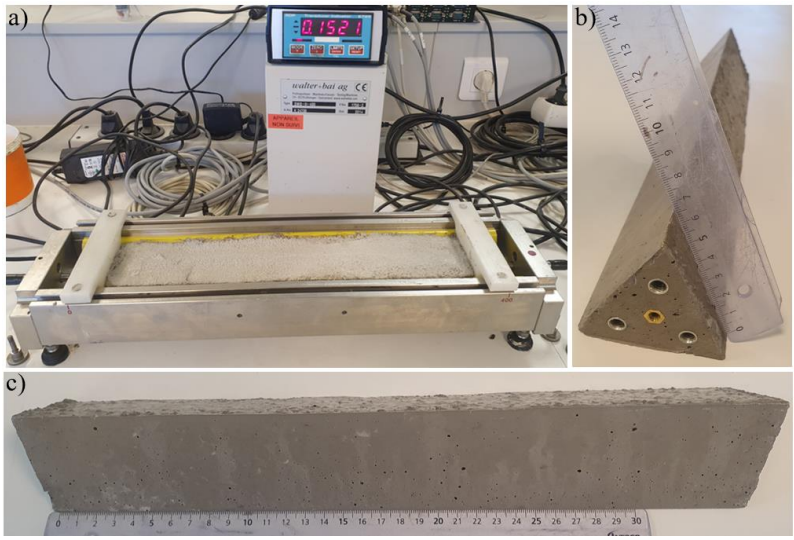

Figure 2.8 *Walter+Bai shrinkage test set up (a) and the dimensions of the triangular prism sample after the in-situ measurements of dimensional change (b, c). Lengths are shown in centimeters.*

Preparation of paste samples for analyzing hydrated blends

The subsequent sections concern several techniques that were used not only to characterize the raw materials but also to investigate the heat release, the phase assemblage evolution and the microstructure of the hydrated binders over time. For these analyses, paste samples were prepared following the formulations presented in **Tables 2.1-2.3**. 100 g of dry mix blend per batch was mixed with 65 g of water and homogenized using a laboratory electric agitator (IKA RW 20 overhead stirrer with centrifugal impeller) at 250 rpm and a mixing time of 2 min. The freshly-

prepared pastes were proportioned into smaller moulds, each representing a curing age (i.e., 1, 7, 28 days). The containers were hermetically sealed and agitated in a Turbula® mixer until the paste hardened, usually between 7-8 min. This protocol aimed to minimize, if not eliminate, the preferential segregation of the higher density solid components of the blends (especially the Fe-rich slags) prior to setting. Furthermore depending on the technique, stopping the hydration in hardened pastes was executed through solvent exchange by immersing the crushed samples in isopropanol for approximately 5 days and subsequently washing with diethyl ether to aid the drying. In most cases, further grinding to obtain a particle size below 100 µm was necessary prior to the characterization.

2.2.3. Thermal and thermo gravimetric analyses

Isothermal calorimetry

Ex-situ isothermal calorimetry was performed at 20°C on 10 g of freshly-prepared paste samples using the TAM air (TA instruments) device.

Thermogravimetric analysis (TGA)

50 mg ground (<100 µm) paste samples were used for the thermogravimetric analysis following solvent exchange to stop the hydration. All tests were performed under N_2 atmosphere at a heating rate of 30 °C/min. Differential thermogravimetric analysis (DTG) curves were generated from the treated data obtained using the Mettler Toledo TGA/DSC simultaneous thermal analyzer. The values of bound water content correspond to the weight loss measured between 50°C and 500°C per 100 g of anhydrous blend at 0.65 w/b ratio (65 g water), calculated according to the following equation:

$$bound\ water\ (g) = total\ water - free\ water \qquad \textbf{Equation 2.3}$$

$$bound\ water\ (g) = total\ water - (total\ mass - total\ solid)$$

$$bound\ water\ (g) = 65 - \left(165 - \frac{100}{1 - \frac{m_{50°C} - m_{500°C}}{m_{50°C}}}\right)$$

where: bound water is expressed in grams (g) and m_x represents the mass of the sample at x = 50°C or 500°C.

2.2.4. Tomography

A methodology to estimate the degree of slag hydration using a combination of X-ray computed tomography (XCT) and volume analysis was introduced in this study. Micro-CT images of hardened slag-containing paste samples were acquired using the Phoenix Nanotom S

XCT (GE Inspection Technologies). This technique takes advantage of the relatively high density and atomic number of Fe resulting in higher greyscale value assignment to the reconstructed slag particles. After 24 hours of curing in plastic containers, a small fracture (≈ 1cm^3) of the hardened paste wrapped in Parafilm® tape was mounted into the sample holder for the scan. For the main results highlighted in the next chapters, the hydration of a single sample per blend was followed over time eliminating the need to perform solvent exchange to stop the hydration.

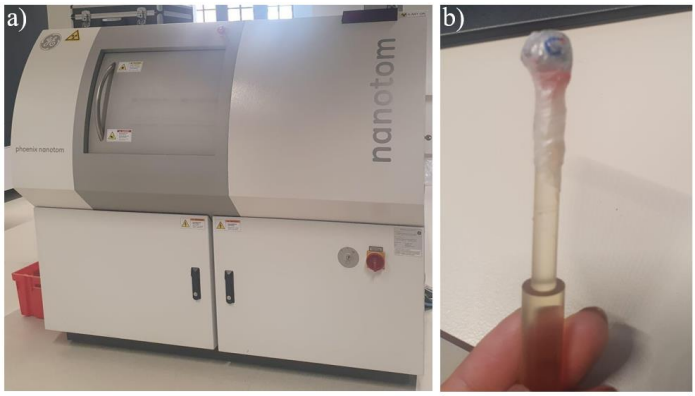

Figure 2.9 *Picture of the XCT unit at the Materials Science Department of KU Leuven used in this study (a) and of a hardened paste wrapped in Parafilm® and mounted in the sample holder for XCT (b)*

A 360° rotation scan using a step size of 0.15° was performed to obtain tomographic projections. The X-ray source was regulated at 90 kV (voltage) and 170 µA (current) in the nano focus mode 1. Tungsten on CVD synthetic diamond was installed as a target and a 0.1mm thick copper filter was mounted to harden the incident X-ray beams. A balance to maximize the scan area while maintaining the precision lead to the selection of 2.15 µm as the isotropic voxel resolution. This means that any change in the scan properties below the particle size 2.15 µm was not detected at this resolution. 2400 projections were taken with 500 ms exposure time yielding a total scan time of 1 hour and 26 min per sample. The position of the sample was saved for the next scan after a pre-determined curing period.

Image reconstruction was performed in the Datos|x software producing cross-sectional stack images. Using the 16-bit greyscale reconstructed projections, threshold segmentation was done in the Bruker CT-Analyser (CTAn) v 1.18.8.0+ software. A standard series of operations for image correction described in Appendix E was followed in order to produce binary image stack and calculate the total volume occupied by either of the components (1 or 0) in the scan volume. This was then uploaded in the

Bruker CTVox v 3.3 software to generate 3D volume renders of the samples at different curing ages. The total slag hydration degree was estimated using the total percent volume of the slag after 1 day of hydration as the zero reactivity reference. It follows the assumption that the degree of slag hydration after 1 day is negligible and that all the slag dissolved participated in the hydration reactions. Therefore, the total percent of hydrated slag was obtained using **Equation 2.4**.

$$\alpha_{slag}\,(\%) = \frac{V_{slag,1d} - V_{slag,i}}{V_{slag,1d}} \times 100 \qquad \textit{Equation 2.4}$$

where: α is degree of hydration; V is the total volume of the slag; and i is the curing time for which the hydration degree is being estimated.

A sensitivity analysis was performed to demonstrate the effect of the lower greyscale threshold limit assigned to the slag particles during the segmentation, to the estimated total volume of the slag. Moreover, a reference hardened paste sample (hydration is stopped) was scanned in the beginning of each test for a curing period in order to correct displacement of the greyscale values due to any possible time-dependent changes in the X-ray beam intensity.

Finally, the same methodology was adapted to hardened paste samples (formulation A, see section 2.1.4) where: (1) the volume of interest (VOI) is changed from cubic to cylindrical; (2) and solvent exchange was performed to stop the hydration after 1 and 90 days of curing. In effect, instead of following the slag hydration degree of a single paste sample, two different samples of the same formulation were scanned for 1 day and 90 days. The estimated hydration degrees were plotted together with those obtained from the 9 mm^3 cubic VOI without stopping the hydration. This is done to demonstrate the precision of the estimation using XCT even when the procedures are modified.

The development of the protocols for this technique was critical in this research work faced with the difficulty of quantifying the dissolution of the highly amorphous Fe-rich slag using the more conventional techniques (i.e., dissolution test, XRD quantification). The protocols developed could be relevant not only for CAC-based systems but also for other binder systems (i.e., PC-based blends) where the components have distinct differences in density and composition.

2.2.5. Spectroscopy

^{57}Fe Mössbauer spectroscopy

This technique was used to elucidate the atomic environment of Fe, being

the main component of the slag, and its evolution during the hydration. ^{57}Fe Mössbauer spectroscopy (WissEl GmbH) was operated using a ^{57}CoRh source and a metallic iron foil for the velocity scale calibration. Although most of the spectra were measured at room temperature, some samples were also analyzed at 77K to extricate overlapping signatures of different Fe species during the fitting. The evaluation of the spectra was performed by least-square minimization fitting of lines using the IMSG software.

The Mössbauer spectra obtained from the raw slag is presented in **Figure 2.10**. Different Fe components were also fitted in this figure, using the parameters presented in **Table 2.7**. More details on the model can be found in Appendix F.

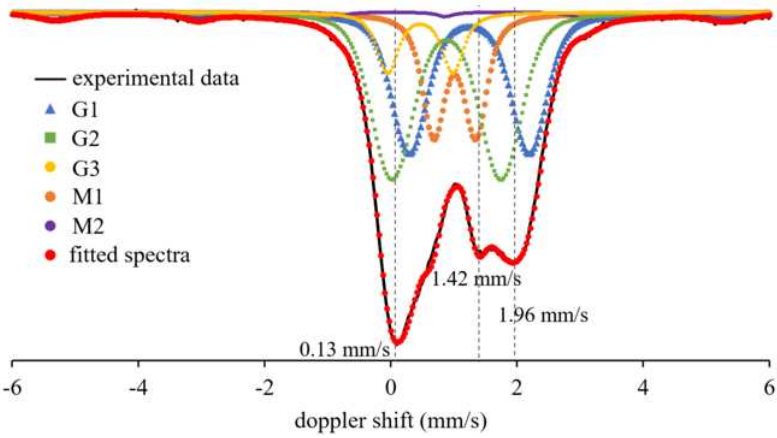

Figure 2.10 *Deconvoluted ^{57}Fe Mössbauer spectra of the slag (granulated FS) measured at room temperature*

Table 2.7 *^{57}Fe Mössbauer hyperfine parameters of the fitting proposed for the slag shown in Figure 2.10. The different parameters are abbreviated as follows: isomer shift (IS); central value of the quadruple splitting (QS); central value of the hyperfine magnetic field (MF); total Gaussian-type spreading of the quadruple splitting (ΔQS) or the hyperfine magnetic field (ΔMF); and total absorption area fitted to the component (AA). The typical errors for the IS and QS is ± 0.02 mm/s and ± 5% for the AA*

Component	IS (mm/s)	QS (mm/s)	MF (kOe)	ΔQS or ΔMF (mm/s or kOe)	AA (%)
G1	1.14	1.91	0.00	0.42	30
G2	0.79	1.73	0.00	0.51	40
G3	0.38	1.04	0.00	0.17	9
M1	0.91	0.67	0.00	0.20	18
M2	-0.08	-0.01	330.93	14.65	3

total	100

The fitting demonstrates the diversity of Fe speciation in the slag despite its seemingly simple crystallography composed of an amorphous phase (92 wt%). Components very similar to those found in Fe-rich slags in Siakati *et al.,* 2020 [117] and Peys *et al.,* 2019 [116] were identified. Based on the combination of Mössbauer parameters, the compositions were assigned as follows: two doublets of Fe^{2+} (G1 and G2) and a doublet of Fe^{3+} (G3) in the glass fraction; a doublet of Fe^{2+} (M1) and a sextet magnetic component (M2) both in the crystalline fraction. The components were selected based on the initial characterization of the slag (section 2.2.1). The reducing environment in the furnace during the slag generation evidently resulted to the dominance of the Fe^{2+} components in the system. The wide spread of the quadruple split (ΔQS) clearly suggests that these components are incorporated in the amorphous fraction. The presence of two Fe^{2+} contributions in a similar slag has been previously reported to be a result of the high irregularity of the Fe ions in the glass network [117] and characterized by the asymmetric velocity resonant intensities. The higher IS and QS values of G1 indicate the higher coordination number of Fe in this component.

Furthermore, a minor Fe^{3+} component (G3) in the glass fraction was also likely to be present in octahedral coordination. Wüstite was assigned as the component M1 with the fitted area fixed according to the measured amount of wüstite using XRD-Rietveld in the preceding section. On the contrary, addition of the minor magnetic component (M2) improved the fitting of the experimental spectrum despite the fact that no ferromagnetic minerals were detected by using the other characterization techniques. Nonetheless, it must be noted that the value could fall well within the measurement error ± 5% for AA in the fitting.

In addition, **Figure 2.11** and **Figure 2.12** show the spectra obtained for the raw cement samples. Despite the indication from XRD (Appendix B) that Fe in both of these materials is part of the C_4AF crystal, a clear difference in the spectra is obtained. That of the pure CAC has a similar pattern to the spectra published in Honeybourne, 1980 [146] for a high alumina cement. The primary contribution was attributed to a non-stoichiometric C_4AF, but also the presence of minor amounts of wüstite and magnetite was noted. On the other hand, the spectra of the raw PC resembled that previously obtained in Rai *et al*., 2009 [147] associated to the contribution of C_4AF in anhydrous PC. The noisy signals were caused by the significantly low Fe content of these materials (< 2 wt% Fe_2O_3, **Table 2.4**) relative to the raw slag. It follows that the signature of Fe that will be detected in the hydrated pastes following the blends in section 2.1.4, can be assumed to almost exclusively originate from the slag rather than the cement components.

Nevertheless obtaining these spectra, although with noisy signals, remained essential in discerning any possible contribution of the cements during the fitting.

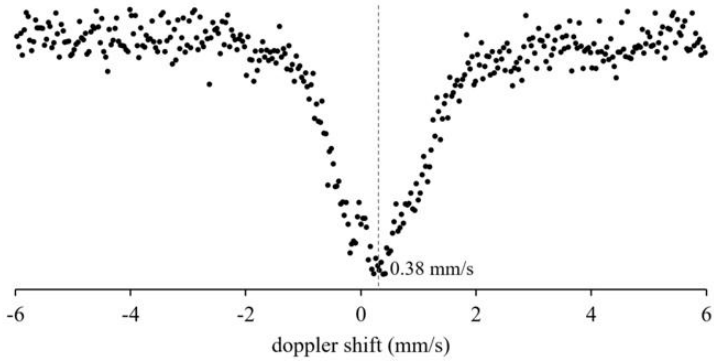

Figure 2.11 *Deconvoluted ^{57}Fe Mössbauer spectra of the CAC (Secar 51®) measured at room temperature*

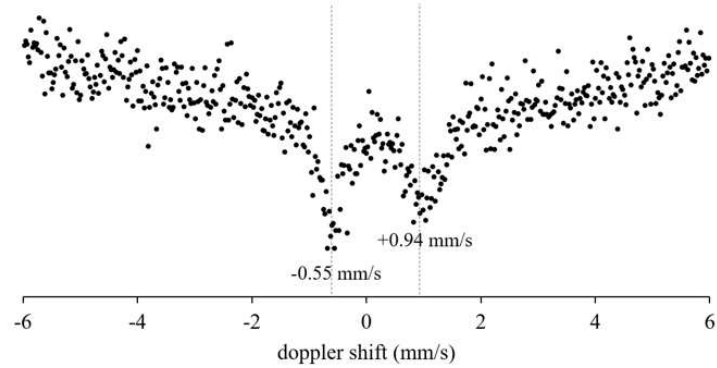

Figure 2.12 *Deconvoluted ^{57}Fe Mössbauer spectra of the PC measured at room temperature*

The evolution of the Mössbauer spectra of hydrated pastes is presented in Chapters 3 and 4. In addition, the slag hydration degrees of formulation A paste samples at different curing ages were also estimated from the absorption areas of the unreacted slag components, using the simplified equation below:

$$\alpha_{slag}\,(\%) = \frac{\Sigma AA_{raw\ slag} - \Sigma AA_{\ unreacted\ slag,i}}{\Sigma AA_{raw\ slag}} \times 100 \qquad \textbf{Equation 2.5}$$

where: α is degree of slag hydration; *AA* is the absorption area obtained from the fitting of the Mössbauer spectra; *i* is the curing time for which α is estimated. More details on this calculation are provided in Appendix H.

Attenuated Total Reflection – Fourier Transform Infrared Spectroscopy (ATR-FTIR)

The ATR-FTIR spectra were obtained using the Bruker Alpha-P spectrometer with diamond crystal. Each measurement consisted of 32 scans with a resolution of 4 cm^{-1} and a range from 380 to 4000 cm^{-1}. The raw results were expressed in transmittance and were then converted to absorbance for the analyses. The average of three runs was used to plot each spectra. The primary objective of this technique in this study is to attempt to demonstrate the reactivity of the slag through the Si-O peak shift similar to what has been previously reported for inorganic polymers [117], elaborated in Chapter 1. This characteristic was claimed [117] to be related to the partial oxidation of the Fe^{2+} in the slag to Fe^{3+} as it participates in the silicate network forming/modification during the polymerization. In addition, the phase assemblage evolution of the hydrated pastes were also followed using this technique. The results obtained were interpreted in conjunction with those of the XRD and TGA.

The ATR-FTIR spectra of the main raw materials used in Chapters 3 and 4 are presented in this section. The assignment of the bands was based on literature data [86, 137, 165, 171, 172, 200] on pure and synthetic systems, better elaborated in sections 3.3.3 and 4.3.3.

For the slag (**Figure 2.13**), the Si-O-T (where T could be Al, Fe or Si) asymmetric stretching vibrations at 900 cm^{-1} and Si-O-T asymmetric bending vibrations at 470 cm^{-1} were detected.

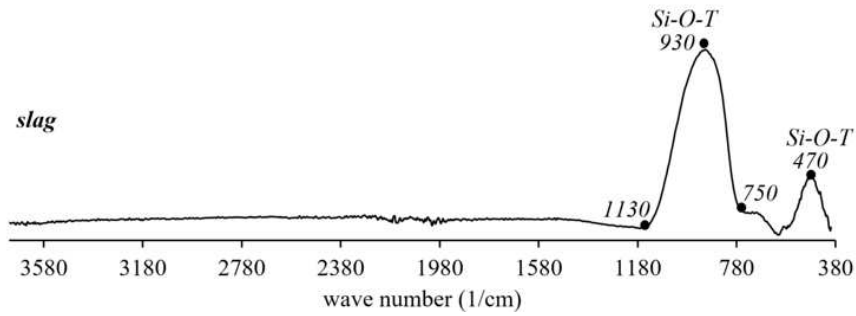

Figure 2.13 *ATR-FTIR of the raw (granulated FS) slag*

A more complex spectrum (**Figure 2.14**) is obtained for the CAC (Secar 51®) consisting of Si-O peaks (around 1030 cm^{-1} and 415 cm^{-1}) and several Al-O peaks (in the region between 521-786 cm^{-1}).

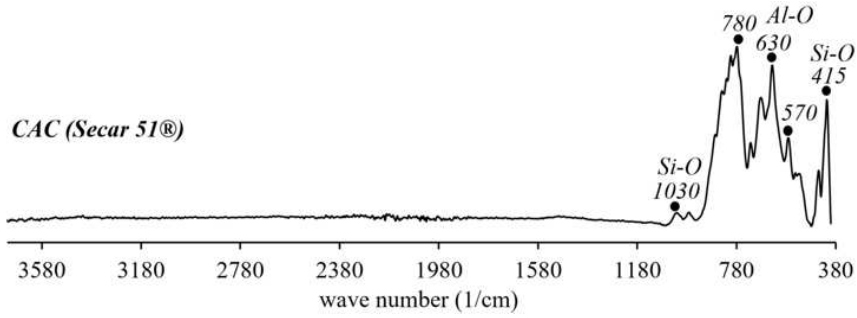

Figure 2.14 *ATR-FTIR of Secar 51®*

For the PC, two main peaks were identified positioned at 880 cm^{-1} and 520 cm^{-1} attributed to the multiple coinciding peaks of Si-O asymmetric stretching vibration bands of C_3S and C_2S.

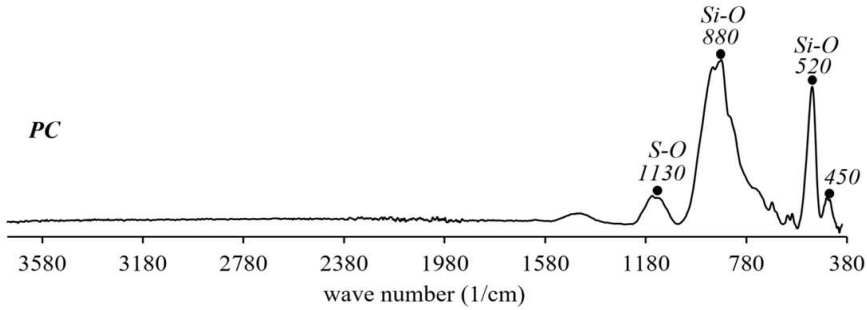

Figure 2.15 *ATR-FTIR of the PC*

Finally for the HH, distinct S-O peaks at: 1150 and 1115 cm^{-1} (mode v3), 1006 cm^{-1} (mode v1), 653 and 593 cm^{-1} (mode v4); and O-H peaks at 1620 cm^{-1}, 3660 cm^{-1} and 3550 cm^{-1} (mode v2, v3 and v1 respectively) were identified.

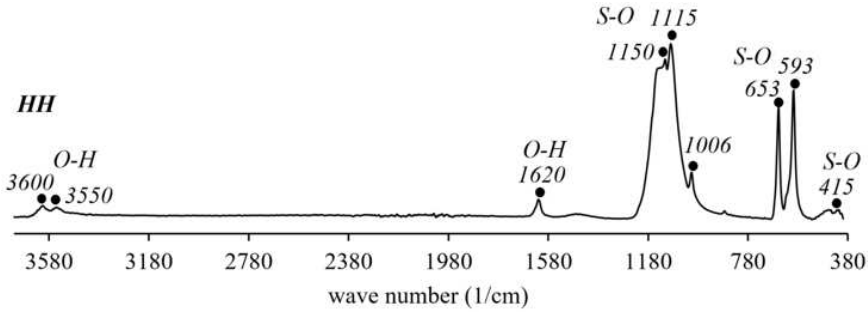

Figure 2.16 *ATR-FTIR of the calcium sulfate hemihydrate (HH)*

2.2.6. Microscopy

Optical Microscope

An initial observation of the hardened paste samples under an optical microscope (Nikon Eclipse LV150) revealed the distinct features of the slag particles. Under polarized light (**Figure 2.17** a), the dark color of the raw slag particles makes them readily distinguishable from the other components present such that a simple image analysis using ImageJ can be used to reconstruct binary images as demonstrated in **Figure 2.17** b. Following the concept and assumptions described in section 2.2.4, a similar methodology for calculating the degree of slag hydration can be performed based on the change in the total slag volume over time. However, the main drawback in using images from the optical microscope is the limited resolution. In order to address this issue, the use of SEM-BSE micrographs was opted in this study. Nonetheless, these initial observations using the optical microscope could be useful for a rapid evaluation for future studies.

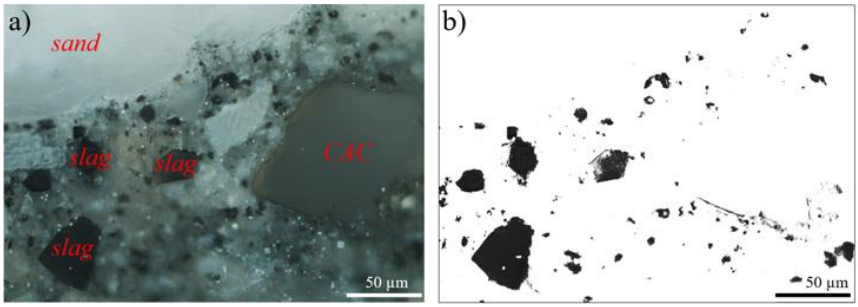

Figure 2.17 *(a) Micrograph of a slag-containing hydrated mortar sample observed under an optical microscope in polarized light. (b) Binary image resulting from image processing using the Image J software.*

Scanning Electron Microscope (SEM)

The ThermoFischer Quanta 250 FEG scanning electron microscope was used to analyze the microstructures of the slag-containing hydrated blends in this study. After stopping the hydration through solvent exchange, fragments of hardened paste and mortar samples were impregnated under vacuum with an epoxy resin (EPOXYPACK 30). This was followed by progressive polishing from 9 to ¼ µm aided by a diamond spray (Struers DP-Lubricant Brown, alcohol-based with polyethylene glycol). The scan was performed at an accelerating voltage of 20 kV using the backscattered electron (BSE) and the energy dispersive X-ray analysis (EDS) detectors.

In **Figure 2.18**, images from optical microscope are presented side by side with that of the SEM in BSE mode. Both techniques revealed the distinct dendritic surface of the raw slag particles, a notable feature rendered by the Fe-O dendrites in granulated slags [148]. This facilitated the identification of the slag particles under the microscope in this study and consequently aided the selection of image analysis operations for the quantification of the degree of slag hydration.

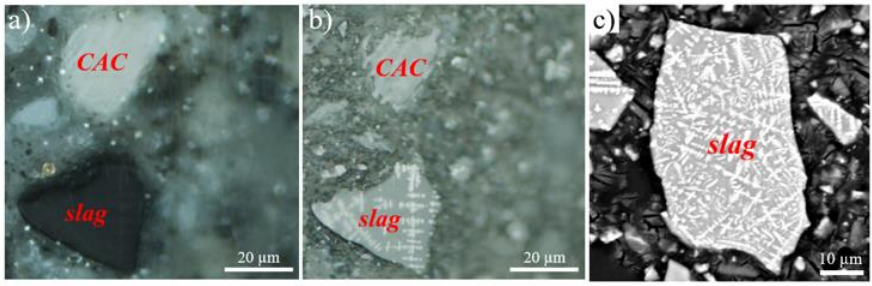

Figure 2.18 *Micrograph of a slag-containing hydrated mortar sample observed under an optical microscope in (a) polarized light and (b) reflected light. (c) SEM-BSE image focused on a raw slag particle.*

Image analysis was employed on SEM-BSE micrographs of formulation A hardened paste samples after 1 and 90 days of hydration. The operations followed are described in detail in Appendix G. The degree of slag hydration was evaluated following the same assumptions as those using tomography (section 2.2.4), however calculating the total slag area (**Equation 2.6**) instead of the slag volume for the latter.

$$\alpha_{slag}\,(\%) = \frac{A_{slag,1d} - A_{slag,90d}}{A_{slag,1d}} \times 100 \qquad \textit{Equation 2.6}$$

where: α is degree of hydration; A is the total area of the slag. In this case, the degree of slag hydration is estimated after 90 days of hydration.

A comparison of the values of the degree of slag hydration obtained using image analysis of SEM-BSE micrographs versus that obtained from the volume analysis of tomography is presented in Chapter 3.

Transmission Electron Microscope (TEM)

The CM200 transmission electron microscope from FEI equipped with an EDS Si (Li) EDAX system, operated at 200 kV, was used to characterize the hydrate phase assemblage on the nano-scale. After stopping the hydration, finely ground paste samples were dispersed in acetone. The suspension was left in an ultrasonic bath for at least 1 min to aid the dispersion. Few drops were extracted, placed in a copper grid and mounted

for analysis. Energy dispersive X-ray spectroscopy (EDS) was used to determine the chemical analysis of the selected areas.

The technique was also used to observe the differences in morphologies with a reduced intermixing of phases in the same analytical volume relative to SEM. This interest was supported by the investigation of Fe uptake on C-S-H in Siramanont *et al.,* 2021 [133] where changes in morphology were observed corresponding to different extents of Fe incorporation (**Figure 2.19**). Those with lower Fe uptake were characterized by typical foil-like morphology for C-S-H, while the formation of Fe-rich spherical nanoparticles distributed around the C-S-H foils was noted at higher uptake [133].

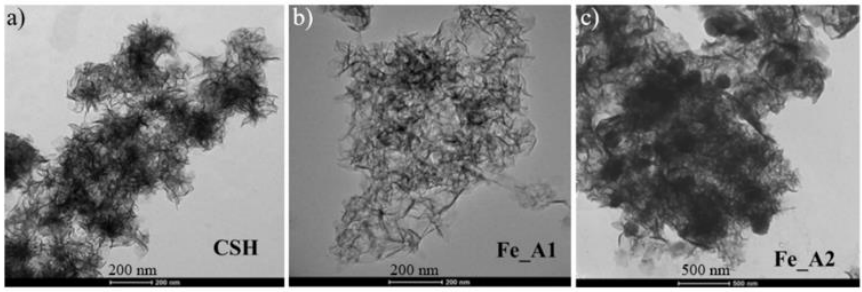

Figure 2.19 *TEM images of pure synthetic C-S-H (a); C-S-H with low, 0.010-0.014 mmol/g, Fe uptake; (b) and C-S-H with high, 0.039-0.048 mmol/g, Fe uptake modified from Siramanont et al., 2021 [133].*

Scanning Transmission Electron Microscope (STEM)

The JEM-ARM 200F Cold FEG scanning transmission electron microscope equipped with a spherical aberration (Cs) probe corrector was operated at 200 kV. EDS spectra and X-maps were recorded on a Jeol spectrometer (SDD, Jeol DRY SD 30 GV). This technique was employed to facilitate the search for the Fe-bearing hydrate phases, similar to the method previously presented in Siramanont *et al*., 2021 [133]. A modified version of Fe-maps from their study shown in **Figure 2.20**, demonstrated the role of STEM in assessing whether Fe is incorporated in the structure of the C-S-H (more uniformly distributed) or in another phase evolving from C-S-H during hydration (presence of high concentration zones).

In Chapters 3 and 4, the percentages associated with the TEM and STEM results pertain to the atomic composition of the marked areas estimated from EDS analysis. It must be emphasized however that these percentages should not be interpreted as the absolute values, considering the semi-quantitative nature of the analysis. Rather, they are indicators of the average proportions of elements interacting with the electron beam. Light (low atomic mass) elements such as O, C and H are often erroneously

estimated in EDS analysis. Considering that these elements are significant components of the hydrate phases, the absolute composition of the areas analyzed could not be accurately determined.

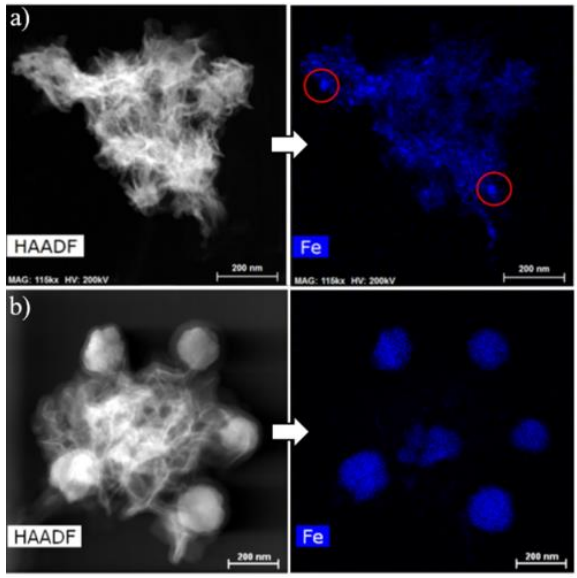

Figure 2.20 *STEM-EDS Fe-maps of C-S-H foils possibly with Fe incorporated in the structure (a); and C-S-H foils intermixed with Fe-rich spherical nanoparticles, possibly ferrihydrites or hydrogarnet. The images were modified from Siramanont et al., 2021 [133].*

In addition, some phases, particularly the hydrated ones, could disintegrate during or after the scans which may result in differences between the theoretical and experimental composition of the identified phases. A pertinent example of this is the analysis of S and O in ettringite. Ettringite forms a hexagonal prismatic crystal consisting of $Ca_6[Al_2(OH)_{12}•24H_2O]^{6+}$ columns bonded through electrostatic interactions with $\{(SO_4)_3•2H_2O\}^{6-}$ in the inter-column channels, illustrated in **Figure 2.21**. With this configuration, the sulfate tetrahedra could potentially disintegrate along with the water molecules when bombarded with electron beams during the EDS analysis. Moreover, the SO_4^{2-} ions in ettringite are easily substituted by OH^-, CO_3^{2-} [149] and even by other oxy-anions (i.e., CrO_4^{2-}, SeO_4^{2-}, SeO_3^{2-}) [150]. The presence of these several solid solutions, in addition to the potential amorphization of ettringite with pressure or at longer ages [151], could be attributed to lower S proportions as opposed to what is theoretical expected for ettringite.

Nonetheless, expressing the values in terms of atomic percentages allows calculation of molar/atomic ratios of the relatively heavier elements especially Ca, Si, and Al. When presented in ratios, they become more

reliable references for phase identification in conjunction with the characteristic morphology of some minerals. This is particularly the case for ettringite, considering its tendency to maintain its distinctive needle/rod-like microstructure even at wide ranges (> 65%) of solid substitution of its sulfate ions [150].

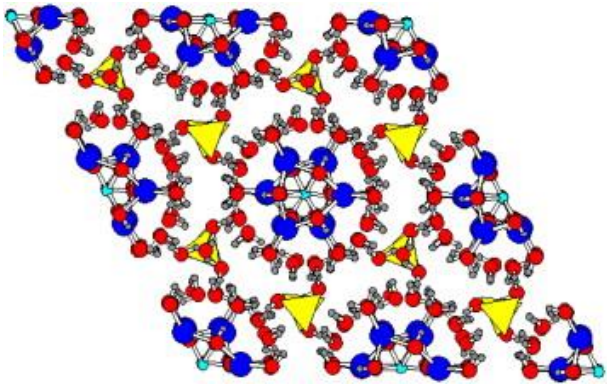

Figure 2.21 *Crystal structure of ettringite projected on to the (0001) plane. Ca atoms are shown as blue circles, oxygen atoms in red, aluminum atoms in light blue, sulfate tetrahedral in yellow and hydrogen atoms in grey [152,153].*

2.2.7. Other techniques

Electric conductivity

Electrical conductivity measurements were made using the Mettler-Toledo SevenMulti for 0.1 g/L and 0.5 g/L suspensions with no pH adjustment. The temperature was controlled at 20°C using a 1 L thermostatic beaker filled with 900 mL of deionized water (pH 7.1) where the solid is introduced. Measurements were taken at 5 s interval and the suspension was constantly agitated at 500 rpm. The beaker was sealed using Parafilm® to limit atmospheric carbonation. A schematic diagram of the set-up adapted from Maach, 2016 [154] is presented in **Figure 2.22**.

ICP-AES

5 mL solution was extracted after 30 min of conductivity test using a syringe equipped with 0.2 µm polyethersulfone filter. The filtrate was stabilized for ICP-AES analysis by adding 5 vol% nitric acid (67%, NORMATOM®).

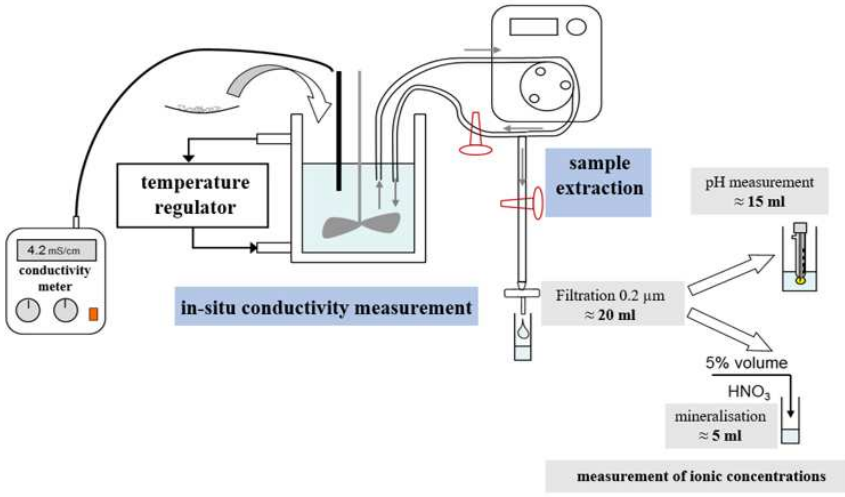

Figure 2.22 *Schematic diagram of the electric conductivity set-up modified from Maach, 2018 [154]*

2.3. Selection of industrial residue

In this section, the potential of the SOCRATES residues as SCM in a CAC-HH binary blend is assessed. Electric conductivity measurement was performed on the raw residues. Isothermal calorimetry, setting time and compressive strength tests used the binder formulations described in **Table 2.1**. At the end of the section, a separate assessment involving the jarosite residue is presented exploring its potential as a sulfate source therefore substituting HH in the system. Following the formulations described in **Table 2.2**, the effect of the substitution level to the compressive strength evolution and to the microstructure of the blends was evaluated.

2.3.1. Electric conductivity measurements

Measurements from the SOCRATES residues are plotted in **Figure 2.23** along with that of the reference cement binder. The passage of ions in the solution was assumed to be related to the dissolution of the residues. Consequently, this technique was considered as a possible measure of SCM reactivity – a concept that has been previously demonstrated [155]. In **Figure 2.23** a, it is evident that the paper residue readily dissolves into the solution which can be attributed to its high free lime content (Appendix B, **Figure B.6**). With a conductivity more than twice as high as the cement binder, it can be deduced that the amount of paper residue addition should be limited in order to mitigate the risk of flash setting. On the contrary, the conductivity of the other SOCRATES residues is significantly lower than

the reference binder. In **Figure 2.23** b, a closer look on the trend shows that although the overall degree of conductivity is closely comparable among these other residues, the kinetics appear to have a particular pattern for the highly amorphous slags. Their conductivities continue to increase throughout the first 30 min unlike the other residues which appear to stabilize even within the first 2 min of the test.

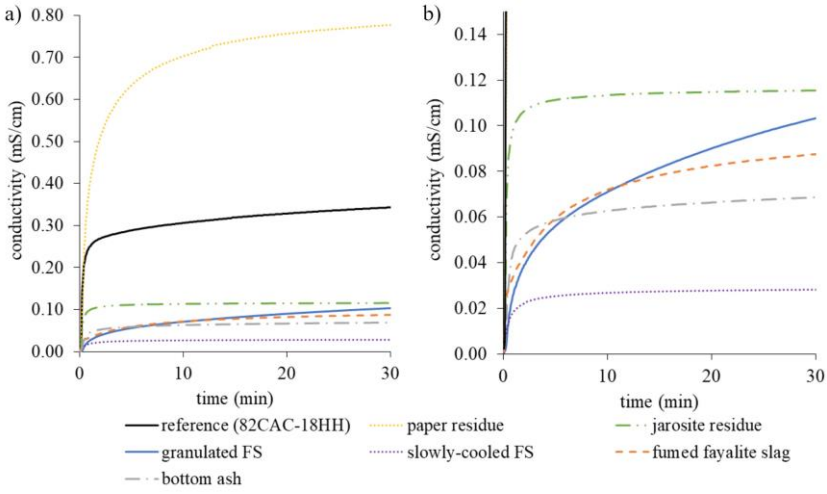

Figure 2.23 *Conductivity measurements on raw materials using 0.5 g/L suspension in deionized water at 20°C*

Considering these initial results along with the mineralogical composition of the residues (Appendix B), it was decided to evaluate the valorization potential of the jarosite and paper residues separately. These residues are sulfate- and lime-rich, respectively, making them distinctive compared to the other SOCRATES residues.

2.3.2. Heat Release

The result of the isothermal calorimetry test on paste samples is presented in **Figure 2.24**. Three main peaks in the heat flow curves (**Figure 2.24** a) similar to those previously identified [9] in low sulfate CAC binders were observed. These peaks have been associated to: (a-b) the fast dissolution of HH leading to rapid gypsum precipitation; (b-c) massive ettringite precipitation resulting from CA and gypsum reaction; and (c-d) monosulfoaluminate formation with the depletion of gypsum. Comparable calorimetry results were identified independently of the type of residue added and therefore during the first hours of reaction, their addition does not appear to significantly alter the hydration of CAC-HH.

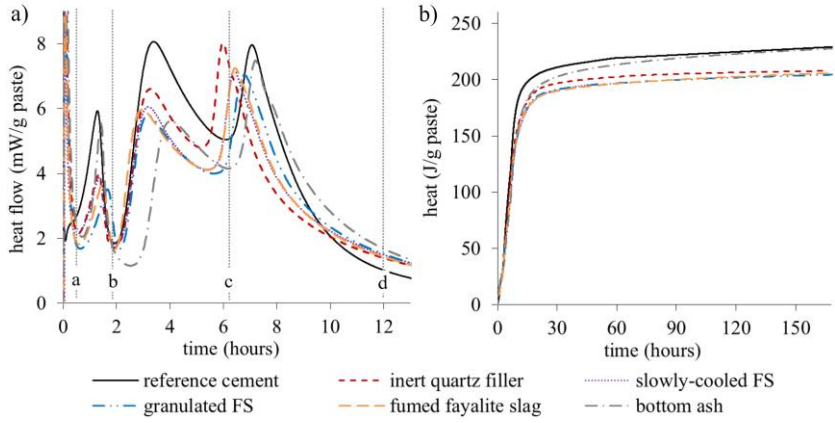

Figure 2.24 *(a) Heat flow and (b) cumulative heat release of paste samples for the screening test*

On the other hand, the cumulative heat release graph shown in **Figure 2.24** b demonstrates the overall decrease in heat release with the addition of the SOCRATES residues. Only the blend incorporating bottom ash has achieved a comparable level of heat release as the reference formulation after more than 90 hours of hydration. This could be related to the relatively high specific surface area (**Table 2.6**) of the bottom ash, possibly providing more nucleation sites for hydration. For the other residues, the differences in heat values may not be sufficient enough to draw conclusive comparisons.

2.3.3. Setting time and mechanical strength

The setting time and compressive strength evolution of standard mortars are presented in **Figure 2.25 and 2.26**, respectively.

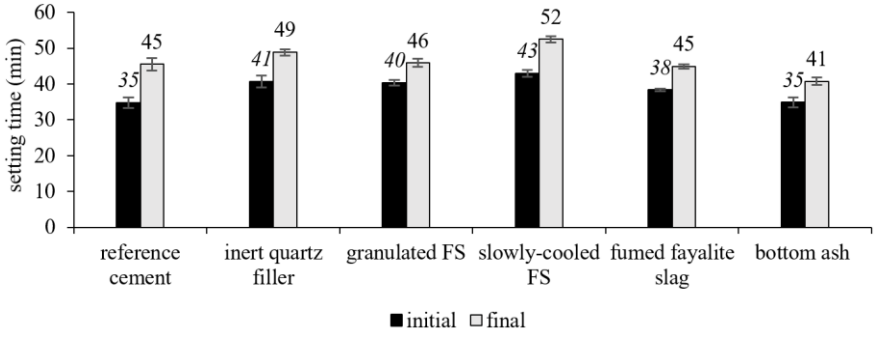

Figure 2.25 *Initial and final setting time of mixtures for the screening test*

The addition of the residues generally, but not substantially, delayed the setting compared to the reference cement formulation. Only the blend

incorporating the bottom ash displayed a shorter final setting time. Although the time reduction is minimal, this could once again be linked to the fineness of the bottom ash supposedly affecting the early hydration reactions as suggested in the preceding section. On the other hand, the highest delay in setting was noted for the blend incorporating the slowly-cooled FS. Since the fast setting property of CAC is among its valued features, such delay might be an issue and therefore, necessitates admixtures for set control.

The strength evolution was used as the main criterion for the screening test. In the first 28 days of hydration, the strength values of the residue-containing blends (**Figure 2.25**) were merely comparable to those obtained from the reference with quartz filler. Despite the overall decrease in strength compared to the reference cement formulation, the evolution of the SAI_{cement} values particularly for the amorphous slags (granulated FS and fumed fayalite slag) could be considered as one of the possible manifestations of slag hydration at long term. At this point however, it is not clear whether the strength development is directly proportional to the reactivity of the residues. Nonetheless, the trends observed demonstrated the possible long term contribution of the residue addition to the physical properties of blend.

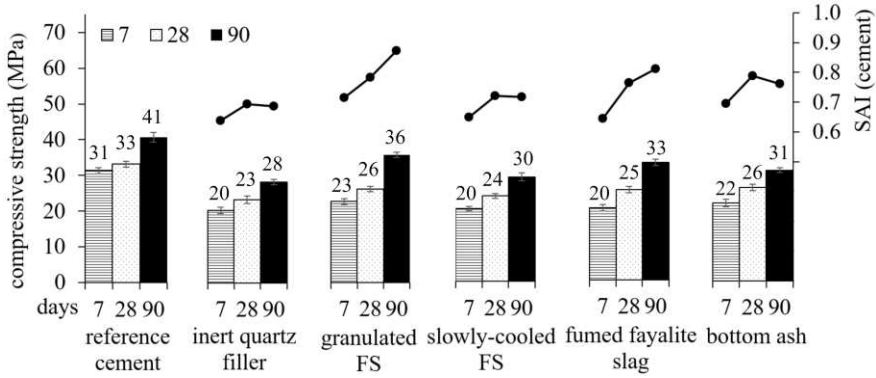

Figure 2.26 *(a) Compressive strength evolution and (b) strength activity index (SAI) of standard mortars for the screening test*

Considering the results from the raw material characterization along with the properties of blends presented in this section, the highly amorphous slags were determined to have the highest potential as SCM (at 30 wt% addition) in the CAC-rich system. Consequently, Chapters 2 and 3 will be focusing on the properties and hydration mechanism of blends incorporating the granulated FS (slag). In addition, the challenge in improving the early age performance of these blends by activating the slag will also be addressed in the next chapters.

2.4. Evaluating jarosite residue as a sulfate source

The high sulfate composition (>50 wt% SO_3, **Table 2.4**) of the jarosite residue draws the interest in its potential valorization as a sulfate source in the CAC-HH binder. However, the mineralogy of this residue (Appendix B, **Figure B.5**) is complex with several crystalline phases contributing to the sulfates content. An initial assessment is presented in this section to demonstrate the relevance of its mineralogy to the properties of the blend.

The compressive strength evolution of the blends (**Table 2.2**) with different levels of jarosite residue substitution is shown in **Figure 2.27**. The substitution clearly resulted in a decrease in strength of the standard mortar samples. The drop was more evident in the first day of curing. This became less significant at 7 and 28 days for 20 wt% and 50 wt% substitution. Although there are many factors influencing the strength of a blend, this observation could be interpreted as a possible indication that the hydration of the residue could contribute to the strength development albeit at a slower rate relative to the HH.

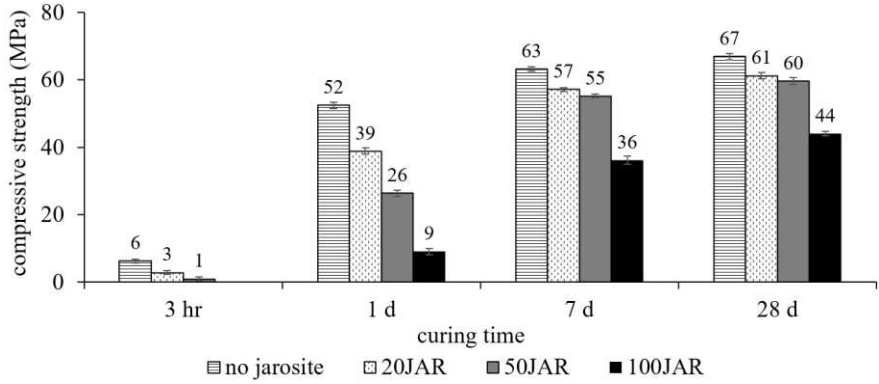

***Figure 2.27** Compressive strength evolution of blends with jarosite residue addition*

Based on the XRD patterns of the hydrated pastes (**Figure 2.28**) after 28 days of curing, the phase assemblage of the reference blend is dominated by ettringite and gibbsite with small amount of monosulfoaluminate. As the jarosite residue is added in higher quantities, the peaks associated to ettringite diminish. However, the patterns generally remained consistent until the HH was completely substituted by the residue (100JAR). At 100 wt% substitution, the peaks associated to the raw jarosite residue (Appendix B, **Figure B.5**) particularly those of jarosite, gypsum and quartz became more apparent. The height of the main ettringite peak detected at around $2\theta = 9.02°$ was greatly reduced and appeared to be slightly shifted to 9.12°. As mentioned in Chapter 1, these shifts are often attributed to Al-Fe solid substitution [131] which could be a possibility considering the

high Fe content (22 wt% Fe_2O_3) of the jarosite residue. Moreover, an amorphous hump in the AFm region (2θ ≈ 9.5-12°) was also detected in the 100JAR blend. The absence of distinct peaks of the pure CAC hydration products (i.e., C_2AH_8, CAH_{10}) could signify the participation of the jarosite residue in altering the hydration reactions of the CAC component. These observations are consistent with the compressive strength evolution (**Figure 2.27**) demonstrating the close resemblance in the properties of the blends at 28 days for 20 wt% and 50 wt% substitution.

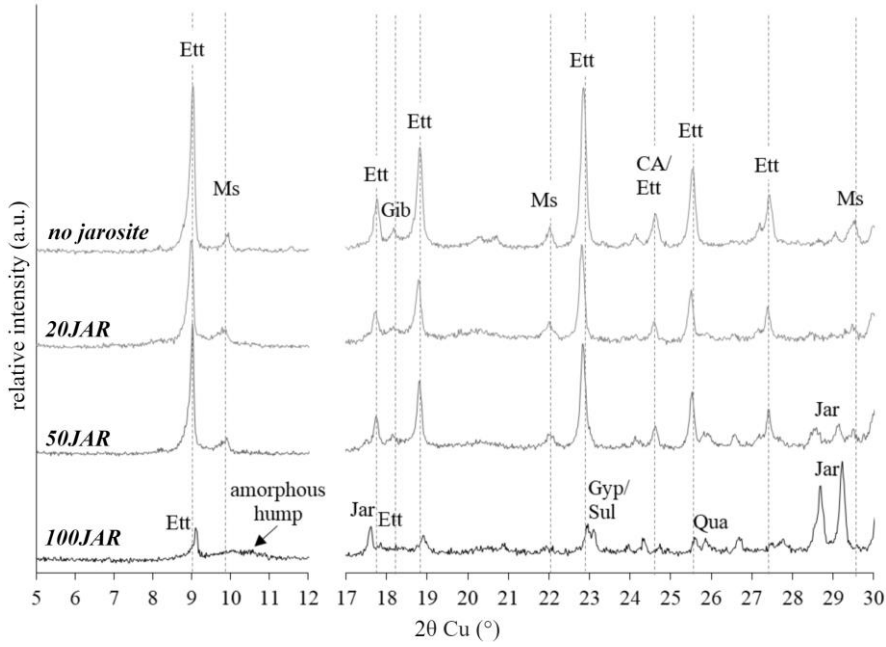

Figure 2.28 *XRD patterns of hydrated pastes with different substitution level of jarosite residue after 28 days of curing. The phases are abbreviated as follows: (Ett) ettringite, (Ms) monosulfoaluminate, (Gib) gibbsite, (CA) monocalcium aluminate, (Jar) jarosite, (Gyp) gypsum, (Sul) elemental sulfur, and (Qua) quartz. Only the principal diffractogram peaks are labelled.*

Additionally, a dissolution test was performed to compare the passage of ions in the solution between HH and the jarosite residue. The methodology for electric conductivity measurement followed by ICP-AES detailed in section 2.2.7 was executed. The conductivity measurements (**Figure 2.29**) demonstrated the faster dissolution of HH in the solution. Using the values of sulfur (S) ion concentration after 30 min obtained from ICP analysis, the percentage of dissolved S was calculated relative to the respective total S content of the raw materials. Despite their comparable SO_3 content (**Table 2.4**), the difference in mineralogy proved to be an important factor affecting the dissolution of ions. The sulfates from the jarosite residue may

not be as readily available to participate in hydration reactions in the solution compared to those of the HH.

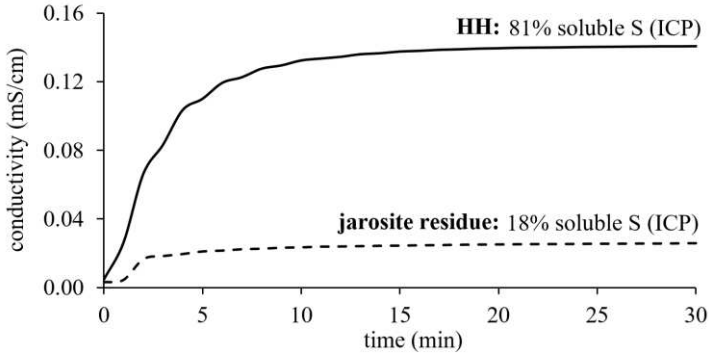

Figure 2.29 *Conductivity of the jarosite residue versus HH using 0.1 g/L suspension in deionized water at 20°C*

Comparing the SEM images of the paste samples at 0 wt% (a) and 100 wt% (b) substitution levels (**Figure 2.30**), ettringite needles are observed to be less abundant as HH is replaced by the jarosite residue.

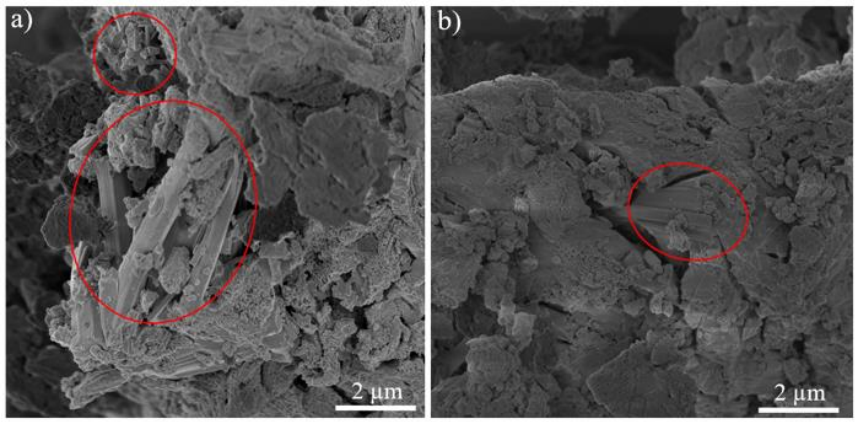

Figure 2.30 *SEM-SE images of (a) no jarosite and (b) 100JAR paste samples after 3 days of curing. Encircled in red are needle-like structures generally associated to ettringite.*

It can be inferred that the lower amount of sulfates available in the solution lead to decreased ettringite formation – an observation consistent with the phase assemblage evolution obtained through XRD. As previously mentioned in Chapter 1, maximizing ettringite formation is often desirable in sulfated CAC systems due to its strength-giving properties [9,156] which could be associated, although not directly correlated, with the obtained strength values of the blends containing the jarosite residue.

Other ions (Na, Al, Si, K, Mg, P and Fe) were also released from the jarosite residue during the dissolution test quantified in **Figure 2.31**. One of the biggest concerns in the valorization of the jarosite residue as SCM is the possible release of toxic elements and heavy metals. Although these components were not analyzed in ICP for this study, the dissolution of the other ions could signal that the jarosite residue is indeed reactive in this system and therefore the toxic components should be monitored more closely. For instance, the sulfur content of the raw residue alone is already alarming (20-30 wt% see Appendix B, **Figure B.5**). It is clear that this residue is not the typical jarosite by-product previously reported to have potential use as raw meal substitute to gypsum [157]; or as mineral additive in non-structural concrete [158]. Going back to the source of this by-product (section 2.2.1), the complexity of the composition of this residue can be traced from combining the streams of different leaching processes into one filtration unit. In fact, the sulfur content can be totally avoided by dedicating separate filtration lines for each reactors. This solution, of course, may not consider the other practical aspects of the production.

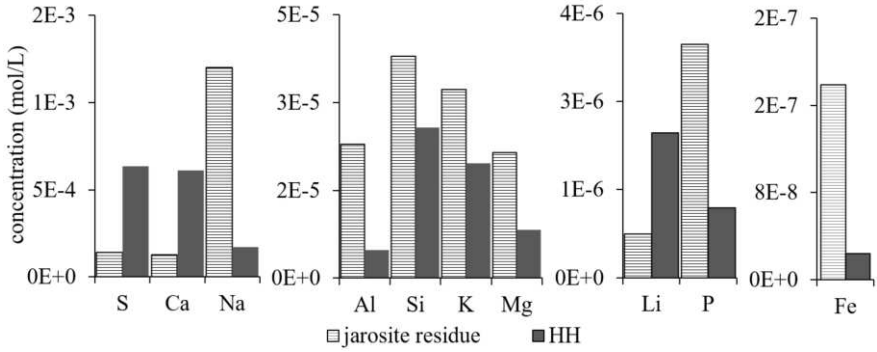

Figure 2.31 *Comparison of the ion concentrations after the dissolution test measured using ICP-AES*

Despite the promising strength evolution at lower substitution rates, the overall evaluation does not support the incorporation of the untreated jarosite residue in the CAC-HH binder system primarily due to its high S (elemental), Pb and Zn contents. Extensive analysis of the toxicity of the residue and its leaching characteristics remains indispensable in evaluating its valorization potential. Pre-treatment is recommended to better tailor the properties of this residue to cementitious applications.

Summary

This chapter details the materials and methods used in this study. Residues coming from a single production batch were used throughout this study to maintain uniform results. They were homogenized, sampled, dried and grinded to obtain a PSD as close as possible to that measured for the CAC. The characterization of the residues revealed a diverse mineralogy related to their origin. Their main properties are highlighted below:

Granulated FS

An iron-rich highly (92 wt%) amorphous slag originating from lead-zinc production. Mössbauer spectroscopy revealed that the Fe speciation in slag is dominated by Fe^{2+}. The Si-O bonds in this material were detected using ATR-FTIR. When added in CAC-rich blended cement, the dark color, high density and Fe content of the unreacted slag particles could facilitate its differentiation from the rest of the cement matrix.

Slowly-cooled FS

An iron-rich slag with the same origin as the granulated FS but more crystalline in nature (only 13 wt% amorphous) due to the slower cooling rate employed. Its composition is dominated by fayalite and spinel.

Fumed fayalite slag

An iron-rich highly (94 wt%) amorphous slag originating from secondary copper production. Although the basic properties are closely comparable to those of the granulated FS, this batch of material still contains 2.3 wt% of ZnO.

Bottom ash

A siliceous by-product of a municipal waste incinerator with a highly heterogenous composition mainly consisting of quartz, calcite, muscovite and wollastonite. Fragments of unburnt components (i.e., plastics, glass) were observed in the sample received. Its SSA was much higher than those of the slags in this study despite displaying a similar PSD.

Jarosite residue

A sulfate-rich (51 wt% SO_3) by-product of zinc leaching. Its mineralogy is dominated by jarosite, gypsum and sulfur. Its substantial Fe content (22 wt% Fe_2O_3) is linked to the jarosite component. Significant traces of Pb and Zn were also detected. Similar to the bottom ash, high SSA value was also obtained.

Paper residue

A lime-rich (68 wt% CaO) by-product of paper recycling. No further grinding was executed due to its very fine nature as-received. The electric

conductivity measurements performed demonstrated its rapid and extensive dissolution in water.

Based on these properties, the Fe-rich slags and the bottom ash were added at 30 wt% to a binary blend of CAC-HH with the goal of evaluating their potential as SCM. A screening test consisting of electric conductivity measurements, isothermal calorimetry, setting time and compressive strength evaluation was performed. Among the residues investigated, the highly amorphous slags displayed the best potential mainly supported by the strength evolution of standard mortars. These slags displayed long term (>28 days) strength contribution with SAI_{cement} values reaching up to as much as 0.9. Considering the results of the screening test along with the raw materials characterization, the granulated FS was selected as the main SCM for further investigation in Chapters 3 and 4.

Moreover, this chapter introduced various techniques for investigating the physical properties (i.e., mechanical strength, dimensional stability, setting time); phase assemblage evolution (XRD, TGA); the dissolution rate of slag (XCT, SEM); and the fate of Fe during hydration (Mössbauer spectroscopy, TEM, STEM). At the end of this chapter, the jarosite residue was evaluated as a sulfate source substituting HH in the CAC-rich blend. The strength evolution, phase assemblage, microstructure and dissolution of ions were examined. Despite the possibility of mitigating the observed strength reduction by controlling the substitution level, the overall findings do not support the incorporation of the untreated residue without prior toxicity evaluation. Pre-treatment will also be necessary to convert the sulfur component of the residue and to tailor its properties in order to improve its potential as SCM.

Chapter 3

Fe-rich slag addition in binary CAC-HH binder

Contents

Introduction

In this chapter, the addition of the highly amorphous Fe-rich non-ferrous metallurgy (NFM) slag in calcium aluminate cement (CAC)-calcium sulfate hemihydrate (HH) binder systems was investigated. In Chapter 2, this slag was identified to have the best potential as a supplementary cementitious material (SCM). The slag displayed contribution to the long term (>28 days) strength development of the standard mortars. In addition, its leachates (CuO and ZnO) were determined to be both below the detection limit, in contrary to the 2.3 wt% ZnO measured in a similar granulated slag among the selection.

The properties of formulations, A, B, and A-TC (Chapter 2, **Table 2.3**) were examined in this chapter. All of these formulations contained ≈ 30 wt% of slag. Formulations A and B have CAC/HH ratio of 4.5 and 1.6, respectively. On the other hand, formulation A-TC has CAC/HH ratio of 4.5 similar to that of the formulation A, but with 5 wt% addition of the paper residue (TC). This lime-rich (68 wt% CaO) material is highly soluble in water and is already being commercially marketed as a mineral additive for cement and concrete. Considering these properties, it has been evaluated separately as a possible activator in formulation A, aiming to induce slag dissolution and contribute Ca^{2+} ions during the early age (<28 days).

Several techniques were employed to characterize the properties of the blends for up to 1 year. Mechanical strength and dimensional stability were monitored using mortar samples. The degree of slag dissolution was estimated using SEM-BSE, X-ray Computed Tomography (XCT) and Mössbauer spectroscopy. The phase assemblage of the binary systems were simulated using thermodynamic modelling in function of the CAC proportion. Experimentally, several techniques, including isothermal calorimetry, XRD, TGA, and ATR-FTIR were used to follow the evolution of the phase assemblage using paste samples. Finally, the fate of the Fe from the slag was described based on the results of Mössbauer spectroscopy, TEM and scanning transmission electron microscope (STEM).

The methodology for the characterization techniques was specifically adapted to the distinct properties of the slag primarily related to its high Fe content (i.e., high density, high atomic mass, Mössbauer effect). For this reason, the CAC used was changed from Ciment Fondu® in the screening test to Secar 51®. The latter contains less Fe_2O_3 (< 2 wt%) and was therefore expected to interfere less with the signals of the Fe from the slag.

3.1. Physical properties

The physical properties of two blends representing a low (formulation A) and a high (formulation B) calcium sulfate system are presented in this section.

3.1.1. Low calcium sulfate system

The initial and final setting times of formulation (A) 4.5CAC-HH mortar blend and its references are presented in **Figure 3.1**. It can be seen that the addition of slag resulted in a minimal delay in the setting compared to the reference cement formulation. Changes in setting time with the addition of SCM have been previously [112,159] linked to the following factors:

- Reactivity of the SCM during the first hours of hydration (typically in the presence of high lime and sulfate content)
- Lower effective w/b ratio
- Absorption/adsorption of admixtures by SCM with high SSA
- Filler effect mechanism

In CAC blended cements, the "rapid setting and hardening" [9] property is often attributed to the fast hydration of the CAC component. With the addition of the slag, the reduced amount of the CAC content can be another reason for the delayed setting along with the factors listed above.

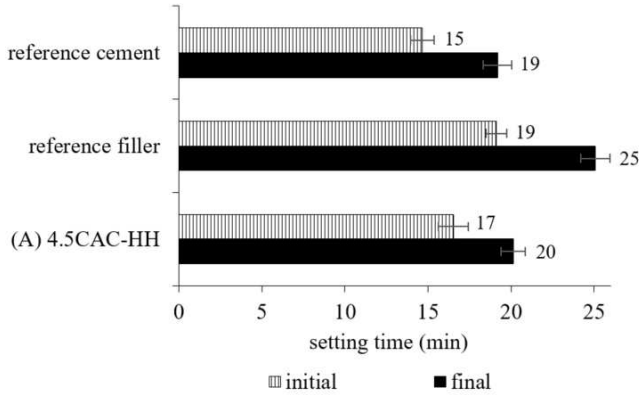

Figure 3.1 *Initial and final setting time of formulation A and its references*

On the other hand, the reference filler formulation displayed a more significant setting retardation despite following an equal volume substitution as the slag. Considering that the quartz filler and the slag have a closely comparable PSD and SSA (Chapter 2, **Table 2.6**), this difference in setting time could be a possible initial indication that the slag's role in the early hydration was not limited to that of an inert filler.

The compressive (**Figure 3.2**) and flexural (**Figure 3.3**) strength evolution of formulation A and its references were followed using standard mortars over 1 year of curing under water. The evolution of the SAI_{cement} values are presented in the secondary axes (right).

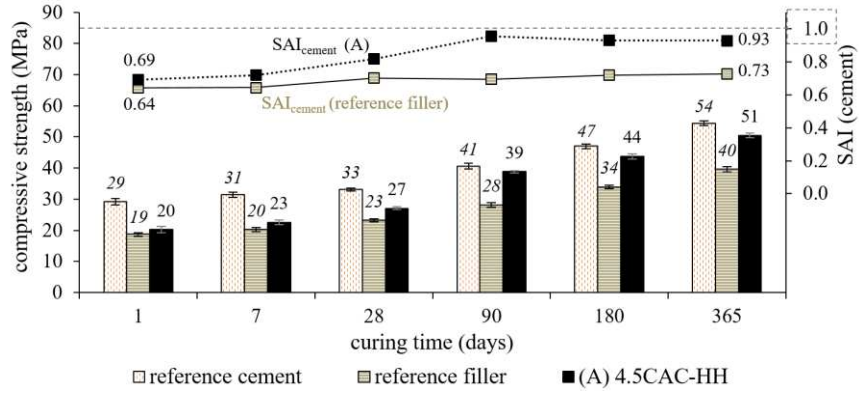

Figure 3.2 *Compressive strength of formulation A (primary axis) and its SAI evolution (secondary axis)*

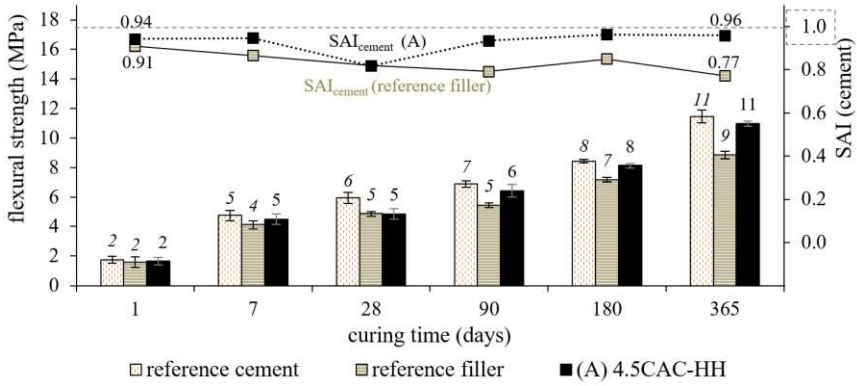

Figure 3.3 *Flexural strength of formulation A (primary axis) and its SAI evolution (secondary axis)*

Similar to the observed trend during the screening test in Chapter 2, the addition of the slag also clearly resulted in the overall decrease in strength compared to the reference cement formulation. The same effect has been previously reported in PC systems during the early hydration stage (<28 days) of a similar NFM slag [160] and as well as other SCM [8]. Although this trend was less evident in terms of the flexural strength, the decrease in the compressive strength reached as much as 31% in the first day of curing with SAI value 0.64. It was not until after more than 28 days that the compressive strengths of formulation A and its reference became comparable at 39 MPa versus 41 MPa, respectively. This was exhibited by the abrupt increase in the SAI values from 28 to 90 days. This could be

linked to slower dissolution of the slag compared to the other binder components (CAC and HH), demonstrated already during the screening test in Chapter 2 (Chapter 2, **Figure 2.23**). In general, slower dissolution rate influencing the strength evolution was reported to be prominent even among traditional SCM [12].

Nevertheless, following the SAI trends for the compressive strength (**Figure 3.2**), it is clear that the slag's hydration was contributing to the long term strength of the blend in a degree different from that of the quartz filler. Beyond 28 days, the strength values of the slag-containing formulation were comparable to the reference cement. On the other hand, the SAI values of the reference filler mortar remained consistent.

Another property that could support the potential of the slag as SCM in this system was the dimensional stability. **Figure 3.4** compares the length variation of formulation A to its reference. The measurements from the first 24 hours were obtained using the Walter+Bai shrinkage test in air-curing condition. Further measurements using the same samples were taken using an extensometer after demoulding and curing under water.

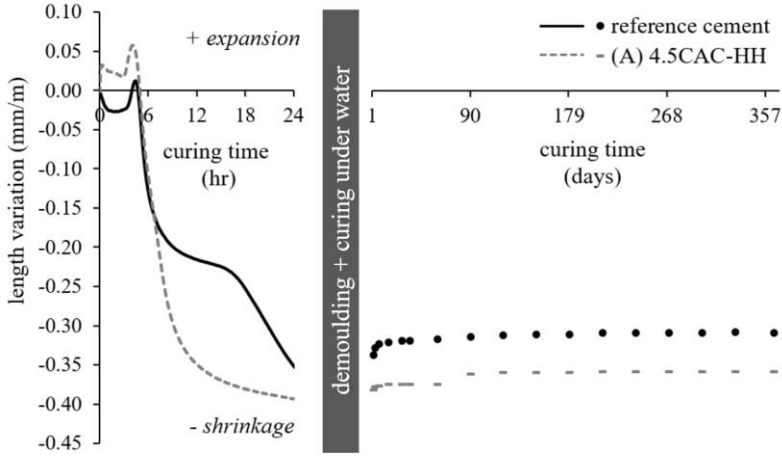

Figure 3.4 *Length variation of formulation A and its reference obtained from Walter+Bai shrinkage test for the first 24 hours of hydration. Measurements were continued using an extensometer for the demoulded samples cured under water.*

It can be seen that the addition of the slag did not significantly alter the dimensional stability of the blend. An overall shrinkage was observed during the first 24 h for both formulations. The mechanism of ettringite formation was hypothesized to slightly alter the early hours' trend, such that shrinkage was counteracted in the reference cement formulation by the fast formation of interlocking ettringite from 6 to 18 h. On the contrary, the slag-containing blend displayed a more abrupt shrinkage at this period, which could be an indication of less amount of expansive hydrates formed.

Beyond 24 hours, curing under water triggered a slight expansion for both formulations. Not only was additional water provided to stimulate hydration in this step, but also drying shrinkage was avoided throughout the remaining duration of curing.

The overall dimensional stability of formulation A was reflected through the progressive strength development in mortar samples. The addition of the slag even appeared to have positively contributed to the stability keeping the values closer to zero in **Figure 3.4**. In the end, it should be considered that despite this observation, the scale of the length measurements presented (difference of ≈ 0.05 mm/m) could fall well within the confidence interval of the test and consequently may not provide conclusive quantitative comparison.

3.1.2. High calcium sulfate system

The physical properties of formulation (B) 1.6CAC-HH with and without slag, are discussed separately since 0.3 wt% of citric acid was added in this dry mix to retard the setting. Recall from Chapter 2 that for some of the formulations in this study, setting was delayed in order to provide sufficient time for placing the freshly-mixed blends in moulds. In this case, the initial and final setting time recorded for formulation B was 38 and 46 min, respectively. As mentioned earlier, however, the influence of such a low amount of citric acid was expected to be limited within the first few hours of hydration and should not significantly alter the long term chemical properties of the blend.

The compressive and flexural strength evolution of formulation B and its references are presented in the primary axes of **Figure 3.5** and **Figure 3.6**, respectively. The evolution of SAI_{cement} values are shown in the secondary axes.

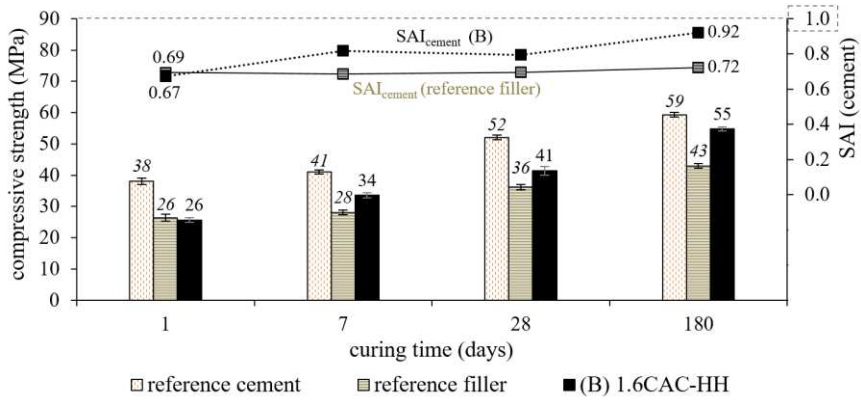

Figure 3.5 *Compressive strength of formulation B* (primary axis) *and its SAI evolution (secondary axis)*

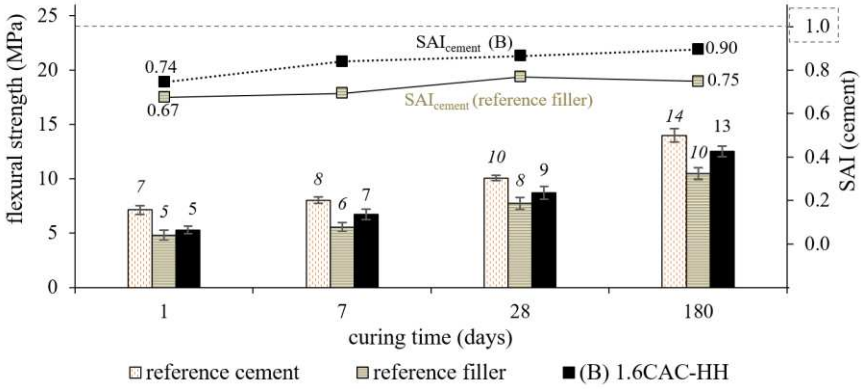

Figure 3.6 *Flexural strength of formulation B* (primary axis) *and its SAI evolution (secondary axis)*

The strength values in this high calcium sulfate system were considerably higher than those obtained from the low calcium sulfate formulation, B. However, the SAI values were generally lower implying that the observed increase in strength was more likely associated to the hydration of CAC and HH, producing more ettringite, rather than an increased rate or extent of slag hydration. An indication of this was the observed expansion of mortars in **Figure 3.7**. It will also be confirmed from the techniques in the following section.

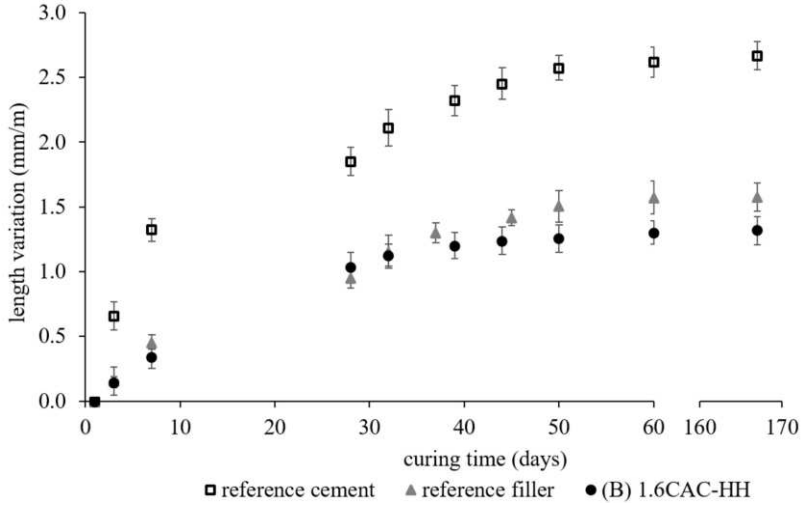

Figure 3.7 *Length variation of formulation B and its references measured for standard mortars cured under water*

While an overall shrinkage was observed in the low-sulfate formulation (A), it was the opposite case in the high-sulfate system (B) reaching as much as 2.5 mm/m expansion for the reference cement mortar. It is clear that the space-filling property [161] of the low density hydrate, ettringite, has directly contributed to the improved early strengths in formulation B. Furthermore, the addition of the slag also appeared to stabilize the blend resulting in lower expansion compared to the reference cement formulation. Although the differences in the expansion degrees between the slag-containing and its reference cement mortar were more significant (higher than the confidence interval) this time, it could be argued that this was mainly due to the filler effect, looking at the length variations of the reference filler mortars in **Figure 3.7**.

Similar to formulation A, the slag's increasing contribution to the strength in formulation B was more significant between the 28 and the 90 days where the slope of the SAI is the steepest. These results also suggest that the CAC/HH ratio used did not have a significant influence on the reactivity of the slag. This could be confirmed by the estimations of the degree of slag dissolution in the next section.

3.2. Quantifying the degree of slag hydration

In this section, two techniques were used to estimate the degree of slag hydration, namely: (1) image analysis of SEM-BSE micrographs; and (2) volume analysis of XCT reconstructed 3D renders. As previously stated in Chapter 2, these methodologies were based on the assumption that slag dissolution was equivalent to reactivity. This means that the total amount of dissolved slag has directly participated in the hydration reactions. In addition, it was also assumed that the slag was unreactive in the first 24 hours due to the absence of data during this period.

3.2.1. SEM-BSE

The SEM was initially used in this study to characterize the microstructure of the blends. **Figure 3.8** (a) shows an SEM-BSE micrograph of formulation A mortar sample after 90 days of hydration. The slag particles appear the brightest due to their high Fe content (high atomic number), and their boundaries remained intact with no apparent formation of hydration rim around the surface of the particles. On the contrary, the hydration of CAC particles was more evident with their dissolved surfaces gradually blending into the matrix. The lower reactivity of the slag versus the other binder components (CAC and HH) was further supported by the EDS maps (**Figure 3.8** b-f) revealing the massive dispersion of Ca, Al and S

throughout the interstices, while Fe and Si are localized in the slag and sand particles, respectively.

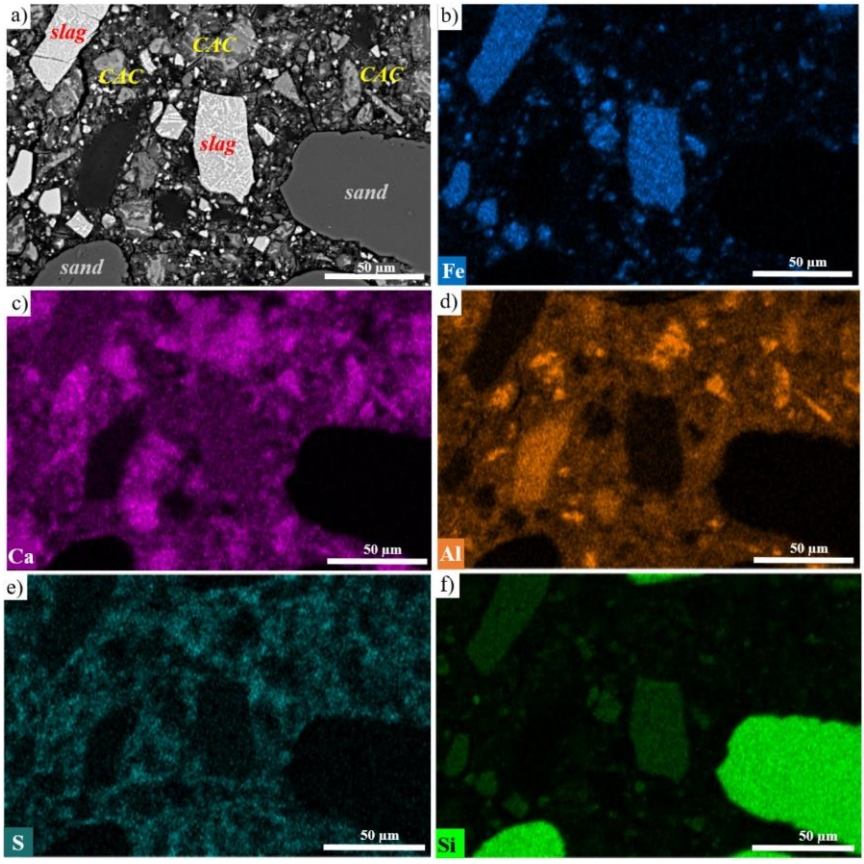

Figure 3.8 *(a) SEM-BSE micrograph of formulation A mortar after 90 days of hydration along with (b-f) the corresponding EDS maps for Fe, Ca, Al, S and Si*

Looking at an SEM micrograph of a reference cement mortar (no slag) in **Figure 3.9**, localized hydrate-rich areas are observed where CAC particles are almost completely dissolved into the matrix. This was not the case for the corresponding slag-containing mortar sample even after 90 days of curing. In addition, the presence of the coarse sand particles greatly diluted the binder in the images leading to the decision to use paste samples instead for the image analysis for slag hydration degree quantification.

Sample image analysis of slag-containing paste micrographs are shown in **Figure 3.10**. These were among the micrographs taken from polished sections of formulation A where hydration was stopped after 1 day (a) and 90 days (b) of curing.

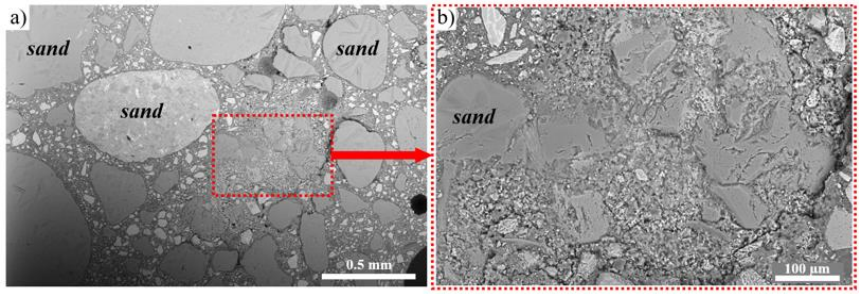

Figure 3.9 *(a) SEM-BSE micrograph of formulation A reference cement mortar after 90 days of hydration; and (b) a focused image of the area marked in red showing a localized hydrate-rich area*

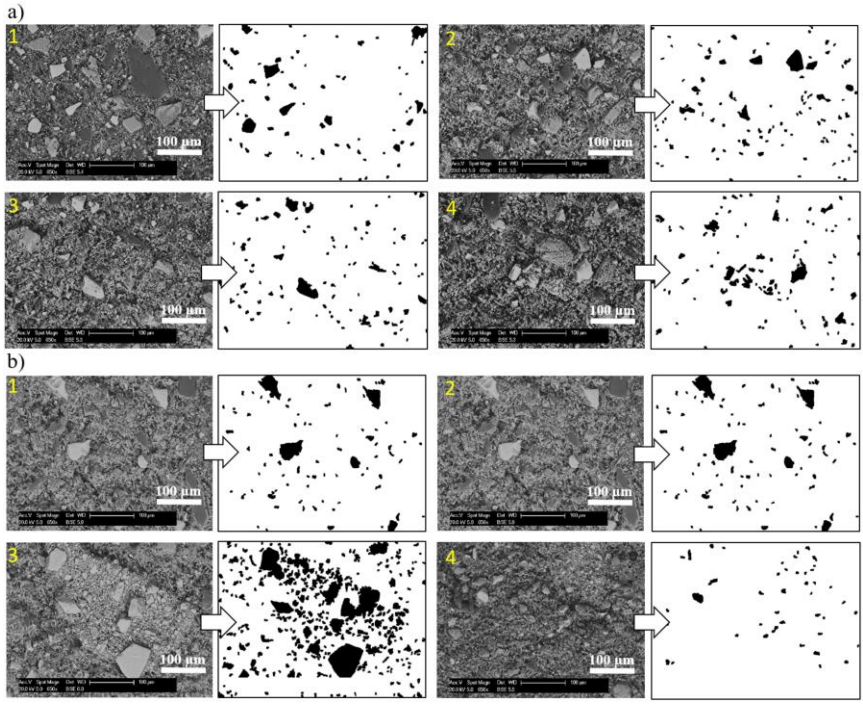

Figure 3.10 *SEM-BSE micrograph of formulation A pastes after (a) 1 day and (b) 90 days and their corresponding binary images obtained using Image J software*

Based on the image analysis, the total slag area and degree of hydration after 90 days of curing were estimated. The results are presented in **Table 3.1**. Despite the abrupt increase in SAI values (**Figure 3.2**) after 90 days of hydration, it turns out that only about 14 % of the slag has reacted at this point. Otherwise, this could also signify that the properties of paste and mortar samples at any given curing time were not directly comparable, particularly considering the difference in their interfacial transition zones [9] resulting from the w/b ratios used.

Table 3.1 *Estimated slag area and hydration degree using SEM-BSE + image analysis*

curing time (days)	total slag area (μm^2)	degree of slag hydration (%)
1	5.63	0
90	4.83	14.2

Although the huge compositional difference between the slag and the rest of the components of the hydrated paste greatly favored this methodology, certain assumptions and challenges encountered must be carefully considered. For instance, the highly contrasting abrasion resistance of the blend components (i.e., slag versus CAC) resulted in uneven surfaces during polishing. The hydrate products and the unreacted CAC were more easily scratched compared to the unreacted slag particles leaving the latter embossed on the surface. This was manifested in the micrographs as shadows around the slag particles which could significantly influence the image analysis. Another important issue was representativeness. The need to prepare polished sections required the use of separate samples to be analyzed per curing time. This means that we were not actually following the dissolution of the same slag particles over time, rather we were simply assuming that the total areas detected were representative of each curing time. Considering that we were working on the micro-scale, the randomly selected micrographs might not accurately represent the overall slag distribution. In fact, areas where slag particles appeared to be agglomerated and areas with particularly low amount of slag were observed as shown in **Figure 3.10** (b) 3 and 4, respectively.

In order to address the above-mentioned challenges, a non-destructive technique using a combination of XCT and volume analysis was discussed in the next section. Although the methodology revolved around the similar principle (following the changes in the slag area/ volume over time), the need for preparing polished sections and using different samples per curing time was eliminated.

3.2.2. Tomography

The degree of slag hydration of formulations A and B were followed after 1, 28, 90, 180 and 365 days using a single hardened paste sample per formulation. The threshold segmentation to select the slag particles was optimized, guided by the observations from the SEM (EDS point ID). The major steps involved were illustrated in **Figure 3.11**. In this figure, a red arrow is drawn in the 2D reconstructed images (a). The plot profiles (b) corresponding to the pixels under the arrows demonstrate that the selection of the lower threshold value for the slag particles was greatly facilitated by the distinct difference in the range of grayscale index between the slag and the rest of the components. The binary images (c) were obtained following

the operations described in Appendix E. Using 1400 binary images per sample, the 3D renders (d) of the undissolved slag particles (shown in white) were built.

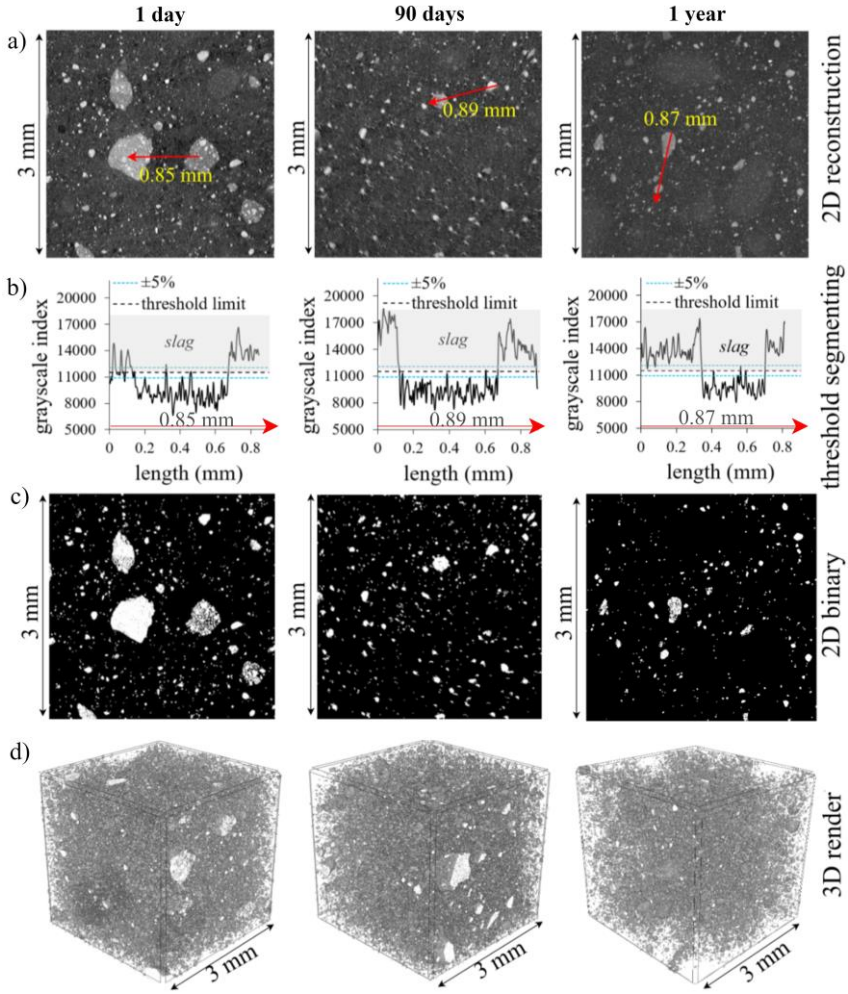

Figure 3.11 *Illustration of the steps involved in the volume analysis of XCT scans*

There were two important details to consider in analyzing the XCT results:

1. Variations in the scanned VOI was inevitable despite using the same paste samples over time mainly due to the dimensional changes during hydration. For instance, the particles in the edges could move in (shrinkage) or out (expansion) of the VOI.
2. The voxel resolution of the scans was set to 2.15 µm in order to cover a sufficiently representative volume while optimizing the scan time. This means however that the slag particles with a diameter

<2.15 µm could not be accurately detected unless it occupies i.e., 70-90 vol% of the voxel, variable according to the threshold segmentation limits imposed during volume reconstruction. This could decrease the accuracy of slag hydration degree estimation, considering that about 20 wt% of the slag particles fall below this size according to the PSD in Appendix C. The direct consequence of increasing the resolution or reducing the voxel size is either an increased scan time, or a smaller sample size. The former is not ideal due to the on-going hydration, while the latter might yield less representative estimation.

Figure 3.12 shows the estimated slag hydration degree (primary axis; vertical left) and their respective total slag volumes (secondary axis; vertical right) obtained from the XCT-volume analysis. The estimated slag volume varying between 6.0-6.5 % for the two formulations at 1 day seems to be reasonable compared to the 8.4 vol% estimated (Appendix H) using the density of the components without accounting for the porosity. Based on these results, the rate and extent of slag reactivity in the low-sulfate system (formulation A) appeared to be 6% higher than in the high-sulfate system (formulation B). Indeed, the higher strength values obtained for formulation B mortars were not proportional to the slag reactivity, rather more related to the hydration of the CAC in a high-sulfate system. Moreover, the converging values at ≈ 10 % of slag hydration degrees after 28 days for the two formulations could support the earlier observation based on the SAI trends that the slag's reactivity during the early stage of curing (<90 days) was not significant enough to contribute to the strength evolution, regardless of the CAC/HH ratio.

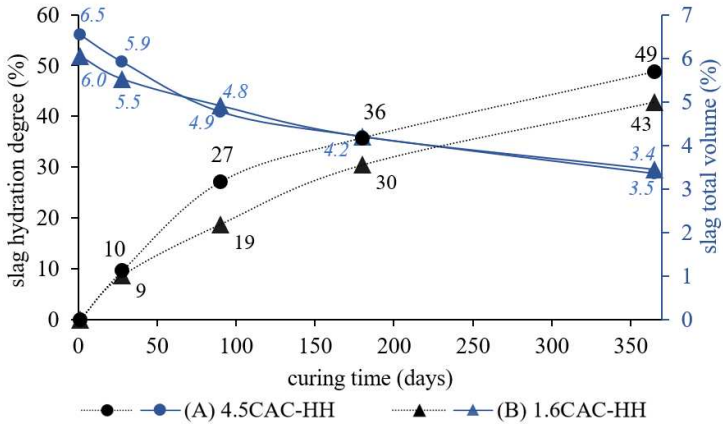

Figure 3.12 *Estimated slag volume and hydration degree using XCT + volume analysis*

Considering that only 40-50 % of the slag has reacted even after 1 year, the interest in exploring the reactivity of slag in modified systems was later

addressed in this study with the addition of the lime-rich paper residue (Chapter 3, section 3.5) and PC (Chapter 4).

Despite the concern on the risk of underestimation due to the voxel resolution, the estimated slag hydration degree (27 %) still ended up higher than that (14 %) from the image analysis using SEM micrographs. Although the two techniques were not directly comparable (i.e., volume- versus area-based calculation; number of images processed), these findings still open questions on the sensitivity of these image-based calculations.

Sensitivity Analysis

The influence of the grayscale threshold segmentation and the use of different samples (hydration stopped) per curing time were evaluated to test the sensitivity of the XCT methodology employed. These were among the critical factors that remained partly subjective to the experimenter's perception in this methodology.

For the first factor, a ±5% deviation was introduced to the lower grayscale threshold assigned to the slag based on the plot profiles (i.e., **Figure 3.11** b) of formulation A. This aimed to quantify the influence of the selected threshold to the estimated total volume of the slag. In effect, it was highly dependent on the divergence of the slag particles' grayscale (the brightness of the slag particles) during the scans compared to the rest of the components (image contrast).

For the second factor, samples of formulation A hardened pastes were scanned after stopping the hydration at 1 and 90 days (one sample per curing time). The VOI used for volume analyses was also changed to cylinder (**Figure 3.13**) as opposed to the previously-presented cubic samples. Smaller volumes (9 mm^3 for the cubic VOI and 6.28 mm^3 for the cylindrical VOI) were scanned and reconstructed.

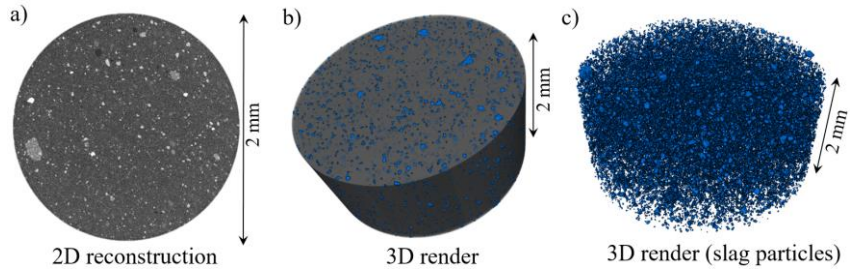

Figure 3.13 *Illustration of XCT analysis using cylindrical volumes*

The results obtained are presented in **Figure 3.14**. The ±5 % deviation in the lower threshold values only equated to a difference of ±0.2 % in volume and consequently ±3 % in slag hydration degree. This low sensitivity to threshold segmentation was consistent with the visual

observation that the slag particles were easily distinguishable from the rest of the components both in the SEM and XCT images.

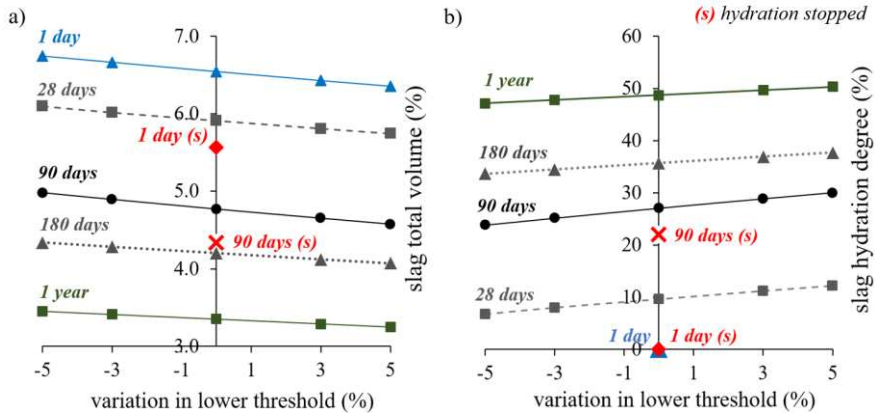

Figure 3.14 *Estimated (a) slag total volume and (b) slag hydration degree from the sensitivity analysis for formulation A*

On the other hand, the use of different samples per curing time and a smaller VOI resulted in -0.43% volume or -5% slag hydration degree difference. This highlights the advantage of using XCT over SEM, as a rapid non-destructive test that could autonomously take a large sample size while minimizing factors that could impose human bias.

In the end, selecting the more suitable methodology is a matter of balancing several factors to satisfy the goal of the study. The focus must be directed towards the rate rather than the absolute values of the slag hydration to avoid misinterpretations. In any case, quantification must be supported by complementary techniques (i.e., selective dissolution) especially if determining the absolute values is crucial.

3.3. Phase assemblage evolution over time

After estimating the degree of slag dissolution, the phase assemblages of the systems were simulated in function of CAC proportion using thermodynamic modelling. The evolution of the phases was also characterized experimentally for formulations A and B using several techniques from the early hours of hydration up to a period of 1 year.

3.3.1. Thermodynamic modelling

The thermodynamic models of the binary CAC-HH systems without and with the 30 wt% slag incorporation are shown in **Figure 3.15** and **Figure 3.16**, respectively. All simulations were based on 20° C, 1 bar pressure

condition and were calculated at infinite curing time (until stability). Other assumptions along with the codes used to generate these models are detailed in Appendix I. The models were calculated in function of the CAC content (x-axis), which could be interpreted in relation to the CAC/HH ratios (1.6 and 4.5) chosen in this study.

In **Figure 3.15**, it can be seen that gypsum is formed with the excessive HH at lower (< 53%) CAC percentages. On the opposite extremity, hydrogarnet is formed from the hydration of the remaining pure CAC when sulfates are depleted. As the model does not consider the kinetics of hydration, the formation of metastable calcium aluminate hydrates mentioned in Chapter 1 is experimentally expected, prior to their ultimate conversion to hydrogarnet at longer curing ages. Moreover, the phase assemblage of reference formulations A and B are shown to be dominated by monosulfoaluminate and ettringite, respectively. This model better illustrates the interest in the CAC/HH ratios selected in this study. These formulations both avoid regions of excessive sulfates marked by gypsum formation, which could have detrimental effects (i.e., cracking, spalling) related to secondary ettringite formation [162].

In both reference formulations, the silicates from the CAC are expected to be incorporated in strätlingite, while the Fe from C_4AF partakes in siliceous hydrogarnet formation. It can also be seen that formulation B dwells within the region of maximum hydrate formation by mass, such that the 65 g of water added to the 100 g of anhydrous blend is barely sufficient for full hydration.

Changes in the phase assemblage are evident with the addition of 30 wt% slag in the system (**Figure 3.16**). As indicated in Appendix I, only 50 vol% of the amorphous fraction of the slag was assumed to react during the modelling, based on the XCT estimations after 1 year of hydration. The rest of the unreacted slag were assigned to the "inert" phase shown as the black region, along with the minor (<1 at%) components of CAC and HH. Fe appears to be incorporated in ferrihydrite at lower CAC percentages. The dominant Fe-bearing phase at higher percentages is still Fe-siliceous hydrogarnet represented in the GEMS in several phases as follows:

- $C_3FS_{0.84}H_{4.32}$
- $C_3FS_{1.34}H_{3.32}$
- $C_3(A,F)S_{0.84}H$ – (solid-solution between Al and Fe)

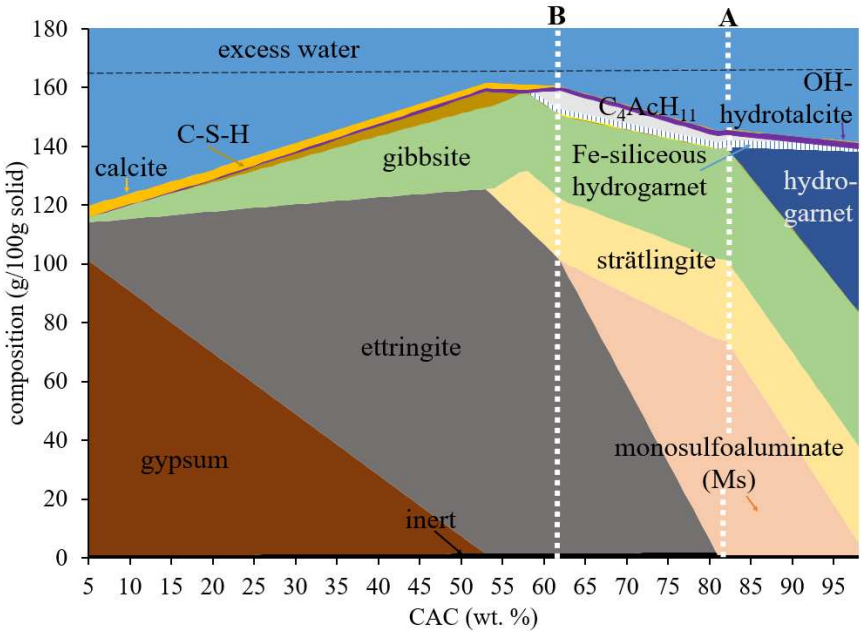

Figure 3.15 *Phase assemblage of the reference (no slag) binary binder calculated from GEMS thermodynamic modelling software. CAC/HH content is varied in the x-axis*

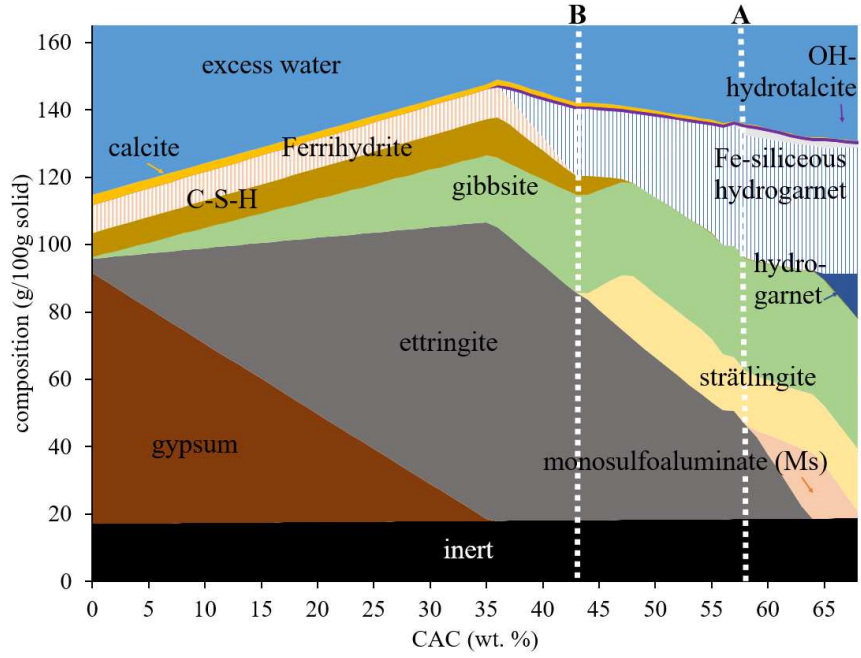

Figure 3.16 *Phase assemblage of the binary binder incorporating 30% slag with varying CAC and HH proportions, calculated from GEMS thermodynamic modelling software*

Unlike the model of the reference formulation, the slag-containing formulation A is dominated by Fe-siliceous hydrogarnet and ettringite instead of monosulfoaluminate. Even prior to experimentation, some deviation of the model from the actual result was already anticipated given the slower kinetics of slag dissolution. This brings forward the importance of kinetics as a factor in validating and later on improving thermodynamic models of cement hydration incorporating SCM.

3.3.2. Early hydration reactions

The first hours of hydration were characterized using ex-situ isothermal calorimetry at 20°C. Note that for both formulations, no citric acid was added to the pastes prepared for this test. The heat flow and cumulative heat release curves are shown in **Figure 3.17** and **Figure 3.18**, respectively.

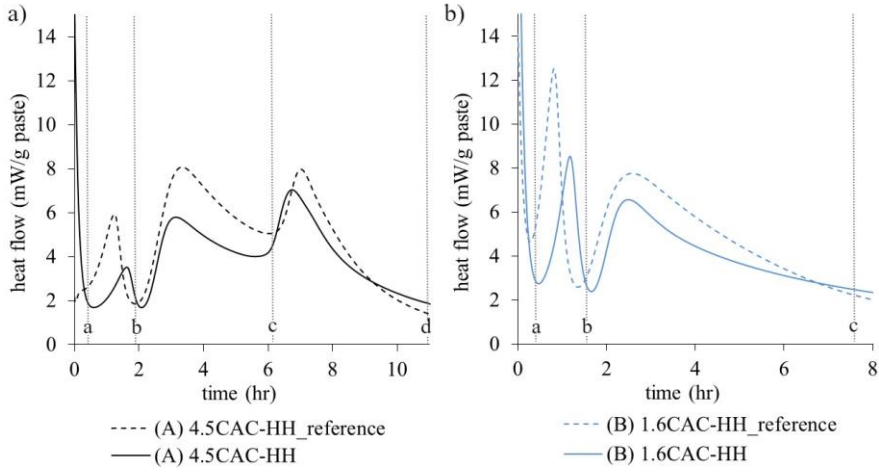

Figure 3.17 *Heat flow measured ex-situ using isothermal calorimetry for (a) formulation A and (b) formulation B pastes*

The three main peaks in the heat flow curves (**Figure 3.17** a) reported for low-sulfate CAC-based systems [9] and similar to those presented in the screening test (section 2.3.2) were observed for formulation A. On the other hand, only two main hydration peaks (**Figure 3.18** b) were found for the high-sulfate system represented by formulation B. In this case, the third peak associated to monosulfoaluminate formation was not detected. This signifies that the abundance of sulfates in formulation B favors the formation of ettringite and gibbsite over that of the monosulfoaluminates in the early age of hydration.

In both formulations, the addition of the slag reduced the peak intensities relative to the reference formulations but did not seem to alter the early

hydration reactions. In terms of reactivity, the trends are consistent with those of the physical properties of the mortars discussed in section 3.1. Recall that the slag appeared to be unreactive and even caused an overall reduction in strength of mortars during the first 28 days of curing. In addition, the more extensive ettringite formation depicted in the isothermal calorimetry curves (a-b region of formulation B versus b-c region of formulation A, **Figure 3.17**) could be linked to the overall expansion observed in formulation B not observed in formulation A. Nonetheless, the high heat release in the first 2 hours due to the extensive ettringite formation did not result to any significant difference in the cumulative heat release curves (**Figure 3.18**) at longer time.

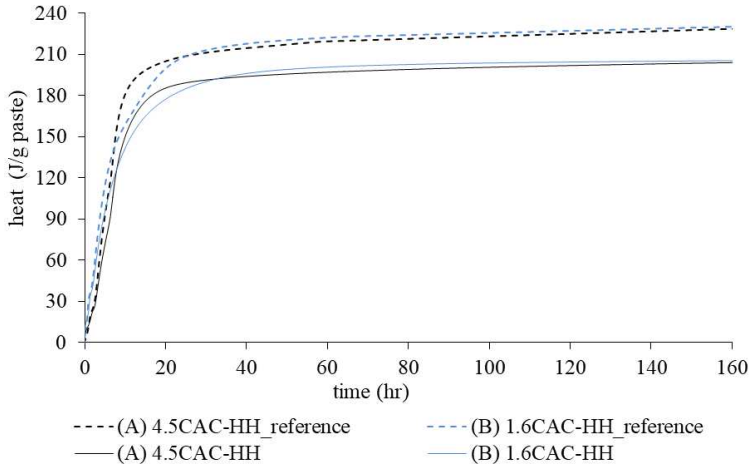

Figure 3.18 *Cumulative heat release measured using isothermal calorimetry*

3.3.3. Long term hydration

Based on the XRD patterns in **Figure 3.19**, the hydrate phase assemblage of formulation A mainly consisted of monosulfoaluminate, ettringite and strätlingite. Although ettringite appeared to dominate the system during the first 7 days, the lower amount of the remaining sulfates has likely resulted in the conversion of ettringite to monosulfoaluminate in the later ages, exhibited through the diminishing peaks of ettringite. However, clearly detecting the diffraction peaks of monosulfoaluminate proved to be a challenge due to its poorly-ordered crystal structure and the possible variability in its composition [163]. This case was also true for gibbsite which could be partly amorphous in these systems, highlighting the significance of complementary techniques such as TGA. In interpreting the XRD patterns, the peak intensities must be interpreted on a relative rather than a quantitative basis considering the presence of several amorphous phases in the system.

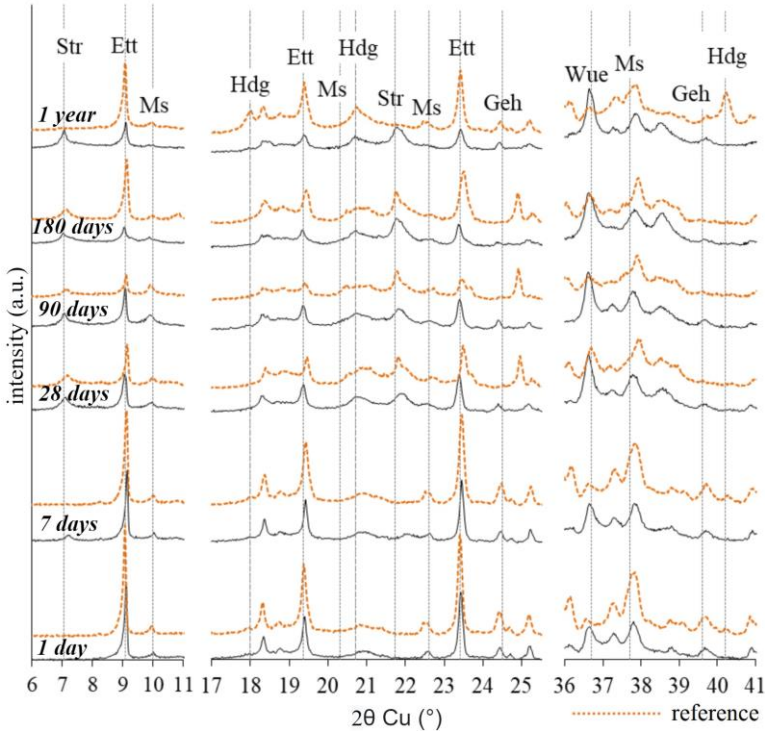

Figure 3.19 *XRD patterns of formulation A (solid black lines) and its reference measured over 1 year of curing. Phases are abbreviated as follows: (Str) strätlingite, (Ett) ettringite, (Ms) monosulfoaluminate, (Geh) gehlenite, (Hdg) hydrogarnet and (Wue) wüstite*

Unlike in the slag-containing formulation, hydrogarnet was detected after 1 year of curing in the reference formulation. It has been demonstrated [163,164] that the formation of hydrogarnet can destabilize several AFm phases in low-sulfate systems below 50°C. Based on thermodynamic modelling [164], AFm only becomes stable when hydrogarnet is suppressed under the assumption that its formation is not thermodynamically-favored in the early age of hydration. This instability could be one of the reasons behind the increasing peak intensities from 90 days to 1 year giving the impression of ettringite re-formation observed in the reference formulation.

Strätlingite peaks were consistently present from 7 days to 1 year in the slag-containing formulation which could have contributed to its strength development, supporting previous studies [165,166] where the strength-giving property of strätlingite has been demonstrated. In general, the addition of siliceous SCM inducing strätlingite formation has been associated to denser pore structures [165,167]. At the same time, the preferential formation of hydrates (i.e., ettringite, strätlingite) other than

the metastable calcium aluminate phases (i.e., CAH_{10}, C_2AH_8) with the addition of SCM and calcium sulfates inhibits the conversion phenomenon [168] typically considered undesirable in pure CAC systems. The acidic nature of the Fe-rich slag could also slow down the conversion reactions [169]. On the contrary, the appearance of strätlingite peaks in the reference formulation occurred later between 7 and 28 days, diminishing again with the formation of hydrogarnet and ettringite from 180 days.

Moreover, gehlenite appeared to be consumed faster in the reference formulation with peaks greatly reduced beyond 7 days. This was not the case for the slag-containing formulation likely due to the additional silicates contributed by the slag in the system. On the other hand, wüstite from the slag seemed to be unreactive, displaying consistent peak intensities throughout the hydration period. This agrees with the findings from a previous study [117] suggesting the preferential dissolution of the amorphous component of similar slags over that of its crystalline component.

Contrary to the more complex phase assemblage evolution of formulation A and its reference, less changes were observed between the XRD patterns of formulation B and its reference shown in **Figure 3.20**. The high-sulfate system was indeed dominated by ettringite, stable throughout the hydration period. This result agrees with the initial findings based on the strength development and heat release. For both formulations, however, no new Fe-containing hydrate was detected based on the XRD patterns alone. Despite previous studies [131,170] suggesting the solid substitution of Fe to Al in hydrates such as ettringite, monosulfoaluminate or siliceous hydrogarnet, there was no clear peak shifts in the diffractograms presented that could support this mechanism. Considering that the slag's reactivity has been established at this point based on the XCT results, this could be an initial indication that the Fe could be incorporated instead in an amorphous or in a nano-crystalline hydrated phase. In order to unravel the fate of the Fe in this system, further complementary techniques were employed.

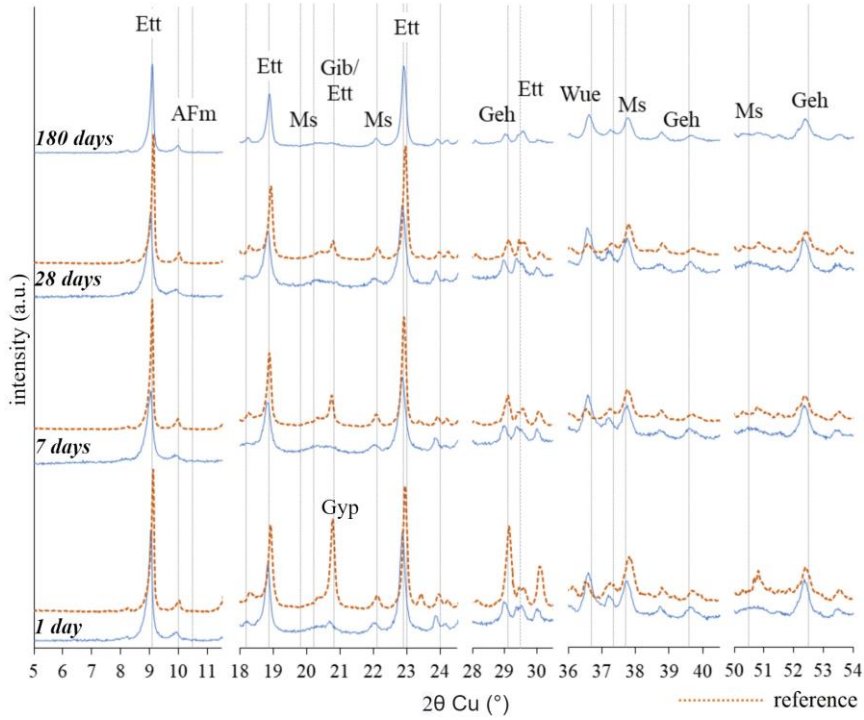

Figure 3.20 *XRD patterns of formulation B (solid blue lines) and its reference measured over 1 year of curing. Phases are abbreviated as follows: (Ett) ettringite, (AFm) AFm, (Ms) monosulfoaluminate, (Gib) gibbsite, (Geh) gehlenite, (Hdg) hydrogarnet, (Gyp) gypsum and (Wue) wüstite*

The evolution of the DTG curves of formulation A and B are presented in **Figure 3.21**. The dominant phase constitutions were consistent with those observed from XRD. Despite the difficulty in distinguishing between the overlapping peaks in certain temperature ranges, it was clear that formulation A has a more complex hydrate assembly compared to formulation B. Moreover, TGA confirmed the substantial amounts of AH_3 and AFm phases (mainly monosulfoaluminate and strätlingite) which were less evident using XRD due to their poor crystallinity.

Following the bound water content in **Figure 3.22**, the high value obtained for formulation B was clearly due to its dominant hydrate, ettringite. This supports the earlier assumptions relating the phase assemblage to the high strength values and the expansive nature of mortars representing the high-sulfate system. Nonetheless, the increasing bound water contents in both formulations confirms continuous formation of hydrates, also reflected through a progressive strength development over time.

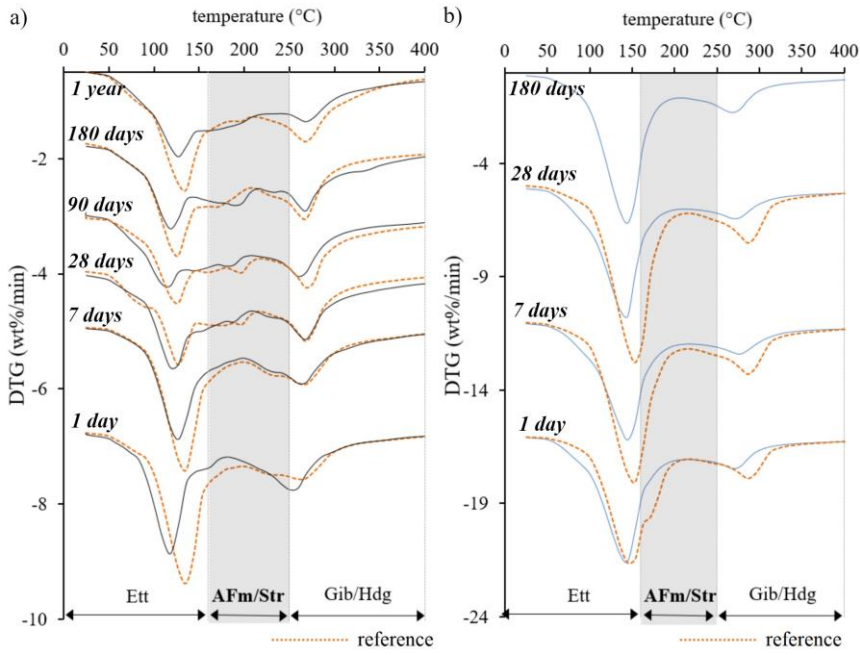

Figure 3.21 *Evolution of the DTG curves of (a) formulation A and (b) formulation B along with their corresponding references. Slag-containing formulations are shown in solid lines. Phases are abbreviated as follows: (Ett) ettringite, (AFm) AFm, (Str) strätlingite, (Gib) gibbsite, (Hdg) hydrogarnet*

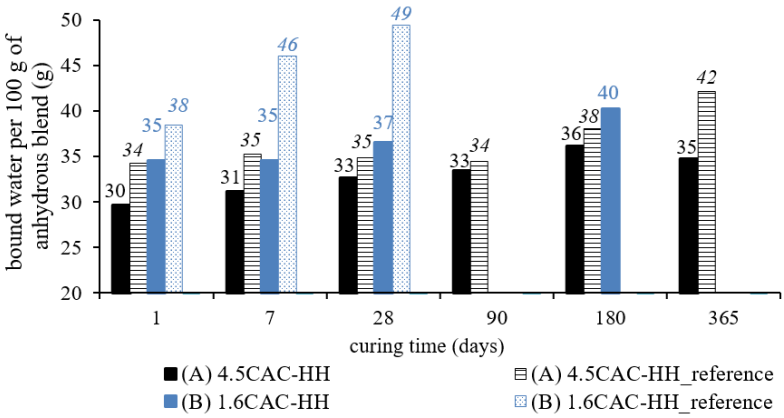

Figure 3.22 *Total bound water content of formulations A, B and their references*

In an attempt to describe the slag hydration using a less conventional technique in characterizing cement hydration, the hydrated paste samples were analyzed using ATR-FTIR. From the preceding chapters, results from previous study [117] have demonstrated formation of new bonds, depicted by peak displacements in the ATR-FTIR spectrum. A shift in the Si-O

asymmetric stretching band (700-1200 cm^{-1}) towards the higher wavenumber accompanied by the less apparent shift of the Si-O rocking band (400-500 cm^{-1}) towards a lower wavenumber were associated with the partial oxidation Fe^{2+} to Fe^{3+} and with the incorporation of the Fe in the polymerized network [116,117]. Although this mechanism was described using a similar Fe-rich NFM slag, the binder investigated was an inorganic polymer as opposed to the blended cements in this study.

The evolution of ATR-FTIR spectra of formulations A and B are presented in **Figure 3.23** and **Figure 3.24**, respectively. Based on literature references, the band assignments of the identified spectral peaks in these figures were listed in **Table 3.2**.

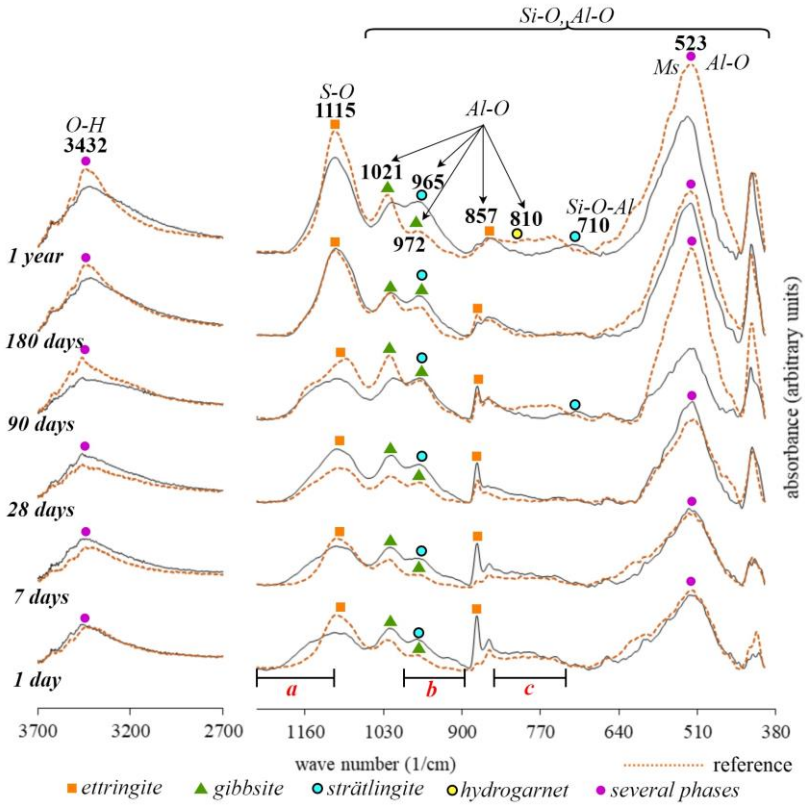

Figure 3.23 *ATR-FTIR spectra of formulation A (solid black lines) and its reference. The designation "several phases" correspond to the combination of all other hydrates identified.*

Compared to the inorganic polymers investigated in Siakati *et al.,* 2020 [117], the cement systems in this study displayed a more complex spectra due to the co-existence of various crystalline and amorphous phases. The general phase assemblages of the two formulations were

consistent to those identified using XRD and TGA. The low-sulfate system, formulation A, displayed signatures of ettringite, monosulfoaluminate, gibbsite and strätlingite. A hydrogarnet peak (Al-O) at around 810 cm^{-1} was also detected at 1 year only for the reference formulation. Unfortunately, the Si-O peaks (930 cm^{-1} and 470 cm^{-1}) detected in the raw slag (Chapter 2, **Figure 2.13**) were hardly identifiable in these systems. Despite the 30 wt% addition in the binders, the signatures of the amorphous slag (low intensity broad peaks) were easily masked by those of the crystalline components (high intensity sharp peaks).

Nonetheless, regions (**Figure 3.23** a-c) where substantial changes in the spectra were present, could be interpreted as indications of slag reactivity considering the initial findings from XRD and TGA. In these areas, most of the changes occur beyond 28 days of hydration. Recall that only about 10% of the slag (**Figure 3.12**) has dissolved at 28 days according to the XCT analysis. One of the marked differences in patterns between the slag-containing and the reference formulation is in region b at around 960-980 cm^{-1} where the Al-O bands of gibbsite and strätlingite coincide. This is around the same region where the Si-O stretching band of the raw slag is expected. These marked differences in regions generally associated to the Al-O bands, could be an initial indication that the slag hydration is altering the formation of the Al-containing hydrates.

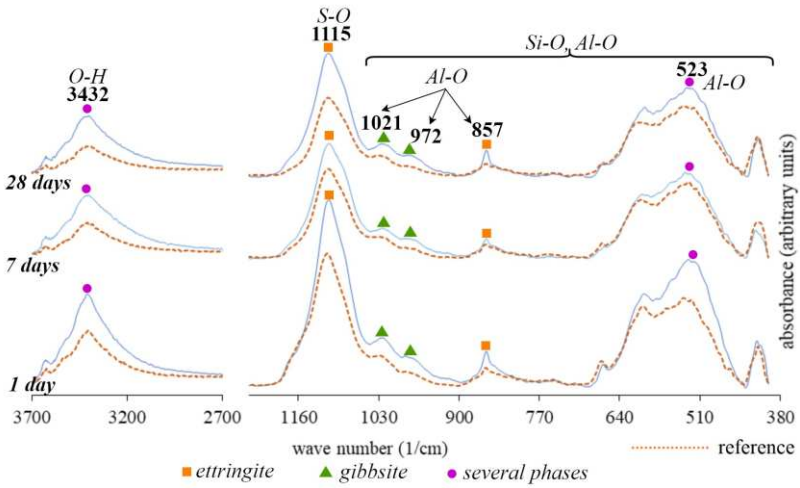

Figure 3.24 *ATR-FTIR spectra of formulation B (solid blue lines) and its reference. The designation "several phases" correspond to the combination of all other hydrates identified*

As expected, the spectra (**Figure 3.24**) of the high-sulfate system exhibited a less complex constitution dominated by distinct peaks assigned to ettringite and gibbsite. The peak at 523 cm^{-1} where monosulfoaluminate

(among other minor phases) was assigned is also less pronounced in formulation B compared to that in formulation A (**Figure 3.23**). Moreover, no discernible difference between the reference and the slag-containing formulations nor throughout the curing period (28 days) was observed in formulation B. This could support the overall lower slag reactivity in the high-sulfate system estimated through XCT analysis (**Figure 3.12**).

Table 3.2 *FTIR band assignments based on the distinct spectral peaks observed from the hydrated paste samples*

Bond	Primary contributor	Wavenumber (cm^{-1})	Reference
O-H	Ms/Ett/Str	3432	Horgnies *et al*., 2013 [137]
		1660	Horgnies *et al*., 2013 [137]
S-O	Ett/Ms	1115	Horgnies *et al*., 2013 [137]
Si-O-Al	Str	1150	Okoronkwo and Glasser, 2016 [165]
		710	Zapanta *et al*., 2020 [171]
Si-O	anhydrous silicates	521	Torréns-Martin *et al*., 2013 [86]
Al-O	Gib	1021	Schroeder, 2002 [172]
		972	Schroeder, 2002 [172]
		751	Schroeder, 2002 [172]
	Str	965	Okoronkwo and Glasser, 2016 [165]
	Hdg	810	Horgnies *et al*., 2013 [137]
	Ett	857	Horgnies *et al*., 2013 [137]
	Gib/Ms/Str/Hdg	523-537	Horgnies *et al*., 2013 [137]
	Hdg	521	Torréns-Martin *et al*., 2013 [86]

In the end, the complexity of the ATR-FTIR spectra proved to be a huge challenge in characterizing the phase assemblage evolution of the blended cement systems. The signature of the slag's Si-O bands could not be clearly detected and therefore, no clear indication on the hydration mechanism of the slag could be derived from this technique alone. Nevertheless, the resulting phase assemblages were consistent with those obtained from the more conventional techniques, XRD and TGA. Considering that each analysis in ATR-FTIR does not require tedious sample preparations, could readily take solid, paste or liquid samples, and takes less than a minute to yield a spectrum, it could remain as a practical option for quick analyses.

3.4. The fate of Fe during hydration

In this section, the fate of Fe, the main component of the slag, was investigated through TEM, STEM and Mössbauer spectroscopy. Although

the general phase assemblages of formulations A and B were already described in the previous section using XRD, TGA and ATR-FTIR, complementary techniques were still needed to elucidate the hydration mechanism of the slag.

3.4.1. TEM

The TEM images of formulation A paste after 1 day of hydration are presented in **Figure 3.25**. The observed phases were consistent with the assemblage described in the preceding section. Several individual rods of ettringite (A2 and A6); plate of anhydrous CA (A4); Al-rich gels (A1, A5, A7 and A8) similar to gibbsite; and intermixed phases (i.e., A3) were observed. No significant amount of Fe was detected in any hydrated phase at this stage of hydration. Moreover, the amount of S detected through EDS analysis in rod/needle-like phases labelled as ettringite was significantly lower compared to what could be theoretically expected. This discrepancy is linked to the uncertainties associated to the EDS analysis particularly for S in ettringite, discussed in section 2.2.6.

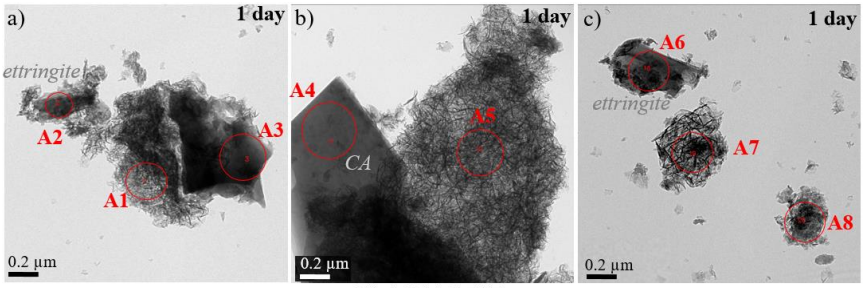

(A) 4.5CAC-HH

At. %	Fe	Ca	Al	Si	S	Mg	K + Na	O	Sum
A1	0.4	5.2	31.7	0.0	0.0	0.0	0.0	62.7	100.0
A2	0.3	16.9	15.1	0.0	5.7	0.0	0.0	62.2	100.0
A3	0.4	15.1	17.1	1.2	0.6	0.0	0.0	65.7	100.0
A4	0.2	13.5	27.0	0.2	2.4	0.0	0.3	56.4	100.0
A5	0.7	6.0	46.3	0.5	0.1	0.0	0.2	46.2	100.0
A6	0.2	26.3	14.8	0.1	8.0	0.0	0.8	49.9	100.0
A7	0.4	5.9	39.5	0.4	0.2	0.0	0.2	53.5	100.0
A8	0.6	8.0	37.6	0.4	0.4	0.0	0.2	52.9	100.0

Figure 3.25 *TEM images and the atomic composition of marked areas in the (A) 4.5CAC- HH paste sample after 1 day of hydration*

At longer curing ages (>28 days) when the degree of slag hydration became more significant, Fe was detected in the Al-rich gels with a slightly higher amount of Si compared to the gels observed in the early days of hydration. **Figure 3.26** shows the general morphologies (a) and the Fe-containing intermixed phases (b-c) observed in formulation A. At 90 days, more plates

of strätlingite (A10) intermixed with Al-rich gels were observed, which were not detected in the samples at 1 day. The term "gel" in this study was used to describe mostly the Fe-containing intermixed phase considering its morphology and poor crystallinity. Although the gel was clearly a part of the solid binder, the use of this term was adapted from Cuesta *et al*., 2017 [173] and related literature [140,174] where amorphous aluminum hydroxide gels were characterized in calcium sulfoaluminate cement systems.

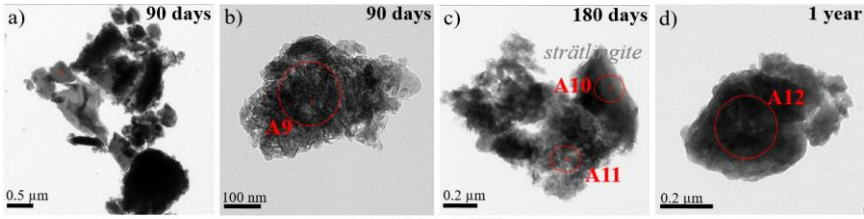

(A) 4.5CAC-HH

At. %	Fe	Ca	Al	Si	S	Mg	K + Na	O	Sum
A9	9.9	5.6	12.8	4.6	0.4	0.0	0.0	66.7	100.0
A10	0.5	10.4	24.7	10.4	0.1	0.7	0.4	52.8	100.0
A11	4.0	5.0	30.4	2.2	0.7	1.7	2.6	53.5	100.0
A12	19.9	3.3	16.4	6.2	0.5	3.0	0.0	50.7	100.0

Figure 3.26 *TEM images and the atomic composition of marked areas in the (A) 4.5CAC-HH paste sample after long term curing*

For some of the Fe-bearing gel phases (i.e., A12), the Fe signal was notably higher than those observed in other gels (i.e., A9 and A11). To better understand their nature, the diffraction mode (**Figure 3.27**) of TEM was used to characterize gels at (a) 180 days and (b) 1 year, both containing comparable signals of Fe (≈ 4%). The A15 gel at 1 year exhibited clearer diffraction spots compared to the A13 gel at 180 days. The former could be interpreted to have some crystalline component/s [175] intermixed with gel phase/s; while the latter was clearly more poorly-structured [176]. The possibility of having erroneously analyzed unreacted slag particles as part of the gels was excluded, not only due to the spot size (only a few hundred nanometers) but also due to the sensitivity (**Figure 3.28**) of these gels. Even the gels at 1 year (A16 and A17) were immediately destroyed after the EDS analysis, suggesting that they were, most likely, hydrated phases.

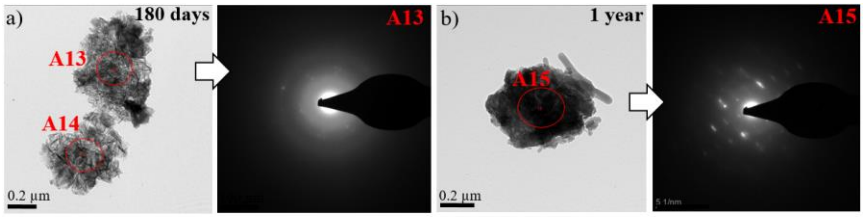

(A) 4.5CAC-HH

At. %	Fe	Ca	Al	Si	S	Mg	K + Na	O	Sum
A13	4.5	4.3	33.6	2.3	0.7	2.4	2.0	50.2	100.0
A14	1.4	2.8	40.0	1.5	0.2	2.1	1.4	50.7	100.0
A15	4.1	7.5	29.7	5.3	3.0	2.1	0.0	48.2	100.0

Figure 3.27 *TEM images, diffraction patterns and the atomic composition of Fe-containing gels in the (A) 4.5CAC-HH paste sample*

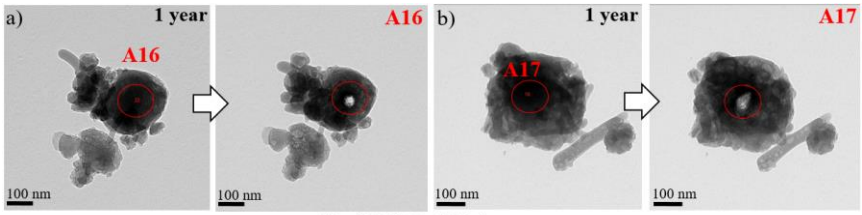

(A) 4.5CAC-HH_1 year

At. %	Fe	Ca	Al	Si	S	Mg	K + Na	O	Sum
A16	10.9	3.7	22.0	11.3	0.6	3.6	0.0	47.9	100.0
A17	10.2	4.3	21.4	7.1	1.1	2.5	0.0	53.4	100.0

Figure 3.28 *TEM images before and after EDS analysis of Fe-containing gels in the (A) 4.5CAC-HH paste sample*

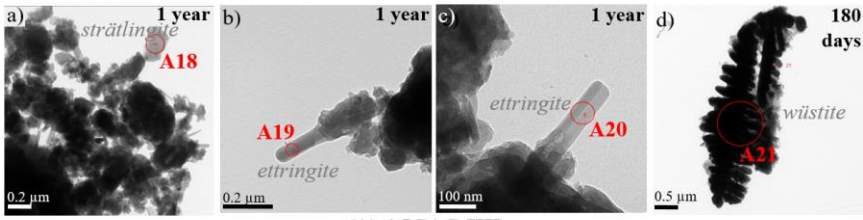

(A) 4.5CAC-HH

At. %	Fe	Ca	Al	Si	S	Mg	K + Na	O	Sum
A18	0.6	28.0	30.6	10.1	1.7	0.9	0.0	28.2	100.0
A19	0.0	25.1	19.7	0.0	3.5	0.0	0.0	51.7	100.0
A20	0.3	32.0	22.6	0.2	6.0	0.0	0.0	38.8	100.0
A21	52.4	0.1	0.3	0.4	0.1	1.3	0.2	45.2	100.0

Figure 3.29 *TEM images and the atomic composition of crystalline phases in the (A) 4.5CAC-HH paste sample*

Contrary to the typical hydrated phases previously reported [170,177] to incorporate Fe in cement systems (i.e., ettringite, strätlingite, AFm), no significant amount of Fe was detected in ettringite (A2, A19, A20) and strätlingite (A10, A18) identified in formulation A. Moreover, dendrites of wüstite (A21) were observed intact after long curing ages, supporting the observation in the previous section that the crystalline fraction of the slag displayed no significant reactivity even after 1 year of hydration.

Similar findings on the fate of Fe were obtained from the TEM analyses (**Figure 3.30**) of formulation B. Although a higher quantity of ettringite rods was observed in the general phase assemblage (**Figure 3.30** a) of this high-sulfate sample, Fe was only found to be incorporated in an Al-rich intermixed gel phase as in formulation A. At longer curing time, 1-2 at% of Mg was generally associated with some of these Fe-bearing phases, which could be an initial indication of an LDH phase formation similar to what was reported in Hallet *et al.*, 2022 [139]. More details on this phase are presented along with the STEM results in the next section.

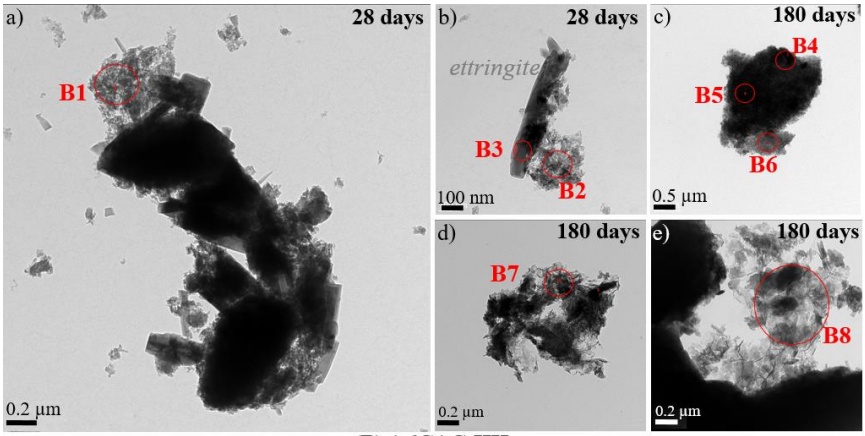

(B) 1.6CAC-HH

At. %	Fe	Ca	Al	Si	S	Mg	K + Na	O	Sum
B1	0.6	5.1	34.2	2.0	1.3	1.3	0.1	55.4	100.0
B2	0.9	6.6	30.2	1.9	1.3	1.4	0.1	57.6	100.0
B3	0.3	32.8	6.8	0.1	0.1	0.0	0.8	59.1	100.0
B4	31.2	0.8	16.1	1.0	0.3	1.5	0.6	48.6	100.0
B5	1.4	1.3	34.7	1.5	0.4	2.0	1.5	57.0	100.0
B6	0.8	0.9	33.3	1.6	0.4	2.0	1.0	60.0	100.0
B7	4.8	2.9	33.6	4.1	0.5	2.9	2.2	49.1	100.0
B8	3.4	6.2	48.6	3.7	1.4	1.3	0.1	35.3	100.0

Figure 3.30 *TEM images and the atomic composition of marked areas in the (B) 1.6CAC-HH paste sample*

3.4.2. STEM

Although TEM facilitated the identification of individual phases with relatively less intermixing compared to the previous attempt using SEM (section 3.2.1), the homogeneity of the Fe-bearing phase observed in TEM was still in question. STEM was therefore employed to create elemental maps focusing on these phases.

In **Figure 3.31**, the distribution of Fe suggests that the phase was comprised of at least two phases: an amorphous gel (A23/A25) and a phase (A24) with clearer diffraction spots. Fe appeared to be homogenously distributed at lower concentration (5 at%) in the amorphous gel. A higher incorporation of Fe (19 at%) was noted for the other phase (A24) intermixed within this gel. For this specific sample, it was observed that the increase in Fe content was accompanied by a decrease in Al proportion which could be a possible indication that these ions were occupying the same sites in the lattice of the intermixed phases. Nonetheless, the possibility that the high-Fe region (A-24) actually corresponds to a component of the raw slag could not be fully excluded, despite the noted sensitivity of the phase to EDS analysis only observed on hydrated phases during this study.

Another area of the same sample was examined and presented in **Figure 3.32**. The Fe content detected for the amorphous hydrate gels (A27 and A28) remained below 12%, consistent with the general trend observed from the TEM and STEM analyses. In addition, unreacted slag particles (i.e., A26, A29) were detected. The EDS analysis (A26) and diffraction pattern (EDS-A29) suggest that these particles could be wüstite rather than the amorphous fraction of the raw slag, supporting the earlier observations that the mineral fraction of the slag was less (if at all) reactive during 1 year of hydration.

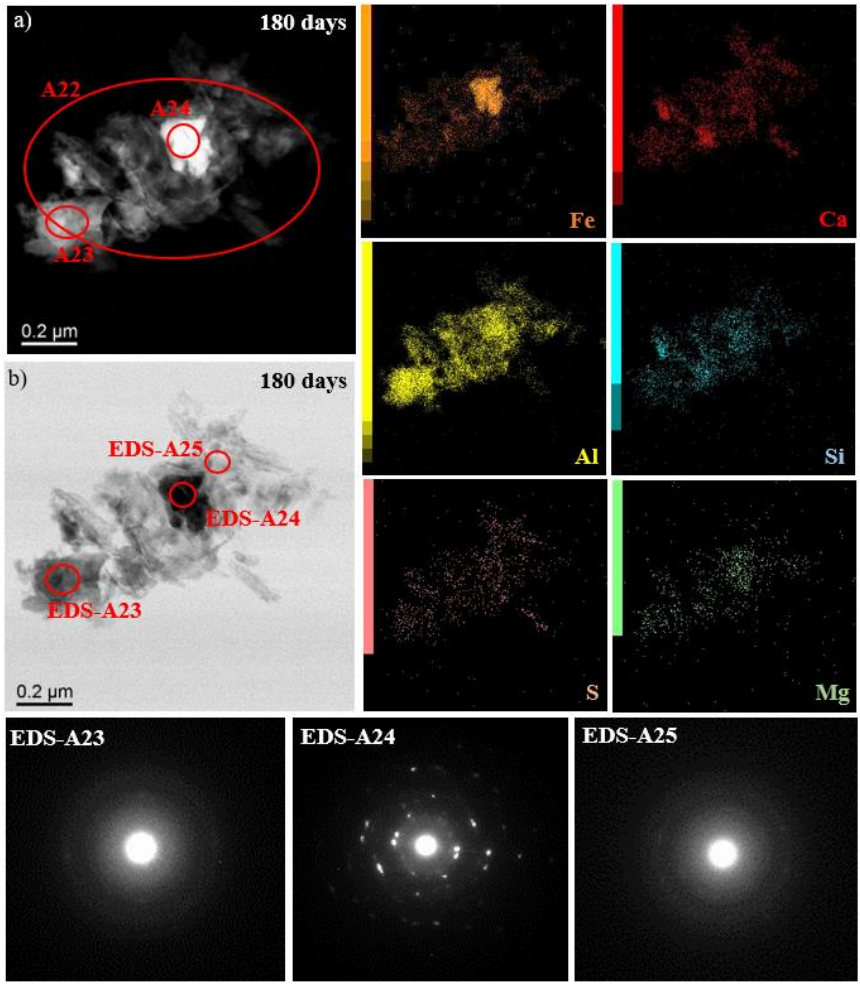

(A) 4.5CAC-HH_180 days

At. %	Fe	Ca	Al	Si	S	Mg	K + Na	O	Sum
A22	5.2	2.9	24.0	3.4	0.6	0.3	0.0	63.6	100.0
A23	0.7	1.9	30.0	1.2	0.2	0.0	0.0	65.9	100.0
A24	18.9	1.6	16.3	2.5	0.3	0.6	0.0	59.8	100.0

Figure 3.31 *STEM elemental mapping, diffraction patterns and atomic composition of marked areas in the (A) 4.5CAC-HH paste sample after 180 days of curing*

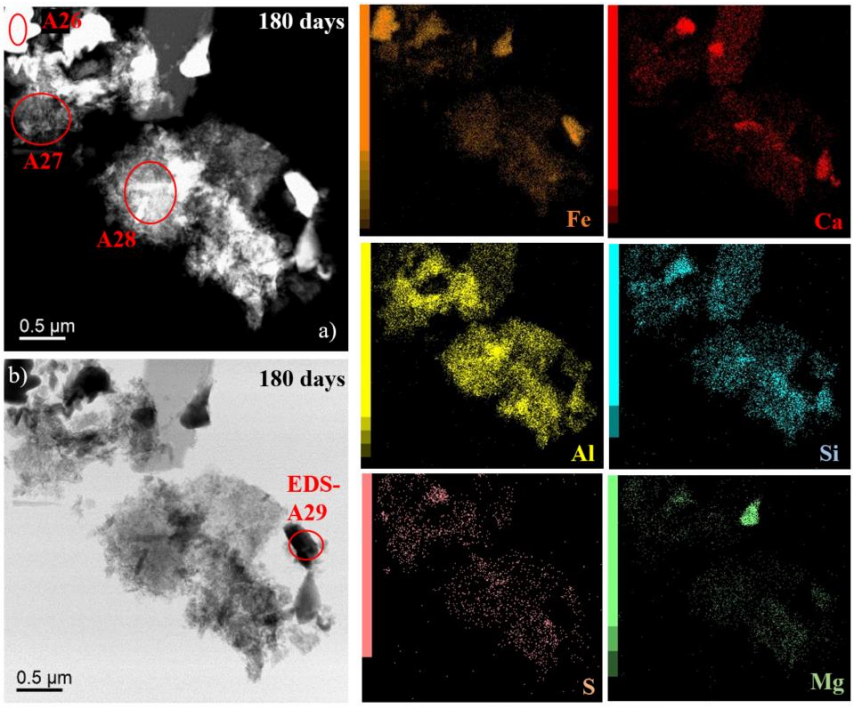

(A) 4.5CAC-HH_180 days

At. %	Fe	Ca	Al	Si	S	Mg	K + Na	O	Sum
A26	47.5	0.0	1.0	0.7	0.1	1.3	0.0	49.5	100.0
A27	1.4	8.6	22.2	4.4	2.1	0.0	0.0	61.4	100.0
A28	7.2	2.1	23.3	4.6	0.3	1.2	0.0	61.4	100.0
A29	28.9	0.2	3.7	1.0	0.0	1.5	0.0	64.7	100.0

Figure 3.32 *STEM elemental mapping, diffraction pattern and atomic composition of marked areas in the (A) 4.5CAC-HH paste sample after 180 days of curing*

The compositions of the Fe-containing intermixed phases were plotted in a Ca-Si-Al ternary diagram in **Figure 3.33**. Only the gels with 1-12 at% Fe were selected in order to avoid analytical volumes with strong intermixing with non Fe-bearing hydrated phases (<1 at% Fe) or with the unreacted slag (> 29 at%). Additionally, values in the ternary diagram were also expressed in atomic percentages, considering that comparison based on atomic ratios rather than the absolute amounts has been cited [178] to reduce errors associated to oxygen quantification in TEM-EDS analyses.

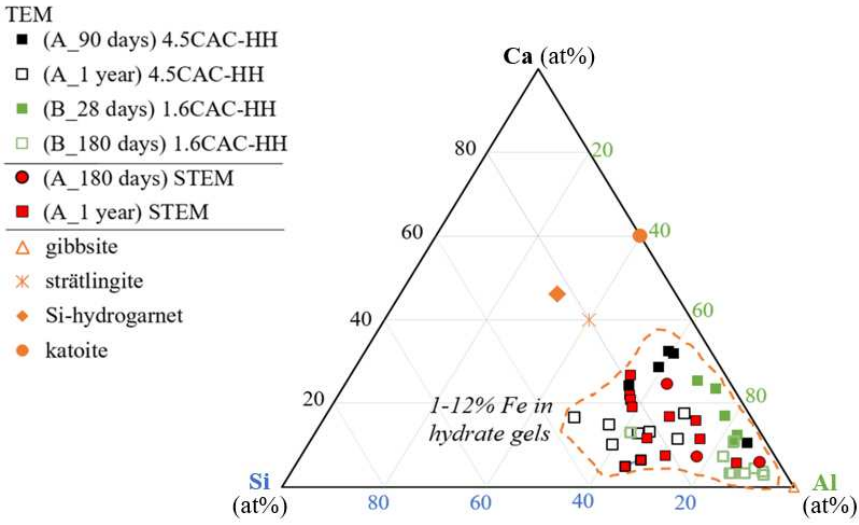

Figure 3.33 *Ternary diagram of Fe-containing hydrate gels with 1-12% Fe observed using TEM and STEM. The values were calculated from the Ca, Si and Al atomic composition from EDS analyses normalized to 100%. Reference points for gibbsite, strätlingite, katoite and Si-hydrogarnet were added in the diagram based on their empirical formula.*

The ternary diagram in **Figure 3.33** shows the distinct Al-rich cluster occupied by the Fe-bearing hydrate gels. In view of the limited number points, however, no definite conclusion could be drawn to compare the variation in the composition between the gels in formulation A or B, nor among the samples at different curing ages. Reference points for gibbsite, strätlingite, katoite and Si-hydrogarnet were also added in the diagram based on their empirical formula. The composition of the hydrate gels was observed to fall between that of gibbsite and stätlingite/katoite, but remained distinct from these pure phases.

Further attempts were made using STEM after 1 year of hydration to identify the Fe-containing phase which exemplified some diffraction spots in previous analyses (i.e., EDS-A24, **Figure 3.31**). Fe maps and diffraction patterns of the Fe-bearing intermixed phases observed in formulation A are presented in **Figure 3.34** and **Figure 3.35**. The inhomogeneity of Fe distribution is clear from the maps, consistent with the observation from 180 days. A distinct rod-like to lamellar morphology was also observed for the phase with higher Fe content (i.e., A30 and A31, **Figure 3.34**) in the updated 1 year sample. In an attempt to measure the interatomic spacing (d-spacing) for the identification of this phase, a more focused STEM image was taken as shown in **Figure 3.36**.

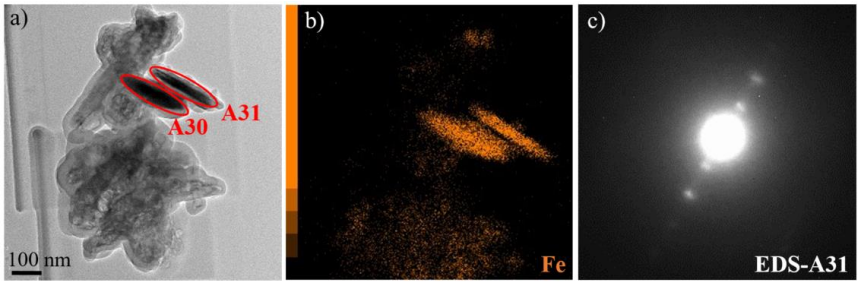

(A) 4.5CAC-HH_1 year

At. %	Fe	Ca	Al	Si	S	Mg	K + Na	O	Sum
A30	13.3	1.2	12.1	4.8	0.2	3.4	0.3	64.6	100.0
A31	13.6	1.0	13.5	6.4	0.1	3.2	0.1	62.3	100.0

Figure 3.34 *STEM image focused on an Fe-rich region (a); along with its corresponding Fe map from EDS analysis (b); and the diffraction pattern of marked area A-31 from the (A) 4.5CAC-HH paste sample after 1 year of curing*

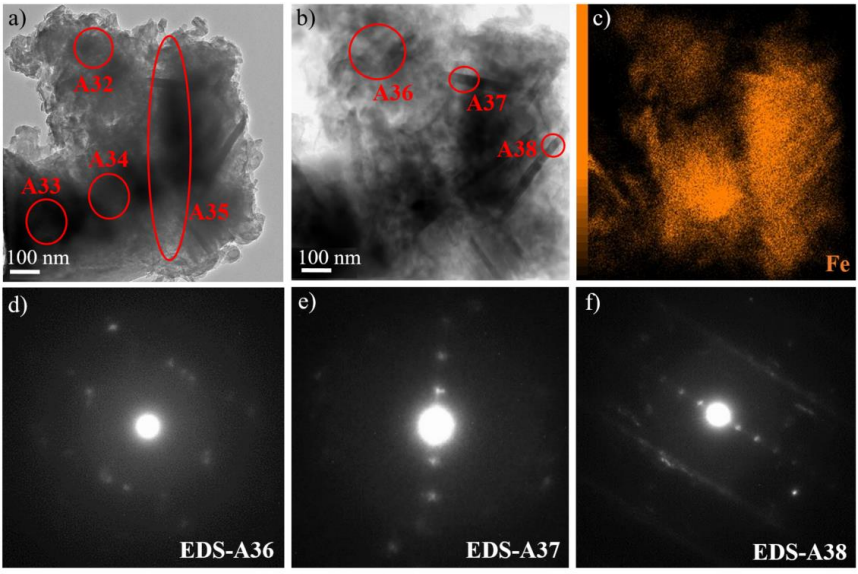

(A) 4.5CAC-HH_1 year

At. %	Fe	Ca	Al	Si	S	Mg	K + Na	O	Sum
A32	5.5	1.5	24.0	2.3	0.6	0.6	0.6	64.5	100.0
A33	1.5	11.3	6.0	1.0	13.2	0.1	1.7	64.5	100.0
A34	12.4	2.0	20.0	5.9	0.3	1.4	0.6	56.9	100.0
A35	6.8	1.5	15.9	2.5	0.3	0.8	0.6	70.9	100.0

Figure 3.35 *STEM image focused on an Fe-rich region (a); along with its corresponding annular dark field image (b); Fe map from EDS analysis (c); and the diffraction pattern of marked areas from the (A) 4.5CAC-HH paste sample after 1 year of curing*

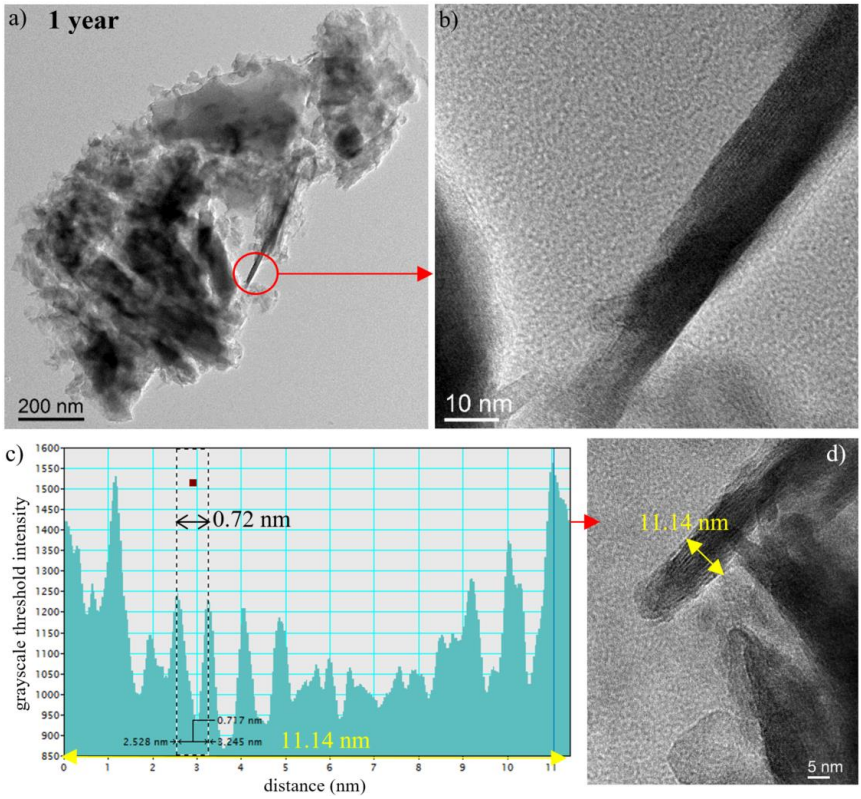

Figure 3.36 *STEM images focused on the needle-like Fe-rich phase (a, b and d), along with a grayscale intensity plot (c) of the pixels under the yellow double-arrow in d. The distances in c represent the atomic layer spacing of the unidentified phase from the (A) 4.5CAC-HH paste sample after 1 year of curing*

The d-spacing of the unidentified high Fe-bearing needle-like phase was estimated at around 0.72 nm or equivalent to 7.2 Å using the grayscale intensity plot (c) in **Figure 3.36**. Unfortunately, it was not possible to perform EDS analysis on this phase due to its size (only a few nanometers) and sensitivity (easily disintegrated), causing them to move out of focus during the imaging. The other Fe-bearing needle-like phases (i.e., A30 and A31) were still intermixed with Al-rich gels and, therefore, would not yield the actual composition of the pure needle-like phase. Nonetheless, the distinct morphology, the estimated d-spacing, and the general idea on the chemistry of this Fe-bearing phase could be compared to those of some relevant phases previously observed and reported in literature. **Figure 3.37** shows some TEM images of Fe hydroxides (a and b) and an Fe-bearing LDH phase (c), appearing to have a similar morphology to those observed in the 1 year sample.

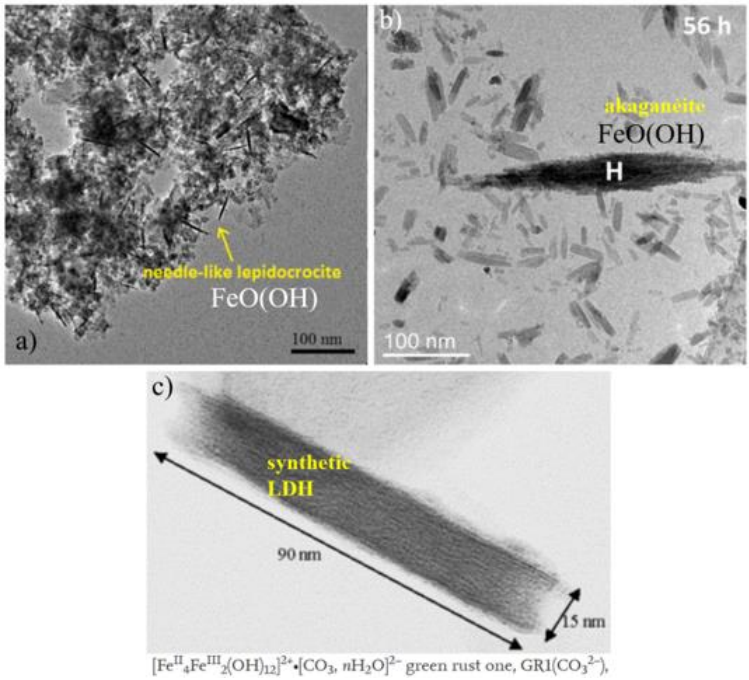

Figure 3.37 *TEM images of needle-like Fe hydroxide phases (a, b); and a lamellar layered double hydroxide (LDH) phase similar to green rust, modified from literature references [179–181].*

Three main possible phases were considered for the identity of the Fe-bearing needle-like phase, described as follows:

i. Al-Fe hydroxide:

After 28 days, Fe signals were detected in $Al(OH)_3$ gels with increasing proportions of Ca and Si. In literature, amorphous $Al(OH)_3$ were observed to form polycrystalline "whiskers" morphology shown in the TEM images in **Figure 3.38** a. The different Fe hydroxides (**Figure 3.37** a and b; **Figure 3.38** b) demonstrated a nano-crystalline needle morphology, similar to those observed in the 1 year samples. The mechanism of transformation from the amorphous end-product ferrihydrite to the needle-like goethite nano-crystals over time, has been extensively discussed in Bazilevskaya, 2009 [182]. In her study, the difference in the kinetics of ion dissolution was attributed to the eventual growth of goethite needles within a poorly-crystalline ferrihydrite matrix, thereby creating polycrystalline ring diffraction patterns.

The d-spacing of Al and Fe hydroxides in literature were reported to be typically below 4 Å [183,184]. However, it has been previously

demonstrated that with an uptake of ion/s, this spacing could drastically change (i.e., 7.4 Å with Cl^- uptake in $Fe^{3+}O(OH,Cl)$, **Figure 3.37** b [180]).

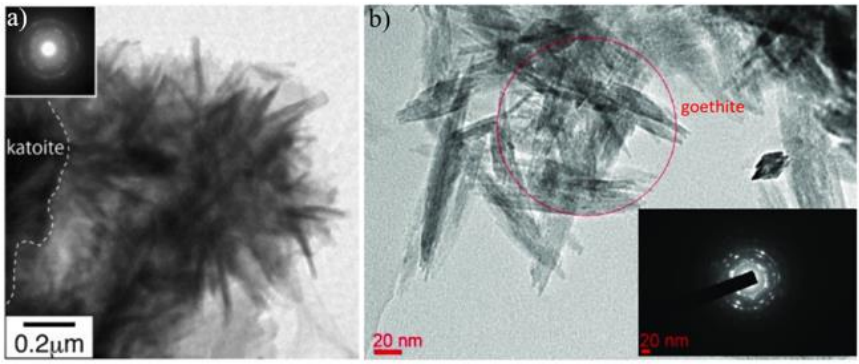

Figure 3.38 *TEM images of (a) $Al(OH)_3$ with its inset selected-area electron diffraction (SAED) pattern [183]; and of goethite, Fe(OH)O, with its inset SAED pattern [184].*

ii. Fe-LDH, $[M^{II}_{(1-x)}M^{III}_x(OH)_2]^{x+}$. $[(x/n)\ A^{n-}, m\ H2O]^{x-}$:

The formation of this phase during the hydration of an NFM slag in a PC-based system has been experimentally demonstrated in Hallet *et al*., 2022 [139]. When taken in a perpendicular angle to the synthetic LDH planes, its TEM image in **Figure 3.37** could also resemble the morphology of the Fe-bearing phase obtained in this study. The presence of this phase might explain the Mg detected in some of the samples (i.e., A30 and A31 in **Figure 3.34**). In the cationic hydroxide layers, Mg, Fe, (Ca, Al) ions octahedrally-coordinated with OH^-, could take the M^{II} and M^{III} roles as seen in previous studies [181,185]. On the other hand, water molecules and CO_2 occupy the anionic interlayers. Recall that the detection of the C is problematic with the EDS analysis due to its low atomic number, which is likely to result in its underestimation.

It was notable that the (Mg+Fe)/Al molar ratio at approximately 1.3 obtained in A30 and A31 was much lower than that of the synthetic $(Mg, Fe)^{2+}$-Al^{3+} LDH (hydrotalcite-like) structure at 3 [186]. This difference could be associated to the high Al content either due to the nature of the system itself (CAC-rich), or to the intermixing with the Al-rich gels within the same analytical volume. Similar deviations have been reported by Hallet *et al*., 2022 [139] due to the latter reason. However, this could not directly explain the Si content detected in the samples which has not been reported to partake in an LDH structure. In terms of the d-spacing, values at 7.42-7.48 Å were reported for the Fe-containing LDH [170,185], making it closer to the 7.2 Å obtained for

the 1 year sample as opposed to those of the Al-Fe hydroxides. One of the factors that these differences in the d-spacing among the Fe-LDH phases can be attributed to was the oxidation state of Fe. The different proportions of Fe^{2+} and Fe^{3+} in the structure can offset the Fe–OH bond configuration, such that a closer interlayer spacing is expected in the oxidized state [139].

iii. Fe-Si hydrogarnet

According to the thermodynamic model in section 3.3.1, this should be the most thermodynamically-favored Fe-bearing phase at long term (infinite time). Given the seemingly increasing proportion of Ca and Si towards 1 year, the formation of this phase at longer curing time could not be eliminated. In terms of d-spacing, the reported values for C_3FH_6 and C_3FSH_4 are at 4.49 Å and 5.14 Å, respectively [132], much lower than those observed for the unidentified Fe-bearing phase observed in this study. Although an uptake of Mg^{2+} in the Ca^{2+} sites can occur in hydrogarnets [132], the Al content of the unidentified phase remains significantly elevated. Moreover, a needle-like or lamellar morphology has not been previously observed, to the best of the author's knowledge, in typically cubic (Chapter 1, **Figure 1.4**) hydrogarnets.

Among the three possible phases presented, Al-Fe hydroxide and Fe-LDH seem to have the closest characteristics with the phase in question. Unfortunately, the data obtained from TEM and STEM were proven not sufficient to draw a concrete conclusion as to its identity, particularly hindered by the intermixing of phases even on the nano-scale. This was aggravated by the sensitivity of the hydrates resulting in their immediate disintegration during the EDS analysis.

3.4.3. Mössbauer spectroscopy

To further describe the fate of Fe during slag hydration, ^{57}Fe Mössbauer spectroscopy was performed on the paste samples. The evolution of the spectra of formulation A over 1 year of curing is presented in **Figure 3.39**. Additionally, the spectra of formulation B at 28 days and the raw slag were superimposed in the same figure for comparison.

It is evident from the general trends that the atomic environment of Fe changes as the slag hydrates over time. In particular, the most drastic transformation took place after more than 7 days (**Figure 3.39**) coinciding with the changes in the phase assemblage in section 3.3 (start of transition from ettringite- to AFm-rich system). The relative intensities of the transmittance diminished over time as the highly amorphous raw slag was diluted by the other components of the blend (CAC, HH) and its Fe was

incorporated into the Al-rich hydrate gel, as seen from the TEM and STEM results. At 28 days, the estimated slag hydration degrees of formulation A and B were similar (10 % and 9 %, respectively, **Figure 3.12**) which could explain the close resemblance of their Mössbauer spectra.

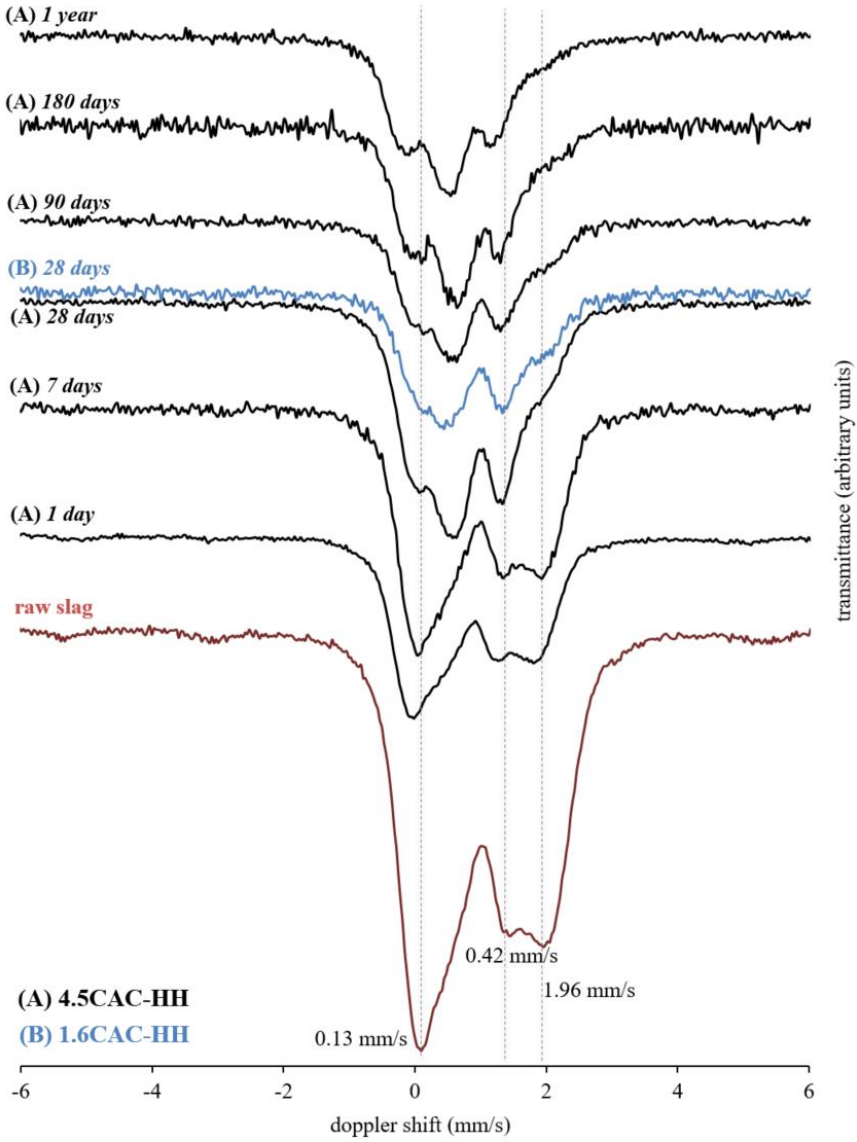

Figure 3.39 *^{57}Fe Mössbauer spectrum evolution of formulation A sample over 1 year of curing. Superimposed are the spectra of formulation B after 28 days of hydration and of the raw slag.*

Two fitting procedures were explored in analyzing the spectra of formulation A, producing a complex (Model 1) and a simplified model (Model 2), described as follows:

- **Model 1,** performed using the IMSG software, adopted most of the Fe speciation of the raw slag presented in Chapter 2 (section 2.2.5) comprising of two Fe^{2+} doublets (G1 and G2) and one Fe^{3+} doublet (G3) in the glass fraction, and a doublet of Fe^{2+} (M1) for wüstite. The sextet magnetic component (M2) was excluded for the paste samples because its signature was almost negligible after the dilution. While the hyperfine parameters of the new hydrates were allowed to vary, those of the raw slag were fixed for all the samples. Based on the findings from the other characterization techniques suggesting that wüstite was unreactive throughout the curing period studied, its absorption area was fixed at 18.2 % which was the value obtained from the raw slag fitting (section 2.2.5). Note that this value was similar to the contribution of wüstite estimated in Appendix J, assuming that the Mössbauer spectra directly reflect the weight percentages of its components. Moreover, the intensities and absorption areas of the glass components were made interdependent, maintaining a similar ratio as hydration proceeds. This was based on the assumption that the amorphous fraction of the slag dissolves uniformly as slag reacts.
- **Model 2,** performed using the WinNormos® software, offered a simplified approach using only three components for the fitting of the hydrated paste spectra consisting of three doublets: one for Fe^{2+} in the amorphous fraction of the slag (G4), one for wüstite (M1), and one for the Fe^{3+} mainly in the hydration product (P3). This model was presented to challenge the integrity of the general trends (qualitative) observed in Model 1 by allowing variations in the intensities and hyperfine parameters of all components without imposing restrictions. For instance, the absorption area of M1 (wüstite) was not fixed like in Model 1. It must be noted that Model 2 was not made to challenge the absolute value of each Fe component estimated from Model 1.

The deconvoluted spectra of formulation A paste after 28 days of hydration, derived from the two models, are presented in **Figure 3.40**. The Mössbauer hyperfine parameters used for the fitting procedures are detailed in **Table 3.3** (Model 1) and **Table 3.4** (Model 2). Supplementary figures obtained during the modelling can be found in Appendix J.

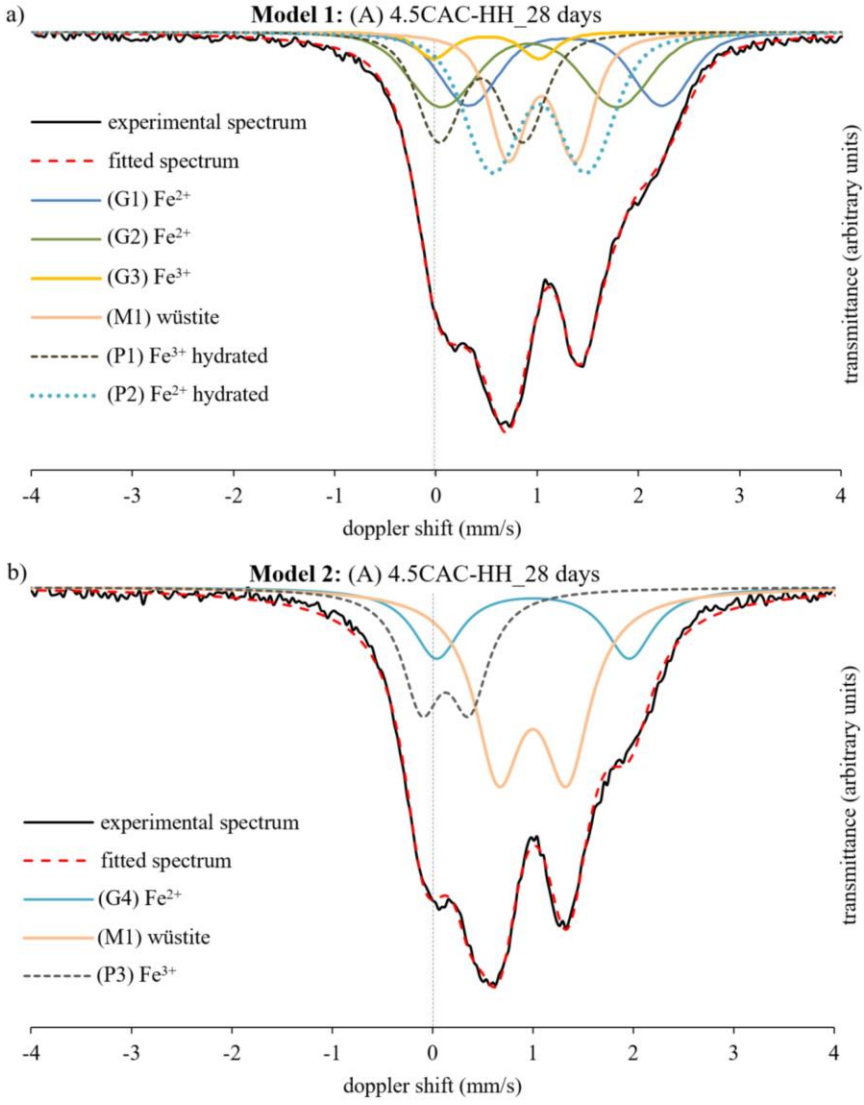

Figure 3.40 *^{57}Fe Mössbauer spectrum of formulation A and its components derived from a (a) complex and a (b) simplified modelling approach*

Table 3.3 *^{57}Fe Mössbauer hyperfine parameters used for Model 1. The abbreviations are designated as follows: isomer shift (IS); central value of the quadruple splitting (QS); central value of the hyperfine magnetic field (MF); total Gaussian-type spreading of the quadruple splitting (ΔQS) or the hyperfine magnetic field (ΔMF); and total absorption area fitted to the component (AA). The typical errors for IS and QS is ± 0.02 mm/s; and ± 5% for A*

Sample	Component	IS (mm/s)	QS (mm/s)	MF (kOe)	ΔQS or ΔMF (mm/s or kOe)	AA (%)
7 days	(G1) Fe^{2+}	1.15	1.91	0.00	0.42	29
	(G2) Fe^{2+}	0.79	1.73	0.00	0.51	39
	(G3) Fe^{3+}	0.37	1.04	0.00	0.17	8
	(M1) wüstite	0.91	0.66	0.00	0.20	18
	(P1) Fe^{3+} hydrated	0.21	0.25	0.00	0.25	3
	(P2) Fe^{2+} hydrated	0.82	0.97	0.00	0.40	3
28 days	(G1) Fe^{2+}	1.15	1.91	0.00	0.42	15
	(G2) Fe^{2+}	0.79	1.73	0.00	0.51	18
	(G3) Fe^{3+}	0.37	1.04	0.00	0.17	4
	(M1) wüstite	0.91	0.66	0.00	0.20	18
	(P1) Fe^{3+} hydrated	0.32	0.83	0.00	0.28	18
	(P2) Fe^{2+} hydrated	0.89	0.93	0.00	0.39	27
90 days	(G1) Fe^{2+}	1.15	1.91	0.00	0.42	14
	(G2) Fe^{2+}	0.79	1.73	0.00	0.51	16
	(G3) Fe^{3+}	0.37	1.04	0.00	0.17	3
	(M1) wüstite	0.91	0.66	0.00	0.20	18
	(P1) Fe^{3+} hydrated	0.24	0.75	0.00	0.35	22
	(P2) Fe^{2+} hydrated	0.83	0.91	0.00	0.45	27
180 days	(G1) Fe^{2+}	1.15	1.91	0.00	0.42	10
	(G2) Fe^{2+}	0.79	1.73	0.00	0.51	13
	(G3) Fe^{3+}	0.37	1.04	0.00	0.17	3
	(M1) wüstite	0.91	0.66	0.00	0.20	18
	(P1) Fe^{3+} hydrated	0.27	0.84	0.00	0.35	34
	(P2) Fe^{2+} hydrated	0.84	0.87	0.00	0.34	22

Table 3.4 *^{57}Fe Mössbauer hyperfine parameters used for Model 2. The abbreviations are designated as follows: isomer shift (IS); central value of the quadruple splitting (QS); central value of the hyperfine magnetic field (MF); total Gaussian-type spreading of the quadruple splitting (ΔQS) or the hyperfine magnetic field (ΔMF); and total absorption area fitted to the component (AA).*

Sample	Component	IS (mm/s)	QS (mm/s)	MF (kOe)	ΔQS or ΔMF (mm/s or kOe)	AA (%)
raw slag	(G4) Fe^{2+}	1.10	2.12	0.00	0.57	39

	(M1) wüstite	1.10	0.95	0.00	0.78	53
	(P3) Fe^{3+}	0.15	0.17	0.00	0.30	6
	(M2) magnetic	0.02	0.00	33.30		2
7 days	(G4) Fe^{2+}	0.95	2.10	0.00	0.53	39
	(M1) wüstite	0.88	0.97	0.00	0.75	50
	(P3) Fe^{3+}	0.14	0.20	0.00	0.31	10
28 days	(G4) Fe^{2+}	1.00	1.92	0.00	0.57	22
	(M1) wüstite	1.00	0.68	0.00	0.57	55
	(P3) Fe^{3+}	0.13	0.47	0.00	0.46	23
90 days	(G4) Fe^{2+}	0.91	2.21	0.00	0.53	20
	(M1) wüstite	1.03	0.59	0.00	0.54	49
	(P3) Fe^{3+}	0.25	0.37	0.00	0.41	30
180 days	(G4) Fe^{2+}	0.91	2.21	0.00	0.52	12
	(M1) wüstite	1.03	0.59	0.00	0.54	48
	(P3) Fe^{3+}	0.22	0.51	0.00	0.51	39

In Model 1, two new doublets (P1 and P2) were introduced as products of hydration. The parameters of the P1 component at 7 days, displaying relatively low IS and QS values, could represent a phase with a similar structure as the $Fe(OH)_3$ gels reported in PC cement systems [106,135,187] which in time develops into Fe-monosulfate [129,136]. This transformation is accompanied by an increased distortion of the atoms surrounding the Fe signaled by the higher QS values at later ages (<7 days). However, given the nature (poor to no crystal structure) of the Fe-bearing hydrate gel observed from TEM and STEM, it was difficult to clearly postulate the exact atomic environment of the new Fe-containing phases detected. As Fe is relatively scarce in conventional cement systems, especially in CAC-based binders, there is no sufficient Mössbauer data on Fe-containing hydrates, at the moment, to compare with those obtained in this study. Although the hyperfine parameters of P1 could only be associated to that of Fe-monosulfate given these constraints, it was clear from the EDS analyses of TEM and STEM that the Fe-bearing hydrates could not be monosulfate considering the extremely low (<1.5 at.%) amount of S detected. Nonetheless, the atomic environment (Fe-Al solid substitution) and oxidation state (Fe^{3+}) of Fe could be very similar, which is also the case for the ferrihydrite gels versus the Al-rich hydrate gels at early ages.

Furthermore, the hyperfine parameters of P2 in Model 1 was even more intriguing with the combination of IS and QS values that has never been observed, to the best of the author's knowledge, in either cement or IP systems. In particular, Fe^{2+} in 4- or 5-fold coordination with oxygen is

considered rare [188]. The closest structure that could be compared to this component is one of the doublets of staurolite ($(Fe,Mg)_2(Al,Fe)_9O_6[SiO_4]_4(O,OH)_2$) reported in Dyar *et al.,* 1991 [189]. This doublet is in the exceptionally low end of the range for 4-fold coordinated Fe^{2+} arising from the delocalization of electrons due to charge transfer phenomena (i.e., $Al^{3+} - Fe^{2+}$ or $Fe^{2+} - Fe$ substitutions) [189]. In addition, the overall lower ΔQS of the newly-formed component P2 versus the Fe^{2+} in G1 and G2 from the raw slag could suggest a generally more ordered environment of Fe. This could well be the case if the component P2 majorly corresponds to the unidentified Fe-bearing phase detected in STEM, such that the Fe^{2+} is transitioning from an amorphous state in the raw slag.

In Model 2, the Fe in the raw slag was assumed to be dominantly Fe^{2+} (G4) with an environment comparable to those in fayalite minerals [114,190]. The hyperfine parameters of the doublet P3 varied significantly as the component shifts from representing a minor Fe^{3+} proportion of the raw slag's glass fraction to the main Fe-bearing hydration product in the paste samples. This was expected given the simplified approach with minimal restrictions imposed on the hyperfine parameters and absorption areas, as described earlier, for Model 2. As hydration proceeds, the best fit obtained for the spectra suggests P3 parameters closer to those of the Fe-bearing hydrates in cement systems represented by P1 in Model 1. In addition, using a single component of Fe for the raw slag's glass fraction clearly resulted in the overestimation of the M1 (wüstite) component.

Nevertheless, it is important to highlight that the exact values of the Mössbauer parameters are difficult to directly relate to the theoretical Fe environment in crystal structures notably due to the presence of long-range interactions and cation substitutions [189]. As mentioned earlier, the interest in this application is to observe the general trends that could elaborate a better understanding of the evolution of Fe speciation during slag hydration. For this purpose, the evolution of the absorption areas estimated from the two models using the formulation A paste samples is presented in **Figure 3.41**. Supplementary figures obtained during the modelling may be referred to in Appendix J.

The diminishing absorption areas over time (**Figure 3.41**) of the components representing the glass fraction of the slag (G1, G2 and G3 for Model 1 and G4 for Model 2) were consistent for both models suggesting slag dissolution. New Fe-bearing phases were generated as the slag hydrates, where Fe was potentially in octahedral coordination with oxygen in the 3+ oxidation state or in tetrahedral coordination with oxygen in the 2+ oxidation state. Despite the overestimation of wüstite in Model 2, the overall steady values of its absorption areas, even when no fitting

constraint was applied for the different samples, supported the assumption in Model 1 suggesting wüstite's low (to negligible) reactivity.

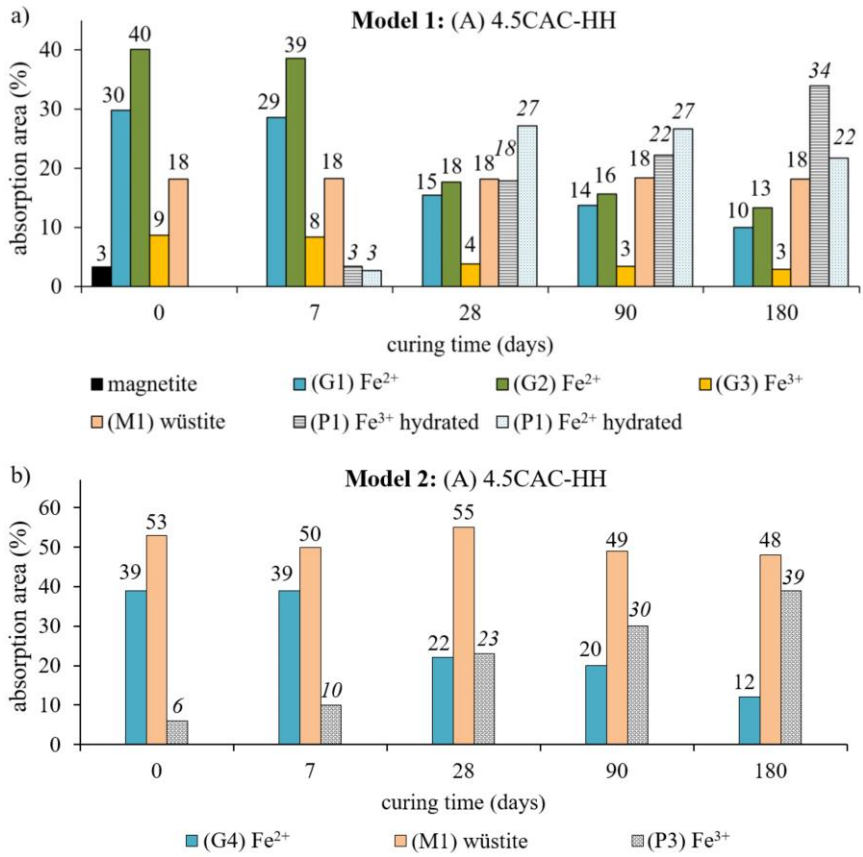

Figure 3.41 *Absorption areas (AA) calculated from the two modelling approaches*

By following the changes in the sum of the absorption areas (AA) of the reactive components of the raw slag (G1, G2 and G3 for Model 1 and G4 for Model 2), the slag hydration degrees of formulation A at different curing ages were estimated (**Figure 3.42**). Similar to the assumption applied in the XCT analysis in section 3.2.2, this estimation equates slag dissolution to slag hydration. Note that the original equation for the slag hydration degree presented in Chapter 2 (section 2.2.5) needed correction due to the apparent overestimation of wüstite especially in Model 2. The details of these calculations can be referred to in Appendix H.

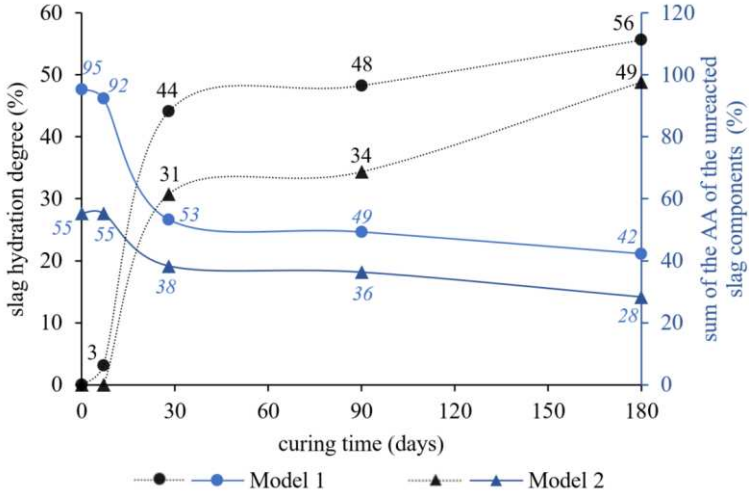

Figure 3.42 *Slag hydration degree in formulation A paste (primary axis) estimated based on the changes in the total absorption areas (secondary axis) of the unreacted slag for Models 1 and 2.*

The estimated values of the slag hydration degree converge at longer curing ages despite the steady difference in the values of the absorption areas between the two models. These estimated values were also higher compared those estimated from the XCT analysis (section 3.2.2). Although the values from these two techniques could not be directly equated, one of the main factors that could explain the lower values obtained from the XCT was the voxel resolution setting, 2.15 µm. The result from the Mössbauer spectra fitting proved to be essential in confirming this issue. Nonetheless, the abrupt changes in the values between 7 and 28 days (**Figure 3.42**) call for further refinement of the Mössbauer fitting procedures. Although it was clearly based on the general trends alone (**Figure 3.39**) that a significant transformation occurred between these curing times, the resulting hyperfine parameters (**Table 3.3** and **Table 3.4**) from the best fit models were also considerably altered. Yet, they were presumed to represent the same components due to the lack of concrete information on the actual structure of the Fe-bearing hydrates.

3.5. Activation through paper residue addition

The combination of various techniques provided abundant information essential in characterizing and estimating the degree of slag hydration in the CAC-based ternary systems investigated. The results presented earlier in this chapter, did not only confirm slag reactivity but also demonstrated its long term positive contribution to compressive strength in dimensionally-stable mortars. Despite these encouraging results, one of the critical challenges that needs to be addressed in order to increase its potential for application is the activation at the early ages (<28 days) of hydration.

In Chapter 2 (section 2.3), the reactivity of several SOCRATES residues was evaluated in a screening test. The distinct mineralogy of the lime-rich paper residue (Top-Crete®) yielding considerably high conductivity values in water, supported its promising potential as a green binder for which it is currently being marketed for. When added at 23 wt% in a CAC-HH binder system (CAC/HH = 1.6), high-intensity rapid heat release (**Figure 3.43** a) in the first hour of hydration was observed. Compared to a formulation with an equivalent volume of slag, the hydration peaks also appeared earlier, likely indicating faster reaction kinetics. However, the cumulative heat release curves (**Figure 3.43** b) show that the total released was, in fact, lower for the paste with the paper residue from about 4 hours onwards.

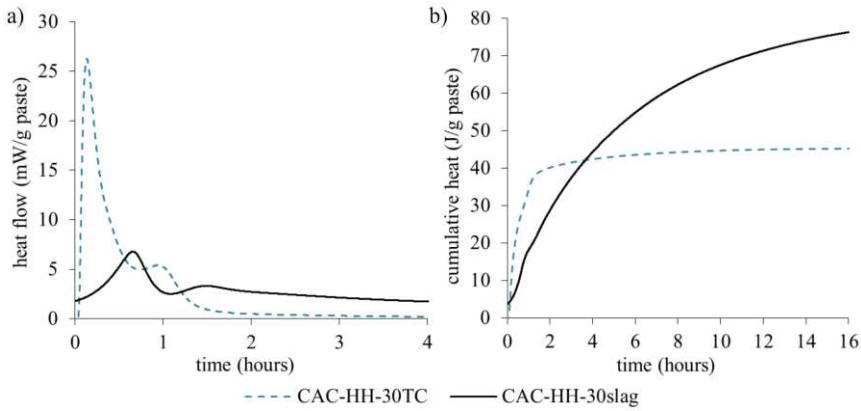

Figure 3.43 *(a) Heat flow and (b) cumulative heat release of pastes containing 23 wt% paper residue (in blue) and 30 wt% slag (in black).*

One concern on the use of this paper residue as SCM is its elevated (23 wt%) free lime content (Appendix B) excessively surpassing the 1 or

2.5[19] wt% limit imposed by the EN-450 [191]. Although this limit was intended for fly ash addition, De Shepper *et al.,* 2011 [192] reiterated the significance of maintaining the free lime content below 3 wt% in cements to prevent undesirable effects such as volume expansion, flash setting and reduced mechanical strength. At 23 wt% addition in the binder, the effective free lime content was 5.2 wt% from the paper residue alone. For this reason, this residue was evaluated separately from the other potential SCM in this study.

In an attempt to increase the slag reactivity in formulation A, the paper residue was added at 5 wt%, following the blend formulation A-TC (**Table 2.3**, where TC stands for Top-Crete® paper residue). Even with this small amount of paper residue, the addition of 0.3 wt% citric acid was needed to prolong the setting time (**Figure 3.44**) allowing the freshly-mixed blends to be properly placed in the moulds. The properties of this blend were then compared to those of formulation A, and a reference formulation (reference no TC) with the citric acid addition but without the paper residue.

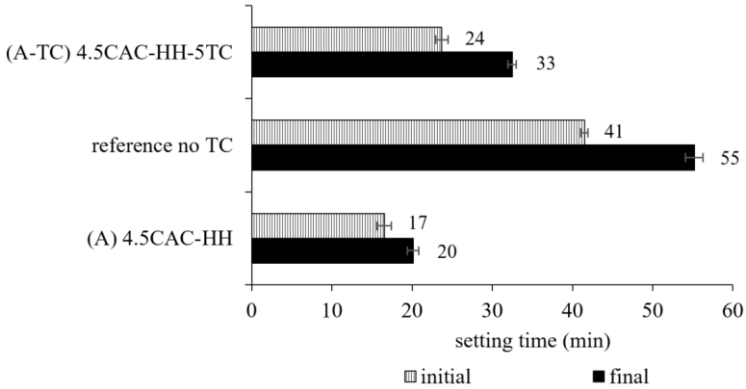

Figure 3.44 *Initial and final setting time of formulations A-TC; reference no TC; and formulation A*

The compressive (**Figure 3.45**) and flexural (**Figure 3.46**) strength evolution along with the SAI values demonstrated the significant contribution of the paper residue addition to the strength of the mortar samples. However, the addition of the citric acid alone also appeared to have contributed to this strength increase based on the values of the reference formulation. For instance, a compressive strength of 27 MPa was obtained without the citric acid addition, while this reached 38 MPa with the citric acid after 28 days of hydration (**Figure 3.45**). The benefit of the

[19] when a complementary autoclave expansion test yields satisfactory results

citric acid addition in improving the workability has been reported [193–195] to have an impact on the mechanical strength, mainly by altering the microstructure and the porosity during the early age hydration. Nonetheless, as previously highlighted in Chapter 2, such a low amount of addition (0.3 wt%) for the binders in this study should not have an influence in the long term phase assemblage of the binders [82].

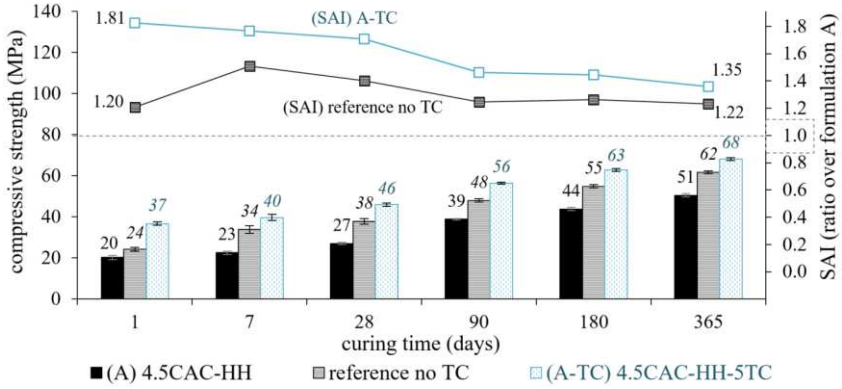

Figure 3.45 *Compressive strength (primary axis) and SAI evolution (secondary axis) of formulation A-TC (blue), its reference formulation (gray) and formulation A (black). SAI was calculated by dividing the strength values of A-TC and the reference by that of the formulation A.*

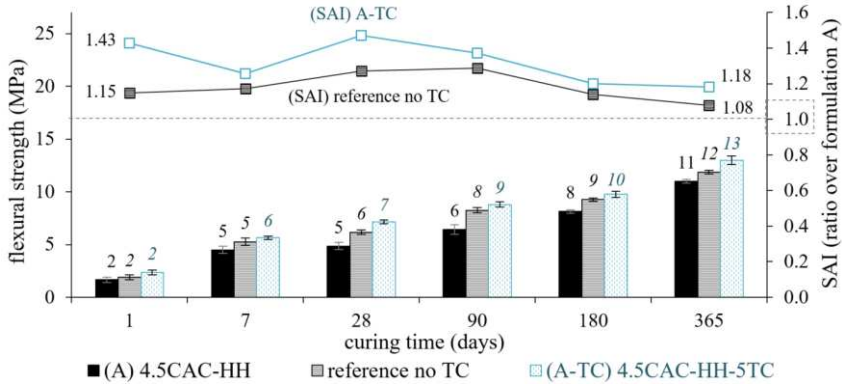

Figure 3.46 *Flexural strength (primary axis) and SAI evolution (secondary axis) of formulation A-TC (blue), its reference formulation (gray) and formulation A (black). SAI was calculated by dividing the strength values of A-TC and the reference by that of the formulation A.*

The SAI values of A-TC, particularly those for the compressive strength (**Figure 3.45**), suggest that the positive contribution of the paper residue addition to the strength was most pronounced in the first day of curing, progressively diminishing over time. This could be related to the length variation in **Figure 3.47** indicating a period of expansion from the 5th hour

or an overall period of shrinkage suppression between 5 and 15 hours. While the paper residue was dissolving extensively during this period according to the electric conductivity measurements in section 2.3.1, a more dimensionally-stable binder was simultaneously obtained using mortar samples at around the same period, leading to high strength values at early ages of hydration.

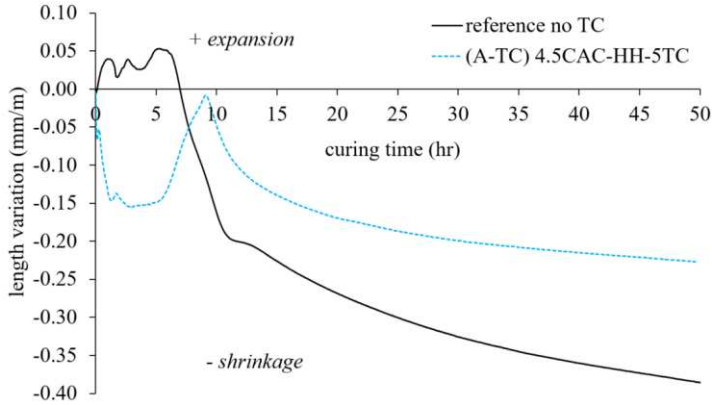

Figure 3.47 *Length variation of formulations A-TC (blue) and A (black) obtained from Walter+Bai shrinkage test*

Furthermore, the slight increase in slag hydration degree was validated by the result of the XCT analysis presented in **Figure 3.48**. Note however that the differences in the values from those obtained for formulation A, were close to the ± 3 % approximate error range of XCT determined from the sensitivity analysis in section 3.2.2. In addition, no significant difference in the Mössbauer spectra (**Figure 3.49** b) between the two formulations was observed at 28 days.

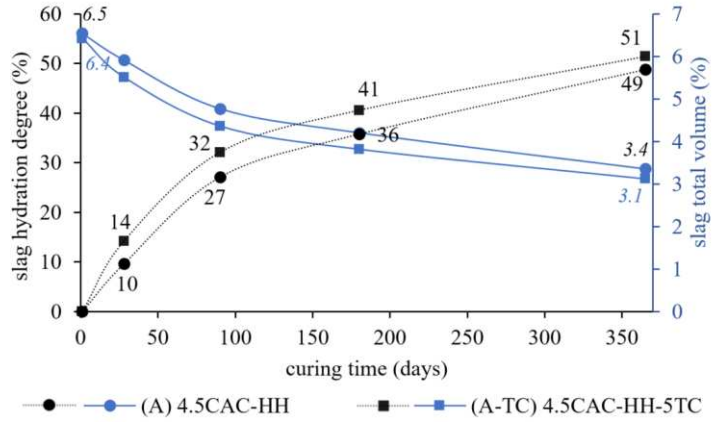

Figure 3.48 *The slag hydration degree (primary axis) and slag total volume of formulations A-TC and A estimated from XCT + volume analysis*

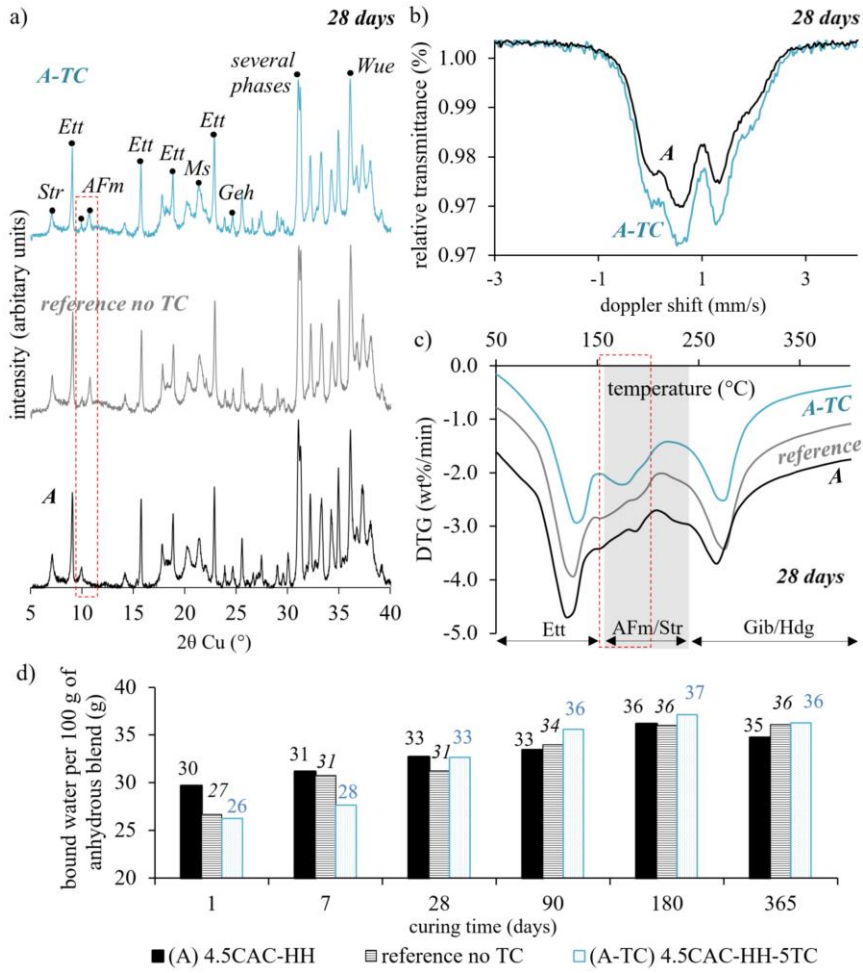

Figure 3.49 *(a) XRD patterns; (b) Mössbauer spectra; (c) DTG curves; and (d) total bound water evolution of formulations A-TC, its reference and formulation A. "Several phases" coinciding at around the 31° XRD peak in graph (a) is principally comprised of gehlenite and monosulfoaluminate.*

Despite the minimal addition, the early hydration reactions of the paper residue appeared to have altered the phase assemblage in the first 28 days by favoring the formation of AFm phases (likely monosulfoaluminates given the peak locations), evident from the regions marked in red in the XRD (a) and DTG (c) patterns in **Figure 3.49**. This is also consistent with the generally lower total bound water content (d) of formulation A-TC at 1 and 7 days. Similar to the previous observations in formulation A, Fe was detected only in Al-rich hydrated phase at long curing times (**Figure 3.50**). After 1 year, the abundance of these hydrate gel phases was apparent throughout the TEM frames observed.

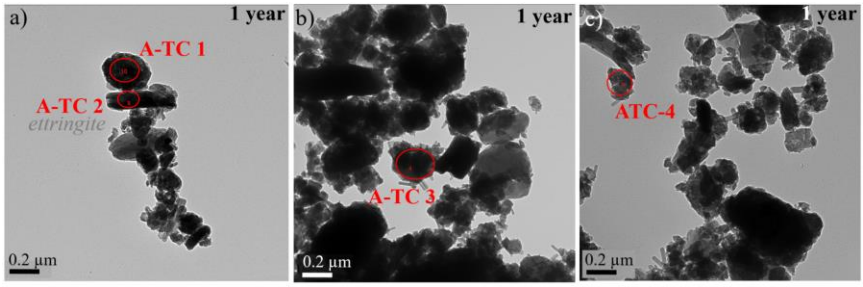

(A-TC) 4.5CAC-HH-5TC_1 year

At. %	Fe	Ca	Al	Si	S	Mg	K + Na	O	Sum
ATC-1	2.4	6.7	22.4	11.0	1.8	0.0	0.0	55.7	100.0
ATC-2	0.4	20.5	13.7	0.9	10.9	0.0	0.0	53.6	100.0
ATC-3	3.1	16.0	37.4	6.2	13.0	0.0	0.0	24.2	100.0
ATC-4	2.3	7.8	23.3	6.0	4.3	0.0	0.0	56.3	100.0

Figure 3.50 *TEM images and the atomic composition of marked areas in the (A-TC) 4.5CAC-HH-5TC paste sample*

While the observed increase in strength in the high-sulfate system (formulation B) was attributed to the increased ettringite formation, that in A-TC could be partly attributed to a marginally higher degree of slag hydration based on the XCT estimations (**Figure 3.48**). These initial results could boost the interest in the valorization of the paper residue as an SCM and an activator for slag. In the end, the mix design selection will be critical in maximizing the synergistic benefits from the slag and the paper residue.

Conclusion

This chapter demonstrated the reactivity of the slag in binary CAC-HH systems. The long term (>28 days) contribution of the slag to the mechanical strength of mortars was confirmed by the evolution of SAI values increasing over time for both the low (formulation A) and the high (formulation B) sulfate systems. Although both produced dimensionally-stable mortars, an overall shrinkage was observed in formulation A as opposed to the expansive nature of formulation B. This was associated to the difference in the phase assemblage of these formulations, generally described using XRD, TGA and ATR-FTIR as follows:

- Formulation (A) 4.5CAC-HH: dominated by monosulfoaluminate; ettringite and gibbsite content decreased over time while strätlingite formed significantly from 7 days onwards
- Formulation (B) 1.6CAC-HH: dominated by ettringite and gibbsite; with small amounts of strätlingite and monosulfoaluminates

Despite the higher strength values of formulation B mortars, the rate of slag dissolution remained comparable to that of the low-sulfate system (A), according to XCT. After 1 year, approximately 49 wt% of the slag dissolved in formulation A and 43 wt% in B. These estimations were lower compared to those obtained from Mössbauer spectroscopy. For instance, 56 wt% of the slag was estimated to have reacted after 180 days based on the latter, while this value was only at 36 % using XCT. This difference was mainly attributed to the voxel resolution setting (2.15 µm) in XCT, which could have underestimated the actual values.

No Fe-containing hydrated phase was detected from XRD, TGA and ATR-FTIR. Using TEM and STEM, Fe was found to be incorporated at low concentrations (≈ 2-5 at%) in an amorphous phase rich in Al. As the slag dissolved more significantly after 90 days, an unidentified needle-like phase with a higher Fe uptake (≈ 13 at%) was detected. This phase contained small amounts of Ca, Si and Mg, and could be similar to Al-Fe-hydroxides or Fe-LDH. Unfortunately, the techniques presented proved to be insufficient for identifying this phase, given the problems with intermixing on the nano-scale, and with the sensitivity of hydrates to EDS analysis. Nonetheless, it was clear that Fe was not detected in the more conventional hydrated phases, such as ettringite, monosulfoaluminate or strätlingite.

Moreover, the evolution of the Mössbauer spectra of formulation A provided strong evidence of the changes in the atomic environment of Fe during hydration. The 4/5-fold coordinated Fe^{2+} dominating the raw slag was transformed into a combination of Fe^{3+} and Fe^{2+} in octahedral and 4/5-

fold coordination, respectively. It was however difficult to postulate the exact atomic environment of the new Fe-containing phases detected through TEM and STEM, needed to validate the fitting models for the Mössbauer spectra. The hyperfine parameters of the new Fe^{3+} component were similar to those of the ferrihydrite gels in cement systems, which in time develops into Fe-monosulfate. On the other hand, the new Fe^{2+} component had parameters comparable to a rare doublet of staurolite ($(Fe,Mg)_2(Al,Fe)_9O_6[SiO_4]_4(O,OH)_2$). It must be emphasized that the author does not imply the presence of this mineral in the system. Rather, the rare Fe environment associated to the charge transfer phenomena (i.e., $Al^{3+} - Fe^{2+}$ or $Fe^{2+} - Fe$ substitutions) in staurolite was similar to what was observed in the new component.

At the end of this chapter, the activating effect to the slag of the lime-rich paper residue (added at 5 wt%) was investigated. The increase in the strength of mortars was accompanied by high SAI values, particularly in the first 28 days. An increased AFm formation was also observed during this period, despite estimating only a minimal augmentation (2-5 %) in the slag hydration degree using XCT. These overall encouraging results could support the need to perform more trials in order to better optimize the mix design and maximize the benefits from the addition of the paper residue.

Chapter 4

Fe-rich slag addition in ternary CAC-HH-PC binder

Contents

Introduction

In this chapter, the reactivity of the Fe-rich non-ferrous metallurgy (NFM) slag, selected during the screening test in Chapter 2, was investigated in ternary calcium aluminate cement (CAC)-calcium sulfate hemihydrate (HH)-Portland cement (PC) binders. The incorporation of PC in these CAC-rich systems serves two main purposes:

- To emulate a system (CAC-HH-PC) closer to the industrial formulations of CAC-based blends for rapid repair applications
- To evaluate the potential of PC as an activator of the slag

Although there have been several studies on the ternary CAC-HH-PC binders, detailed in Chapter 1, these preceding investigations were limited to PC-rich (60-80 wt%) systems. By introducing the slag in formulations dominated by CAC and HH, the lower carbon footprint and special properties (i.e., self-drying capacity, rapid hardening) of such binders are better maximized. Moreover, PC is evaluated as a possible activator of the slag in these ternary binders. In Chapter 3, the addition of 5 wt% paper residue slightly increased the rate of slag dissolution while significantly enhancing the mechanical strength of the mortars. However, due to the exceptionally elevated free lime content (23 wt%) of this residue, higher incorporation was not recommended. On the contrary, PC can provide additional Ca^{2+} and increase the alkalinity of the hydrated system without significantly contributing to the free lime content of the raw blend.

The properties of formulations A-PC and B-PC (**Table 2.3**) were examined in this chapter. Both of these formulations contained 30 wt% slag and 30 wt% PC. The CAC/HH ratio in formulation A-PC was 4.5 just like in formulation A. The CAC/HH ratio in formulation B-PC was 1.6 adapted from formulation B. Several techniques used in Chapter 3 were similarly employed in this chapter to characterize the hydrated blends over time. Mechanical strength and dimensional stability were monitored using mortar samples. The early hydration reactions were compared using isothermal calorimetry. The degree of slag hydration was estimated using X-ray Computed Tomography (XCT). The phase assemblage evolution was followed using XRD, TGA and ATR-FTIR of paste samples. Finally, Mössbauer spectroscopy, TEM and STEM were used to describe the fate of Fe during the hydration.

4.1. Physical properties

The physical properties of two ternary blends representing a low (formulation A-PC) and a high (formulation B-PC) calcium sulfate system are presented in this section. The addition of PC resulted in a shorter setting time preventing the freshly-mixed blends to be properly placed in the moulds. For this reason, 0.3 wt% citric acid was added in A-PC, B-PC and their references. This is the similar citric acid dosage used in A-TC and B in the previous chapter. **Figure 4.1** shows the initial and final setting times obtained from these formulations.

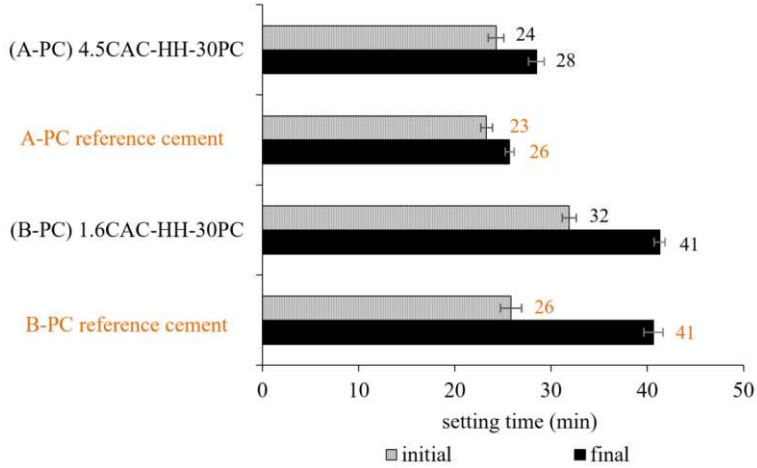

Figure 4.1 *Initial and final setting time of formulation A-PC, B-PC and their references*

Similar to the observation from the previous formulations (A, B and A-TC), the addition of the slag resulted in a minimal delay (1-6 min) in the setting time of mortars. Considering that the slag was unreactive during the first hour of hydration (assumed based on the results from Chapter 3), it is likely that the higher effective w/b ratio was one of the main factors causing this prolonged setting consistent with the observations in Stefanou and Larsinos, 1981 [196] and Dodson, 1994 [197]. Although this agrees with the general trends observed with the addition of SCM at low (< 40 wt%) replacement levels [112], Juenger *et al.,* 2008 [198] performed a number of elaborated studies showing conflicting trends depending on slag composition, fineness, curing conditions and replacement level. The changes in setting time observed were also almost negligible compared to the 20-30 min differences reported in the aforementioned studies. Nonetheless, this very minimal delay in setting resulting from the slag addition could have a positive implication in minimizing the amount of citric acid needed in order to obtain a comparable setting time as the reference cement mortars.

4.1.1. Low calcium sulfate system

The compressive and flexural strength evolution of formulation A-PC and its references are presented in **Figure 4.2** and **Figure 4.3**, respectively. The evolution of SAI values are shown in the secondary axes.

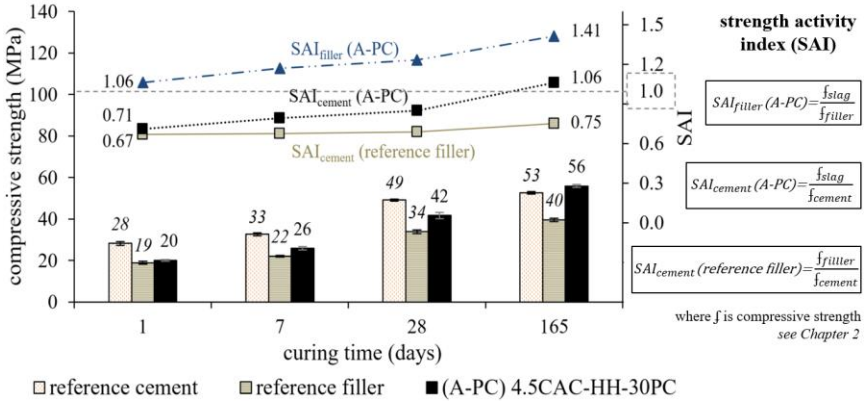

Figure 4.2 *Compressive strength of formulation A-PC* (primary axis) *and its SAI evolution (secondary axis)*

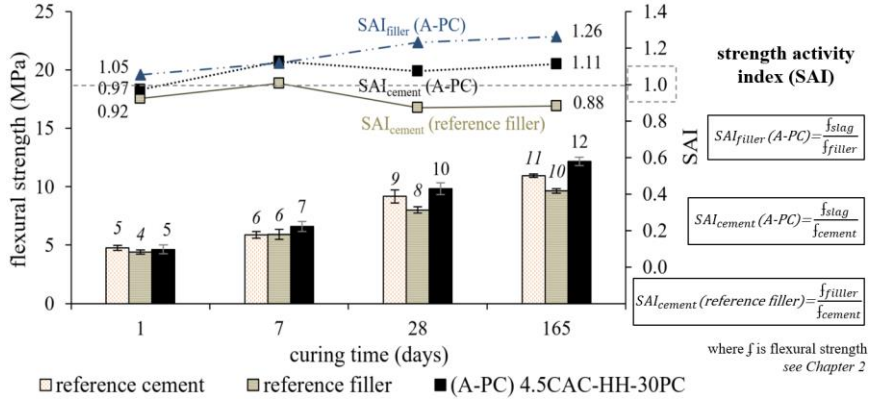

Figure 4.3 *Flexural strength of formulation A-PC* (primary axis) *and its SAI evolution (secondary axis)*

Overall, the strength was improved relative to formulation A with no PC (section 3.1.1) especially at 28 days. This was even more evident with the SAI_{cement} values exceeding 1 as hydration proceeds. It implies that the slag-containing mortars were able to surpass the strength values of their reference cement mortars. In **Figure 4.2**, the increasing difference between the SAI_{cement} values of the slag-containing formulation and that of the reference filler clearly indicates that the incorporation of slag positively contributed to the strength development of mortars. In addition, SAI_{filler} was plotted in the same figures to confirm whether the SAI_{cement} reflected

the trends correctly or the values were overestimated due to a possible excessive expansion in the reference cement mortars leading to cracks and compromised strength values. Contrary to the minimal length variations observed earlier in the binary CAC-HH binders, more significant expansion was detected in the ternary systems. **Figure 4.4** shows the length variations in A-PC obtained from Walter+Bai shrinkage test (a) and water-cured standard mortar samples (b).

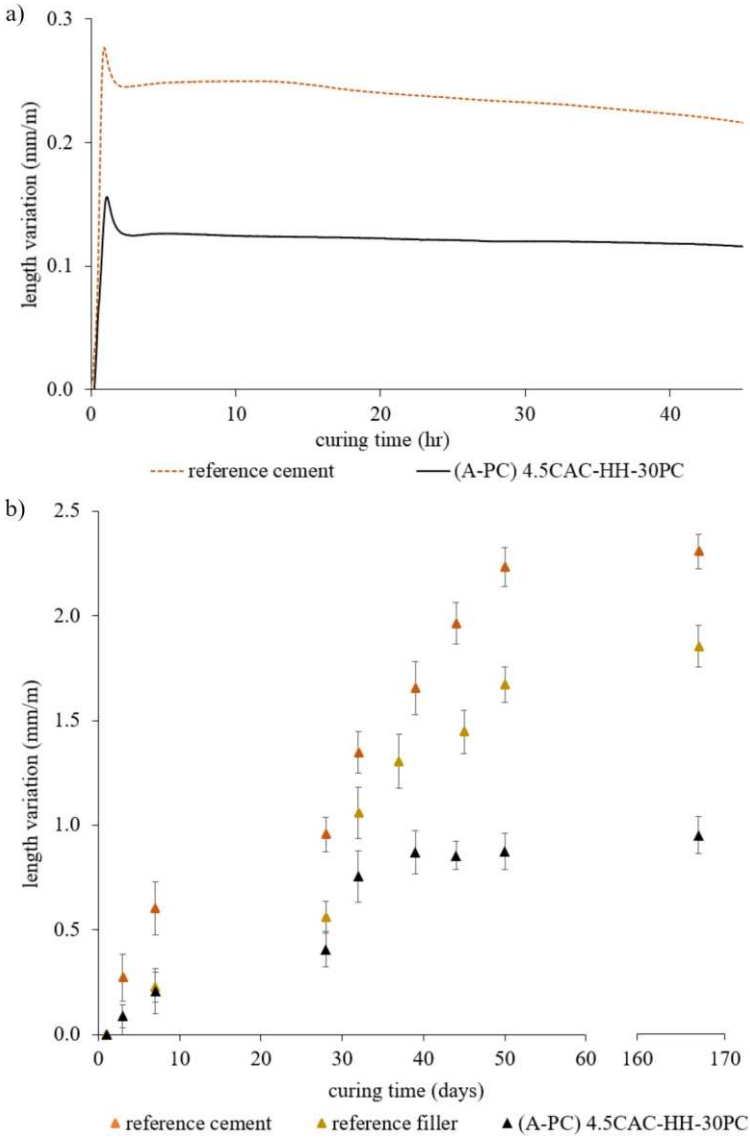

Figure 4.4 *Length variation of formulation A-PC and its references obtained from Walter+Bai shrinkage (a) and water-cured mortars (b)*

After a high and rapid expansion during the first hour, the momentary period of shrinkage between the second and third hour in the Walter+Bai test (**Figure 4.4** a) could be an initial indication of ettringite to monosulfoaluminate conversion as the sulfates were depleted in the system. This was however simultaneous to other factors affecting the dimensional changes at early hours such as self-desiccation and drying shrinkage.

Despite the continuous expansion of the blends during the 2 months of curing under water (reaching up to 2.3 mm/m for the reference cement), the mortars appeared to be generally stable and exhibited strength development. The slag addition seemed to have improved the dimensional stability of the blend by mitigating the expansion, consistent with its behavior in the binary systems. With no visible macro cracks signaling excessive expansion in this low calcium sulfate system (see **Figure 4.8**), the SAI_{cement} values were deemed to be acceptable. Nonetheless, the increasing SAI_{filler} values confirmed the positive contribution of the slag addition to the strength, as a reactive, rather than an inert, component.

4.1.2. High calcium sulfate system

In Chapter 3, increasing the HH content in a binary CAC-HH system up to 1.6 CAC/HH ratio, resulted in significantly higher strength values of mortars. Nonetheless, this was explained by the increase in ettringite formation predominantly from CAC and HH reaction, rather a manifestation of increased slag reactivity.

With the PC addition in a high calcium sulfate system (B-PC), the strength values (**Figure 4.5** and **Figure 4.6**) obtained were rather comparable to those in the low-sulfate system, A-PC. However, excessive expansion (**Figure 4.7**) was observed specifically in the reference formulations (reference filler and reference cement) resulting in poor strength development. For this reason, there were no strength data points beyond 28 days as the mortars no longer fitted in the extensometer. In **Figure 4.8**, actual images of A-PC and B-PC mortars with their respective references are shown after 45 days of curing under water.

Due to the excessive expansion in the reference mortars, the resulting SAI_{cement} values were disproportionate and therefore did not represent the slag contribution to the strength as intended. In this case, SAI_{filler} was a better criterion to delineate the influence of the slag as a reactive SCM. At least in the first 28 days, no macro cracks were observed in the reference mortars. Once again, the results highlight that the addition of the slag stabilized the dimensional variation in these blends, consistent with the previous observations for formulations A, B, A-TC and A-PC. The

mitigation of the destructive expansion is evident in the rapid setting and hardening properties of B-PC reaching > 20 MPa just after 1 day of curing and as much as 49 MPa after 28 days.

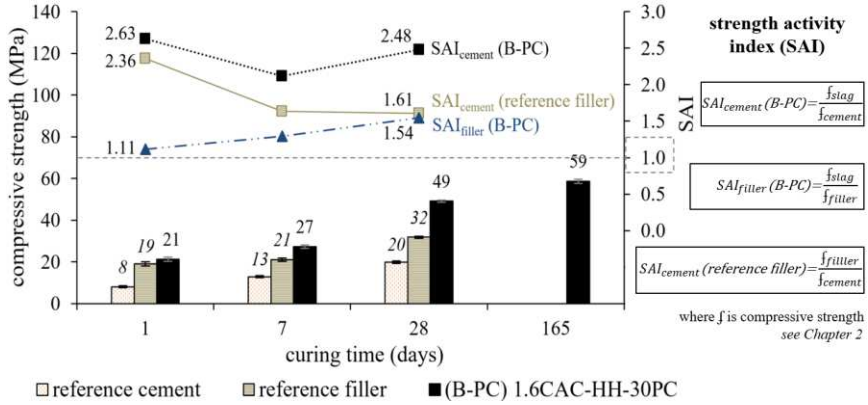

Figure 4.5 *Compressive strength of formulation B-PC* (primary axis) *and its SAI evolution (secondary axis)*

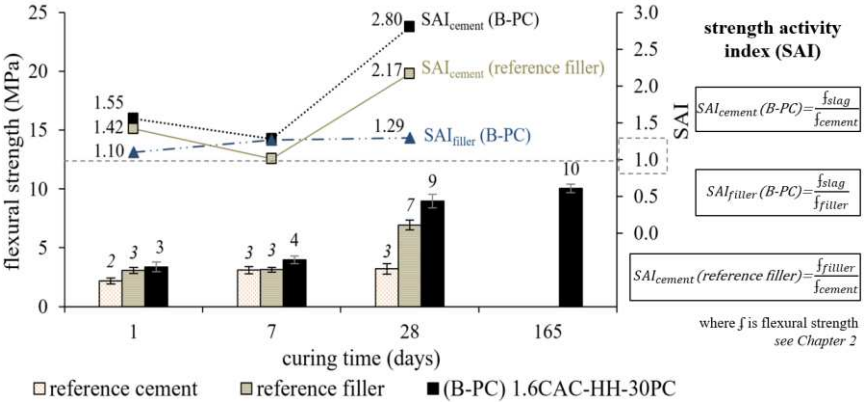

Figure 4.6 *Flexural strength of formulation B-PC* (primary axis) *and its SAI evolution (secondary axis)*

Furthermore, the momentary period of shrinkage between 2 and 3 h detected in A-PC (**Figure 4.4** a) was not observed in B-PC. It is most likely that the high amount of sulfates in the latter system resulted in the formation of stable ettringite, contrary to those converting to monosulfoaluminate in the former. It can also be observed in B-PC (**Figure 4.7** a) that the rate of expansion was slower compared to what was observed in the reference cement with a steep length variation curve in the first 3 h of hydration. It follows that the addition of the slag did not only mitigate the overall length variation at long term, but also reduced the kinetics of expansion in air-curing conditions.

Less difference in the trends was observed for underwater curing condition (**Figure 4.7** b), where the shape of the curves remained consistent even at varying expansion degrees. Relative to what was observed from the reference fillers, it can be said that the stability of the slag-containing mortars was not exclusively due to binder dilution (less CAC and HH proportion in the mortars). Instead, the dissolution of the slag likely had an impact on the phase assemblage and/or the microstructure, manifesting through the dimensional stability.

Macro cracks started to become apparent after 45 days for the reference mortars cured under water, where the length variations surpassed 13.7 mm/m (**Figure 4.7** b). It is important to mention that despite the absence of macro cracks and the superior mechanical strength performance of the slag-containing mortars, the expansion observed in this formulation, reaching 8 mm/m, was far beyond the standard expansion limits reported for sulfated PC and CSA systems typically between 0.04 % (0.4 mm/m) and 0.5 % (5 mm/m), respectively [85,199]. Nonetheless, this degree of expansion was still below the reported crack threshold limit of 2.25 % [85] in binary CAC-HH systems, demonstrating the exceptional property of these CAC-rich blends as expansive binders. Considering that there was no extensive mix design optimization (i.e., to determine the ideal w/b ratio and the proportion of each component) and the admixture used was limited to citric acid, the rapid setting and hardening properties and the expansive nature of the slag-containing formulations could be considered as remarkable properties for fast repair applications.

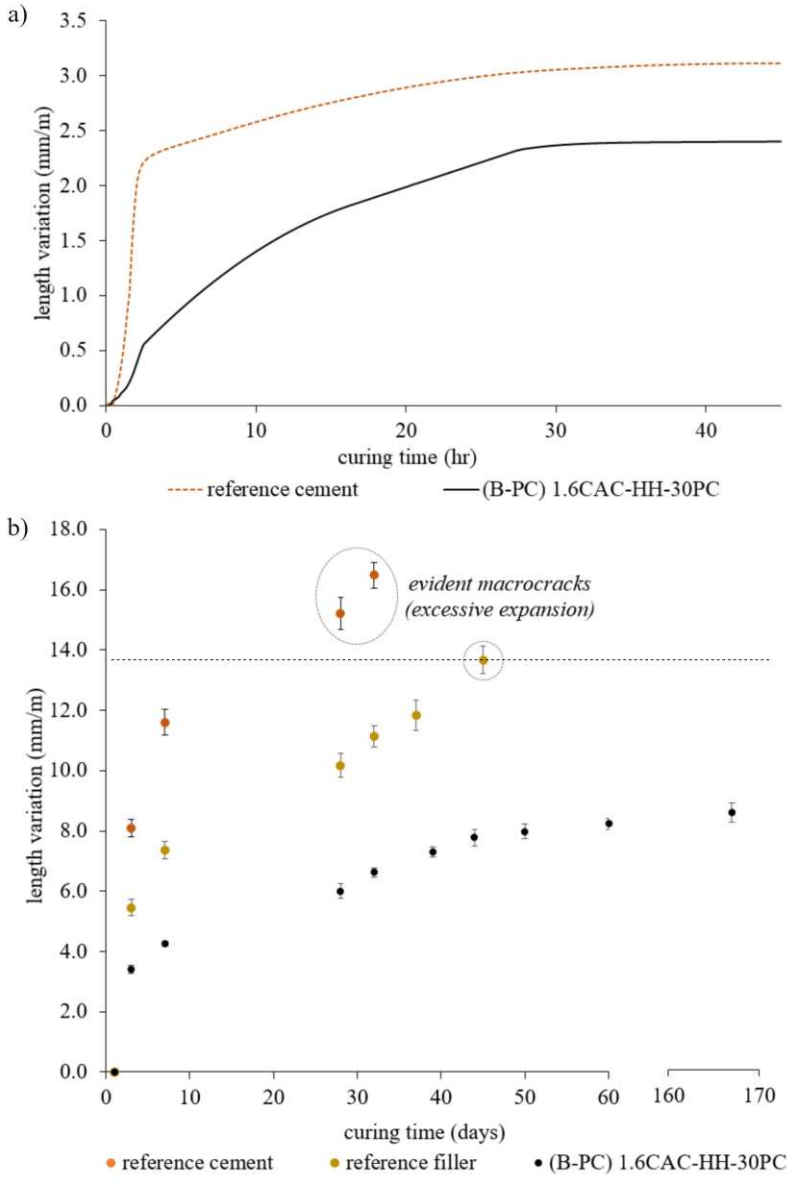

Figure 4.7 *Length variation of formulation B-PC and its references obtained from Walter+Bai shrinkage (a) and water-cured mortars (b)*

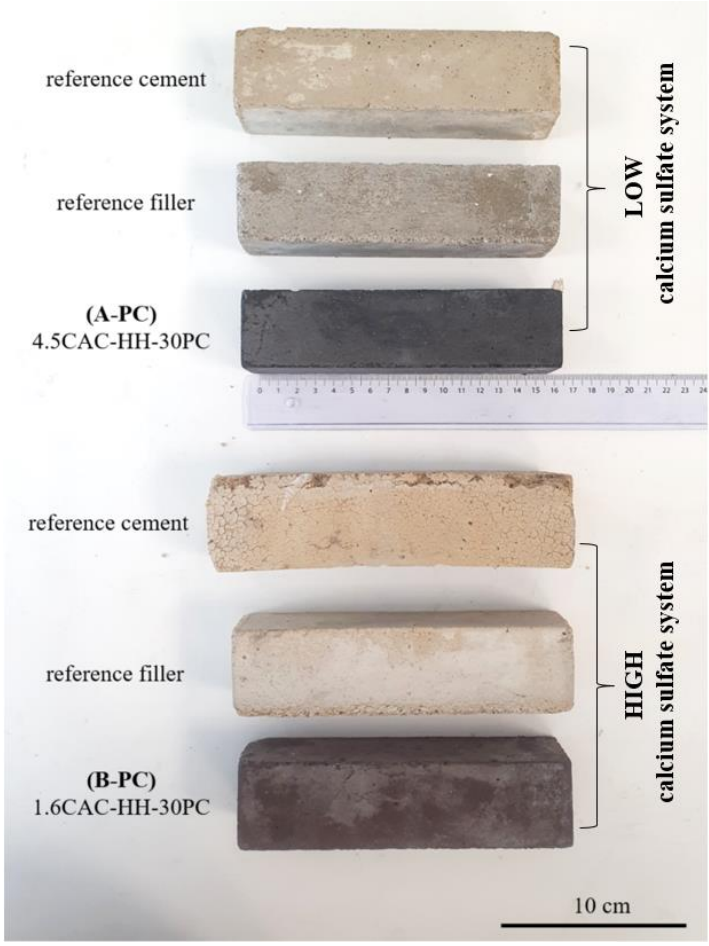

Figure 4.8 *Pictures of A-PC and B-PC mortars with their references after 45 days of curing under water*

4.2. Quantifying the degree of slag hydration using XCT

The degree of slag hydration of formulations A-PC and B-PC were estimated using a combination of XCT and volume analysis as previously employed in section 3.2. **Figure 4.9** illustrates the main operations involved in the analysis including: (a) 2D reconstruction of the XCT scans; (b) threshold segmentation to extricate the unreacted slag particles; (c) creation of 2D binary images based on the threshold segmentation; and (d) generation of 3D volume renders interpolated from 1400 frames of 2D binary images per sample.

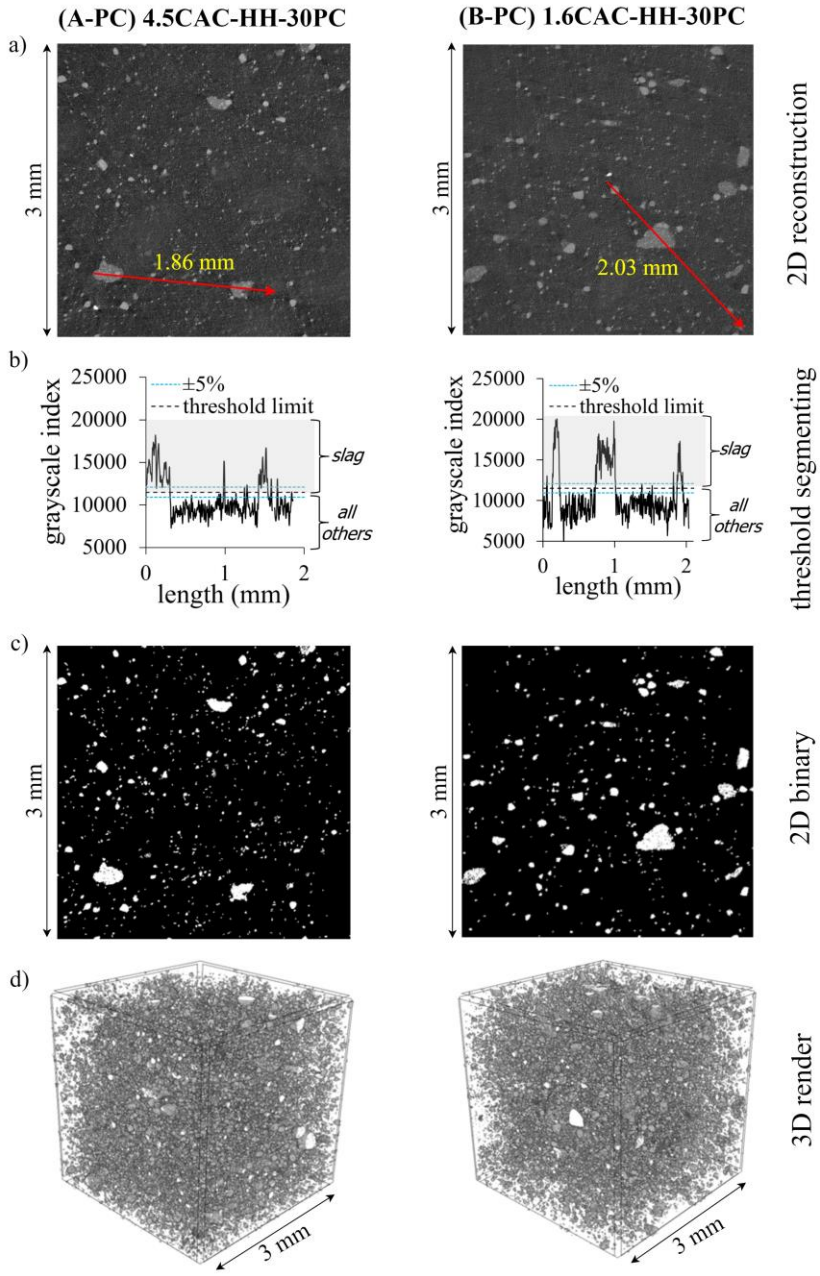

Figure 4.9 *Illustration of the steps involved in the volume analysis of XCT scans using samples after 28 days of hydration*

The plot profiles (b) shown in **Figure 4.9** correspond to the 16-bit grayscale indices of the pixels under the red arrow drawn in their corresponding 2D reconstructed images (a). The same lower threshold index limit was used as in the samples from the binary CAC-HH binders in the previous section. The parameters of the scans and the image analyses were likewise kept constant for all the samples in this study. It is important to reiterate that the estimation uses the total volume of the unreacted slag particles at 1 day as the zero reactivity reference (see section 2.2.4) such that any slag dissolution occurring before this period were assumed to be negligible and consequently not accounted in the estimations.

Similar to the scans for formulations A, B and A-TC, high grayscale contrasts were observed between the slag particles and the rest of the cement and hydrate matrix even with the addition of PC. It was evident that the slightly higher density of PC (3.11 g/cm^3) compared to that of the CAC (3.02 g/cm^3) was counterbalanced by the former's lower Fe content (1.4 % Fe_2O_3 for PC versus 1.8 % Fe_2O_3 for CAC) and thus yielding a grayscale index comparable to that of the latter. The combination of these factors preserved the advantage of the distinct properties of the slag in using XCT to estimate the degree of slag hydration.

Figure 4.10 presents the estimated degree of slag hydration in formulations A-PC and B-PC along with those in formulations A, B and A-TC discussed in the preceding chapter. Note that the estimation was only performed after 28 days for formulation A-PC and thus the absence of some data points in the figure.

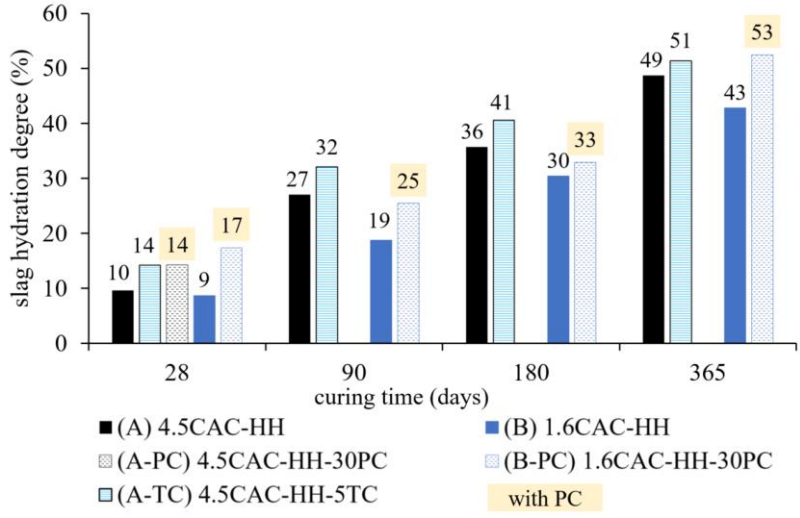

Figure 4.10 *Estimated slag volume and hydration degree using XCT + volume analysis.*

Overall, higher degree of slag hydration was estimated for the formulations incorporating PC as illustrated in **Figure 4.10**. In the first 28 days, the XCT results suggest a considerable increase from 9 % (B) to 17 % (B-PC) of the amount of the dissolved slag with the addition of 30 wt% PC while keeping the CAC/HH ratio constant at 1.6. Although this increase was less significant between formulations A and A-PC (4.5 CAC/HH ratio), the seemingly improved slag reactivity might be considered as a good direction in improving the 28-day performance of the binders to address the goal of early-age slag activation. The mechanism could be similar to what was observed for the paper residue in section 3.5, with the PC increasing the pH and contributing ions, particularly Ca^{2+}, which participate in hydrates formation. However, the increased reactivity became less pronounced beyond 28 days with the differences approaching a more comparable estimation (≈ 50%) towards 1 year.

It is also critical to take into account the possible consequence of the observed expansion in these PC-containing binders. Although the paste samples were not subjected to underwater curing, unlike the mortars, the w/b ratio used was higher (0.65 vs 0.50) for the pastes, failing to exclude the possibility of expansive behavior. Substantial expansion occurring after the first day of hydration could result in overestimation of slag hydration degree as the unreacted slag particles initially located close to the borders of the assigned scan volume may be slightly displaced out of the frames. In effect, less unreacted slag volume is estimated not because of the increased slag reactivity but because of the expansion. In order to address this possible issue in future analyses of expansive binders, it is recommended to run a full scan of a smaller sample, rather than setting fixed dimensions of scan volume which is more ideal for bigger samples with irregular dimensions.

Nonetheless, the impact of paper residue addition (where shrinkage is observed) to the estimated slag hydration degree is a clear indication that the increase in lime content and pH were beneficial in marginally improving the early-age reactivity of slag according to the XCT estimations. A similar case is expected with the PC addition despite any possible contribution of the expansion to the estimated values. Furthermore, higher slag reactivity was noted in the ternary formulation with higher sulfate content (B-PC) in the first 28 days of hydration. This is in contrary with the overall trend observed in the binary systems (A and B). With these observations, the phase assemblage evolution of both the systems are discussed in the subsequent section in order to further describe the possible impact of the blend proportions to the reactivity of the slag.

4.3. Phase assemblage evolution over time

4.3.1. Thermodynamic modelling

The thermodynamic models of the ternary CAC-HH-PC systems without and with the 30 wt% slag addition are presented in **Figure 4.11** and **Figure 4.12**, respectively. The models were generated in function of CAC content (x-axis), which could be interpreted in relation to the CAC/HH ratio. Only 50 wt% of the amorphous fraction of the slag was assumed to hydrate based on the estimations derived from XCT. The rest of the unreacted slag were assigned to the "inert" phase shown in black along with the minor (<1 wt%) components of CAC, HH and PC. More details on the assumptions and the codes used to generate the models are detailed in Appendix I.

According to the models (**Figure 4.11** and **Figure 4.12**), gypsum is formed with the excessive HH at lower CAC proportions: <21 % for the reference, and <11 % for the slag-containing sample. In the reference formulation (**Figure 4.11**), the model suggests a phase assemblage dominated by strätlingite and monosulfoaluminate for the low-sulfate system, A-PC; and an assemblage dominated by strätlingite and ettringite for the high-sulfate system, B-PC. Comparing this reference formulation model with that of the binary systems in section 3.3.1, it can be said that the addition of PC results in the increased quantity of strätlingite. Furthermore, the model suggests that a minor amount of C-S-H is only formed in B-PC.

Despite the addition of 30 wt% PC in the modelled system, the typical hydration product of pure PC, portlandite (CH), was not predicted to form in regions with more than 15 wt% CAC. This is because CH and gibbsite cannot co-exist thermodynamically and thus favoring their conversion into other hydrate products, as demonstrated in Bizzozero and Scrivener, 2014 [85]. Some of the possible reactions are presented in **Equation 4.1-4.3**.

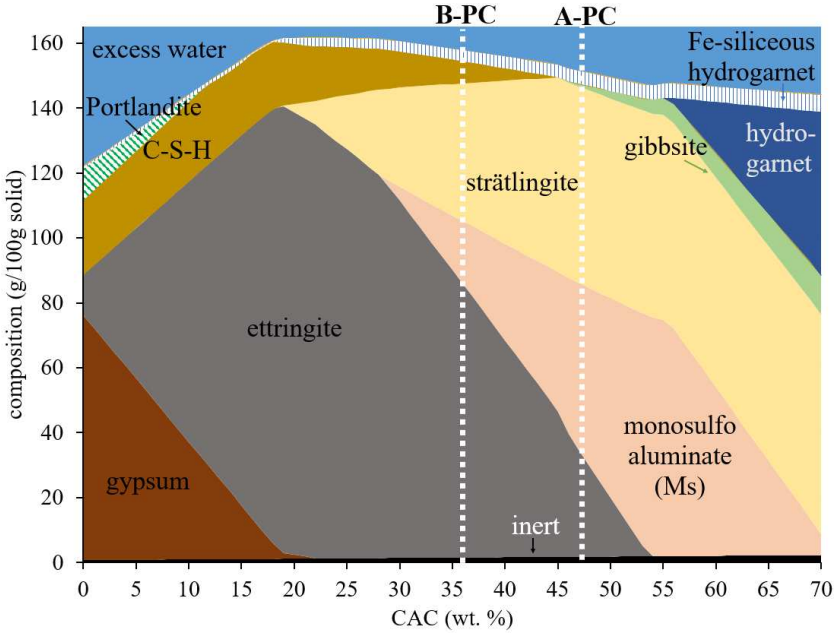

Figure 4.11 *Phase assemblage of the reference (no slag) ternary CAC-HH-PC binder with varying CAC and HH proportions calculated from thermodynamic modelling*

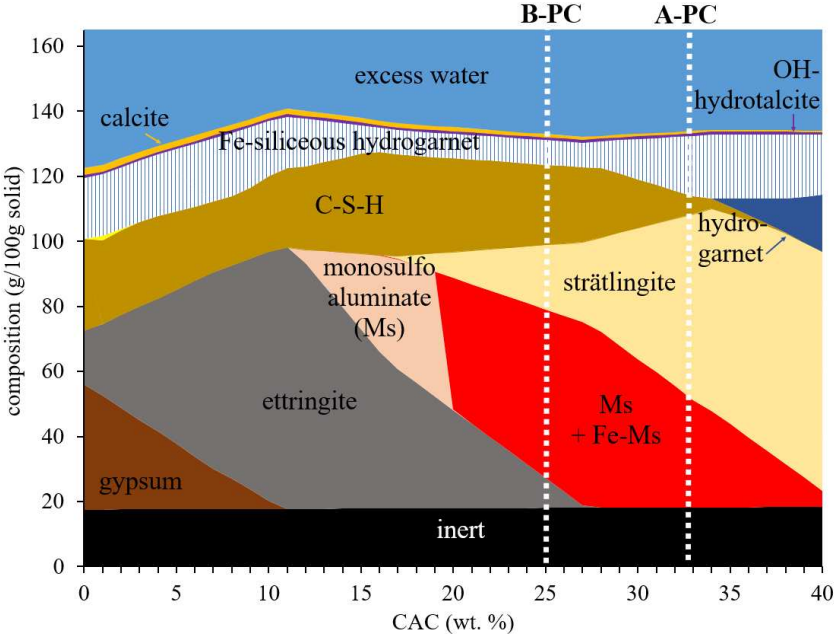

Figure 4.12 *Phase assemblage of the ternary binder incorporating 30 wt% slag and 30 wt% PC with varying CAC and HH proportions calculated from thermodynamic modelling. Only 50 wt% of the amorphous fraction of the slag was assumed to hydrate.*

In **Equation 4.1**, CH and gibbsite react with C\$$H_x$ to form additional ettringite. This case is likely to occur if all the anhydrous components simultaneously hydrate, therefore not considering the actual kinetics of the reactions. The late reaction of PC relative to CAC and HH is however expected as discussed in the previous section, such that it is more likely that the sulfates are already consumed before the reaction indicated could take place. Instead the reactions in **Equation 4.2** and **Equation 4.3**, suggesting the formation of monosulfoaluminates and strätlingite are more realistic, experimentally.

$$AH_3 + 3CH + 3C\$H_X + (26 - 3x)H \rightarrow C_6A\$_3H_{32} \qquad \textit{Equation 4.1}$$

$$2AH_3 + 6CH + C_6A\$_3H_{32} \rightarrow 3C_4A\$H_{12} + 8H \qquad \textit{Equation 4.2}$$

$$AH_3 + C_2S + 5H \rightarrow C_2ASH_8 \qquad \textit{Equation 4.3}$$

where x is equal to 2 for gypsum, 0.5 for hemihydrate and 0 for anhydrite

The models suggest that the addition of slag favors C-S-H formation over that of ettringite and strätlingite, throughout a wide range of CAC/HH ratio (**Figure 4.12**). This is even more evident in the high-sulfate formulation B-PC for which the model displays a significant proportion of C-S-H along with monosulfoaluminates (Ms) and strätlingite as dominant phases. In the A-PC model, on the other hand, the assemblage is dominated by strätlingite, Ms, and Fe-containing siliceous hydrogarnet. In both formulations, Fe is incorporated in siliceous hydrogarnet and in an Fe-containing Ms (Fe-Ms).

The regions labelled "Ms + Fe-Ms" correspond to the phase "monosulph-AlFe" in the modelling software, GEMS. This phase is comprised of a major component (≈ 99 wt%) Ms, $C_4A\$H_{12}$, and a minor component (≈ 1 wt%) Fe-Ms, $C_4(A,F)\$H_{12}$. In the latter, the solid solution allows a variation of the Al/(Al+Fe) ratio between 0 and 0.45. The stability of this phase is described in detail in Dilnesa *et al*., 2011 [132]. As this phase was not suggested to form in the previous models for the binary CAC-HH systems (Chapter 3), its formation is likely associated to the increased in Ms (**Equation 4.2**) and strätlingite (**Equation 4.3**) proportions resulting from the instability of CH and gibbsite with the addition PC. In addition, minor amounts of calcite and O-H hydrotalcite were consistently present throughout the range to accommodate the C and Mg, respectively, coming from the PC.

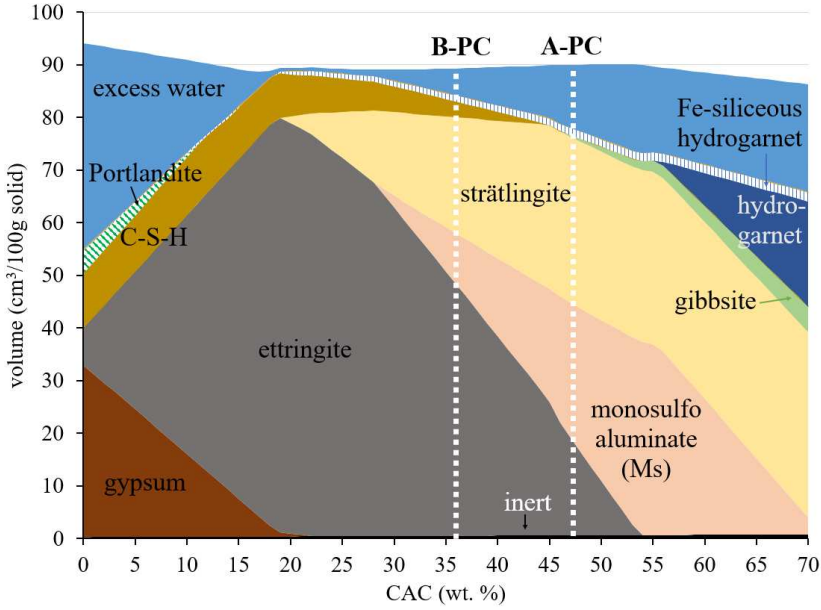

Figure 4.13 *Composition by volume of the reference (no slag) ternary binder with varying CAC and HH proportions simulated from GEMS.*

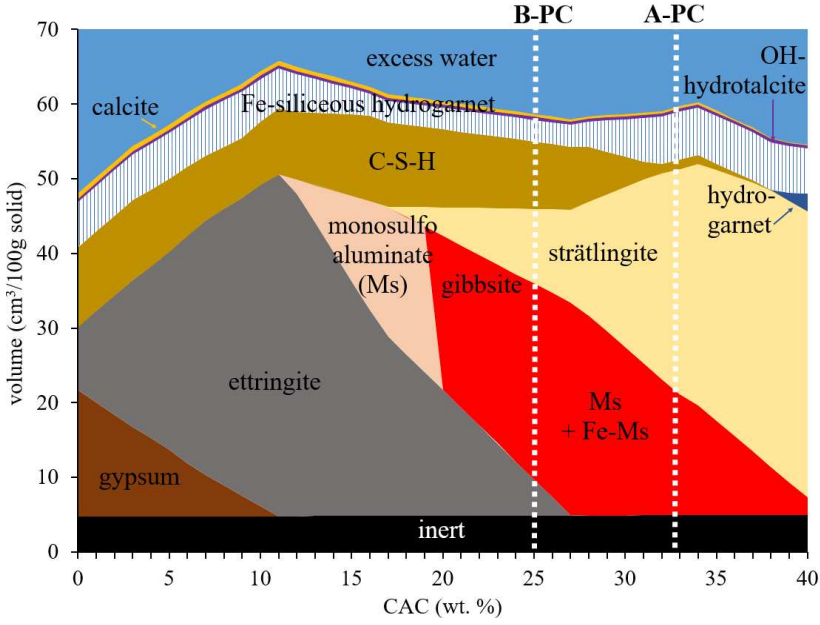

Figure 4.14 *Composition by volume of the ternary binder incorporating 30 wt% slag and 30 wt% PC with varying CAC and HH proportions calculated from GEMS.*

In terms of volumetric composition (**Figure 4.14**), the maximum total solid volume coincides with the peak of ettringite formation at around 11 wt% CAC – 29 wt% HH. This is explained by the expansive behavior of the low-density hydrate ettringite, previously described in section 1.2.2. The huge difference between the total solid volume of the reference (**Figure 4.13**) and the slag-containing (**Figure 4.14**) formulations, can explain the excessive expansion observed for the reference mortars in section 4.1.

On the other hand, there is only a slight difference in the total solid volume between formulations A-PC and B-PC, with the former being slightly more expansive according to the model. This is in contrary to the more extensive expansion observed experimentally in formulation B-PC. This suggests that the model does not entirely reflect the actual phase assemblage obtained experimentally. This could be similar to the observed deviation in the models for formulation A and B in Chapter 3. It is important to reiterate that the GEMS models presented here do not consider the kinetics of hydration. In particular, the phase assemblage shown are the thermodynamically stable phases in equilibrium state (given an infinite reaction time). For this reason, the possibility of eventual conversion, after long hydration ages, into more closely resembling these modelled phase assemblages could not be excluded.

4.3.2. Early hydration reactions

The heat flow and cumulative heat release curves of the two ternary binders are shown in **Figure 4.15** and **Figure 4.16**, respectively.

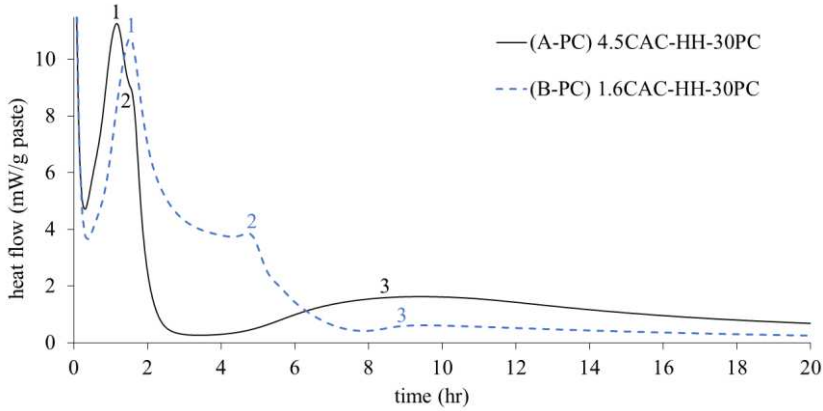

Figure 4.15 *Heat flow measured ex-situ using isothermal calorimetry for A-PC (solid black curve) and B-PC (dotted blue curve) pastes*

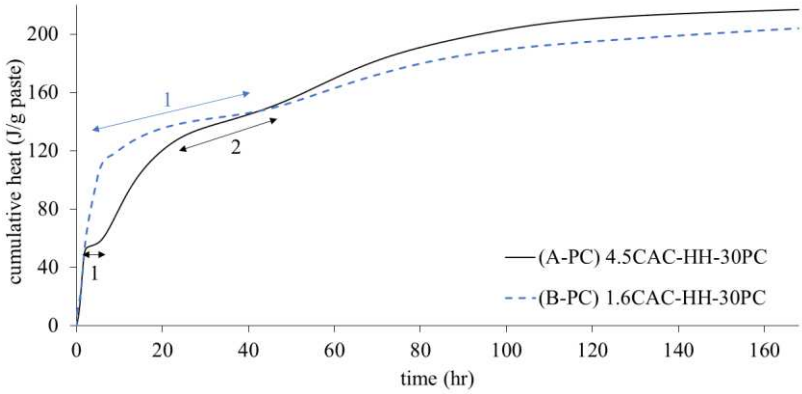

Figure 4.16 *Cumulative heat release measured using isothermal calorimetry*

With the addition of PC in the system, it became more difficult to associate each exothermic peak to a single hydration reaction, as opposed to formulations A and B in the preceding chapter. Nevertheless, three main peaks are recognizable in both formulations which likely correspond to the main peaks identified in CAC-HH-slag binders in section 3.3.

The fast dissolution of several anhydrous phases, principally the HH, in the first two hours of hydration is marked by the first exothermic peaks in both formulations. During the first six hours, extensive ettringite formation is anticipated in these systems supported by the expansive property previously observed in mortar samples. Consequently, it can be deduced that the second exothermic peak is primarily linked to ettringite formation. Afterwards, the formation of AFm phases follows as the sulfates are depleted, particularly in A-PC, possibly constituting the third exothermic peak. Approximately during the same period, the PC components react in parallel, liberating Ca^{2+} ions, subsequently raising the pH of the pore solution. Silicates from the PC also contribute to the formation of hydrate phases, C-S-H and strätlingite, later in the hydration.

In similar ternary binders, CAC hydration is believed to delay the hydration of PC through the mechanism of ettringite barrier formation [86]. It is proposed that ettringite, resulting from the reaction of CA and calcium sulfate, forms a film-like layer around the anhydrous grains provisionally delaying silicates (mainly C_3S and C_2S) hydration. This retardation in the diffusion process could be associated to the momentary plateaus marked (1 and 2) in the cumulative heat release curves (**Figure 4.16**). The reaction occurs in multiple stages and the heat release is resumed when the barrier layers are broken with the destabilization of ettringite.

Despite the differences in the heat release curves (**Figure 4.15**) between formulations A-PC and B-PC, their cumulative heat release beyond 40 hours remain comparable. This observation is consistent with the trends observed between the low (A) and high (B) sulfate systems in the binary blends in Chapter 3.

4.3.3. Long term hydration

The addition of the PC in the system clearly modified the phase assemblage formed after hydration looking at the XRD, TGA and ATR-FTIR results presented in this section. The interpretation of the trends was guided by the characterization of pure PC paste, hydrated in the same conditions as the A-PC and B-PC samples, with results presented in Appendix K.

Consistent with thermodynamic modelling, strätlingite appears to take a major proportion of formulation A-PC's hydrate phase assemblage with well-defined diffraction peaks at $2\theta = 7°$ and 21.2° (**Figure 4.17**). The signature of Si-O-Al asymmetric stretching band at 710 cm^{-1} (**Figure 4.20**) associated with strätlingite is also exclusively present in this formulation affirming the significant difference in the quantity of strätlingite between the low- and high-sulfate blends. Although barely noticeable at a quick glance, changes in the phase assemblage are generally more pronounced between 7 and 28 days for formulation A-PC. These include the variations in the AFm peaks between 2θ values of 10-11° along with calcite formation (29.5°) in XRD (**Figure 4.17**); and the increasing amount of C-S-H as a bump below 100°C forms in the DTG profile (**Figure 4.19**) between 7 and 28 days. The increase in AFm phases could be related to the conversion of ettringite to monosulfoaluminate as the sulfate is depleted in this low-sulfate blend. On the other hand, the delayed hydration of PC previously suggested by the cumulative heat release curve could explain the increase in C-S-H at later ages. The sharp peak majorly associated to calcite could be a result of carbonation during sample preparation.

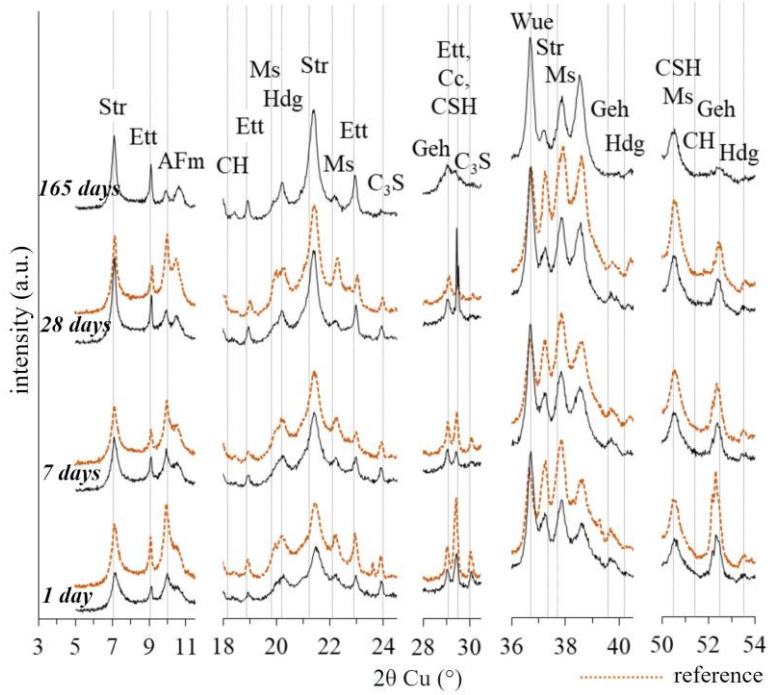

Figure 4.17 *XRD patterns of formulation A-PC (solid black lines) and its reference. Phases are abbreviated as follows: (Str) strätlingite, (Ett) ettringite, (Ms) monosulfoaluminate, (Geh) gehlenite, (Cc) calcite, (CSH) C-S-H, (CH) Portlandite, (Hdg) hydrogarnet and (Wue) wüstite. Note that some of the phases are indicated only to mark the position of their main peaks, despite their absence in the phase assemblage*

Despite the variations mentioned above, there was no drastic change in the phase assemblage nor was there an appearance of new peaks that could be directly associated to the hydration products of the slag in A-PC. Only 14 % of the slag has reacted after 28 days according to the XCT results (**Figure 4.10**). This is likewise reflected through the stable ATR-FTIR spectra over time (**Figure 4.20**) for this formulation. On the contrary, the changes in formulation B-PC, which contains higher amount of sulfates, are more apparent particularly between 1 and 7 days. The actual phase assemblage also appears to be ettringite-rich, in contrary to the thermodynamically-predicted system rich in monosulfoaluminates. This could be explained by the lower slag reaction in the real system yielding an assemblage closer to what was observed for the reference formulation. Nonetheless, the model was able to predict the instability of CH and gibbsite in these systems.

Strong ettringite peaks from the XRD patterns (**Figure 4.18**) alone are clearly evident, primarily resulting from the fast hydration of CA (from the CAC) and calcium sulfate (from the HH). The ettringite formed appears to

be generally stable throughout the curing period. Strätlingite forms between 1 and 7 days marked by the appearance of XRD peaks at 7° and 21.2° for the slag-containing formulation. In the same period, drastic changes in the XRD pattern between 28°-30° where several silicate phases coincide, is noted. These changes could be relevant to slag reactivity considering the findings in section 3.3, indicating the effect of the added silicates from the slag to the formation of strätlingite and subsequently, the reduced consumption of gehlenite from the CAC.

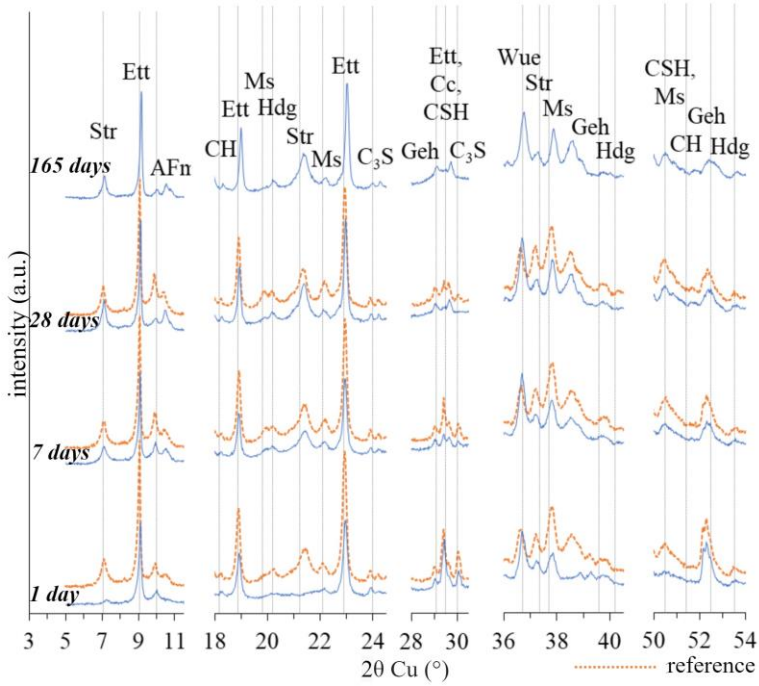

Figure 4.18 *XRD patterns of formulation B-PC (solid blue lines) and its reference. Phases are abbreviated as follows: (Ett) ettringite, (AFm) AFm, (Ms) monosulfoaluminate, (Gib) gibbsite, (Geh) gehlenite, (Gyp) gypsum and (Wue) wüstite.*

Similar to the observation in formulation A-PC, the formation of C-S-H in B-PC is indicated by the peak shift in DTG (**Figure 4.19**) resulting to distinct ettringite (≈ 140°C) and C-S-H (90-140°C) peaks at 165 days. Note that this distinction was guided by the DTG curves obtained from pure PC systems presented in Appendix K which delineates the ettringite and C-S-H peaks, accordingly.

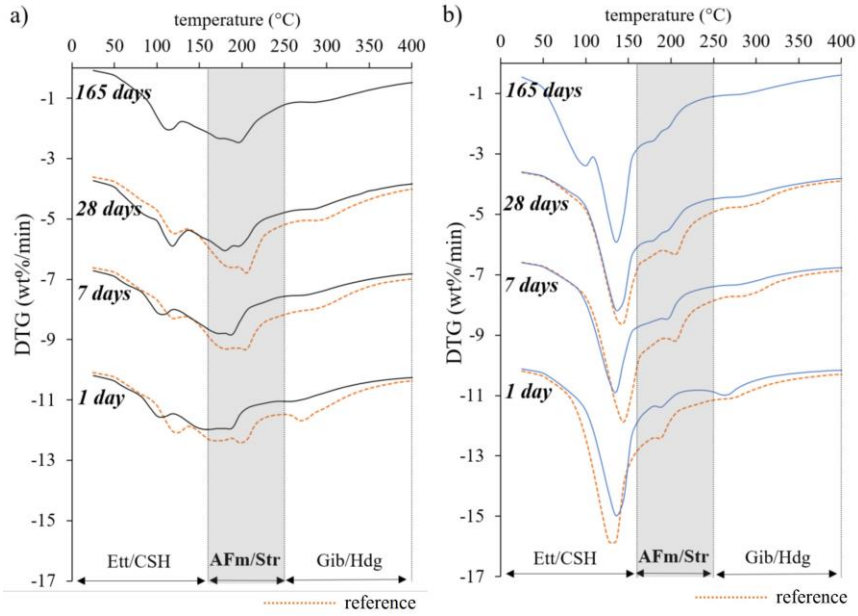

Figure 4.19 *DTG curves of (a) formulation A-PC and (b) formulation B-PC along with their corresponding references. Slag-containing formulations are shown in solid lines. Phases are abbreviated as follows: (Ett) ettringite, (CSH) C-S-H, (AFm) AFm, (Str) strätlingite, (Gib) gibbsite, (Hdg) hydrogarnet*

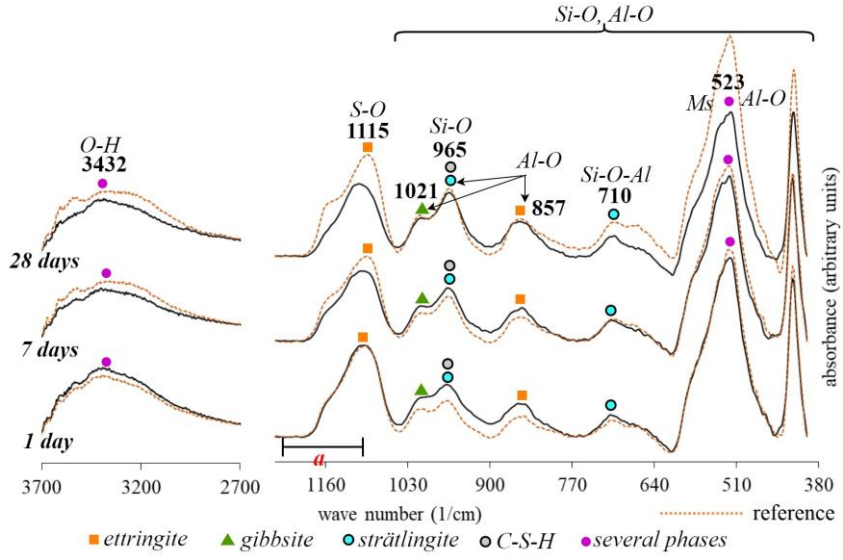

Figure 4.20 *ATR-FTIR spectra of formulation A-PC (solid black lines) and its reference. The designation "several phases" correspond to the combination of all other hydrate phases identified.*

The ATR-FTIR spectra of formulation B-PC (**Figure 4.21**) are dominated by the asymmetric stretching band of S-O for ettringite (and minimally for C-S-H) at 1115 cm^{-1}. Moreover, an additional contributor to the 965 cm^{-1} peak for both the PC-containing formulations is the Si-O-Si stretching vibration band assigned to C-S-H. This coincides with the previously observed Al-O vibration band in the binary systems. Overall, the phase assemblages deduced from these spectra are generally consistent with those identified according to the XRD and DTG patterns, as follows:

- **A-PC**: dominated by strätlingite and monosulfate; with minor amount of C-S-H
- **B-PC**: dominated by ettringite; with strätlingite content increasing over time; minor C-S-H content

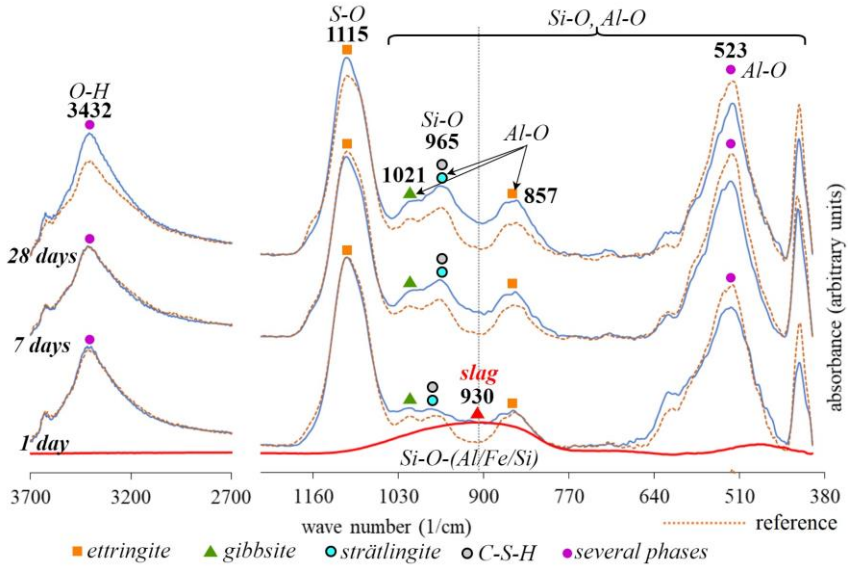

Figure 4.21 *ATR-FTIR spectra of formulation B-PC (solid blue lines) and its reference. The designation "several phases" correspond to the combination of all other hydrate phases identified.*

Table 4.1 *FTIR band assignments based on the distinct spectral peaks observed*

Bond	Primary contributor	Wavenumber (cm^{-1})	Reference
O-H	Ms/Ett/Str	3432	Horgnies *et al.*, 2013 [137]
		1660	Horgnies *et al.*, 2013 [137]
S-O	Ett/Ms	1115	Horgnies *et al.*, 2013 [137]
Si-O-Al	Str	1150	Okoronkwo and Glasser , 2016 [165]
		710	Zapanta *et al.*, 2020 [171]

Si-O	C-S-H	965	Guan *et al.,* 2013 [200]
	anhydrous silicates	521	Torréns-Martin *et al.,* 2013 [86]
Al-O	Gib	1021	Schroeder, 2002 [172]
		972	Schroeder, 2002 [172]
		751	Schroeder, 2002 [172]
	Str	965	Okoronkwo and Glasser, 2016 [165]
	Hdg	810	Horgnies *et al.,* 2013 [137]
	Ett	857	Horgnies *et al.,* 2013 [137]
	Gib/Ms/Str/Hdg	523-537	Horgnies *et al.,* 2013 [137]
	Hdg	521	Torréns-Martin *et al.,* 2013 [86]

Having estimated the highest slag hydration degree using XCT for B-PC as against all the other formulations studied, the ATR-FTIR spectrum of the raw slag is superimposed to that of formulation B-PC at 1 day in **Figure 4.21**. The intensity of the slag's spectrum (in solid red line) was fitted to that of the B-PC in order to estimate the possible contribution of the unreacted slag to the peak intensities of the hydrated blends. The unadjusted spectrum of the raw slag was previously presented in **Figure 2.13**. Notice that the Si-O asymmetric stretching band of the raw slag at around 930 cm^{-1} coincided with the region (between 857 and 965 cm^{-1}) where the difference between the spectra of the reference and the slag-containing formulations are observed at 1 day. Assuming that the slag has barely reacted at this period, it could be assumed that the raw slag is contributing to the spectrum of the blend in a similar manner to the one illustrated.

In section 1.4.3, it was highlighted that an evidence of slag reactivity was depicted in Siakati *et al*., 2020 [117] principally through peak shift of the Si-O asymmetric stretching band (700-1200 cm^{-1}) towards a higher wavenumber. The disappearance of the gaps (red double arrows) in the superimposed spectra in **Figure 4.22** could be interpreted as a possible consequence of a similar peak displacement towards the higher wavenumber, causing the unreacted slag peaks to be concealed in the adjacent areas. Although this could have been accompanied by a shift of the Si-O rocking band (400-500 cm^{-1}) towards a lower wavenumber, it could not be clearly distinguished due to the very weak intensity of the second peak after the dilution in the blend.

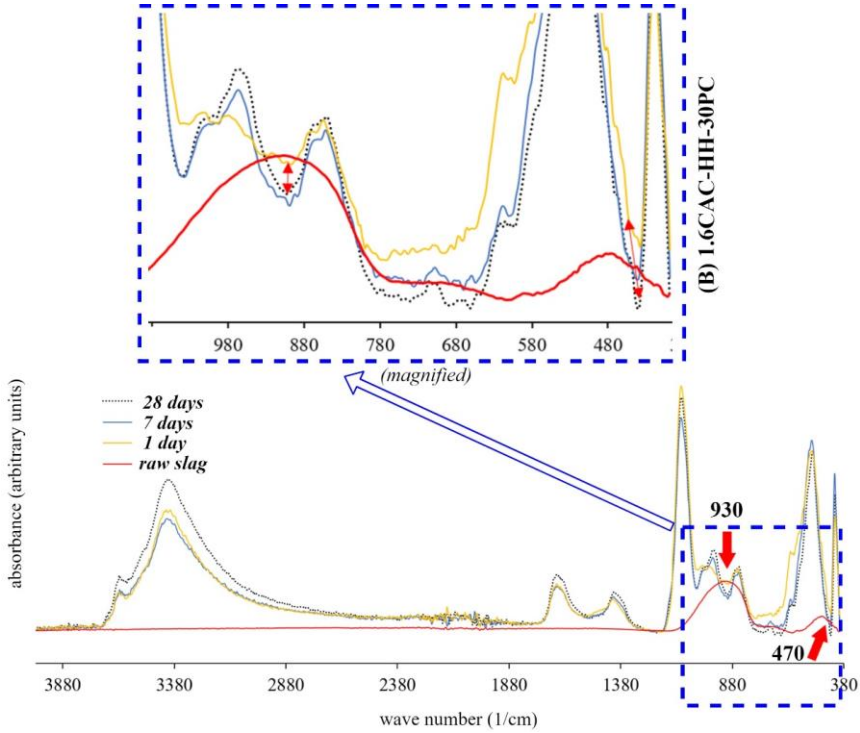

Figure 4.22 *Superimposed ATR-FTIR spectra of the raw slag (red) to those of the B-PC at different curing times. It aims to highlight how the gaps formed over time (red double arrows), could be an evidence of the proposed peak-displacement scenario signifying slag hydration.*

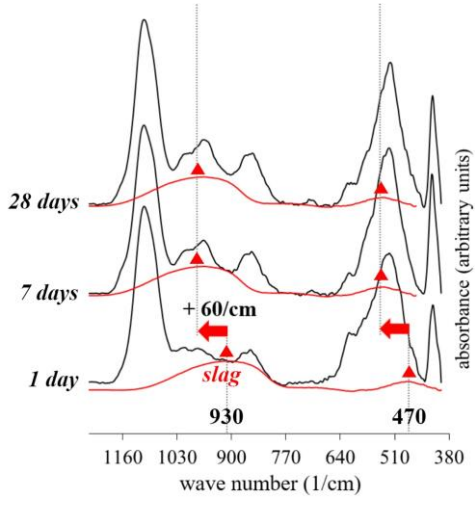

Figure 4.23 *Raw slag's ATR-FTIR spectrum superimposed to that of the B-PC to demonstrate a possible configuration of reactivity-related peak shift*

A hypothetical scenario demonstrating the possible peak shift is illustrated in **Figure 4.23** for formulation B-PC where the highest degree of slag hydration after 28 days was observed. Between 1 and 7 days, a 60 cm^{-1} shift towards a higher wavenumber is presumed to allow the slag spectra to fit into that of the blend. This fitting could be more relevant if the intensity of the slag's contribution remained relatively consistent throughout the hydration period considering its expected poor reactivity during the first 7 days.

To reiterate, such a peak shift has been previously linked [116,117] to the partial oxidation of Fe^{2+} to Fe^{3+} accompanying the change in the overall atomic environment of Fe during polymerization. For the cement blends investigated in this study, this could correspond to the formation of Fe-containing hydrates, such as those suggested by the thermodynamic models or those previously detected in Chapter 3. Similar to the binary systems (formulations A and B), most of the discernible changes were concentrated in the Si-O and Al-O regions particularly between 857 cm^{-1} and 1021 cm^{-1} coincident with the dominant peak of the raw slag. This could indirectly support the role of the slag's dissolution in altering the hydrate phase assemblage.

Although the evolution of the phase assemblages over time observed from the ATR-FTIR followed the trend of those from XRD and TGA, it can be said that the results obtained did not particularly contribute to a clearer understanding of the slag's hydration mechanism. This was similarly noted for the ATR-FTIR results obtained in Chapter 3. The demonstrated peak shift in **Figure 4.23** remains hypothetical and further tests ideally using less complex cement systems or even synthetic systems are recommended to confirm the proposed fitting. Nevertheless, this technique could be considered as an alternative or exploratory step to XRD and TGA, for a rapid (2 min) non-destructive testing when a limited (0.05-0.1 g) amount of sample is available.

Lastly, the total bound water contents of the ternary binders, A-PC and B-PC, were plotted together with their respective references in **Figure 4.24**. Overall, the higher bound water contents of the reference formulations confirm the prediction from the thermodynamic models (section 4.3.1) where a higher total mass of hydrates is estimated to form relative to the slag-containing pastes. Furthermore, the late reaction of the slag (versus the cement components) is reflected through the differences in the increments of the values. The reference formulations appear to have obtained their maximum hydration earlier on followed by only minimal increase in the total bound water content. Whereas the slag-containing formulations displayed more significant increments per curing time. The drastic increase in the bound water content of formulation B-PC between

28 days (34 g) and 165 days (47 g) is in agreement with the slag hydration degree quantified though XCT, discussed earlier in section 4.2. For this reason, a greater focus is dedicated on this formulation in the subsequent sections for the investigation on the fate of Fe particularly between 28 to 165 days of curing.

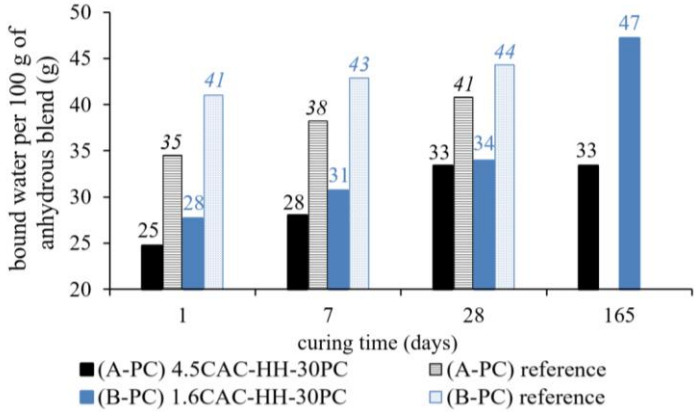

Figure 4.24 *Total bound water content of formulations A-PC, B-PC and their references*

4.4. The fate of Fe during hydration

In this section, the fate of Fe, the main component of the slag, is investigated through TEM, STEM and Mössbauer spectroscopy. These advanced techniques proved to be essential in elucidating a better understanding of the hydration mechanism of the slag in Chapter 3. With the addition of the PC, the phase assemblages of the ternary (CAC-HH-PC) systems have evidently changed compared to those of the binary (CAC-HH) systems. PC contributed Ca and Si components leading to the more extensive strätlingite formation and C-S-H generation, while increasing the alkalinity of the system, and thereby influencing slag dissolution.

Although the characterization techniques in the previous section were able to describe the general phase assemblage of formulations A-PC and B-PC, no clear indication was derived as to the fate of Fe upon slag dissolution. The formation of Fe-containing hydrogarnet and/or monosulfoaluminates, as predicted from thermodynamic modelling, could not be confirmed from XRD, TGA nor FTIR alone due to the complexity of the systems with overlapping signatures. Neither can the formation of similar Fe-containing hydrated gels, as those observed in the binary systems in Chapter 3, could be confirmed mainly due to their poor crystallinity. Analyses through

TEM, STEM and Mössbauer spectroscopy in the subsequent sections are expected to provide more information on the nature of the hydrated phase/s incorporating Fe.

4.4.1. TEM

The general phase assemblage of formulation A-PC is reflected in the TEM images shown in **Figure 4.25** and **Figure 4.26**. In these images, the abundance of strätlingite is apparent with its distinct plate-like morphology and siliceous composition marked in blue. Most of the particles are agglomerated in **Figure 4.25** a and b, making it difficult for them to be analyzed individually.

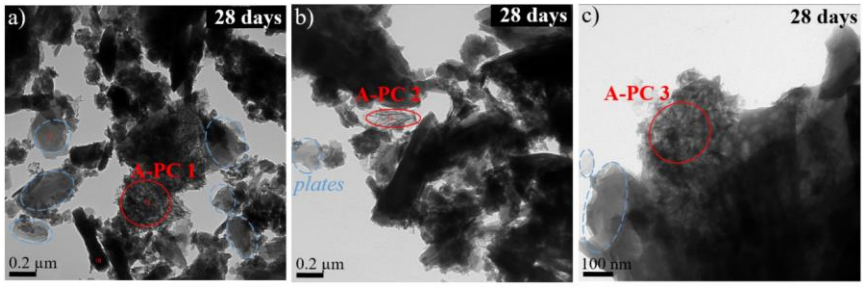

(A-PC) 4.5CAC-HH-30PC_28 days

At. %	Fe	Ca	Al	Si	S	Mg	K + Na	O	Sum
A-PC 1	10.2	16.2	7.7	16.8	0.8	5.5	0.5	42.4	100.0
A-PC 2	3.0	17.9	6.3	14.1	0.5	0.3	0.5	57.5	100.0
A-PC 3	3.3	17.1	12.2	10.3	3.6	9.6	0.6	43.3	100.0

Figure 4.25 *TEM images and the atomic composition of marked areas in the (A-PC)*

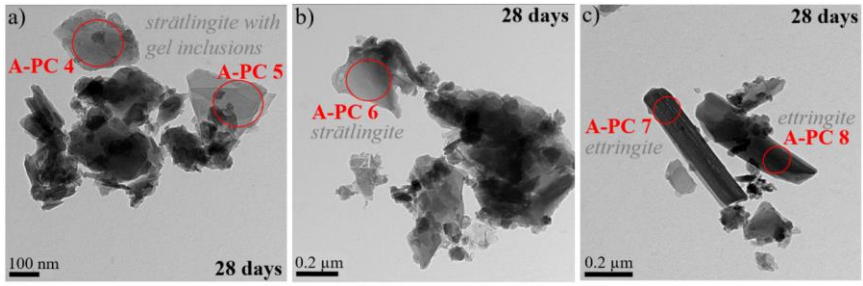

(A-PC) 4.5CAC-HH-30PC_28 days

At. %	Fe	Ca	Al	Si	S	Mg	K + Na	O	Sum
A-PC 4	0.8	18.2	16.7	8.8	0.6	0.3	0.6	54.1	100.0
A-PC 5	1.0	16.7	16.1	8.9	0.5	0.7	0.5	55.7	100.0
A-PC 6	0.5	16.2	16.9	7.7	1.3	0.0	0.5	57.0	100.0
A-PC 7	0.2	30.5	10.7	1.0	7.3	0.1	0.6	49.7	100.0
A-PC 8	0.2	29.8	9.2	1.2	7.8	0.0	0.8	51.1	100.0

Figure 4.26 *TEM images and the atomic composition of marked areas in the (A-PC) 4.5CAC-HH-30PC paste sample after 28 days of hydration*

Significant amounts of hydrated gels are also detected throughout the samples exhibiting a combination of foil-like or fibrous (i.e., A-PC 1-3) and granular (B-PC 1, 3 and 6) morphologies. Similar forms have been previously observed for C-S-H morphologies according to the investigation in Techer *et al.,* 2012 [201]. Having detected Ca, Al, and Si in these hydrated gels, it is convenient to associate them to C-S-H at first glance. The selected electron diffraction pattern for B-PC 1 (**Figure 4.27**) also confirmed the poorly-crystalline to amorphous nature of this phase with the absence of clear diffraction spots. However, compared to C-S-H, the Al estimated was significantly higher depicted in the ternary diagram (**Figure 4.32**).

No significant amount of Fe was detected in the crystalline hydrate phases such as in strätlingite (i.e., A-PC 4-6), nor in ettringite (i.e., A-PC 7-8) even in the high calcium sulfate system (i.e., B-PC 14, **Figure 4.28**). This is consistent with the findings from the binary system in Chapter 3. Less than 1 at% of Fe was estimated in all these phases (**Figure 4.26** and **Figure 4.28**), which could well fall within the analytical sensitivity of the device or could be influenced by the hydrated gels superimposed within the target area. In addition, monosulfoaluminates and siliceous hydrogarnet predicted to incorporate Fe based on thermodynamic modelling, could not be clearly identified from the TEM results.

Instead, Fe was detected in the hydrated gels rich in Ca, Si and Al. The addition of PC appeared to have altered the composition of these Fe-containing hydrates as opposed to the Al-rich gels previously observed in the binary systems. It is postulated that the kinetics of hydration hindered the incorporation of Fe in the crystalline phases considering their relatively faster formation and stability early in the hydration. Whereas Fe is released slowly as the slag dissolves over time.

Some of the TEM images of formulation B-PC after 28 and 150 days of curing are presented in **Figure 4.27** and **Figure 4.28**, respectively. As expected, less particles with plate-like morphology (encircled in blue) mainly associated to strätlingite due their silicates content, were observed. Instead, more ettringite rods (marked in orange) were present as a consequence of higher amount of sulfate in this formulation. In the first 28 days of curing, the Fe content in the intermixed Ca-Al-Si rich hydrated gels was mostly limited to < 4 at%. The diffraction pattern of B-PC 1 demonstrates the amorphous nature of the phase. Similar to the Al-rich gels in the binary blends in Chapter 3, these hydrated gels exhibit inconsistent thickness with certain regions appearing to be darker in the images than the rest of the matrix (i.e., B-PC 3). For this reason, the possibility of nano-crystals inclusion comparable to what was presented in the binary systems

could not be excluded. In addition, the Fe-containing gels also displayed high sensitivity to the analysis and were easily disintegrated after the scans, similar to what was demonstrated in section 3.4.1. This is critical to take into consideration when interpreting the variation in the chemical composition of the gels. When disintegrated, it is possible that certain components have been volatilized resulting in their reduced atomic percentage.

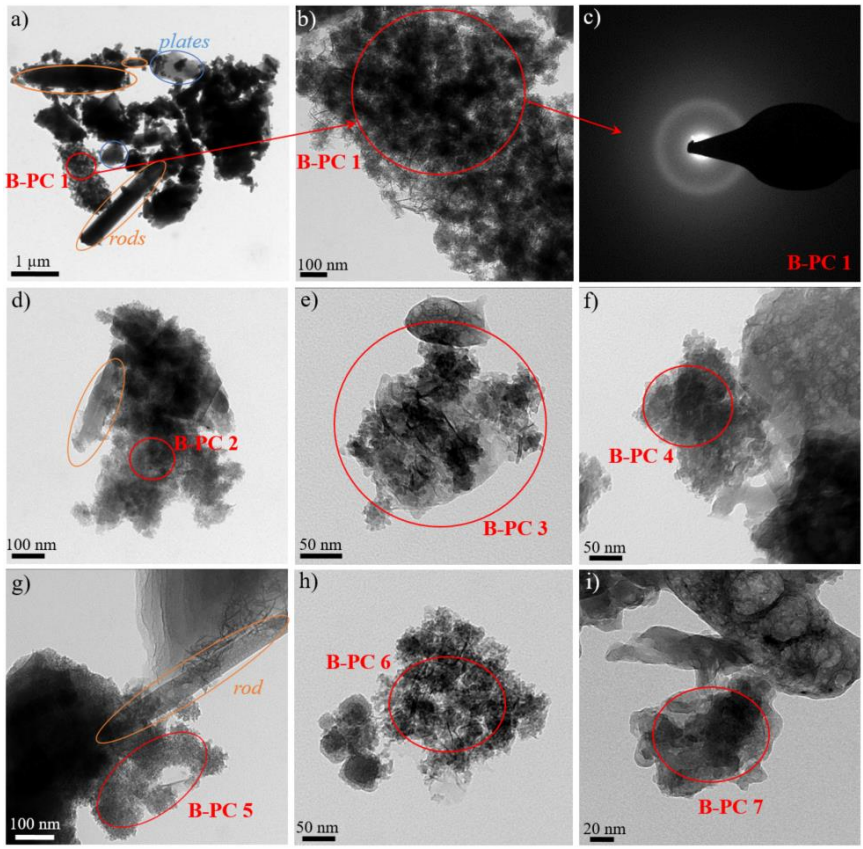

(B-PC) 1.6CAC-HH-30PC_28 days

At. %	Fe	Ca	Al	Si	S	Mg	K + Na	O	Sum
B-PC 1	3.2	10.4	6.6	8.6	0.3	–	–	70.9	100.0
B-PC 2	2.9	11.0	9.2	10.4	0.2	–	–	66.2	100.0
B-PC 3	2.0	9.1	10.5	8.2	0.2	–	–	70.0	100.0
B-PC 4	2.2	9.8	4.4	6.6	0.2	–	–	76.8	100.0
B-PC 5	2.5	9.1	3.0	5.9	0.2	–	–	79.4	100.0
B-PC 6	3.3	15.3	5.4	7.6	0.1	–	–	68.3	100.0
B-PC 7	2.4	11.9	4.8	7.0	0.2	–	–	73.7	100.0

Figure 4.27 *TEM images, diffraction pattern and the atomic composition of Fe-containing gels in the (B-PC) 1.6CAC-HH-30PC paste sample after 28 days of hydration*

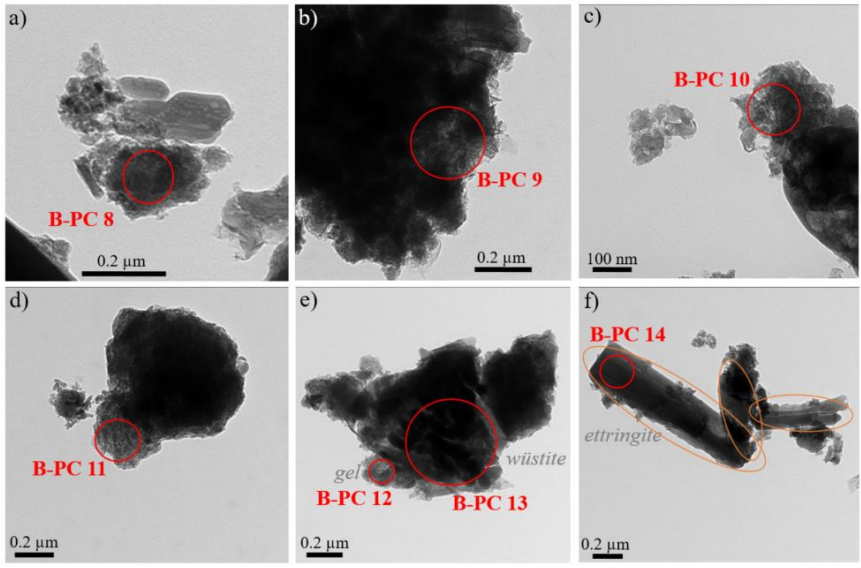

(B-PC) 1.6CAC-HH-30PC_150 days

At. %	Fe	Ca	Al	Si	S	Mg	K + Na	O	Sum
B-PC 8	7.6	17.3	6.6	17.8	0.8	0.4	0.7	48.7	100.0
B-PC 9	3.4	15.6	9.5	9.8	1.2	1.5	1.8	57.3	100.0
B-PC 10	4.4	16.6	8.8	22.6	1.1	0.1	1.3	45.2	100.0
B-PC 11	4.0	11.3	4.1	15.0	0.3	1.9	1.1	62.4	100.0
B-PC 12	2.9	9.9	4.1	16.2	0.5	0.2	0.9	65.3	100.0
B-PC 13	35.1	3.7	3.4	3.2	0.1	1.2	0.4	53.0	100.0
B-PC 14	0.2	24.5	8.1	1.2	6.7	0.0	0.6	58.8	100.0

Figure 4.28 *TEM images and the atomic composition of marked areas in the (B-PC) 1.6CAC-HH-30PC paste sample after 150 days of hydration*

The Fe content after 150 days of curing was generally elevated as the hydrated gels (B-PC 8-11) appear to be thicker in **Figure 4.28**. This was accompanied by an increase in the atomic percentages of Ca and Si almost twice as those obtained for the gels at 28 days. It is probable that the late dissolution of PC and slag contributed to this increase. Since CAC was reacting immediately in the early days of curing, the Al content of the gels remained stable between 28 and 150 days.

Once again, no significant amount of Fe was detected in ettringite (B-PC 14) even after longer curing time. Unreacted wüstite was detected at 150 days (**Figure 4.28** B-PC 13) exhibiting its distinct dendritic morphology. This supports the earlier remark that only the amorphous fraction of the slag is dissolving during the hydration. Adjacent to the Fe-rich wüstite (35 at% Fe in **Figure 4.28** e), a hydrated gel (B-PC 12) with ≈ 3 at% Fe was distinguished with a highly contrasting Fe signal. This demonstrates the precision of the EDS in analyzing different phases on a nano-scale. Although the intermixing of phases due to the complex nature of the

samples could not be completely eliminated, TEM still yielded more precise analysis compared to the SEM used in section 3.2.1.

4.4.2. STEM

In Chapter 3, the elemental maps obtained from STEM demonstrated the non-uniform distribution of Fe in the hydrated gels. It has driven the proposition that there are at least two Fe-containing hydrate phases in the CAC-based systems: (1) an amorphous part with a lower Fe concentration; (2) and an unidentified nano-crystalline phase comprising the darker regions of the gels, with a higher Fe content. Although the TEM results in the preceding section indicated a different composition of the gels in the ternary binders, the inhomogeneity of these gels provided an initial evidence of the possible presence of intermixed phases congruent to the binary systems.

STEM bright field images of a generally homogenous gel (B-PC 15-16) and an intermixed gel (B-PC 17-18) along with their corresponding elemental maps are presented in **Figure 4.29** and **Figure 4.30**, respectively. The uniform distribution of Fe in gels with lower Fe content (< 4 at%) is evident in the maps of **Figure 4.29** a. This clearly confirms that Fe is indeed incorporated in the gels instead of being simply measured from a neighboring unreacted slag particle. On the contrary, Fe was clearly more concentrated in the darker region of the gel in B-PC 17 compared to the B-PC 18 region in **Figure 4.30**. The proportions of Ca, Si and Al remained consistent despite the huge difference in the Fe content.

To further highlight the absence of Fe in the crystalline hydrates, particularly in ettringite (the dominant hydrate phase in B-PC), Fe and S maps of STEM bright field images containing rods of ettringite (B-PC 19 and B-PC 20) are shown in **Figure 4.31**. Both the maps and the EDS analyses confirmed the absence of Fe in ettringite. The rapid formation of ettringite during the first hours of hydration and its stability over time driven by the abundance of sulfate in the system, were assumed to inhibit the incorporation of Fe in this phase.

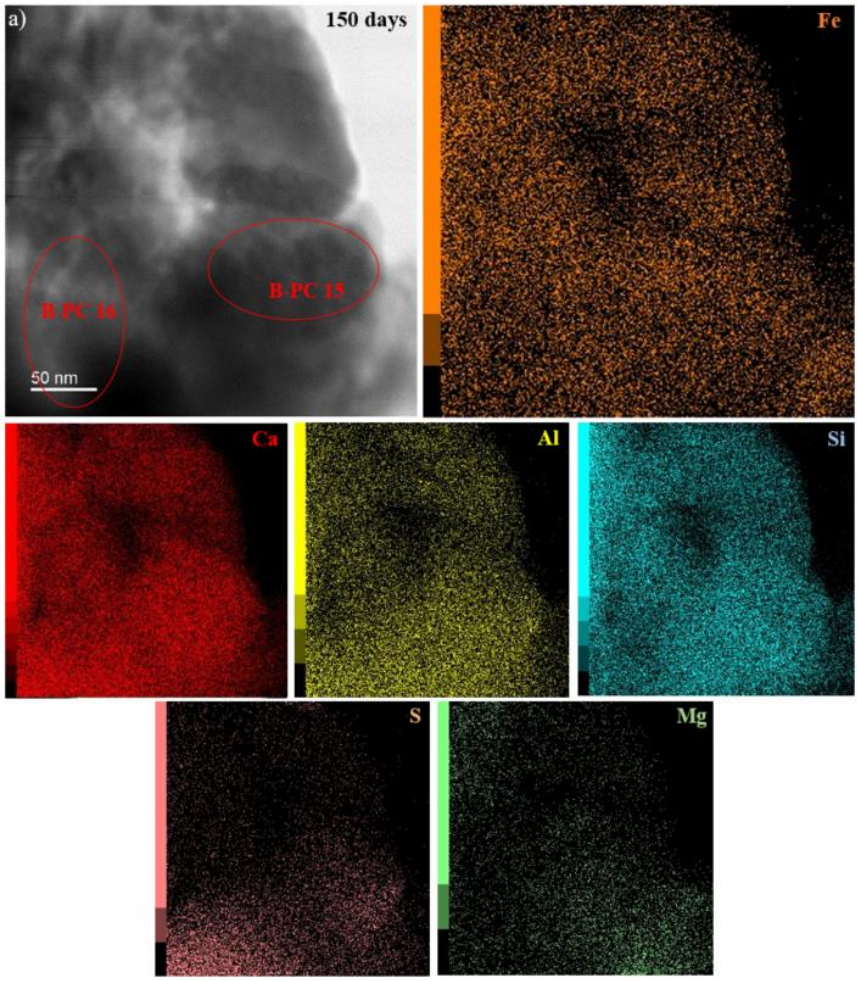

(B-PC) 1.6CAC-HH-30PC_150 days

At. %	Fe	Ca	Al	Si	S	Mg	K + Na	O	Sum
B-PC 15	3.5	18.6	5.4	15.6	1.2	0.9	0.6	54.1	100.0
B-PC 16	3.8	21.2	7.2	14.1	2.5	0.3	0.6	50.2	100.0

Figure 4.29 *STEM elemental mapping of a hydrated gel phase in the (B-PC) 1.6CAC-HH-30PC paste sample after 150 days of curing. In analyzing the STEM elemental maps, note that the color intensities were independent for each element.*

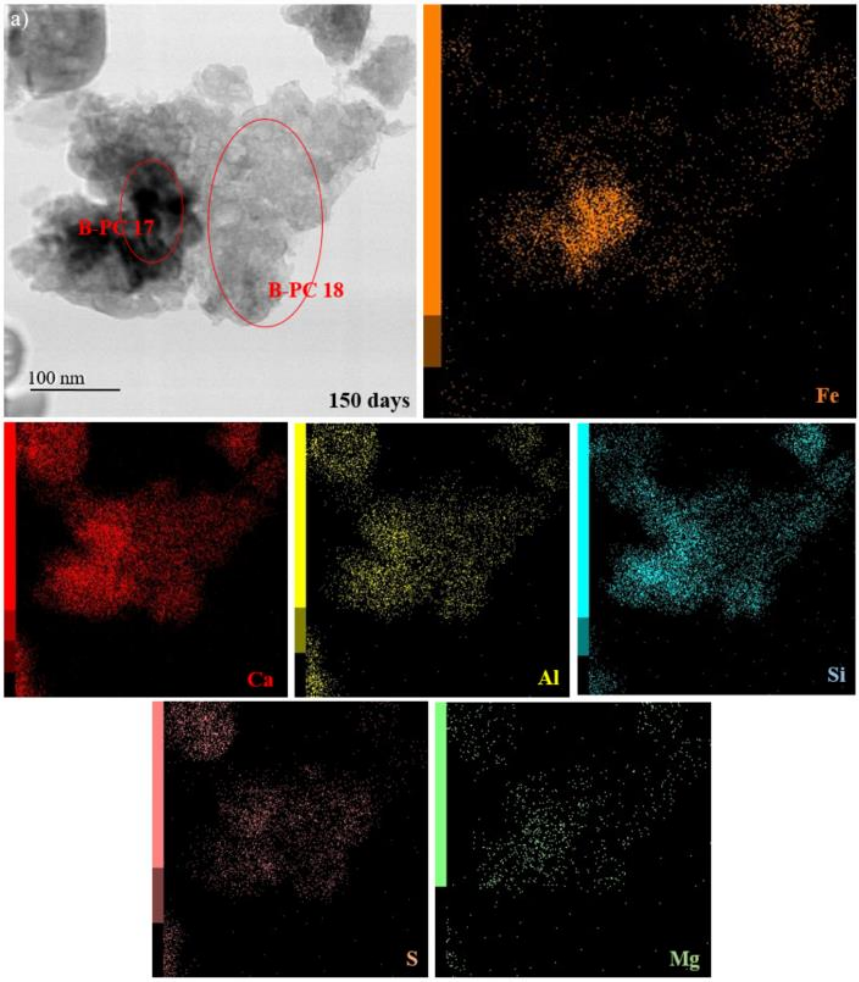

(B-PC) 1.6CAC-HH-30PC_150 days

At. %	Fe	Ca	Al	Si	S	Mg	K + Na	O	Sum
B-PC 17	11.4	14.6	4.7	9.9	2.0	0.6	1.3	55.6	100.0
B-PC 18	1.7	16.5	6.0	11.2	3.7	0.5	1.3	59.2	100.0

Figure 4.30 *STEM elemental mapping for a selected area in the (B-PC) 1.6CAC-HH-30PC paste sample after 150 days of curing.*

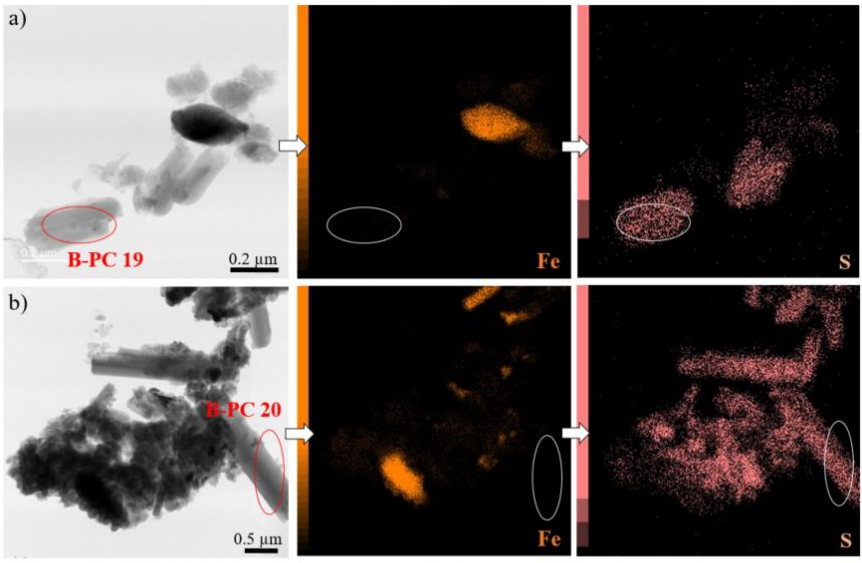

(B-PC) 1.6CAC-HH-30PC_150 days

At. %	Fe	Ca	Al	Si	S	Mg	K + Na	O	Sum
B-PC 19	0.4	19.0	7.0	2.4	7.1	0.0	0.3	63.7	100.0
B-PC 20	<dl	22.6	6.3	2.7	7.2	0.0	<dl	61.2	100.0

Figure 4.31 *STEM images and their corresponding Fe and S maps from (B-PC) 1.6CAC- HH-30PC paste sample after 150 days of curing.*

The composition of the Fe-containing hydrated gels were plotted in a Ca-Si-Al ternary diagram in **Figure 4.32**, following the similar conditions applied to the binary system. Only the gels with 1-12 at% Fe were selected in order to minimize the inclusion of analytical volumes where strong intermixing of phases could influence the composition. Values were also expressed in atomic percentages to reduce errors associated to O quantification in TEM-EDS analyses [178].

The difference in composition of the hydrated gels between the binary (no PC) and ternary (with PC) blends is clearly depicted in **Figure 4.32**, as each system occupies a distinct cluster in the diagram. The hydrated gels in the ternary blends contained considerably lower proportions of Al. Instead, they were enriched in Ca and Si approaching the region between the Si-hydrogarnet and the C-A-S-H region reported in Portland cement systems [202]. As the hydration advanced from 28 to 150 days for formulation B-PC, the TEM results alone appear to suggest the tendency to move towards the region of lower Ca content in the ternary diagram. A relevant trend on decreasing Ca/Si ratio in C-S-H has been previously associated to the addition of siliceous SCM [11,203,204]. This trend could be related to the possible incorporation of Fe in the interlayer of C-A-S-H gels demonstrated in Mancini *et al.,* 2020 [113] using ^{29}Si NMR and XAS

spectroscopy in a co-precipitation experiment. As explained in their study, both Fe^{2+} and Fe^{3+} could compete with Ca^{2+} ions octahedrally-coordinated to the adjacent Si tetrahedra in the interlayer of C-S-H at high Ca/Si ratios (1.2-1.5). This has been demonstrated despite the substantial difference in the ionic radii of these cations (i.e., Ca^{2+} with r= 1.08-1.20 Å; $Fe^{2+/3+}$ with 0.64-0.86 Å), exemplifying the remarkable stoichiometric and structural variability of C-S-H [113,124,205].

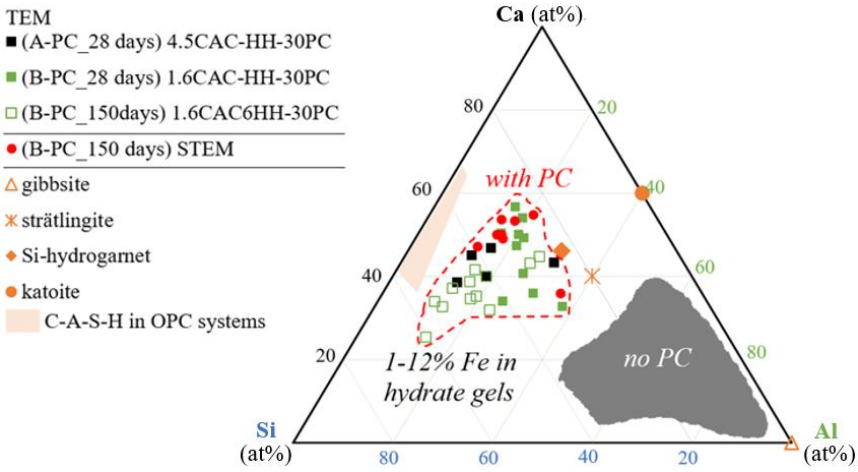

Figure 4.32 *Ternary diagram of Fe-containing hydrated gels with 1-12 at% Fe observed using TEM and STEM. The values were calculated from the Ca, Si and Al atomic composition from EDS analyses normalized to 100 at%. Reference points for, gibbsite, strätlingite, katoite and Si-hydrogarnet were added in the diagram based on their empirical formula while the C-A-S-H region was estimated based on the reported stable composition in Portland cement system [202]. The area covered by the Al-rich gels in chapter 3 is also shown as the "no PC" area in this figure.*

However, additional STEM analyses plotted in **Figure 4.32** suggest instead that the composition of the amorphous gels were rather more consistent over time with Ca/Si ratio between 1.2 and 2.2. The Al content of the gels was also significantly higher compared to the previously obtained [202,205] experimental composition of C-S-H. It is possible that the deviation observed was influenced by the presence of the nano-crystalline phase intermixed with the amorphous hydrated gel. In the end, it is difficult to establish concrete trends as to the changes in the composition of the Fe-bearing hydrated gels over time considering the limited number of data points and the complexity of the system.

The challenge remains when the phases are superimposed or intermixed within the same analytical volume. This would support the importance of working with synthetic systems with less components as a complementary characterization of the Fe-containing hydrated gels to be considered in future works. Nonetheless, demonstrating the fate of Fe using the actual

raw materials has contributed to a critical outlook on an industrial point of view. It is possible that other factors, such as the presence of minor impurities and the kinetics of hydration, could have an impact to the hydration mechanism of the slag causing the difference in the fate of Fe from the collated reports in Chapter 1 on synthetic and modelled systems, versus that in the blends presented in this study.

4.4.3. Mössbauer spectroscopy

Mössbauer spectroscopy was used in the preceding chapter to describe the changes in the oxidation state and the atomic environment of Fe during the slag hydration in binary CAC-HH systems. In addition, a quantification of hydration degree was likewise presented using a fitting model to deconvolute the spectra.

The evolution of the spectra of B-PC paste after 1, 7 and 28 days of hydration is presented in **Figure 4.33**. Note that the focus for further analysis was dedicated to this formulation due to the indication of higher degree of slag hydration from the previously presented results. The spectra of the raw slag and PC are also shown in this figure for reference. Unlike the slow transition observed in the binary systems (section 3.4.3) during the first 28 days, the difference in the spectrum of the raw slag to that of B-PC immediately after 1 day is already remarkable. This could support the faster rate of slag dissolution proposed based on the other techniques highlighting the activating effect of PC addition.

A comparable transition was only observed between 7 and 90 days for the binary systems. The difference in the spectrum could also not be explained simply by the contribution of the Fe from the PC. Not only that this contribution is minimal (1.4 % Fe_2O_3 in pure PC corresponding to only 2.9 % of the total Fe in the blend) to begin with, but it is also clear from **Figure 4.33** that the positions of the PC peaks do not correspond to the main peaks of the hydrated paste. Moreover, the spectrum of B-PC at 1 day closely resembles that of the binary blend (B) at 28 days (**Figure 3.39**), while the B-PC spectrum at 28 days is similar to the binary blend (A) spectrum at 90 days. This further supports the suggested faster kinetics of slag hydration when the PC is added in the system.

The spectrum of the blend at each curing time was deconvoluted following the fitting procedures for Model 1 in section 3.4.3. This model utilizes four Fe components for the unreacted fraction of the blend and two Fe components after hydration. The former consists of two Fe^{2+} doublets (G1 and G2) and one Fe^{3+} doublet (G3) in the glass fraction; and a doublet of Fe^{2+} (M1) for wüstite. On the other hand, the reacted components include a doublet of Fe^{3+} (P1) and Fe^{2+} (P2). In addition, a sextet magnetic

component (M2) was used only for the raw slag fitting. The modeled spectrum of the B-PC paste after 28 days is shown in **Figure 4.34**.

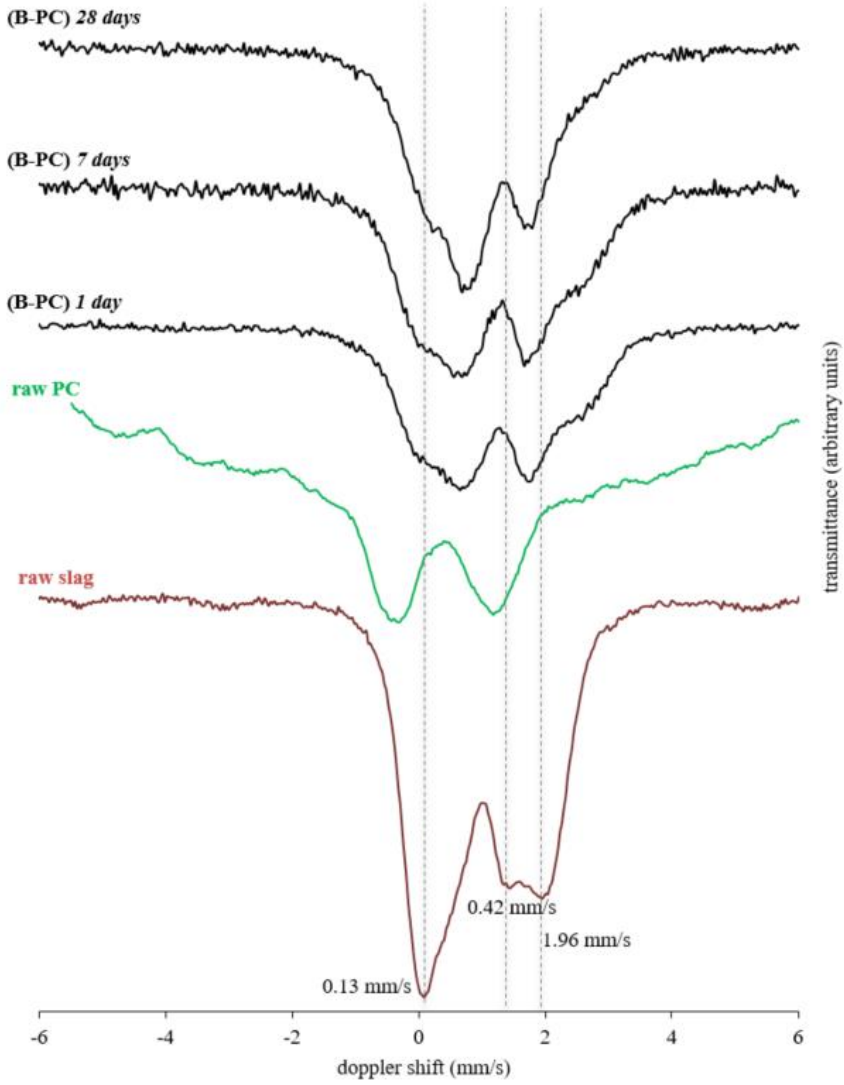

Figure 4.33 *^{57}Fe Mössbauer spectrum evolution of formulation B-PC after 28 days along with the spectra of the raw slag and the raw PC used in the formulations. Running average per 10 data points was used to fit a curve for the PC spectrum (section 2.2.5) in order to minimize the noisy signature resulting from its low (1.4% Fe_2O_3) Fe content.*

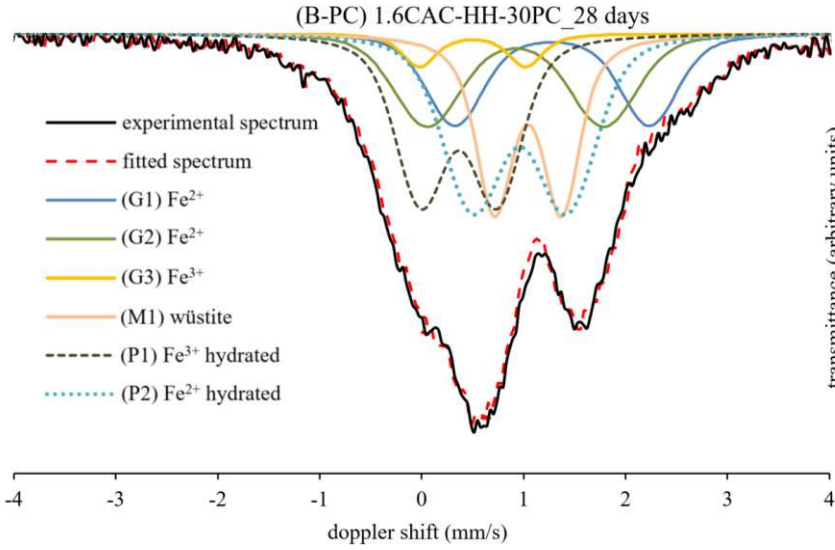

Figure 4.34 *^{57}Fe Mössbauer spectrum of formulation B-PC at 28 days and its deconvoluted components*

The absorption areas (AA) obtained from the fitted models at different curing time are presented in **Figure 4.35**. Using the same equation elaborated in Appendix J, the degree of slag hydration was estimated based on the changes in the sum of the AA of the unreacted slag components. The results of this estimation is presented in **Figure 4.36**.

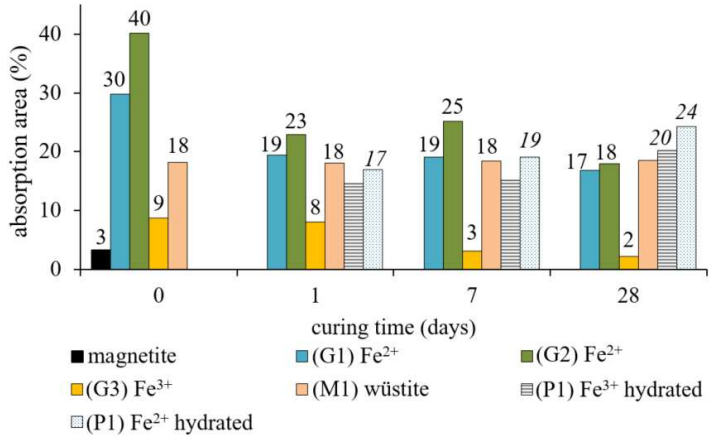

Figure 4.35 *Evolution of B-PC absorption areas (AA) calculated based on the models. Values at 0 day corresponds to the fitting of the raw slag.*

The results confirm the earlier remark on the resemblance of the B-PC spectrum at 28 days (with 42 % slag hydration degree) to that of the A spectrum at 90 days (with 48 % slag hydration degree). The slower

increase in the values between 1 and 28 days relative to the trend for the binary systems in section 3.4.3 suggests that a similar extent of dissolution was achieved faster in the ternary blends with PC. This is evident from the steep slope between 0 and 1 day in **Figure 4.36**.

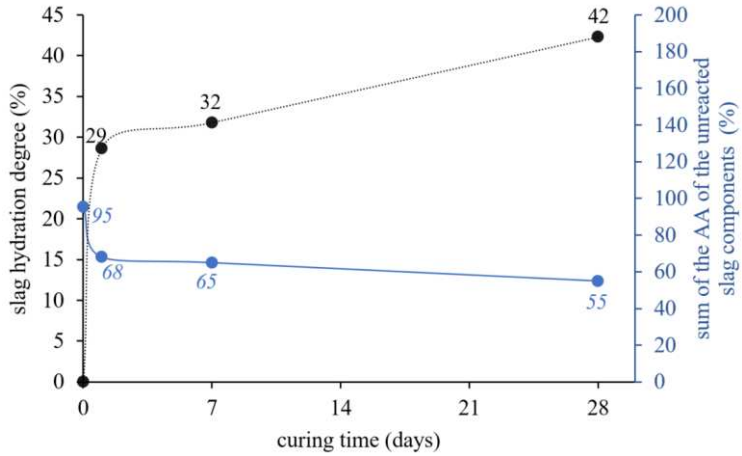

Figure 4.36 *Slag hydration degree of formulation B-PC (primary axis) estimated based on the changes in the total absorption areas (secondary axis) of the unreacted slag*

Nonetheless, it is important to remark the huge difference in the slag hydration degree values obtained from this estimation compared to those from the XCT in section 4.2. As mentioned for binary systems, underestimation from XCT could be linked to two main factors: (1) the assumption that the slag is completely unreactive in the first 24 hours of hydration; and (2) the 2.15 µm voxel resolution setting which excluded the contribution of the finer slag particles. This could be addressed in the future works by performing faster scans immediately after the paste hardens and several others within the first 24 hours of curing. Sensitivity analysis on the voxel resolution setting could also be performed in order to quantify the influence of this factor to the estimation.

Finally, the components of the fitting procedure followed for the Mössbauer spectroscopy could be further refined and adapted for the ternary systems. Although Fe was detected in intermixed hydrated gels in both the binary and ternary systems, the difference in their compositions merits a re-evaluation of the fitted components, P1 and P2. Further characterization preferably using synthetic systems with less components will be a critical prerequisite in identifying the better adapted components for the re-evaluation.

Conclusion

This chapter demonstrated the reactivity of the slag in ternary CAC-HH-PC systems. The binders exhibited an expansive nature, particularly those of formulation B-PC which had the higher sulfate content. In comparison to the reference mortars, the addition of the slag proved to be beneficial in mitigating excessive expansion such that macro cracks and consequently the decrease in mechanical strength were avoided even when the mortars were cured under water. In addition, promising SAI values (>1) exceeding those obtained in the binary system were achieved. High compressive strengths at around 20 MPa were obtained at 1 day, which increased to more than 40 MPa at 28 days for the slag-containing mortars. However, the addition of the PC significantly accelerated the setting time prompting the need for 0.3 wt% citric acid addition to provide sufficient time for the mixtures to be placed in the moulds. This resulted in setting time ranging from 20-40 min.

Estimation of the degree of slag hydration using Mössbauer spectroscopy and XCT both supported the faster kinetics of slag hydration with the addition of PC. The reactivity of the slag in the first 28 days of hydration was reflected through the drastic changes in the Mössbauer spectra, particularly of the high-sulfate formulation. On the other hand, the XCT results showed that although the slag was more reactive for the ternary binders in the first 28 days, the difference in the hydration degree was less pronounced at a longer curing time. Despite the consistency in the trends observed between these two techniques, however, significant differences in the estimated values were linked to two main factors: (1) the assumption that the slag is completely unreactive in the first 24 hours of hydration; and (2) the 2.15 µm voxel resolution setting which excluded the contribution of the finer particles.

The phase assemblages obtained experimentally based on the XRD, TGA and ATR-FTIR results could be summarized as follows:

- Formulation (A-PC) 4.5CAC-HH-30PC: dominated by strätlingite and monosulfate; with minor amount of C-S-H
- Formulation (B-PC) 1.6CAC-HH-30PC: dominated by ettringite; with strätlingite amount increasing over time; minor C-S-H content

According to the thermodynamic models, the addition of the slag should favor a more extensive formation of monosulfates and C-S-H. However, the experimental results demonstrated an extensive ettringite formation instead, especially for the high-sulfate system. This difference could be explained by the kinetics of the hydration, not considered in the models.

Ettringite is formed in the early ages of hydration and remains generally stable throughout the 165 days covered by the study. Furthermore, although the models suggest the incorporation of Fe in monosulfoaluminates and siliceous hydrogarnet, there was no sufficient evidence confirming the uptake of Fe in these phases.

Using TEM, no significant amount of Fe was detected in the more conventional hydrated phases such as ettringite, monosulfoaluminate or strätlingite, similar to the findings in the binary systems. Instead, Fe was found to be incorporated in Ca-Al-Si-rich intermixed hydrated gel. Elemental maps from STEM suggest that Fe could be in at least two hydrate phases: (1) an amorphous gel with a lower (1-4 at%) Fe concentration; (2) and an unidentified nano-crystalline phase comprising the gels with higher (5-13 at%) Fe content. Nevertheless, the possibility that the Fe-bearing intermixed phases could evolve into other hydrate phases (i.e., Si-hydrogarnet, C-A-S-H) over time could not be excluded.

Although a huge gap still needs to be filled towards fully unravelling the slag's hydration mechanism, the initial results supported its potential valorization as an SCM in an expansive CAC-HH-PC ternary binder. The chapter also demonstrated that PC could moderately act as an activator of the slag theoretically by increasing the alkalinity of the system and by providing additional elements (Ca and Si) that participate in the formation of Fe-bearing hydrates.

Conclusions and Perspectives

The EU MSCA-ETN SOCRATES Project promotes circular economy by creating near-zero-waste flow sheets for the valorization of industrial by-products. After the extraction of high-value components and the removal of toxic compounds, the use of the remaining residues as supplementary cementitious materials (SCM) in calcium aluminate cement (CAC)-based binders was explored.

The evolution of the mechanical strength of standard mortars containing highly-amorphous Fe-rich slags (30 wt% replacement) demonstrated their positive contribution to this property of the blend. For this reason, the main focus of this study was dedicated to the best-performing NFM slag in binary CAC - calcium sulfate hemihydrate (HH) and ternary CAC – HH – Portland cement (PC) blends. The principal formulations evaluated are presented in **Table 5.1**. The influence of the sulfate proportion to the properties of the binders was also investigated, using a low- (4.5 CAC/HH ratio) and a high- (1.6 CAC/HH ratio) calcium sulfate systems.

Table 5.1 Composition of binders incorporating the granulated Fe-rich slag

code	*(in wt%)*	slag	CAC	HH	PC	total binder	CAC/HH ratio
A	4.5CAC-HH	30	57	13	0	100	4.5
B	1.6CAC-HH	30	43	27	0	100	1.6
A-PC	4.5CAC-HH-30PC	30	33	7	30	100	4.5
B-PC	1.6CAC-HH-30PC	30	25	15	30	100	1.6

reference formulations:

(reference cement) no SCM nor quartz filler added

(reference filler) slag replaced by equal volume of quartz

Physical Properties

As presented in **Figure 5.1**, high compressive strengths were obtained for mortars incorporating the slag and 1.3 wt% citric acid. The latter, initially added to delay the setting, also assisted in the early strength development. Overall, higher compressive strengths were achieved in the high-sulfate systems due to the more extensive ettringite formation. However, the expansive nature of ettringite proved to be problematic in reference cement mortars containing PC (formulation B-PC) for which excessive expansion eventually led to macro cracks (**Figure 5.2**) and loss in strength. The addition of slag mitigated this expansion, producing more dimensionally-stable mortars. This is likely governed by the dilution effect (physical

factor) in the early hydration ages, and by the resulting phase assemblage (chemical contribution of the slag) at long term.

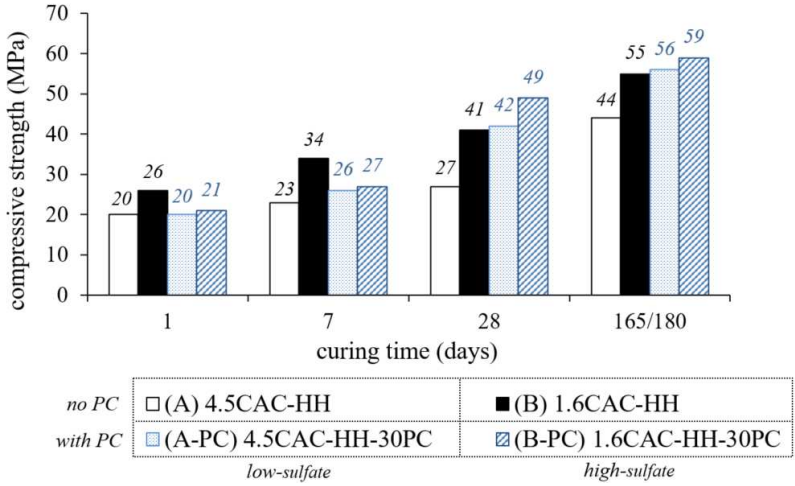

Figure 5.1 Summary of the compressive strength results

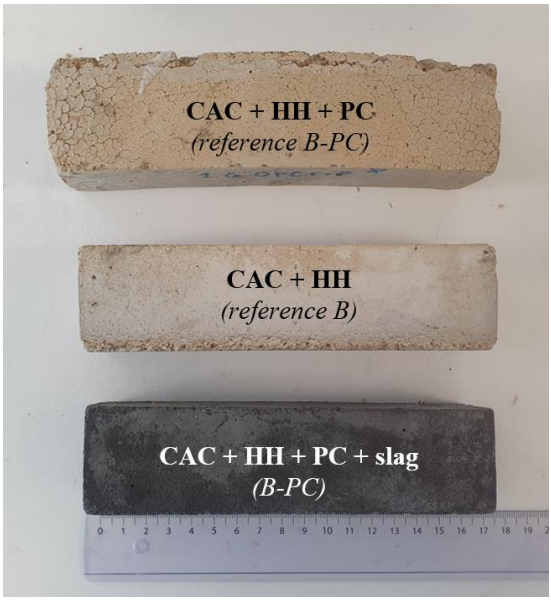

Figure 5.2 Pictures of the B-PC and B (high-sulfate) mortars after 45 days of curing under water

Quantifying the degree of slag hydration

A methodology to estimate the degree of the slag hydration was developed based on image analysis using X-ray computed tomography (XCT). The technique took advantage of the contrasting X-ray signals from the high-density Fe-rich slag and the cement matrix. The results were compared to those obtained from Mössbauer spectroscopy in **Figure 5.3**. The latter was based on the relative amounts of the absorption areas attributed to the newly-formed Fe component during slag hydration.

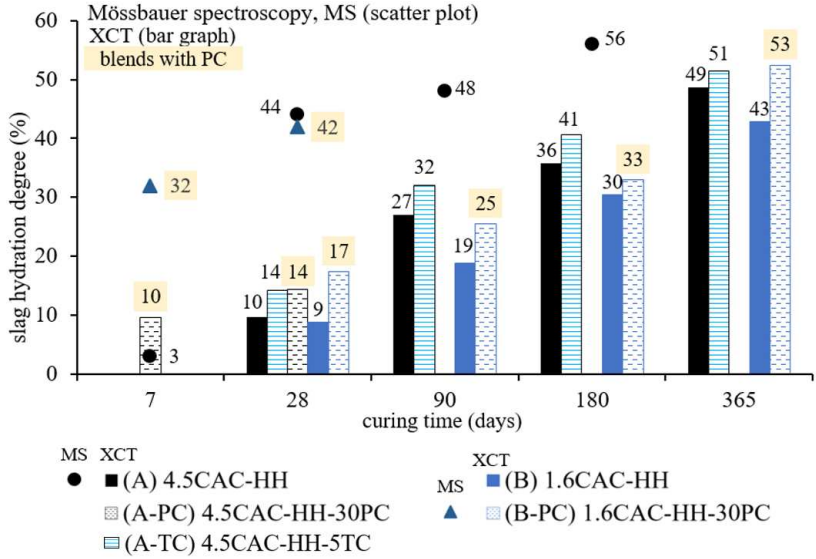

Figure 5.3 *Consolidated slag hydration degree estimated using XCT and Mössbauer spectroscopy*

Both results supported the faster kinetics of slag hydration with the addition of PC. At longer curing period however, the estimated values all converged towards 50 %. The generally lower values obtained from XCT were linked to two main factors: (1) the assumption made in XCT that the slag is completely unreactive in the first 24 hours of hydration; and (2) the 2.15 µm voxel resolution setting in XCT which excluded the contribution of the finer slag particles or of other phases present at this scale.

Phase assemblage evolution

The phase assemblages of the slag-containing formulations were simulated using GEMS thermodynamic modelling and were compared to those observed experimentally at long term (>165 days) using XRD, TGA and

ATR-FTIR. Only 50 % of the amorphous fraction of the slag was assumed to react in GEMS following the estimations from XCT for the experimental samples. A summary of the results is provided in **Table 5.2**.

Table 5.2 *Consolidated phase assemblage based on thermodynamic modelling and experimental results (after >165 days). Monosulfoaluminate is abbreviated as Ms.*

	thermodynamic modelling		**experimental results**	
components:	major	minor	major	minor
A	ettringite, hydrogarnet	gibbsite, strätlingite	Ms	ettringite, gibbsite, strätlingite
B	ettringite	hydrogarnet, gibbsite	ettringite, gibbsite	Ms, strätlingite
A-PC	strätlingite, Ms	hydrogarnet, C-S-H	strätlingite, Ms	C-S-H
B-PC	Ms, C-S-H	strätlingite, ettringite, hydrogarnet	ettringite	strätlingite, C-S-H, Ms

While the experimental results are generally in agreement with the models, the differences were attributed predominantly to the kinetics of hydration, not accounted for during the simulation. Experimentally, ettringite dominated the high-sulfate systems in the early hydration ages, while the slag and PC exhibited slower hydration kinetics relative to the CAC and HH. The ettringite formed was stable over time, therefore modifying the proportion of the ions available for hydration at later ages. This could also be the reason why the Fe-containing hydrogarnet and Fe-monosulfoaluminate predicted in the models were not detected experimentally.

Following the experimental phase assemblage evolution over time, the influence of the slag was manifested in the silicates (i.e., strätlingite, gehlenite, C-S-H) regions where the major changes were observed, relative to the reference formulations. The crystalline component of the slag, wüstite, also appeared unreactive over time, demonstrating that only the glass fraction was dissolving throughout the 1-year-curing period. Moreover, another evidence of slag reactivity was proposed using the ATR-FTIR spectra through a hypothetical peak-displacement of the raw slag's Si-O asymmetric stretching band at 930 cm^{-1}. However, the complexity of the systems studied and the difficulty in characterizing the amorphous phases did not allow a conclusive answer as to the fate of Fe using the more common characterization techniques in cement hydration.

The fate of Fe during hydration

Fe was detected using TEM and STEM mainly in hydrated amorphous gel phases grouped into two compositional clusters, as shown in **Figure 5.4**. The gels were richer in Al in the binary systems, while the proportions of Ca and Si were higher in the ternary systems. This difference was due to the contribution of PC in the latter.

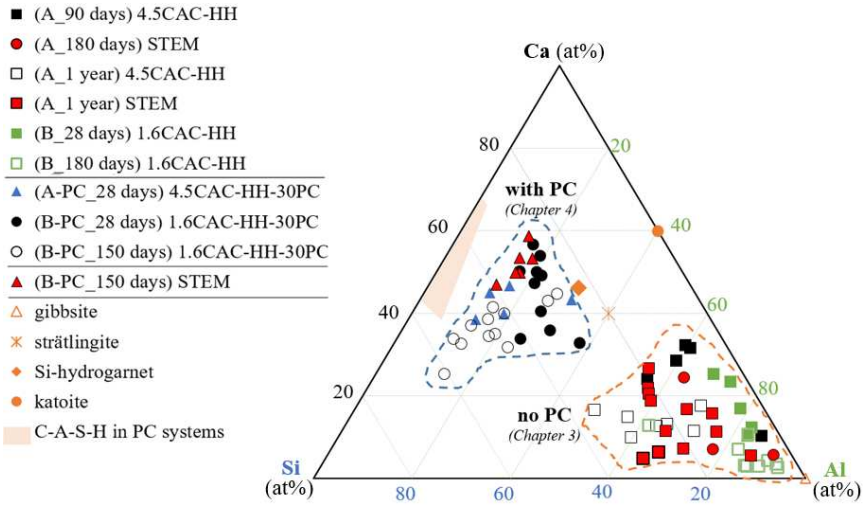

Figure 5.4 *Consolidated ternary diagram of Fe-containing hydrate gels with 1-12% Fe obtained from (TEM-) EDS analyses. Reference points for, gibbsite, strätlingite, katoite, Si-hydrogarnet and C-A-S-H were added from literature data [202].*

At longer curing ages, the TEM results revealed the tendency of the gels' composition to move towards regions of lower Ca content in the ternary diagram. On the other hand, the STEM maps revealed the formation of an Fe-rich nano-crystalline phase in the binary system after longer curing period (>180 days). This unidentified phase exhibited a rod/needle-like morphology with a d-spacing of approximately 7.2 Å. The phase matching these characteristics the closest would be Al-Fe hydroxide or Fe-containing layered double hydroxide (LDH). The latter could further explain the significant amount of Mg detected. Unfortunately, these techniques alone were not sufficient in revealing the identity of this Fe-bearing phase. Complementary techniques or methodology are needed for this purpose. Nonetheless, the possibility of its ultimate transformation at long term into Fe-containing hydrogarnet or Fe-monosulfates, as suggested by the thermodynamic models, could not be eliminated.

In addition to the above, the evolution of the Mössbauer spectra during hydration clearly demonstrated the change in the atomic environment of

Fe as new components emerged. The fittings from two independent models consistently suggested that the hydration of the slag was accompanied by Fe oxidation from the 2+ to 3+ state and a change from tetrahedral to octahedral coordination. The new Fe components displayed Mössbauer parameters similar to those reported for ferrihydrite gels and Fe-monosulfates in cement systems. One of the two Mössbauer models further suggested an additional 4- to 5-fold coordinated Fe^{2+} component in a hydrated phase. The closest structure was comparable to the Fe environment in a rare doublet of straurolite, $(Fe,Mg)_2(Al,Fe)_9O_6[SiO_4]_4(O,OH)_2$, arising from the delocalization of electrons due to a charge transfer phenomenon (i.e., $Al^{3+}-Fe^{2+}$ or $Fe^{2+}-Fe$ substitutions). The decrease in the total Gaussian-type spreading of the quadruple splitting parameter (ΔQS) of this new Fe component could be a consequence of the transition from amorphous to nano-crystalline state, and related to the formation of the unidentified Fe-bearing nano-crystalline phase detected using STEM.

Other SOCRATES residues

The potential use of the jarosite residue as a sulfate source, and the paper residue as an activator in binary CAC-HH systems were explored in separate case studies.

The results showed that when the jarosite residue replaced the calcium sulfate source by up to 50 wt%, high compressive strength values of 26 MPa after 1 day and 60 MPa after 28 days of hydration were attained. This was the case despite the lower soluble sulfur in the jarosite residue based on conductivity measurements. This implies that the change in the phase assemblage brought by the reaction of sulfur was not drastic enough to manifest physically. However, its environmental behavior needs to be assessed and potentially develop pre-treatment processes, considering the presence of significant heavy metals and elemental sulfur in its components. On the other hand, the addition of 5 wt% lime-rich paper residue to induce slag dissolution, accompanied by 1.3 wt% citric acid for set control, significantly increased (> 10 MPa difference) the mechanical strength of the CAC-HH-slag blend. This has been associated to the anticipated increase in pH with the addition the lime-rich residue, and improved packing of the blend prior to setting. While only a minimal augmentation (2-5 %) in the slag hydration degree was estimated using XCT, the addition of the paper residue appeared to influence the phase assemblage with an increased AFm formation.

Future Outlook

The extensive characterization of the physical and mineralogical properties of the CAC-based binders incorporating some of the SOCRATES residues, demonstrated the positive potential of this valorization pathway. Nonetheless, better understanding of the hydration mechanism of the slag will be needed to eventually adapt the properties of the binders to their target applications.

Future works should focus on complementary analyses to identify the Fe-bearing nano-crystalline phase detected using STEM. This could be done by employing other advanced characterization methods such as nuclear magnetic resonance (NMR) or X-ray absorption (XAS) spectroscopy, which have been previously used [113,123,206] in studying the uptake of Fe in hydrated phases in cement systems. The identification could also be facilitated by reproducing the phase synthetically and at higher concentrations, in order to minimize the problem of intermixing on a nano-scale.

Moreover, the methodology developed for quantifying the degree of slag hydration using XCT could be optimized by reducing the voxel resolution and including the finer fractions in the estimation. Although this would imply a scan with longer duration or smaller volume. A refined selective dissolution procedure based on salicylic acid-methanol [141] or NaOH-EDTA [139,207] could also be developed to validate the estimations.

The models used for the fitting of the Mössbauer spectra could be improved by finding the compromise between the simplistic and complex models in order to reflect the reality more accurately. The selection of the fitting parameters could be supported by complementary techniques, such as titration using H_2SO_4, HF, and H_3BO_3 [208] to confirm the oxidation state of Fe before and after hydration.

Optimizing the proportions of CAC, HH and PC aided by design of experiment (DOE) could also potentially improve the reactivity of the slag and the overall properties of the blend. From an industrial point of view, this could be beneficial as the applicative performance, along with economic factors, are crucial considerations. Finally, the long-term durability of the optimized formulation in different chemical environments must be tested to better understand the behavior of the blend and adapt it according to the application.

Appendices

A. Life cycle assessment and exergy analysis on the use of industrial by-products as SCM in PC system

The paper attached in this section was presented by the author at the Forum of Young Researchers in Sustainable Building 2019 (YRSB19) in Prague, Czech Republic on July 2, 2019. This work focused on the addition of fumed fayalite slag (Koranel®), one of the SOCRATES residues, in a pure PC system. These results were excluded from the main part of the thesis which involved CAC-rich binders.

Industrial By-Products as Non-Conventional Supplementary Cementitious Material

Jennifer ASTOVEZA[a,b,c], Alejandro ABADIAS[d], Ratana SOTH[a], Romain TRAUCHESSEC[b], Markus A. REUTER[d] , Yiannis PONTIKES[c]

[a] *Science and Technology Department, Imerys Technology Centre- Lyon, 38090 Vaulx-Milieu, France, jennifer.astoveza@imerys.com, ratana.soth@imerys.com*
[b] *Institut Jean Lamour, UMR CNRS 7198, Université de Lorraine, IUT NB, BP 90137, 54600 Villers-lès-Nancy, France, romain.trauchessec@univ-lorraine.fr*
[c] *KU Leuven, Department of Metallurgy and Materials Engineering, 3001 Leuven, Belgium, yiannis.pontikes@kuleuven.be*
[d] *Helmholtz Institute Freiberg for Resource Technology, 09599 Freiberg, Germany, a.abadias@hzdr.de , m.reuter@hzdr.de*

Abstract

The extensive efforts on reducing the carbon footprint of cement production have motivated the investigations on the use of supplementary cementitious materials (SCM) as additive and/or substitute in cement blends. However, previous studies were focused on limited types of SCM including natural pozzolans, ground granulated blast furnace slag (GGBFS) and fly ash – which could readily exhibit reactivity in cementitious systems. In this article, a review on the advances in the valorisation of novel industrial by-products (non-ferrous slag, municipal incinerator bottom ash, and jarosite waste) are presented to provide solution in reducing the volume of industrial landfills while creating greener materials for building applications. The second part of this paper demonstrates a case study applying exergy to compare the footprint of the flowsheets derived from the valorisation of industrial by-products as SCM.

Keywords: *green cements, slag, supplementary cementitious materials, bottom ash, jarosite, exergy, life cycle assessment*

1 Introduction

The use of green/eco-efficient cements incorporating supplementary cementitious materials (SCM) poses to be one of the promising solutions to promote sustainability in the building sector [1]. Green cements or eco-efficient cements [2] generally refer to cementitious binders produced through a more sustainable process utilizing materials or energy sources that would decrease the total environmental footprint of the final product relative to the more traditional system. Ideally, the substitute material incorporated has a lower carbon footprint than the cement component while maintaining a comparable or even a superior performance than the substituted binder formulation. On an industrial point of view, the economic advantage of a cheaper substitute along with a process suitable for upscaling and commercialization is among the critical factors in the definition.

A comprehensive review on traditional SCM is given by Snellings et al [3]. Among the numerous types described, only three materials are considered to take a

major role as SCM in the market over the past 25 years, namely: granulated blast furnace slag (GBFS), fly ash and limestone [2]. However, despite recognizing the numerous types of traditional SCM and their seemingly growing acceptance on a commercial scale, their limited and often localized availability remains to be a main challenge impeding the green cement market. To answer these staggering needs for alternative sources, a promising approach of the Enhanced Landfill Mining (ELFM) concept [4] opens new pathways for potential types of novel SCM. In landfill mining, the high-value metal components are extracted from ancillary sources particularly pre-existing landfills. For the building sector, ELFM is a driver for novel construction materials and binder formulations. Typically, the metal-depleted by-products in the ELFM flowsheets [4] contribute a relatively low-cost stream of materials with major volume fraction. These could be good initial criteria for a mineral additive or a precursor to building materials: clean (metal-depleted), low-cost and high volume.

In this paper, the use of three landfilled industrial by-products (non-ferrous slag, municipal incinerator bottom ash, and jarosite waste) as non-conventional SCM is presented as a viable pathway for stimulating the green cement market. A review on the previous studies concerning the utilization of these by-products in the building sector is presented in the first part of the paper. The second part demonstrates a case study applying exergy to compare the footprint of the flowsheets derived from the valorisation of industrial by-products as SCM.

2 Studies on non-conventional SCM

Compared to traditional SCM, the chemistry and other properties of these landfilled by-products remain a challenge in their utilization as additive in cement blends. Whereas traditional types of SCM consist mainly of CaO, SiO_2 and Al_2O_3 similar to an Ordinary Portland cement (OPC), non-ferrous slags and jarosite waste are Fe rich. On the other hand, although municipal incinerator (MI) bottom ashes could have major proportions of CaO, SiO_2 and Al_2O_3, they typically have a much lower degree of vitrification as opposed to fly ashes (a traditional SCM) due to the slower cooling rate for the former. The chemical composition and the degree of vitrification are only two of the many factors considered to define the reactivity of residues and consequently their potential for valorization as SCM. A detailed discussion of these factors specifically adopted for slags is presented in the work of Chen and Brouwers [5].

Despite the striking differences in the properties of these landfilled industrial by-products compared to OPC and traditional SCM, it is important to note that in the concept of ELFM, these by-products are valorized as raw materials in a flowsheet which still require pre-treatment (extraction of valuable metals and hazardous components) prior to their possible utilization as building materials. This means that there is still a margin for engineering these by-products to induce or increase reactivity and likewise to reduce heavy metals and hazardous contents making them more suitable for building applications. Case in point, a zero-waste recycling scheme is presented in Hunt [6] providing elaborated flowsheets in the metals processing chain. In their paper, one of the flowsheets shows a lead-zinc ore processing that incorporates a slag fuming step (metal extraction by reduction to gaseous phase) for zinc recovery. To reflect this on an existing industrial application, an improved fuming process that yields a clean slag has been developed and is currently being further refined at Metallo-Chimique, for a combined metal and slag valorization [7]. This kind of zero-waste approach has given rise to the now commercialized “clean synthetic” slag (or fumed fayalite slag) of Metallo: Koranel® specifically adapted for sustainable

building applications [8].This material will be the subject of the case study in the latter part of this paper to demonstrate an exergy analysis on its role as an SCM.

2.1 Non-ferrous slag

Among the wide variety of non-ferrous slags, copper, lead and zinc slags are some of the few generated in quantities that could allow viable utilization in building applications [9]. Non-ferrous slags are well dominated by Fe and Si existing as fayalite (Fe_2SiO_4) along with the other olivine group and spinel group phases [10]. Reactivity in cement blend is more often associated with non-ferrous slags having a summation of SiO_2, Al_2O_3 and FeO above that of the 70% percentile requirement for class N pozzolans. While their trace elements (As, Cd, Co, Cu, Cr, Mn, Ni, Pb, and Zn) content and sulfidic ore origin have previously triggered concerns on their weathering behavior and leachability that question their suitability to building applications [9,10]. Non-ferrous slags generally have high specific gravity (increases with the Fe content) and sharp angular particles. These properties are said to favor the soundness, stability and abrasion resistance of concretes incorporating these non-ferrous slags. However, at high replacement levels (>40 wt.%), the slow reactivity of slags in general yields slower strength development over time which is another impeding challenge on their valorization as SCM [9].

Alp et al [11] demonstrated the use of a metal-depleted copper slag recovered after flotation as an iron source in an OPC clinker production. This has been performed on an industrial scale as 100% substitute to the iron ore, constituting 2.5-6 wt.% of the raw meal. The mechanical performance of the standard mortars made with the clinker incorporating the clean copper slag was reported to be similar to a reference mortar without the slag. The leachability of heavy metals, Cu and Zn, was also reduced below the environmental limits in the crushed mortars made from the clinker incorporating the clean copper slag [11]. Similarly, previous studies [12,13,14] on the use of zinc and lead slags as SCM have demonstrated promising mechanical performance, along with other advantageous properties such as increased in gamma ray attenuation (capability to protect from radiation) [14] and suitability to high density special applications (such as noise barriers). In addition, a study by Penpolcharoen [12] highlighted an interesting role of a secondary lead slag's magnetic property in improving the mechanical performance of concrete blocks having 20 wt.% slag as cement substituent and simultaneously 100 wt.% slag as aggregate replacement. The study claims that the magnetic force strengthened the microstructure by magnetizing the water in the pore solution. An earlier study [15] explained that a complete hydration can be achieved when water molecules are preliminarily broken down by magnetic force, thus resulting to improved workability and compressive strength of mortars incorporating iron-rich slags.

2.2 MI bottom ash

MI bottom ash is generally categorized as a non-hazardous material coming from the incineration of municipal waste [16]. The composition of this residue can widely vary depending on the local source. In many cases it may contain pieces of plastics, stones, bricks, glass, ferrous and non-ferrous matters, and an assortment of other unburnt materials [17]. They typically display a porous microstructure in irregularly shaped particles that yields large surface area and a low specific gravity, consequently resulting to higher water absorption capacity versus natural aggregates [16,18]. Studies on its valorization as partial OPC and aggregate replacement in cement and concrete samples reported that its high metallic aluminum and bottle glass content can cause extensive spalling, expansion and susceptibility to alkali-silica reaction [16,19].

These support the need for pre-treatment (aging and chemical extraction [20]; pre-sorting, sieving and thermal treatment [17,21,22]) of the MI bottom ash to adapt its properties for cementitious applications.

The thermal pre-treatment procedures for MI bottom ash performed in previous studies [17,21,22] have highlighted the importance of vitrification of this SCM for cementitious applications. The paper by Ferraris et al [22] demonstrated that a maximum 20 wt.% substitution to OPC of a pre-treated Italian MI bottom ash could yield a comparable compressive strength after 150 days as the reference cement mortar containing no ash. The pre-treatment involved screening, magnetic separation, thermal treatment at 1450^0C and fine milling. The vitrification step is accounted for the inertisation of heavy metal ions and prevention of alkali-silica reaction throughout the 2 years span of monitoring [22]. A paper by Cheng [21] similarly demonstrated the benefits of combining sieving with thermal treatment to improve the strength of mortars incorporating pre-treated MI bottom ash originating from Taiwan. The decrease in total capillary porosity with the denser microstructure is attributed for the higher strength of mortars containing pre-treated MI bottom ash versus a reference mortar containing the raw MI bottom ash. However, a generally lower strength is obtained when compared to a pure OPC reference mortar along with observations of lower flowability, bleeding, increased shrinkage and higher total porosity [21]. Lastly, thermal treatment at lower temperature (550^0C) demonstrated in Tang et al [17] has proven to maintain the viability at 30 wt.% OPC replacement level using MI bottom ash from Netherlands. The key to mitigating the strength reduction in this study was the effective reduction of the metallic aluminum content in the MI bottom ash by a strategic sieving sequence; in parallel with the increased chemical activity brought by the reduction of organic matter content through thermal treatment [17].

2.3 Jarosite waste

Jarosite waste ($KFe_3(OH)_6(SO_4)_2$ as a pure mineral) is an iron and sulfur-rich by product of lead-zinc metallurgical plants, which high toxicity, acidity (pH ≈ 2) and heavy metals (As, V, Cr) content impose issues on its disposal and containment [23]. Previous studies have explored the viability of using jarosite as a substitute to aggregate in OPC-based concrete [24,25]; in combination with slag in pressed activated binders [23]; and as source of sulfate added to the raw meal during OPC and sulfoaluminate cement production [26,27]. As an aggregate replacement, the concrete samples formulated with 25% volume replacement displays appreciable durability and passes a toxicity characteristic leaching procedure citing chemical bonding and physical entrapment as the mechanism for its low leachability. Moreover, it is noted that at higher replacement percentage, the reduction of pH due to the acidic nature of jarosite could impose corrosion risk to reinforcement bars [24]. When pressed with iron slag, liquid activator and <5% OPC, an increased strength is attributed to the formation of amorphous gel hydrates, while heavy metals favourably show low leachability [23]. Meanwhile, as a raw meal substitute to gypsum in an OPC system, it is demonstrated that an optimum substitution of 20 wt.% will not affect the strength development of the binder [26]. The effect of different cations released by jarosite to the rheological properties of the cement are also discussed in Katsioti et al [26]. Lastly, as a raw meal addition for sulfoaluminate cement, the complete substitution of gypsum by jarosite shows to have no significant effect to the grindability, setting time, compressive strength and dimensional stability of cement pastes [27]. All these above mentioned results support the possible valorization of jarosite in cementitious formulations. In fact, a commercial product called Jarofix (50-75 wt.% jarosite with about 10 wt.% OPC and 2 wt.% lime addition) is being produced annually at 160,000 tons per year by CEZinc Refinery in Canada mainly for stabilization of waste [28];

and at 500,000 tons per year by Hindustan Zinc Ltd. in India with variations having soil and bottom ash additions for construction applications [29].

It is important to note however, that the most viable approach is to directly minimize creation of this waste by pre-treatment. As in the case of MI bottom ash, thermal pre-treatment has been proposed for jarosite waste to valorize the remaining metals and convert this residue to a clean slag. For instance, a commercial-scale process such as the Ausmelt TSL (Top Submerged Lance) technology has long existed for the recovery of zinc derived by fuming leaching residues such as jarosite [30,31] for the recovery of valuable elements such as In, Ge, Ag etc. In this way, jarosite can be converted to a slag with more suitable properties for building applications.

3 Case study on a non-ferrous slag as SCM

In this section, the impact of using a clean non-ferrous slag as an SCM has been evaluated through a simulation-based exergy and Life Cycle Assessment (LCA) perspective [40].

It must be noted, if the impact of including the cement flowsheet into the metallurgical one to generate a "zero-waste", a comprehensive flowsheet would need to be evaluated to understand what routes are the best. Fig.1 shows various options to deal with intermediates to produce slags, which can be used in various further downstream processes. In this analysis the SCM is a clean residue generated after a fuming process of the slags produced during non-ferrous metallurgy. For this analysis the SCM is produced in an arbitrary process, the footprint of which is not included in the analysis. Only the cement production is evaluated using exergy and environmental footprint.

The first indicator is exergy, which is a thermodynamic property based on the second law of thermodynamics. It is defined as the maximum work that a flow or a system can produce when it interacts with the environment, but also, the minimum work needed for producing that flow or system from the environment [32]. As exergy is always destroyed when a process is performed, it is a suitable property to evaluate the thermodynamic downgrading of the resources along an industrial process since energy and material flows can be measured with the same units (energy units) and thus integrated [33]. Irreversibility implies that every product of an industrial process will have an exergy cost (i.e. exergy destruction) i.e. an indicator of how many resources have been used to produce it [34]. As industrial processes can be very complex, with many interactions between units, recirculation, bifurcations, etc., a methodology that connects the irreversibility and the exergy cost of a product is required. This methodology, thermoeconomics [35–37] has been largely applied for the analysis of energy systems, but it can be applied to other different industrial processes such as industrial symbiosis [33, 38, 39] or metallurgy [40].

The second indicator is environmental impact. The LCA is a methodology for the environmental impact evaluation of the different stages of the life of a product, from raw materials to end-of-life [44]. This methodology has been already applied to evaluate the environmental impact of cement production processes [41–43]. Therefore, the combination of these two indicators is a good starting point to discuss the sustainability of an industrial process. This simulation-based approach has been already applied in process metallurgy e.g. in the assessment of the primary copper production and e-waste recycling [40,44].

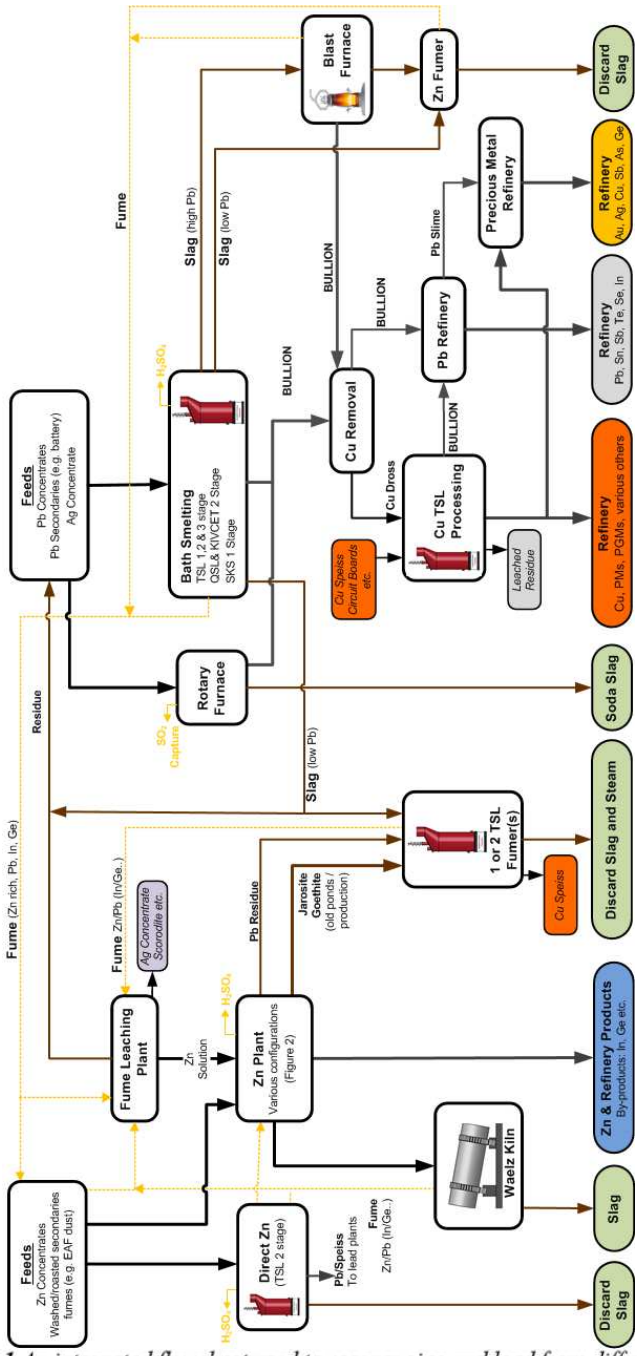

Fig. 1 *An integrated flowsheet used to recover zinc and lead from different slags and residues (e.g. Jarosite or Geothite) created during non-ferrous metallurgy, producing clean slags that can be used as building material or SCM [47].*

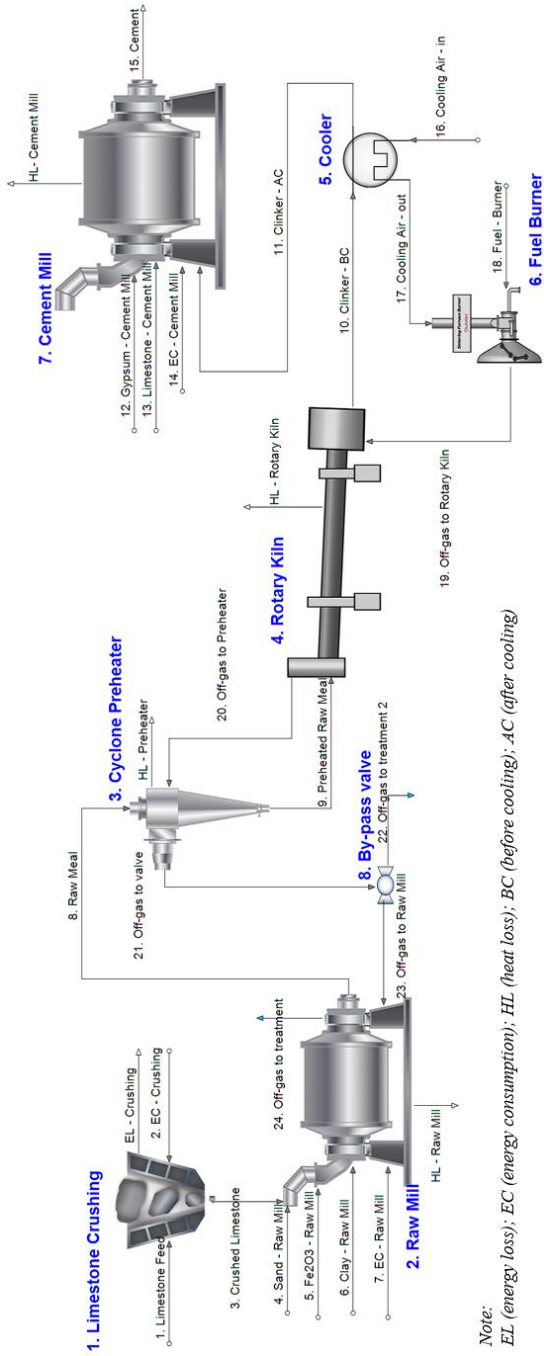

Fig. 2 Flowsheet of the cement production process simulated with HSC Sim, showing the units considered and how they are connected between material and energy flows. This flowsheet would be linked to Fig. 1 to obtain a complete picture

The dry cement production process has been simulated with HSC Sim (HSC Chemistry 9, Outotec [48]), from raw materials to cement (see **Fig. 2**). Through this simulation, the mass and energy balances have been performed, as well as the exergy values of all the streams of the cement plant were obtained. Subsequently the exergy and thermoeconomic analysis were conducted through the dedicated tool of HSC Sim based on the theory of the exergy cost [36] and symbolic Thermoeconomics [45]. The parameters of the exergy and thermoeconomic analysis used to evaluate the results of the simulation were:

- **Irreversibility:** Exergy destroyed along a unit or process.
- **Exergy cost:** The exergy cost of a flow is the quantity of exergy needed to produce it. Therefore, it is a cumulative indicator

Furthermore, as the mass and energy balances of the cement process have been performed through the simulation, the information required to perform the Life Cycle Inventory (LCI) of the process is also obtained. Using HSC Sim's LCA tool that links the results of the simulation with the environmental impact assessment (GaBi [49]), the process can be easily imported into GaBi to perform the environmental evaluation [44]. The indicators used to describe the process are:

- Global Warming Potential (GWP).
- Photochemical Ozone Formation (POCP).
- Acidification Potential (AP).
- Eutrophication Potential (EP)

Two cases (**Tab. 1**) for a fixed amount of cement produced of 100 t/h have been studied and compared (after normalization) through the indicators previously mentioned.

Tab. 1 *Formulations used for the two cases in this simulation*

in tons		Clinker	Limestone	Gypsum	Slag (SCM)	Sum
Case 1	no SCM	90	5	5	0	100
Case 2	with SCM	61.6	5	3.4	30	100

3.1 Exergy and thermoeconomic analysis

Despite the larger exergy destruction during the grinding of the fumed fayalite slag, the irreversibility analysis shows that the total exergy destruction along the process decreases around 30%, as **Tab. 2** shows. The reason of this decrease is the lower amount of material circulating through the raw mill and rotary kiln since a lower amount of clinker is required to obtain the 100t/h of cement.

Tab. 2 *Total irreversibility and exergy cost of the cement production*

	Case 1	**Case 2**
Total Irreversibility [MW]	79.8	56.2
Exergy Cost of the cement production [MW]	92.8	68.7

Furthermore, the exergy cost of the clinker is decreased around 32% when the slag is added to the cement mill. This drop on the exergy cost is due to the lower quantity of material circulating through the flowsheet, as exhibited with the irreversibility.

However, as the slag must be grinded and added to the cement mill, the reduction of the exergy cost of the cement becomes 26% in total with respect to case 1.

Fig. 3 shows, that the main contributors to the exergy cost of the cement are the cyclone preheater and the rotary kiln, because of their heat losses, and the fuel burner due to the large amount of fuel required to perform the process. However, as the breakdown of the case 2 shows, the slag grinding has a considerable exergy cost. Around 3% of the cost of producing the cement is due to the electricity required to grind the slag.

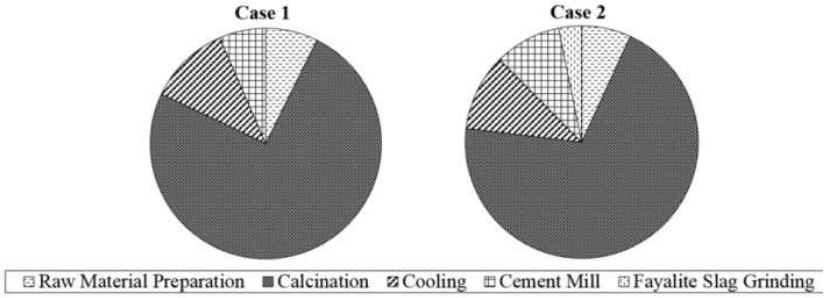

Fig. 3 Exergy cost breakdown of the cement production (Note, the transportation cost for the SCM to the cement plant was not considered in this case study)

3.2 Environmental footprint analysis

Tab. 3 summarizes the environmental footprint analysis of the two process routes. The GWP results obtained in this study are aligned with other LCA of cement processes. For instance, Moretti and Caro [42] reported a CO_2 emission for cements produced without SCM at around 960 kg CO_2 per ton of cement produced while the value obtained in this study for Case 1 is 1002 kg CO_2 per ton of cement. When SCM are utilized, values around 600-700 kg CO_2 per ton of cement are reported in literature, e.g. [41,42,46].

The results of this paper show that the environmental impact is decreased when fumed/cleaned fayalite slag is used as SCM. For instance, the Global Warming Potential is around 32% lower in the case 2 with respect to the base case. It is because the quantity of limestone required to produce the 100 t/h of cement is lower (32% less clinker required), thus, the emissions related to the calcination process decrease. However, as the slag must be grinded, the electricity production contributes more to the CO_2 emissions in the case 2, as **Fig. 4** illustrates. Nevertheless, the calcination process is still the main contributor to the carbon footprint constituting around 90% of the CO_2 emissions.

***Tab. 3** Normalized LCA indicators of producing 1 ton of cement without including the larger flowsheet as depicted by Fig. 1.*

	GWP [kg CO_2 eq.]	**POCP** [kg NMVOC eq.]	**AP** [Mole of H+ eq.]	**EP** [Mole of N eq.]
Case 1	100	100	100	100
Case 2	68.4	73.9	74.3	75
% Reduction	**31.6 %**	**26.1 %**	**25.7 %**	**25.0 %**

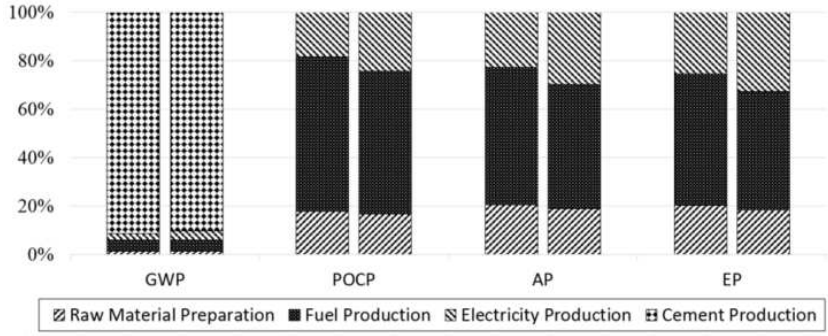

Fig. 4 LCA Indicators Breakdown. Each indicator represents its breakdown for the case 1 (left column) and for the case 2 (right column)

The other indicators, such as Photochemical Ozone Formation (POCP), Acidification (AP) and Eutrophication (EP) follow the same tendency as the GWP. The reason for this is that the use of slag in cement process decreases the specific raw material consumption. Therefore, the environmental impact generated to produce those raw materials, such as pet coke, limestone or sand, are lower. However, the contribution of the electricity generation to these indicators is higher than in the case 1 because of the extra electricity required to grind the slag.

4 Conclusions

The use of non-conventional SCM derived from landfilled industrial by-products opens a promising pathway to promote sustainability in the building sector. It addresses the limited and often localized supply of traditional SCM while reducing the volume of landfilled industrial by-products. Previous studies presented in this review have demonstrated the viability and discussed the challenges in incorporating these non-conventional SCM to create green cements. In the second part of this paper, the case study presented shows the benefits of cement substitution with a non-ferrous slag as SCM both through exergy and environmental footprint analysis. The lower material circulation in rotary kiln during calcination is shown to greatly decrease the associated irreversibility and exergy cost of the process. The calculated Global Warming Potential from the LCA is reduced by 32% with 30 wt.% incorporation of SCM in an OPC-based system.

5 Acknowledgement

This research has received funding from the European Union Framework Program for Research and Innovation Horizon 2020 under Grant Agreement No.721385 (EU MSCA-ETN SOCRATES; project website: http://etn-socrates.eu)

6 References

[1] UNEP Buildings and Climate Change Summary for Decision Makers *Sust. Build. Clim. Init.* 3

[2] Scrivener K, John V, Gartner E 2016 Eco-efficient cements: Potential, economically viable solutions for a low-CO2, cement-based materials industry

[3] Snellings R, Mertens G and Elsen J 2012 Supplementary Cementitious Materials *Rev. Min. Geochem.* **74** 211–78

[4] Jones P T, Geysen D, Tielemans Y, van Passel S, Pontikes Y, Blanpain B, Quaghebeur M and Hoekstra N 2013 Enhanced Landfill Mining in view of multiple resource recovery: A critical review *J. Cle. Pro.* **55** 45–55

[5] Chen, W.; Brouwers, H. J. H. 2006 *The reaction of slag in cement, theory and computer modelling* ed. H. B. Fischer 10 (Weimar: F.A. Finger-Institut für Baustoffkunde)

[6] Hunt A 2013 *Element Recovery and Sustainability* (Cambridge: Royal Society of Chemistry)

[7] Malfliet, Annelies; Pontikes; Yiannis 2015 *Combined Metal and Slag Valorisation at Metallo-Chimique* (Leuven) 12

[8] Metallo-ChimiqueProduct range 2018 Minerals and granulates *https://www.metallo.com/services*

[9] Emery, J. J. 1982 Slag utilization in pavement construction Extending aggregate resources ASTM STP

[10] Piatak N M, Parsons M B and Seal R R 2015 Characteristics and environmental aspects of slag A review *J. Ap. Geo. Chem.* **57** 236–66

[11] Alp I, Deveci H and Süngün H 2008 Utilization of flotation wastes of copper slag as raw material in cement production *J. Haz. Mat.* **159** 390–5

[12] Penpolcharoen M 2005 Utilization of secondary lead slag as construction material *Cem. Con. Res.* **35** 1050–5

[13] Mosavinezhad S H and Nabavi S E 2012 Effect of 30% Ground Granulated Blast Furnace, Lead and Zinc Slags as sand replacements on the strength of concrete *KSCE J. Civ. Eng.* **16** 989–93

[14] Alwaeli M 2013 Application of granulated lead–zinc slag in concrete as an opportunity to save natural resources *J. Rad. Phys. Chem.* **83** 54–60

[15] Su N, Wu Y-H and Mar C-Y 2000 Effect of magnetic water on the engineering properties of concrete containing granulated blast-furnace slag *Cem. Con. Res.* **30** 599–605

[16] An J, Kim J and Nam B H 2017 Investigation on impacts of municipal solid waste incineration bottom ash on cement hydration *ACI Mat. J.* **114**

[17] Tang, P., Florea, M. V. A., Spiesz, P. R., & Brouwers, H. J. H 2014 *The application of treated bottom ash in mortar as cement replacement* (Istanbul, Turkey) 6

[18] Lynn C J, Ghataora G S and Dhir OBE R K 2017 Municipal incinerated bottom ash (MIBA) characteristics and potential for use in road pavements *I. J. Pav. Res. Tech.* **10** 185–201

[19] Müller U and Rübner K 2006 The microstructure of concrete made with municipal waste incinerator bottom ash as an aggregate component *Cem. Con. Res.* **36** 1434–43

[20] Saikia N, Mertens G, van Balen K, Elsen J, van Gerven T and Vandecasteele C 2015 Pre-treatment of municipal solid waste incineration (MSWI) bottom ash for utilisation in cement mortar *J. Con. Build. Mat.* **96** 76–85

[21] Cheng A 2012 Effect of incinerator bottom ash properties on mechanical and pore size of blended cement mortars *J. Mat. Des.* **36** 859–64

[22] Ferraris M, Salvo M, Ventrella A, Buzzi L and Veglia M 2009 Use of vitrified MSWI bottom ashes for concrete production *J. Was. Man.* **29** 1041–7

[23] Mymrin V A, A. Ponte H and Impinnisi P R 2005 Potential application of acid jarosite wastes as the main component of construction materials *J. Con. Build. Mat.* **19** 141–6

[24] Mehra P, Gupta R C and Thomas B S 2016 Assessment of durability characteristics of cement concrete containing jarosite *J. Cle. Pro.* **119** 59–65

[25] Mehra P, Thomas B S, Kumar S and Gupta R C 2016 Jarosite added concrete along with fly ash Properties and characteristics in fresh state *J. Pisc.* **8** 69–71

[26] Katsioti M, Boura P, Agatzini S, Tsakiridis P E and Oustadakis P 2005 Use of jarosite/alunite precipitate as a substitute for gypsum in Portland cement *J. Cem. Con. Comp.* **27** 3–9

[27] Katsioti M, Tsakiridis P E, Leonardou-Agatzini S and Oustadakis P 2006 Examination of the jarosite-alunite precipitate addition in the raw meal for the production of sulfoaluminate cement clinker *J. Haz. Mat.* **131** 187–94

[28] Chen T and Dutrizac J 2001 Jarofix Addressing iron disposal in the zinc industry *JOM* **53** 32–5

[29] Sinha A K, Havanagi V G, Arora V K, Ranjan A and Mathur S 2012 Recycling Jarofix waste as a construction material for embankment and sub grade *J. Sol. Tech. Man.* **38** 169–81

[30] Creedy, S.; Glinin, A.; Matusewicz; R.; Hughes, Stephen; Reuter, M. A. 2013 Outotec Ausmelt Technology for treating zinc residues ERZMETALL 6

[31] Sudhölter S, Reuter M A and Kruger J 1996 Eco-Techno-Economic synthesis of process routes for the production of zinc using combinatorial optimization *Met. Mat. Trans.* **27B** 1031–44

[32] Szargut J, Morris D R and Steward F R 1988 *Exergy analysis of thermal, chemical, and metallurgical processes* (New York: Hemisphere)

[33] Usón S, Valero A and Agudelo A 2012 Thermoeconomics and Industrial Symbiosis. Effect of by-product integration in cost assessment *J. Energy* **45** 43–51

[34] Lozano M A and Valero A 1993 Theory of the exergetic cost *J. Energy* **18** 939–60

[35] Tribus M and Evans R B 1962 *A contribution to the theory of thermoeconomics* Technical report, Report no. 62e63 (Los Angeles, CA, USA: Department of Engineering UCLA)

[36] Valero, A.; Torres, C.; Serra, L. 1992 A general theory of thermoeconomics: part I. structural analysis

[37] Tsatsaronis G 1993 Thermoeconomic analysis and optimization of energy systems *Prog. in Ener. and Comb. Sci.* **19** 227–57

[38] Torres, C.; Usón, S.; Valero, A. 2011 *Thermoeconomics meets industrial ecology* (Laussane: CreateSpace) 5

[39] Valero A, Usón S, Torres C and Valero A 2010 Application of Thermoeconomics to Industrial Ecology *J. Entropy* **12** 591–612

[40] Abadías Llamas A, Valero Delgado A, Valero Capilla A, Torres Cuadra C, Hultgren M, Peltomäki M, Roine A, Stelter M and Reuter M A 2019 Simulation-based exergy, thermo-economic and environmental footprint analysis of primary copper production *Min. Eng.* **131** 51–65

[41] Song D, Yang J, Chen B, Hayat T and Alsaedi A 2016 Life-cycle environmental impact analysis of a typical cement production chain *J. App. Energy* **164** 916–23

[42] Moretti L and Caro S 2017 Critical analysis of the Life Cycle Assessment of the Italian cement industry *J. Cle. Pro.* **152** 198–210

[43] Stafford F N, Raupp-Pereira F, Labrincha J A and Hotza D 2016 Life cycle assessment of the production of cement A Brazilian case study *J. Cle. Pro.* **137** 1293–9

[44] Reuter M A, van Schaik A and Gediga J 2015 Simulation-based design for resource efficiency of metal production and recycling systems Cases - copper production and recycling, e-waste (LED lamps) and nickel pig iron *Int. J. Life Cycle Assess.* **20** 671–93

[45] Torres C 2009 Symbolic thermoeconomic analysis of energy systems. In: Exergy Energy System Analysis and Optimization 61–81

[46] Chen C, Habert G, Bouzidi Y and Jullien A 2010 Environmental impact of cement production Detail of the different processes and cement plant variability evaluation *J. Cle. Pro.* **18** 478–85

[47] Hoang J, Reuter M A, Matusewicz R, Hughes S and Piret N (2009) Top Submerged Lance Direct Zinc Smelting. Minerals Engineering, **22** 742-751

[48] HSC Chemistry 9.8 www.outotec.com

[49] GaBi www.thinkstep.com

B. Mineralogy of the raw materials using XRD

This section contains the XRD patterns of the raw materials obtained following the methodology described in chapter 2.2.1. The references used for peak identification were taken from an internal database for the cements, and from the inorganic crystal structure database of NIST, 2020 [209] for the other raw materials. Note that only the ranges of values are indicated for some of the SOCRATES residues due to confidentiality agreements. The composition of the commercial products may vary according to their production batch.

The SOCRATES residues

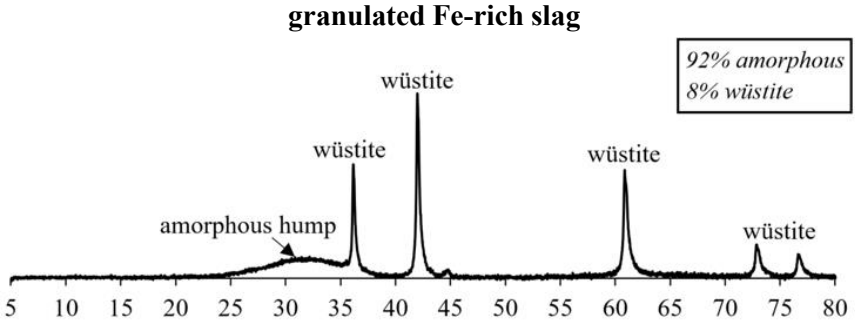

Figure B.1 *XRD pattern and Rietveld analysis of the granulated Fe-rich slag abbreviated as "granulated FS" or "slag" in this study*

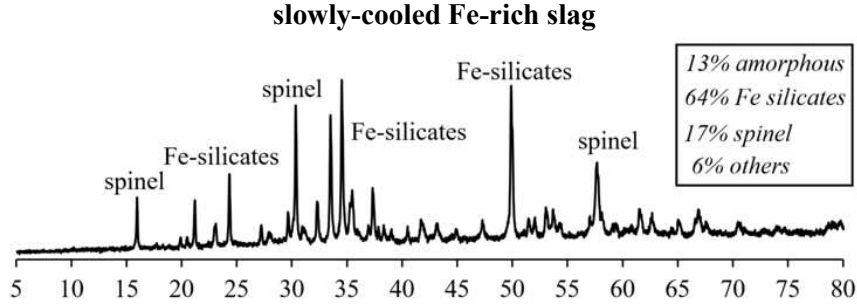

Figure B.2 *XRD pattern and Rietveld analysis of the slowly-cooled Fe-rich slag abbreviated as "slowly-cooled FS" in this study*

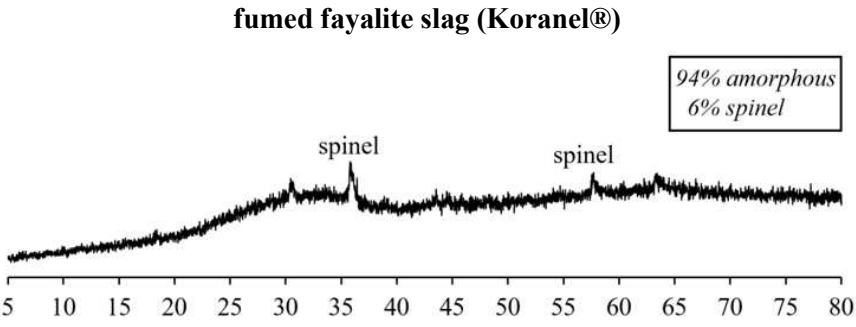

Figure B.3 *XRD pattern and Rietveld analysis of the fumed fayalite slag (Koranel®)*

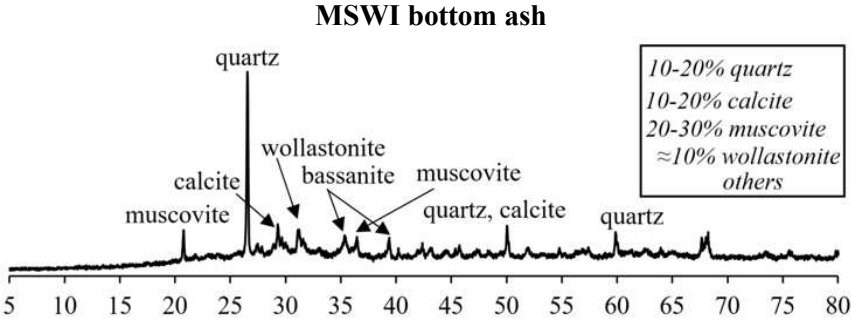

Figure B.4 *XRD pattern and Rietveld analysis of the bottom ash*

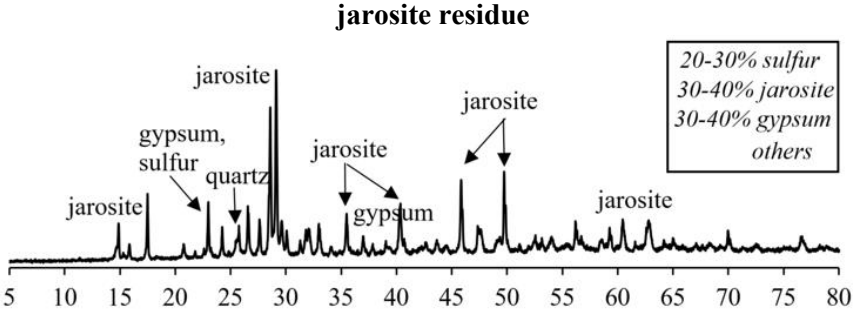

Figure B.5 *XRD pattern and Rietveld analysis of the jarosite residue*

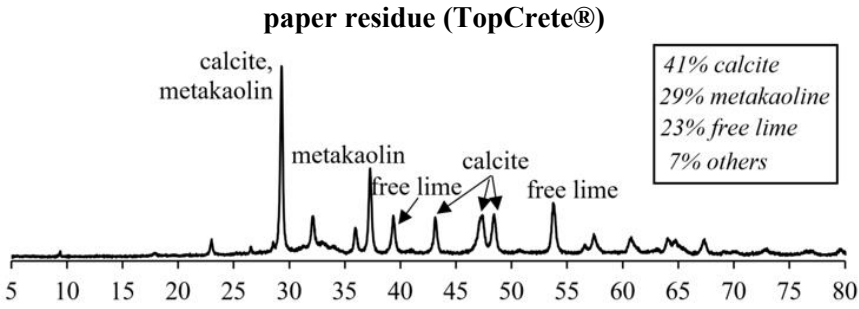

Figure B.6 *XRD pattern and Rietveld analysis of the paper residue*

Cements

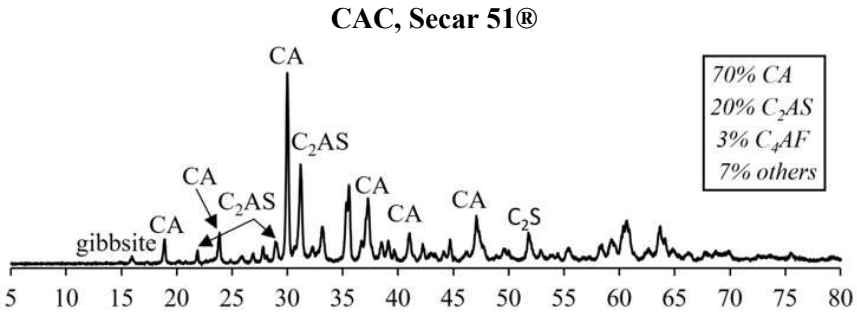

Figure B.7 *XRD pattern and Rietveld analysis of the CAC (Secar 51®) abbreviated as "CAC" in Chapters 3 and 4*

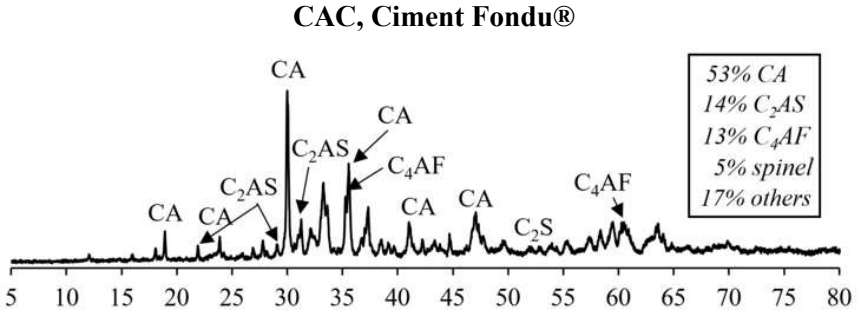

Figure B.8 *XRD pattern and Rietveld analysis of the CAC (Ciment Fondue®) abbreviated as "CAC" in Chapter 2.3.5*

Ordinary Portland cement, OPC Milke®

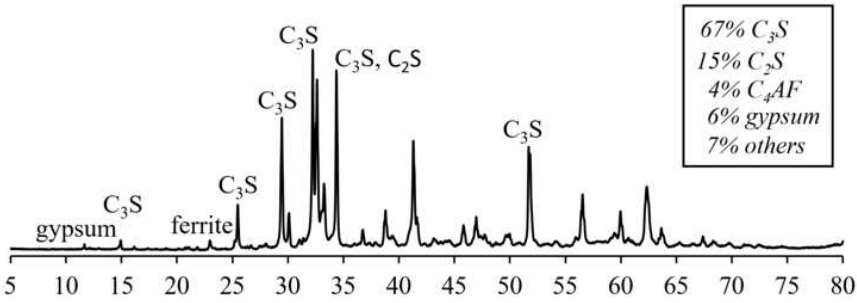

Figure B.9 *XRD pattern and Rietveld analysis of the ordinary Portland cement*

Other blend components

calcium sulfate hemihydrate, Prestia Selecta β-Hemihydrate®

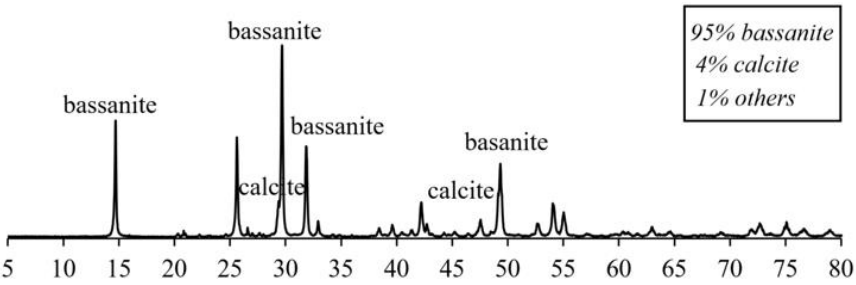

Figure B.10 *XRD pattern and Rietveld analysis of the calcium sulfate hemihydrate abbreviated as "HH" in this study*

quartz filler, Silice E400®

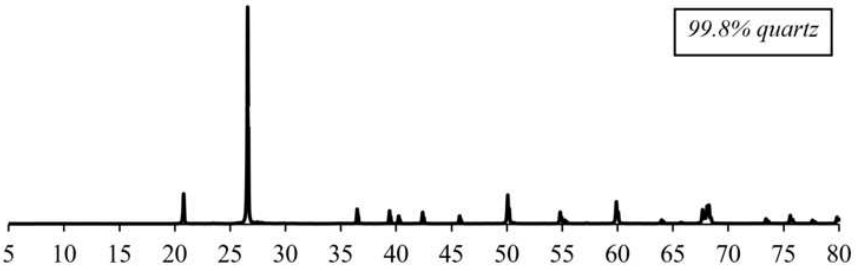

Figure B.11 *XRD pattern and Rietveld analysis of the quartz filler abbreviated as "filler" in this study*

C. Particle size distribution of raw materials

The particle size distribution of the raw materials are plotted altogether in **Figure C.1** below.

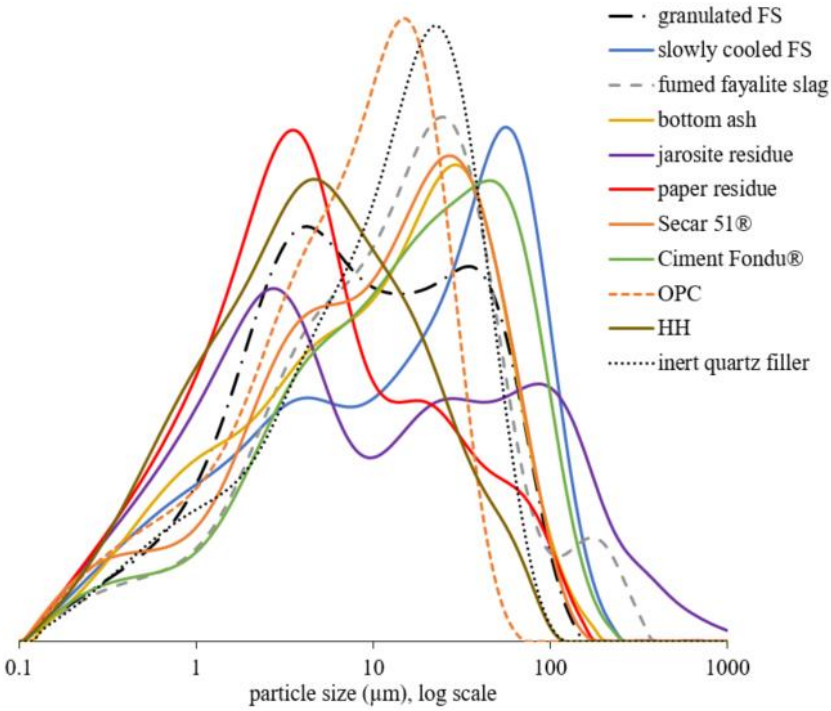

Figure C.1 *The particle size distribution of the raw materials*

D. Effect of curing condition to the mechanical strength of the mortars

In this section, the mechanical strength of mortars are compared between air-curing and under water curing conditions both at 20°C. Measurements from the slag-containing blends (A) 4.5CAC-HH and (A-TC) 4.5 CAC-HH-5TC (refer to **Table 2.3**); and their reference formulations (no SCM) are presented in **Figure D.1 and D.2**. Each data point represents the average value taken from three mortar samples. Error bars are partly presented for some of the data points for the valuation of the significance of the deviations observed among the measurements. The dotted diagonal line represents the values where the strengths measured between the two curing conditions are equal.

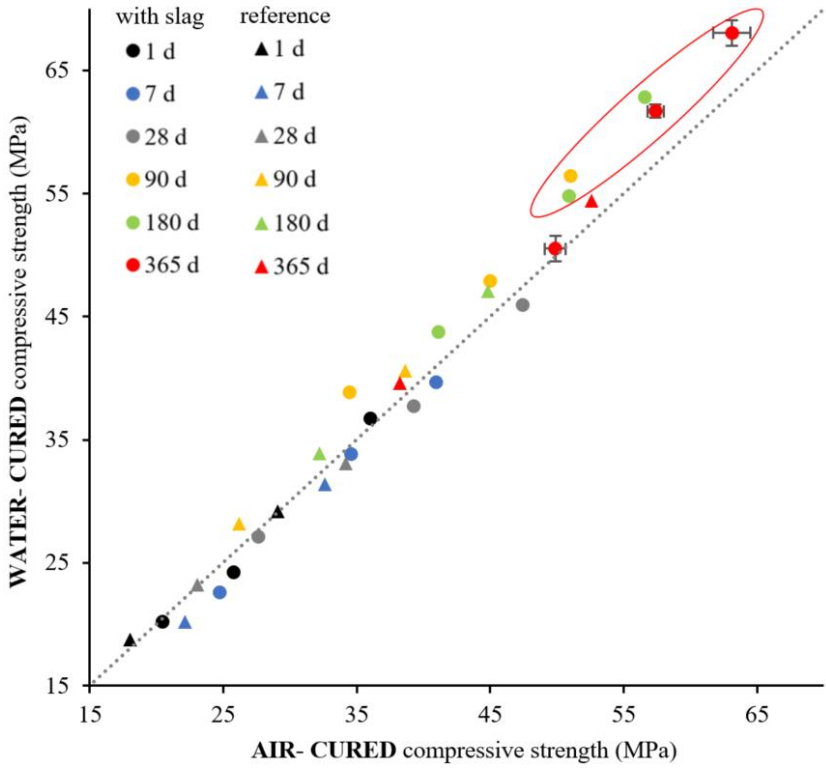

Figure D.1 *Comparison of the compressive strengths of air-cured versus water-cured mortar samples. The dotted diagonal line represents values at 1:1 ratio*

In the early stage of hydration (<90 days), no significant difference is observed between the compressive strengths of air- and water-cured mortars for all the formulations. This could support that there is sufficient

amount of water at w/b = 0.5 for the hydration reactions in the monosulfoaluminate-dominated system (section 3.3 and 3.5). However, as the slag starts to react more significantly from 90 days (section 3.2), it could be argued that more water is consumed during hydration to produce phases that contributes to the strength of the water-cured mortars. This deviation towards values above the line (ratio 1:1) at longer curing time is more evident for the slag containing samples circled in red in **Figure D.1**.

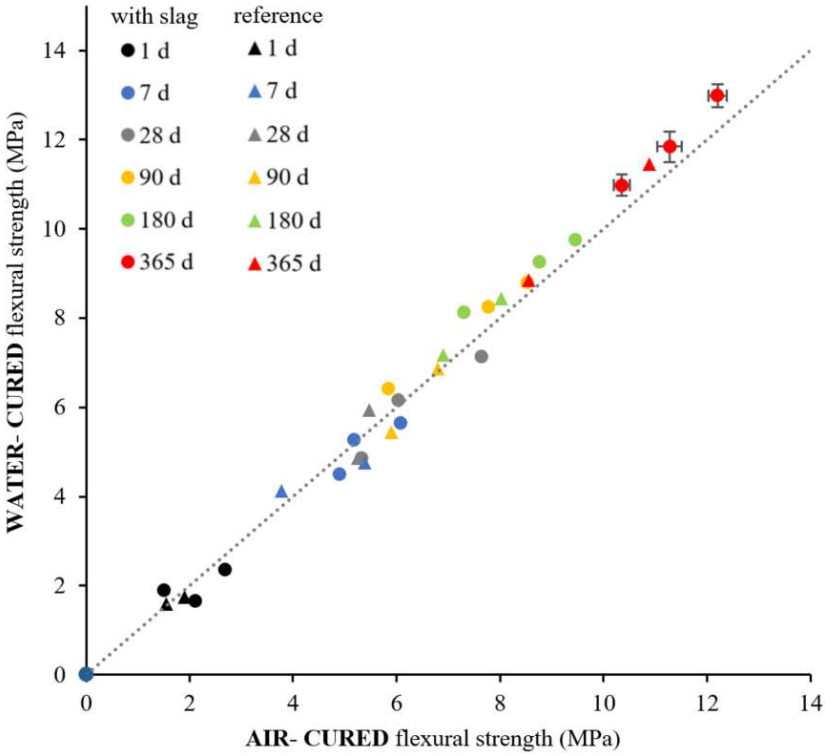

Figure D.2 *Comparison of the flexural strengths of air-cured versus water-cured mortar samples. The dotted diagonal line represents values at 1:1 ratio*

The difference observed is less pronounced for the flexural strengths (**Figure D.2**) most likely due to the smaller range of values measured from all the samples. Nonetheless, the observations in this section highlight the importance of the water-curing condition in discerning the possible long term contribution of the slag hydration to the properties of the mortars.

E. Image processing operations performed for the quantification of slag hydration degree using XCT

Image processing of the greyscale reconstructed stack images to obtain their binary stacks is executed in the the Bruker CT-Analyzer (v 1.18.8.0+) software. The series of operations programmed and performed consistently to all the converted cross sections at all curing ages consisted of the following:

Step 1: Filtering (median\round\radius 1, unsharp mask\round\radius 1)

Step 2: Global thresholding (global\83-255)

Step 3: Despeckle (remove white speckle\ less than 20 pixels)

Step 4: 3D Analysis (check: number of objects)

Step 5: Save Bitmaps

All these steps are pre-programmed in the software and can only be customized using general pre-set properties specified inside the parentheses in each step enumerated above. These filters were selected during pre-trials guided by the SEM micrographs observed under BSE and EDS detectors.

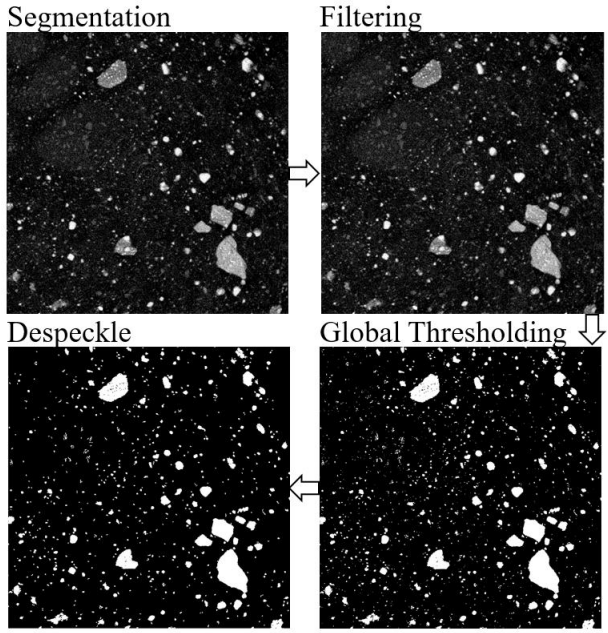

Figure E.1 *Sample image correction in Brucker CTAn software*

F. Mössbauer Spectroscopy Parameters

Using the combination of Mössbauer parameters, the Fe speciations and their atomic environment in the raw slag sample were hypothesized. The description of the relevant Mössbauer parameters presented in this section were taken from Bill, 2013 [210] and Yoshida *et al.,* 2013 [211]. An illustration is shown below for their graphical representation.

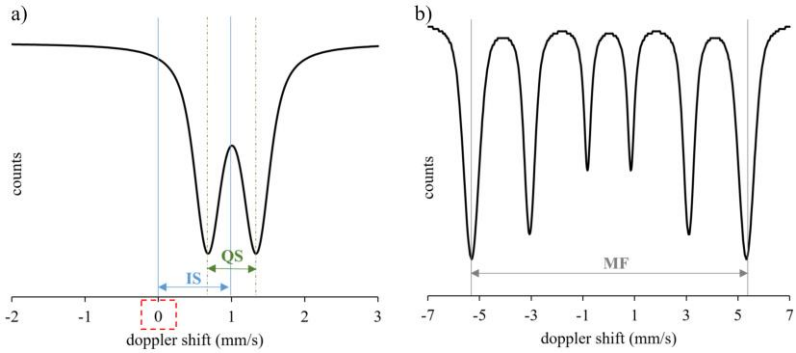

Figure F.1 *Illustration of IS, QS and MF using the Mössbauer spectra of wüstite (a) and magnetite (b)*

Isomer shift (IS)

Refers to the shift of resonance spectrum resulting from the change in the electron density around the Mössbauer nucleus. Graphically, it is depicted as the distance between the peaks and the zero on the relative velocity scale. For ^{57}Fe Mössbauer, this value describes the valence state of Fe atom.

Quadruple splitting (QS)

Describes the asymmetry of the electric filed around the Mössbauer nucleus. It measures the energy difference between the two γ-transitions for the ^{57}Fe with electric quadruple interaction. Graphically, this is represented by the difference of the velocity values corresponding to the peaks of the doublet.

Hyperfine magnetic field (MF)

A property exclusive to magnetic materials. The energy levels in the Fe nucleus splits into multiple components (6 components for magnetite) due to the presence of magnetic field.

Total Gaussian-type spreading of the quadruple split (ΔQS)

Statistical parameter related to the QS derived from the least square minimization fitting in the IMSG software. Gaussian-type symmetric spreading of the QS values was allowed during the fitting.

Total area (A)

The total area fitted to each Fe component proportional to the quantity (percent composition) that they represent in the modelled spectrum.

During the fitting, the typical errors for the IS and QS were ± 0.02 mm/s and ± 5 % for the A. The components selected were based on the results from complementary characterization techniques and literature data on synthetic systems. Chi-squared test was used to evaluate the best fit for each dataset evaluated.

G. Estimation of slag hydration degree using SEM-BSE and image analysis

Using the ImageJ software integrated with the MorpholibJ plug-in, the image correction and the total slag area quantification using the SEM-BSE micrographs is achieved following the operations described below:

Step 1: Adjust threshold (155-254)

Step 2: Area opening: remove particles below 100 pixels (MorpholibJ)

Step 3: Fill holes (MorpholibJ)

Step 4: Opening: removing long particles (square/3, MorpholibJ)

Step 5: Area opening: remove particles below 100 pixels (MorpholibJ)

Step 6: Dilation (square/1, MorpholibJ)

Step 7: Set the scale according to the known distance

Step 8: Calculate total area in binary image (Analyze Particles)

All these steps are consistently followed in the software. The figure below demonstrates these operations:

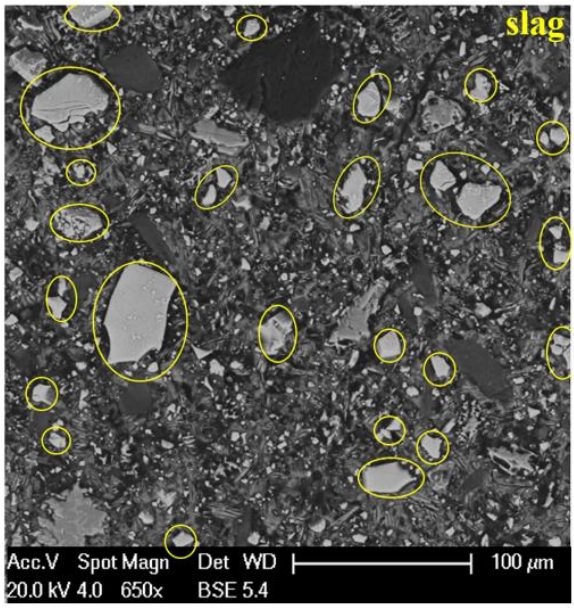

Figure G.1 *SEM-BSE image of formulation A.*
Some of the slag particles are marked in yellow identified with the help of EDS analyses

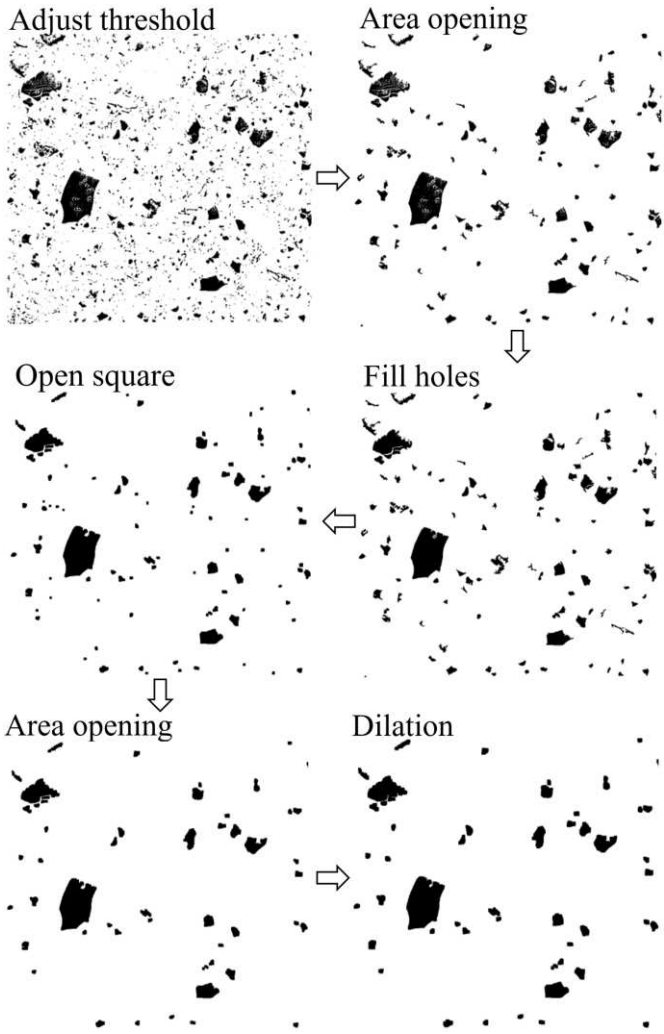

Figure G.2 *Sample image correction using Image J software*

H. Estimation of the theoretical slag volume in paste sample for XCT

Estimated for 100 g of anhydrous paste prior to hydration and without accounting for porosity:

	wt, g	wt, %	density, g/cm^3	vol, cm^3	vol, %
CAC	57.3	34.7	3.0	11.4	19.5
HH	12.7	7.7	2.6	3.0	5.1
slag	**30.0**	**18.2**	**3.7**	**5.0**	**8.4**
water	65.0	39.4	1.0	39.4	67.0
total	165.0	100.0	10.3	58.8	100.0

I. Supplementary data for thermodynamic modelling

GEMS thermodynamic models calculate the chemical speciation from a bulk composition in the equilibrium state, by minimizing the Gibbs free energy of a system at a given temperature and pressure.

The following were applied during the modelling:

- The databases psi-nagra, cemdata 18.01 and claysor 18-12 v0.1 were activated in creating the Project files
- The w/b ratio used for the models was 0.65 corresponding to the experimental value used for the paste samples. The only exception made was for the reference formulation in the binary system (section 3.3.1) where the w/b ratio was increased to 0.80 in order to provide sufficient water for complete hydration, particularly in regions between 50-60 wt% CAC content.
- CAC, HH and PC components were introduced in their mineral forms while oxides were used for the slag's amorphous components
- Some minor (< 1 wt%) components of the raw materials (i.e., ZnO, CuO, P_2O_5 from the slag) were considered unreactive during the modelling and therefore assigned to the "inert" phase. The components used could be referred to in the codes provided.
- Wüstite from the slag was considered unreactive and was added in the "inert" component. For the amorphous fraction of the slag, only 50% was allowed to react roughly guided by the estimations from XCT after 1 year of hydration.
- Fe-bearing hydrates that were permitted in the equilibrium state include CSH, ettringite, monosulfates, hydrogarnet, monocarbonate, ferrihydrites and other AFm and AFt phases. Phases that were deactivated included pyrite, goethite, elemental iron, hematite, magnetite, etc.
- The mineralogical composition (CAC, HH and PC) and chemical assay (slag) of each component presented in Chapter 2 were entered in the modC array columns.
- For some models, extra O_2 component was added to aid the balance

CAC-HH (reference) system

In the Process Simulators of GEMS, the code used for the **Controls** section was as follows:

```
$modC0 CAC modC1 HH
xa_[{Al2O3}] =: 0.01* (modC[0][0]*cNu+ modC[0][1]*(100-cNu));
```

```
xa_[{C2S}] =: 0.01* (modC[1][0]*cNu+ modC[1][1]*(100-cNu));
xa_[{CA}] =: 0.01* (modC[2][0]*cNu+ modC[2][1]*(100-cNu));
xa_[{CaCO3}] =: 0.01* (modC[3][0]*cNu+ modC[3][1]*(100-cNu));
xa_[{CaO}] =: 0.01* (modC[4][0]*cNu+ modC[4][1]*(100-cNu));
xa_[{CaSO4_05H2O}] =: 0.01* (modC[5][0]*cNu+ modC[5][1]*(100-cNu));
xa_[{MgO}] =: 0.01* (modC[6][0]*cNu+ modC[6][1]*(100-cNu));
xa_[{SiO2}] =: 0.01* (modC[7][0]*cNu+ modC[7][1]*(100-cNu));
xa_[{C4AF}] =: 0.01* (modC[8][0]*cNu+ modC[8][1]*(100-cNu));
xa_[{K2O}] =: 0.01* (modC[9][0]*cNu+ modC[9][1]*(100-cNu));
xa_[{Aqua}] =: 65;
xa_[{O2}] =: 10;
```

In the **Sampling** section of the Process Simulators, the following code was used to calculate the phase assemblage composition in weight percentages:

```
xp[J] =: J;
yp[J][0] =: phM[{CSHQ}];
yp[J][1] =: phM[{straetlingite}];
yp[J][2] =: phM[{ettringite}];
yp[J][3] =: phM[{SO4_OH_AFm}];
yp[J][4] =: phM[{OH_SO4_AFm}];
yp[J][5] =: phM[{SO4_CO3_AFt}];
yp[J][6] =: phM[{CO3_SO4_AFt}];
yp[J][7] =: phM[{Gibbsite}];
yp[J][8] =: phM[{C3AH6}];
yp[J][9] =: phM[{CAH10}];
yp[J][10] =: phM[{C4AH11}];
yp[J][11] =: phM[{C4AsH12}];
yp[J][12] =: phM[{Calcite}];
yp[J][13] =: phM[{C3FS0.84H4.32}];
yp[J][14] =: phM[{C3FS1.34H3.32}];
yp[J][15] =: phM[{Gypsum}];
yp[J][16] =: phM[{hemihydrate}];
yp[J][17] =: phM[{Ferrihydrite-am}];
yp[J][18] =: phM[{OH-hydrotalcite}];
yp[J][19] =: phM[{aq_gen}];
yp[J][20] =: 0.01* (modC[10][0]*cNu+ modC[10][1]*(100-cNu));
```

CAC-HH-slag system

In the Process Simulators of GEMS, the code used for the **Controls** section was as follows:

```
$modC0 S51 modC1 HH modC2 slag

xa_[{Al2O3}] =: 0.01*(cNu*modC[0][0]+modC[0][1]*(70-cNu)+modC[0][2]*30);
xa_[{C2S}] =: 0.01*(cNu*modC[1][0]+modC[1][1]*(70-cNu)+modC[1][2]*30);
xa_[{CA}] =: 0.01*(cNu*modC[2][0]+modC[2][1]*(70-cNu)+modC[2][2]*30);
xa_[{CaCO3}] =: 0.01*(cNu*modC[3][0]+modC[3][1]*(70-cNu)+modC[3][2]*30);
xa_[{CaO}] =: 0.01*(cNu*modC[4][0]+modC[4][1]*(70-cNu)+modC[4][2]*30);
xa_[{CaSO4_05H2O}] =: 0.01*(cNu*modC[5][0]+modC[5][1]*(70-
cNu)+modC[5][2]*30);
xa_[{SiO2}] =: 0.01*(cNu*modC[6][0]+modC[6][1]*(70-cNu)+modC[6][2]*30);
xa_[{C4AF}] =: 0.01*(cNu*modC[7][0]+modC[7][1]*(70-cNu)+modC[7][2]*30);
xa_[{FeO}] =: 0.01*(cNu*modC[8][0]+modC[8][1]*(70-cNu)+modC[8][2]*30);
xa_[{MgO}] =: 0.01*(cNu*modC[9][0]+modC[9][1]*(70-cNu)+modC[9][2]*30);
xa_[{Na2O}] =: 0.01*(cNu*modC[10][0]+modC[10][1]*(70-cNu)+modC[10][2]*30);
xa_[{K2O}] =: 0.01*(cNu*modC[11][0]+modC[11][1]*(70-cNu)+modC[11][2]*30);

xa_[{Aqua}] =: 65;
xa_[{O2}] =: 10;
```

CAC-HH-PC (reference) system

In the Process Simulators of GEMS, the code used for the **Controls** section was as follows:

```
$modC0 S51 modC1 HH modC2 PC

xa_[{Gypsum}] =:0.01*(cNu*modC[0][0]+modC[0][1]*(70-cNu)+modC[0][2]*30);
xa_[{C3A}] =: 0.01*(cNu*modC[1][0]+modC[1][1]*(70-cNu)+modC[1][2]*30);
xa_[{C3S}] =: 0.01*(cNu*modC[2][0]+modC[2][1]*(70-cNu)+modC[2][2]*30);
xa_[{Al2O3}] =: 0.01*(cNu*modC[3][0]+modC[3][1]*(70-cNu)+modC[3][2]*30);
xa_[{C2S}] =: 0.01*(cNu*modC[4][0]+modC[4][1]*(70-cNu)+modC[4][2]*30);
xa_[{CA}] =: 0.01*(cNu*modC[5][0]+modC[5][1]*(70-cNu)+modC[5][2]*30);
xa_[{CaCO3}] =: 0.01*(cNu*modC[6][0]+modC[6][1]*(70-cNu)+modC[6][2]*30);
xa_[{CaO}] =: 0.01*(cNu*modC[7][0]+modC[7][1]*(70-cNu)+modC[7][2]*30);
xa_[{CaSO4_05H2O}] =: 0.01*(cNu*modC[8][0]+modC[8][1]*(70-
cNu)+modC[8][2]*30);
xa_[{SiO2}] =: 0.01*(cNu*modC[9][0]+modC[9][1]*(70-cNu)+modC[9][2]*30);
xa_[{C4AF}] =: 0.01*(cNu*modC[10][0]+modC[10][1]*(70-cNu)+modC[10][2]*30);
xa_[{K2O}] =: 0.01*(cNu*modC[11][0]+modC[11][1]*(70-cNu)+modC[11][2]*30);
xa_[{Aqua}] =: 65;
```

In the Process Simulators of GEMS, the code used for the **Controls** section was as follows:

```
xp[J] =: J;
yp[J][0] =: phM[{Gypsum}];
yp[J][1] =: phM[{ettringite}];
yp[J][2] =: phM[{SO4_OH_AFm}];
yp[J][3] =: phM[{straetlingite}];
yp[J][4] =: phM[{Gibbsite}];
yp[J][5] =: phM[{CSHQ}];
yp[J][6] =: phM[{C3AH6}];
yp[J][7] =: phM[{Portlandite}];
yp[J][8] =: phM[{C3(AF)S0.84H}];
yp[J][9] =: phM[{Ferrihydrite-am}];
yp[J][10] =: phM[{Ferrihydrite-mc}];
yp[J][11] =: 0.01*(cNu*modC[12][0]+modC[12][1]*(70-cNu)+modC[12][2]*30);
yp[J][12] =: phM[{aq_gen}];
```

This was changed to the following code to obtain the composition in volume percentages instead:

```
xp[J] =: J;
yp[J][0] =: phVol[{Gypsum}];
yp[J][1] =: phVol[{ettringite}];
yp[J][2] =: phVol[{SO4_OH_AFm}];
yp[J][3] =: phVol[{straetlingite}];
yp[J][4] =: phVol[{Gibbsite}];
yp[J][5] =: phVol[{CSHQ}];
yp[J][6] =: phVol[{C3AH6}];
yp[J][7] =: phVol[{Portlandite}];
yp[J][8] =: phVol[{C3(AF)S0.84H}];
yp[J][9] =: phVol[{Ferrihydrite-am}];
yp[J][10] =: phVol[{Ferrihydrite-mc}];
yp[J][11] =: 0.01*((cNu*modC[12][0]+modC[12][1]*(70-cNu)+modC[12][2]*30)/3);
yp[J][12] =: phVol[{aq_gen}];
```

CAC-HH-PC-slag system

In the Process Simulators of GEMS, the code used for the **Controls** section was as follows:

```
$modC0 Secar51 modC1 HH modC2PC mod3slag
```

```
xa_[{Gypsum}] =:0.01*(cNu*modC[0][0]+modC[0][1]*(40-cNu)+modC[0][2]*30+
modC[0][3]*30);
xa_[{C3A}] =: 0.01*(cNu*modC[1][0]+modC[1][1]*(40-cNu)+modC[1][2]*30+
modC[1][3]*30);
xa_[{C3S}] =: 0.01*(cNu*modC[2][0]+modC[2][1]*(40-cNu)+modC[2][2]*30+
modC[2][3]*30);
xa_[{Al2O3}] =: 0.01*(cNu*modC[3][0]+modC[3][1]*(40-cNu)+modC[3][2]*30+
modC[3][3]*30);
xa_[{C2S}] =: 0.01*(cNu*modC[4][0]+modC[4][1]*(40-cNu)+modC[4][2]*30+
modC[4][3]*30);
xa_[{CA}] =: 0.01*(cNu*modC[5][0]+modC[5][1]*(40-cNu)+modC[5][2]*30+
modC[5][3]*30);
xa_[{CaCO3}] =: 0.01*(cNu*modC[6][0]+modC[6][1]*(40-cNu)+modC[6][2]*30+
modC[6][3]*30);
xa_[{CaO}] =: 0.01*(cNu*modC[7][0]+modC[7][1]*(40-cNu)+modC[7][2]*30+
modC[7][3]*30);
xa_[{CaSO4_05H2O}] =: 0.01*(cNu*modC[8][0]+modC[8][1]*(40-cNu)+
modC[8][2]*30+modC[8][3]*30);
xa_[{SiO2}] =: 0.01*(cNu*modC[9][0]+modC[9][1]*(40-cNu)+modC[9][2]*30+
modC[9][3]*30);
xa_[{C4AF}] =: 0.01*(cNu*modC[10][0]+modC[10][1]*(40-cNu)+modC[10][2]*30+
modC[10][3]*30);
xa_[{FeO}] =: 0.01*(cNu*modC[11][0]+modC[11][1]*(40-
cNu)+modC[11][2]*30+modC[11][3]*30);
xa_[{MgO}] =: 0.01*(cNu*modC[12][0]+modC[12][1]*(40-
cNu)+modC[12][2]*30+modC[12][3]*30);
xa_[{Na2O}] =: 0.01*(cNu*modC[13][0]+modC[13][1]*(40-
cNu)+modC[13][2]*30+modC[13][3]*30);
xa_[{K2O}] =: 0.01*(cNu*modC[14][0]+modC[14][1]*(40-
cNu)+modC[14][2]*30+modC[14][3]*30);
xa_[{Aqua}] =: 65;
xa_[{O2}] =: 25;
```

In the **Sampling** section of the Process Simulators, the following code was used to calculate the phase assemblage composition in weight percentages:

```
xp[J] =: J;
yp[J][0] =: phM[{Gypsum}];
yp[J][1] =: phM[{ettringite}];
yp[J][2] =: phM[{ettringite-AlFe}];
yp[J][3] =: phM[{SO4_OH_AFm}];
yp[J][4] =: phM[{monosulph-AlFe}];
yp[J][5] =: phM[{straetlingite}];
yp[J][6] =: phM[{Gibbsite}];
```

```
yp[J][7] =: phM[{CSHQ}];
yp[J][8] =: phM[{CNASH}];
yp[J][9] =: phM[{C3AH6}];
yp[J][10] =: phM[{Portlandite}];
yp[J][11] =: phM[{C3(AF)S0.84H}];
yp[J][12] =: phM[{Ferrihydrite-am}];
yp[J][13] =: phM[{Calcite}];
yp[J][14] =: phM[{C3FS0.84H4.32}];
yp[J][15] =: phM[{C3FS1.34H3.32}];
yp[J][16] =: phM[{MgAl-OH-LDH}];
yp[J][17] =: phM[{OH-hydrotalcite}];
yp[J][18]] =: 0.01*(cNu*modC[15][0]+modC[15][1]*(40-cNu)+modC[15][2]*30+
modC[15][3]*30);
yp[J][19] =: phM[{aq_gen}];
```

This was changed to the following code to obtain the composition in volume percentages instead:

```
xp[J] =: J;
yp[J][0] =: phVol[{Gypsum}];
yp[J][1] =: phVol[{ettringite}];
yp[J][2] =: phVol[{ettringite-AlFe}];
yp[J][3] =: phVol[{SO4_OH_AFm}];
yp[J][4] =: phVol[{monosulph-AlFe}];
yp[J][5] =: phVol[{straetlingite}];
yp[J][6] =: phVol[{Gibbsite}];
yp[J][7] =: phVol[{CSHQ}];
yp[J][8] =: phVol[{CNASH}];
yp[J][9] =: phVol[{C3AH6}];
yp[J][10] =: phVol[{Portlandite}];
yp[J][11] =: phVol[{C3(AF)S0.84H}];
yp[J][12] =: phVol[{Ferrihydrite-am}];
yp[J][13] =: phVol[{Calcite}];
yp[J][14] =: phVol[{C3FS0.84H4.32}];
yp[J][15] =: phVol[{C3FS1.34H3.32}];
yp[J][16] =: phVol[{MgAl-OH-LDH}];
yp[J][17] =: phVol[{OH-hydrotalcite}];
yp[J][18]] =: 0.01*(((cNu*modC[15][0]+modC[15][1]*(40-cNu)+modC[15][2]*30+
modC[15][3]*30))/3.5);
yp[J][19] =: phVol[{aq_gen}];
```

J. Supplementary data for Mössbauer spectroscopy

This appendix contains supplementary calculations and graphs used in the Mössbauer spectra fitting discussed in Chapters 3 and 4.

Estimating the expected absorption area of wüstite

Assuming that the wüstite from slag is not participating in hydration based on the findings from several characterization techniques, its absorption area is expected to be consistent throughout the curing period and could be roughly estimated as follows:

$$AA_{T,w\ddot{u}stite} = \frac{W_{slag} in\ 100\ g\ paste \times W_{w\ddot{u}stite}\ in\ slag}{Fe\ contribution_{slag} + Fe\ contribution_{cement}\ in\ 100 g\ paste} \times 100$$

$$AA_{T,w\ddot{u}stite} = \frac{(30)(8\%)}{(46)(30) + (1.6)(57)} \times 100$$

$$AA_{T,w\ddot{u}stite} = 16.3\ \%$$

where: AA_T is the estimated theoretical absorption area; W is weight; and the Fe contributions are calculated by multiplying the Fe_2O_3 analysis of slag and CAC from XRD to their corresponding weights in 100 g of paste.

The estimated area increases up to 17.4 % when the Fe contribution of the CAC is not considered (given the poor signals presented in Chapter 2 section 2.2.5), which makes the value closer to the 18.2 % obtained from the Mössbauer spectrum of the raw slag. Other source of deviation could be attributed to the fact that Fe was measured only as Fe_2O_3 in the XRD to be consistent with the cement samples, whereas it is clear that various other speciation exist.

Calculating the slag hydration degree based on the absorption areas

As mentioned in the Methodology (Chapter 2), the slag hydration degree was estimated based on the changes in the total absorption areas assigned to the components of the unreacted slag particles (**Equation 2.5**). These components consist of G1, G2, G3 and M1 for Model 1; and G4 and M1 for Model 2. Using the absorption areas obtained for these components (section 3.4.3), the results were plotted in **Figure J.1**. However, these values are problematic due to the overestimation of wüstite, especially in Model 2, as discussed in Chapter 3. In fact, when the M1 (wüstite)

component was eliminated from the calculations for both models, the resulting hydration degrees became more comparable (**Figure J.2**).

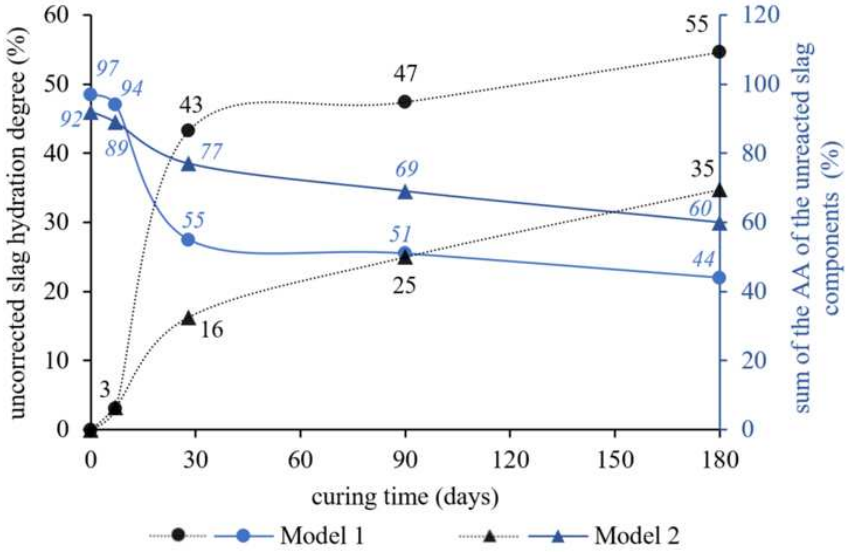

Figure J.1 *The uncorrected slag hydration degree (primary axis) and the sum of AA of the unreacted slag components (secondary axis)*

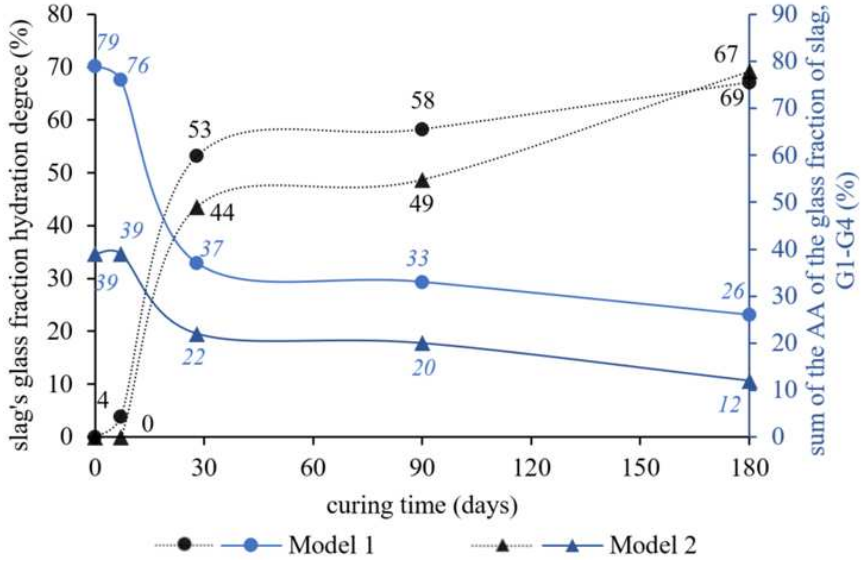

Figure J.2 *The hydration degree of the slag's glass fraction (primary axis) and the sum of the AA of the unreacted slag's glass components (secondary axis)*

$$\alpha_{slag,corrected}\,(\%) = \frac{(\Sigma AA_{Gx,raw\ slag} + AA_{T,wüstite}) - (\Sigma AA_{Gx,unreacted\ slag,i} + AA_{T,wüstite})}{\Sigma AA_{Gx,raw\ slag} + AA_{T,wüstite}} \times 100$$

Or simply:

$$\alpha_{slag,corrected}\,(\%) = \frac{\Sigma AA_{Gx,raw\ slag} - \Sigma AA_{Gx,unreacted\ slag,i}}{\Sigma AA_{raw\ slag} + AA_{T,wüstite}} \times 100$$

where: α is degree of slag hydration; ΣAA is the summation of the absorption areas; *Gx* are the glass components G1-G3 for Model 1 and G4 for Model 2; $AA_{T,wüstite}$ is equal to 16.3% as shown in the preceding section of this appendix; and *i* is the curing time for which α is estimated

Note that this calculation assumes that wüstite is unreactive throughout the 1 year curing and that the signature from the Fe in the CAC is negligible. Both assumptions were supported by the findings from the other techniques.

Additional figures from Model 1

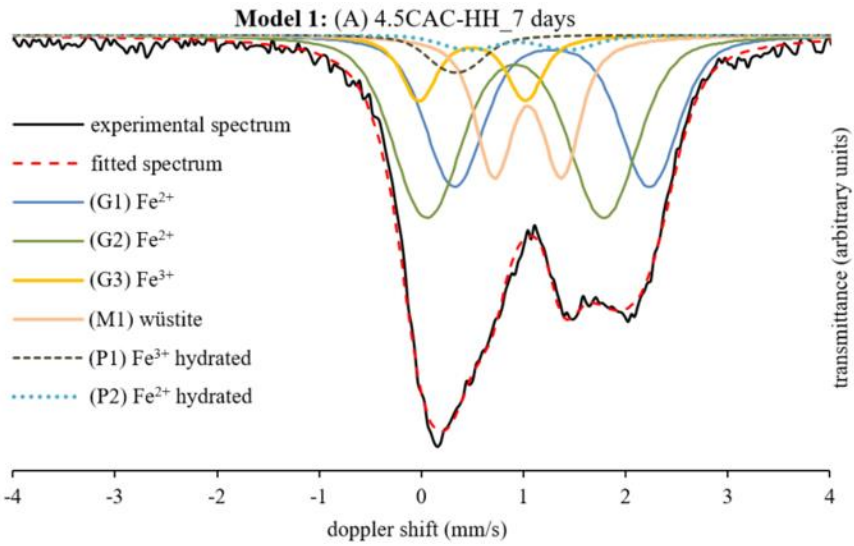

Figure J.3 *Mössbauer spectrum and components of formulation A (after 7 days of curing) derived using Model 1*

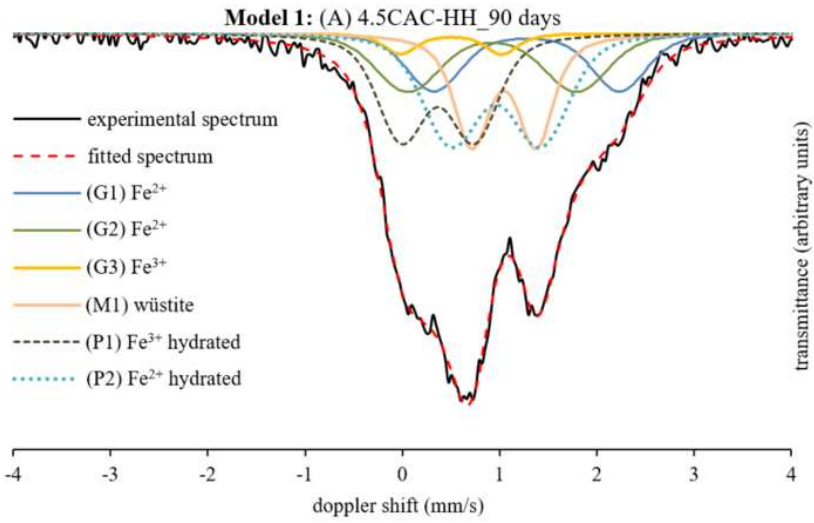

Figure J.4 *Mössbauer spectrum and components of formulation A (after 90 days of curing) derived using Model 1*

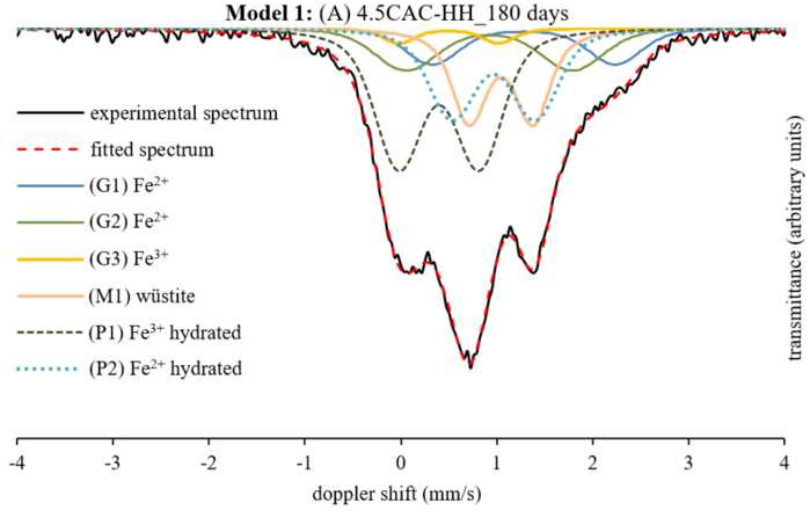

Figure J.5 *Mössbauer spectrum and components of formulation A (after 180 days of curing) derived using Model 1*

Additional figures from Model 2

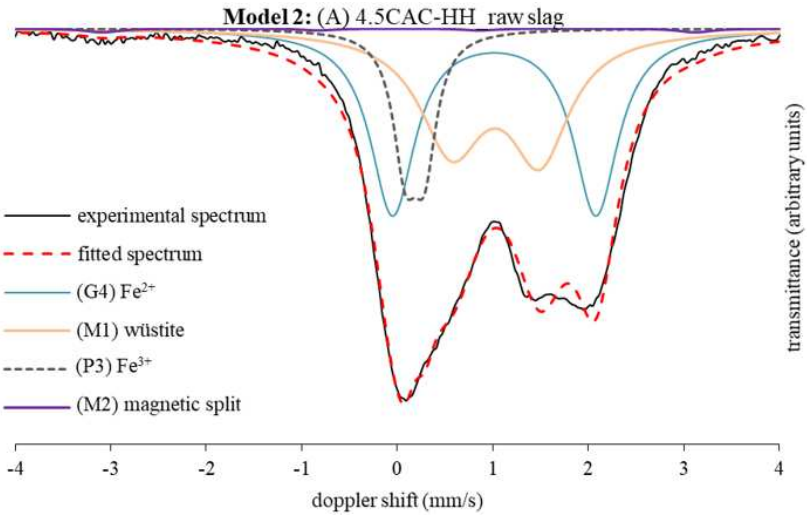

Figure J.6 *Mössbauer spectrum and components of the raw slag derived using Model 2*

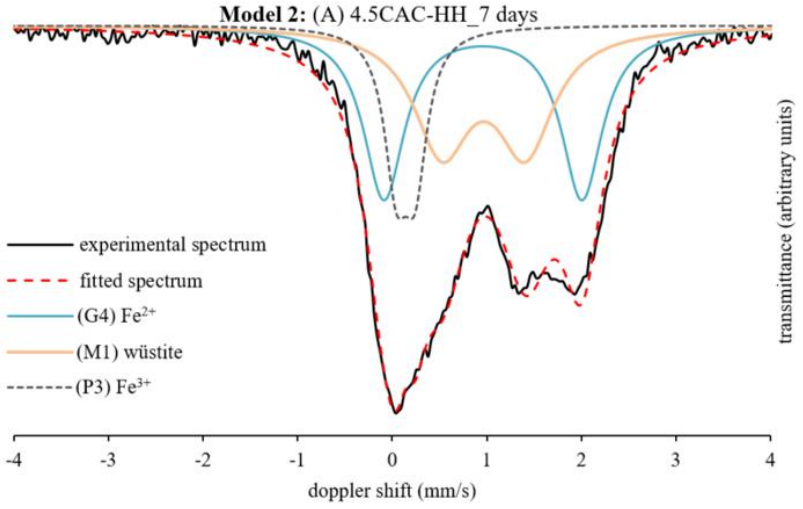

Figure J.7 *Mössbauer spectrum and components of formulation A (after 7 days of curing) derived using Model 2*

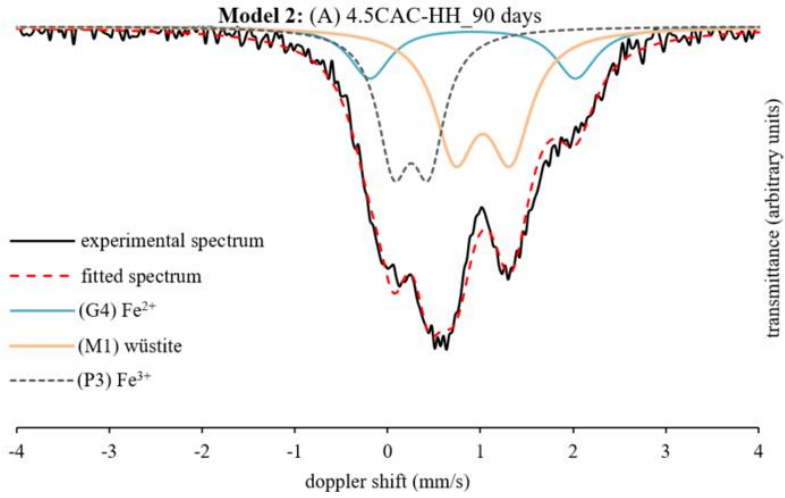

Figure J.8 *Mössbauer spectrum and components of formulation A (after 90 days of curing) derived using Model 2*

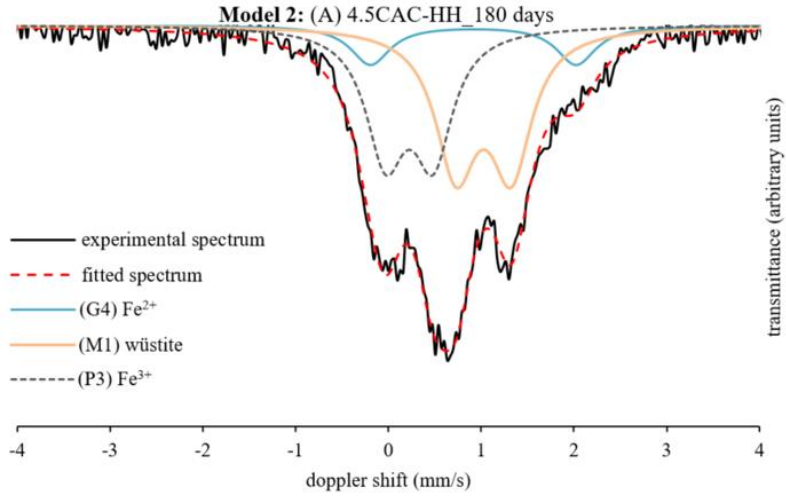

Figure J.9 *Mössbauer spectrum and components of formulation A (after 180 days of curing) derived using Model 2*

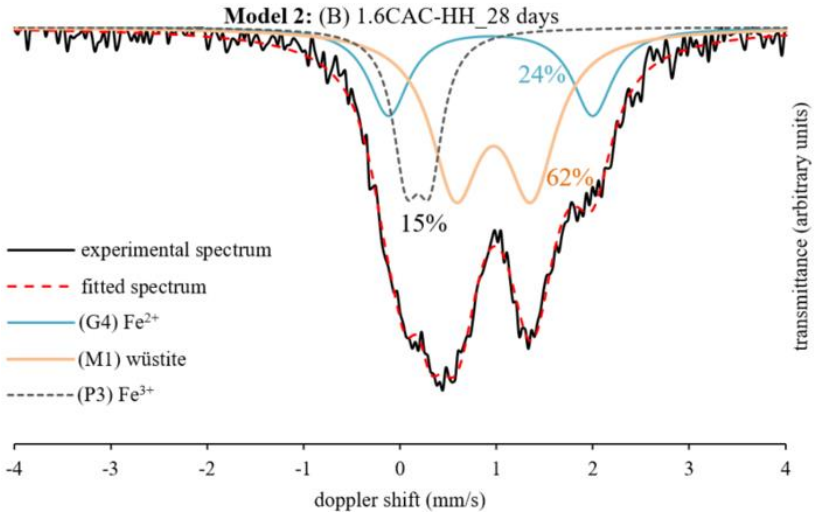

Figure J.10 *Mössbauer spectrum and components of formulation B (after 28 days of curing) derived using Model 2*

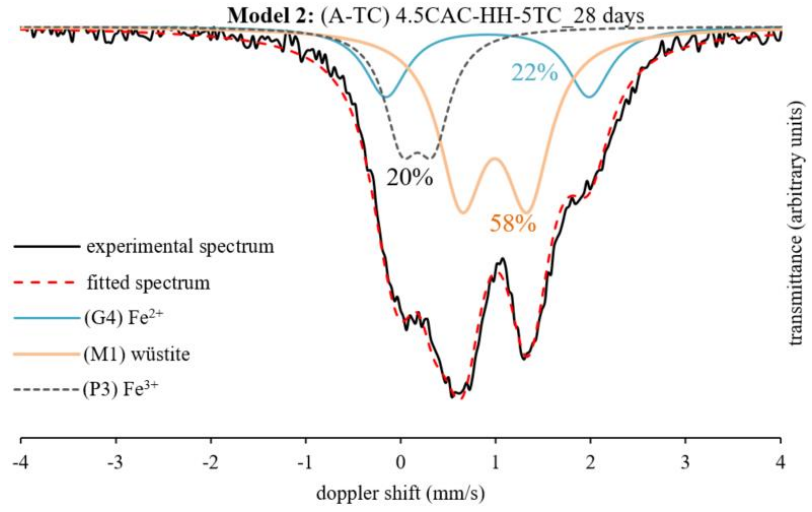

Figure J.11 *Mössbauer spectrum and components of formulation A-TC (after 28 days of curing) derived using Model 2*

K. Hydration of pure PC system

Pure PC was hydrated at 0.6 w/c ratio following the same procedure for the paste samples described in section 2.1.4. XRD, TGA, and ATR-FTIR were used to characterize the phase assemblage of the hydrated samples after 1, 7 and 28 days of hydration.

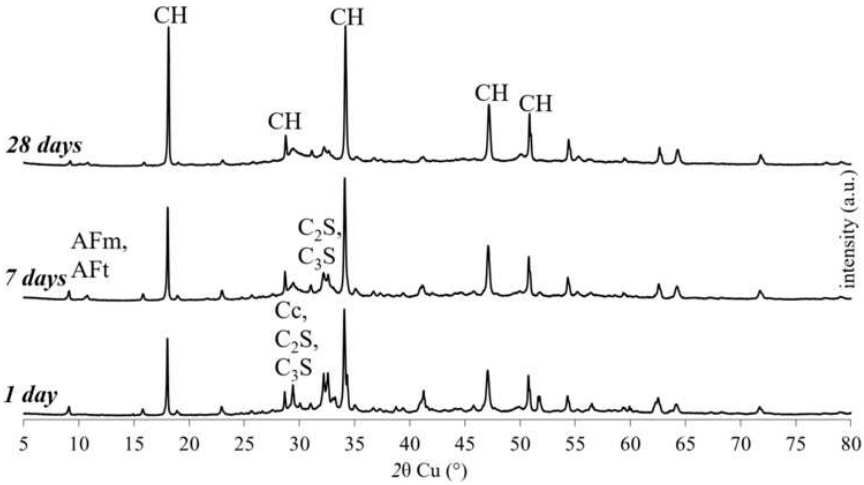

Figure K.1 *XRD patterns of pure PC paste after 1, 7 and 28 days of hydration*

From both the XRD and DTG patterns alone, it is clear that the hydrated system is dominated by portlandite (CH) and the amorphous C-S-H (CSH). The sharp diffraction peak of the CH easily masked the peaks of the minor hydrate phases such as calcite, ettringite and other calcium aluminate hydrate phases. The DTG curves were critical in characterizing the presence of amorphous C-S-H and in delineating the position of its peak relative to ettringite: C-S-H at 90-140°C, and ettringite at around 140°C. The latter proves to be essential in interpreting the patterns of formulations A-PC and B-PC in chapter 4. In addition, the peaks at around 172°C could be assigned to the formation of minor amounts of monosulfoaluminates. A small shoulder at 92°C could be due to residual water or isopropanol during the sample preparation.

The ATR-FTIR spectra are dominated by the strong Si-O peak at 950 cm^{-1} assigned to the asymmetric stretching vibration band of C-S-H. Out of plane and in plane vibration bands between 450 and 500 cm^{-1} were also assigned to C-S-H. The sharp peaks at around 3600 cm^{-1} are the signature of the O-H band in portlandite. The diminishing peak at around 1110cm^{-1}

most likely corresponds to the Si-O asymmetric vibration bands of the anhydrous alite and belite phases of PC.

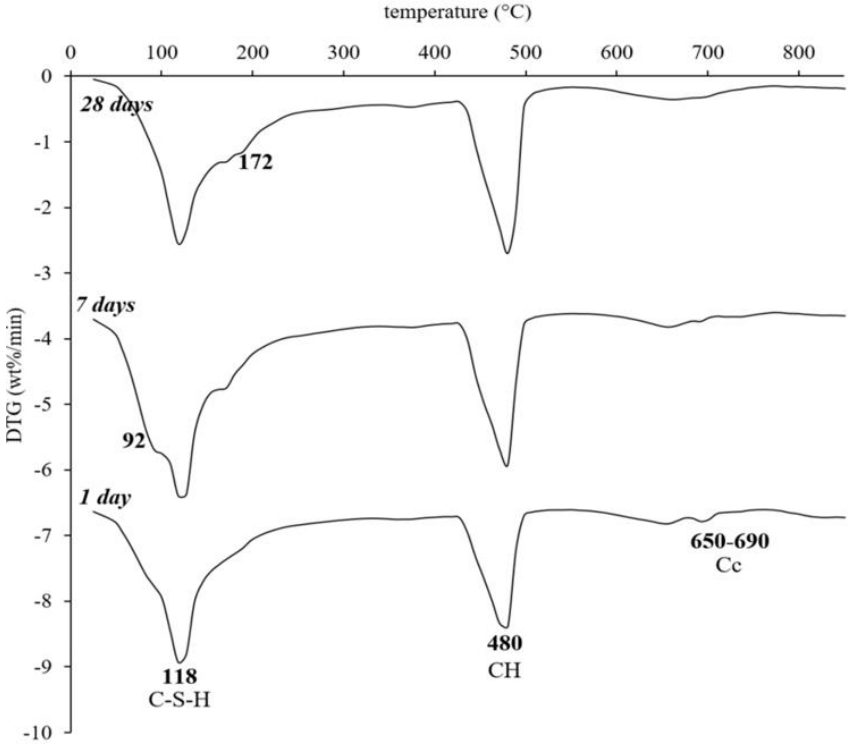

Figure K.2 *DTG curves of pure PC paste after 1, 7 and 28 days of hydration*

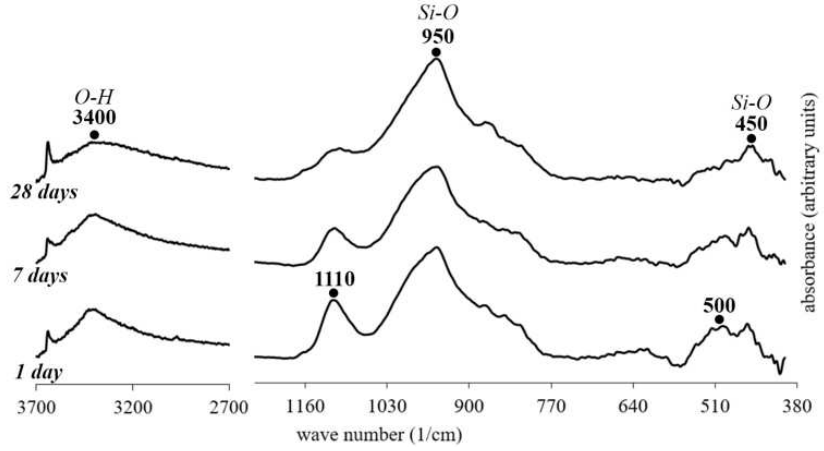

Figure K.3 *ATR-FTIR spectra of pure PC paste after 1, 7 and 28 days of hydration*

List of Publications

Part of the results of this work has been previously presented by the author in the following publications:

Journal articles

- J. Astoveza; R. Trauchessec; R. Soth ; Y. Pontikes, Properties of Calcium Aluminate Blended Cement incorporating Fe-rich Slag: Evolution over a Curing Period of 1 Year . Journal of Construction and Building Materials. (2021).

  https://doi.org/10.1016/j.conbuildmat.2021.122569

- J. Astoveza; R. Trauchessec; S. Migot-Choux; R. Soth; Y. Pontikes, Fe-rich slag addition in ternary Portland cement, aluminate cement and calcium sulfate binders. Journal of Cement and Concrete Research (2022).

  https://doi.org/10.1016/j.cemconres.2021.106689

Conferences

- 6th International Slag Valorisation Symposium. Mechelen (Belgium). 1-5 April 2019 – poster presentation and conference paper entitled: Assessing the reactivity of industrial by-products in calcium aluminate cement-based formulations

- Forum of Young Researchers in Sustainable Building 2019. Prague (Czech Republic). 2-4 July 2019 – oral presentation and conference paper entitled: Industrial By-Products as Non-Conventional Supplementary Cementitious Material.

- International Process Metallurgy Symposium. Espoo (Finland). 5-6 November 2019 – oral presentation entitled: Quantifying the Degree of Fe-rich Slag Hydration in Calcium Aluminate Blended Cement by Image Analysis of SEM-BSE and XCT.

- Concrete Solutions towards Carbon Neutral Construction by 2050, Advanced Materials for Sustainable Infrastructure Development, Gordon Research Conference. Ventura (USA), 22-23 February 2020 – poster presentation entitled: Calcium Aluminate Blended Cement incorporating Fe-rich Slag: Overview and Characterization Techniques.

- 43èmes Journées du Groupe Francophone de Spectrométrie Mössbauer, Nancy (France). 18-19 May 2022 - poster and oral presentation entitled: Étude de l'hydratation des laitiers riches en fer dans des ciments à l'aide de la spectroscopie Mössbauer

Seminars

- Séminaire de l'Ecole Doctorale C2MP, Metz (France). 6 June 2019 - poster presentation entitled: Calcium Aluminate Blended Cements Incorporating Engineered Residues.

The submission of a third journal article is planned for the third quarter of 2022. The paper will cover the results of the STEM and Mössbauer spectroscopy on formulation (A) 4.5CAC-HH.

References

[1] European Commission, Circular Economy Action Plan: The European Green Deal, (2021), https://ec.europa.eu/.

[2] SOCRATES EU MSCA-ETN, Project proposal: Innovative training networks (ITN) call: H2020-MSCA-ITN-2016, Part B, (2016), https://etn-socrates.eu/.

[3] United Nations Environement Program (UNEP), Buildings and climate change: Summary for decision-makers, (2009), www.unep.fr/scp/sun.

[4] K.L. Scrivener, V.M. John, E.M. Gartner, Eco-efficient cements: Potential economically viable solutions for a low-CO2 cement-based materials industry, Cement and Concrete Research 114 (2018) 2–26.

[5] P.J.M. Monteiro, S.A. Miller, A. Horvath, Towards sustainable concrete, Nature materials 16 (2017) 698–699.

[6] A. Vollpracht, B. Lothenbach, R. Snellings, J. Haufe, The pore solution of blended cements: a review, Mater Struct 49 (2016) 3341–3367.

[7] S. Samad, A. Shah, M.C. Limbachiya, Strength development characteristics of concrete produced with blended cement using ground granulated blast furnace slag (GGBS) under various curing conditions, Sādhanā 42 (2017) 1203–1213.

[8] B. Lothenbach, K. Scrivener, R.D. Hooton, Supplementary cementitious materials, Cement and Concrete Research 41 (2011) 1244–1256.

[9] J. Bizzozero, Hydration and dimensional stability of calcium aluminate cement based systems, (Doctorate thesis): Faculté des sciences et techniques de l'ingénieur, Laboratoire des matériaux de constrcution, Lausanne, EPFL, (2014).

[10] International Energy Agency, Technology Roadmap: Low-Carbon Transition in the Cement Industry, (2018), https://iea.blob.core.windows.net/.

[11] J.E. Rossen, Composition and morphology of C-A-S-H in pastes of alite and cement blended with supplementary cementitious materials, Lausanne, EPFL, (2014).

[12] R. Snellings, G. Mertens, J. Elsen, Supplementary Cementitious Materials, Reviews in Mineralogy and Geochemistry 74 (2012) 211–278.

[13] D. Marchon, S. Kawashima, H. Bessaies-Bey, S. Mantellato, S. Ng, Hydration and rheology control of concrete for digital fabrication: Potential admixtures and cement chemistry, Cement and Concrete Research 112 (2018) 96–110.

[14] AVR, TopCrete: Binder properties. Composition, particle size and basic properties, (2021), https://www.avr.nl/.

[15] W. Chen, H.J.H. Brouwers, The reaction of slag in cement, theory and computer modelling: Materials Science, (2006).

[16] M.F. Zawrah, A.B. Shehata, E.A. Kishar, R.N. Yamani, Synthesis, hydration and sintering of calcium aluminate nanopowder for advanced applications, Comptes Rendus Chimie 14 (2011) 611–618.

[17] P.C. Hewlett, F.M. Lea, Lea's chemistry of cement and concrete, 4th ed., Butterworth-Heinemann, (2003).

[18] Imerys, CAC Process and Mineralogy. Construction Academy (internal document), (2018), https://www.imerys.com/.

[19] E. Qoku, Characterization and Quantification of Crystalline and Amorphous Phase Assemblage in Ternary Binders During Hydration, (Doctorate thesis): Faculty of Mechanical, Process and Energy Engineering, Technische Universität Bergakademie Freiberg, (2019).

[20] L. Xu, P. Wang, G. de Schutter, G. Wu, Effect of calcium aluminate cement variety on the hydration of portland cement in blended system, J. Wuhan Univ. Technol.-Mat. Sci. Edit. 29 (2014) 751–756.

[21] A.M. Dunster, F. Moulinier, K.C. Quillin, G.J. Osborne, Durability of concrete made with calcium aluminate cement and ground granulated blastfurnace slag in sulfate and marine environments, in: C.H. Fentiman, R.J. Mangabhai, K. Scrivener (Eds.), Calcium Aluminate Cements: Proceedings of a centenary conference, IHS BRE Press, (2008).

[22] A.J. Majumdar, R.N. Edmonds, B. Singh, Hydration of Secar 71 aluminous cement in presence of granulated blast furnace slag, Cement and Concrete Research 20 (1990) 7–14.

[23] L. Fernández-Carrasco, E. Vázquez, Reactions of fly ash with calcium aluminate cement and calcium sulphate, Fuel 88 (2009) 1533–1538.

[24] E. Henry-Lanier, B. Espinosa, C. Eychenne-Baron, Environmental footprint of calcium aluminate cement (CAC), in: C.H. Fentiman, R.J. Mangabhai, K. Scrivener (Eds.), Calcium aluminates: Proceedings of the international conference 2014, Palais des Papes, Avignon, France, 18-21 May 2014 / edited by Charles Fentiman, Raman Mangabhai and Karen Scrivener, IHS, Bracknell, Berkshire, (2014), pp. 3–16.

[25] U.S. Geological Survey, Minerals Commodity Summaries, (2014), http://minerals.usgs.gov/minerals/pubs/commodity/cement/.

[26] European Commission (main authors: G. Magnus, M. Grohol), Report on critical raw materials and the circular economy, (2018), http://publications.europa.eu/.

[27] P.T. Jones, D. Geysen, Y. Tielemans, S. van Passel, Y. Pontikes, B. Blanpain, M. Quaghebeur, N. Hoekstra, Enhanced Landfill Mining in view of multiple resource recovery: a critical review, Journal of Cleaner Production 55 (2013) 45–55.

[28] European Commission, European Enhanced Landfill Mining Consortium: Internal Market, Industry, Entrepreneurship and SMEs, (2014), https://ec.europa.eu/growth/sectors/raw-materials/.

[29] I. Korolev, P. Altınkaya, P. Halli, P.-M. Hannula, K. Yliniemi, M. Lundström, Electrochemical recovery of minor concentrations of gold from cyanide-free cupric chloride leaching solutions, Journal of Cleaner Production 186 (2018) 840–850.

[30] P. Altinkaya, J. Mäkinen, P. Kinnunen, E. Kolehmainen, M. Haapalainen, M. Lundström, Effect of biological pretreatment on metal extraction from flotation tailings for chloride leaching, Minerals Engineering 129 (2018) 47–53.

[31] T. Palden, M. Regadío, B. Onghena, K. Binnemans, Selective Metal Recovery from Jarosite Residue by Leaching with Acid-Equilibrated Ionic Liquids and Precipitation-Stripping, ACS Sustainable Chem. Eng. 7 (2019) 4239–4246.

[32] S. Spathariotis, N. Peeters, K.S. Ryder, A.P. Abbott, K. Binnemans, S. Riaño, Separation of iron(iii), zinc(ii) and lead(ii) from a choline chloride–ethylene glycol deep eutectic solvent by solvent extraction, RSC Adv. 10 (2020) 33161–33170.

[33] I.M. Pateli, A.P. Abbott, G.R.T. Jenkin, J.M. Hartley, Electrochemical oxidation as alternative for dissolution of metal oxides in deep eutectic solvents, Green Chem. 22 (2020) 8360–8368.

[34] N.M. Piatak, M.B. Parsons, R.R. Seal, Characteristics and environmental aspects of slag: A review, Applied Geochemistry 57 (2015) 236–266.

[35] M. Chintinne, C. Geenen, B. Coletti, S. Smets, Production of clean slag at Metallo Belgium, in: European Metallurgical Conference: Leipzig, (2017), pp. 1463–1474.

[36] NEW-MINE, Green slag valorisation is now an industrial success story, (2019), https://new-mine.eu/green-slag-valorisation-industrial-success-story/.

[37] H. Middelweerd, AVR pioniert met grootschalige CO2-afvang, (2020), https://www.change.inc/retail/avr-pioniert-met-grootschalige-co2-afvang-34249.

[38] P. Cogram, Jarosite, in: Reference Module in Earth Systems and Environmental Sciences, Elsevier, (2018).

[39] J. Li, H. Ma, Zinc and lead recovery from jarosite residues produced in zinc hydrometallurgy by vacuum reduction and distillation, Green Processing and Synthesis 7 (2018) 552–557.

[40] M. Rämä, S. Nurmi, A. Jokilaakso, L. Klemettinen, P. Taskinen, J. Salminen, Thermal Processing of Jarosite Leach Residue for a Safe Disposable Slag and Valuable Metals Recovery, Metals 8 (2018) 744.

[41] J. An, J. Kim, B.H. Nam, Investigation on Impacts of Municipal Solid Waste Incineration Bottom Ash on Cement Hydration, ACI Materials Journal 114 (2017).

[42] an Cheng, Effect of incinerator bottom ash properties on mechanical and pore size of blended cement mortars, Materials & Design (1980-2015) 36 (2012) 859–864.

[43] H.-C. Chiu, W.-H. Huang, L.-C. Hsu, Y.-G. Lin, Y.-H. Lai, C.-Y. Lin, Calcium containing iron oxide as an efficient and robust catalyst in (photo-)electrocatalytic water oxidation at neutral pH, Sustainable Energy Fuels 2 (2018) 271–279.

[44] Y. Pontikes, L. Machiels, S. Onisei, L. Pandelaers, D. Geysen, P.T. Jones, B. Blanpain, Slags with a high Al and Fe content as precursors for inorganic polymers, Applied Clay Science 73 (2013) 93–102.

[45] I. Maragkos, I.P. Giannopoulou, D. Panias, Synthesis of ferronickel slag-based geopolymers, Minerals Engineering 22 (2009) 196–203.

[46] Y. Pontikes, Introducing the Extraordinary Leuven Cement: Raw Materials, Process, Performance, and First Real-Life Applications, in: G. Gaustad, C. Fleuriault, M. Gökelma, J.A. Howarter, R. Kirchain, K. Ma, C. Meskers, N.R. Neelameggham, E. Olivetti, A.C. Powell, F. Tesfaye, D. Verhulst, M. Zhang (Eds.), REWAS 2019, Springer International Publishing, Cham, 2019, pp. 165–166.

[47] A. Peys, Inorganic polymers from CaO-FeO-SiO2 slags: Processing, reaction mechanism and molecular structure, (Doctorate thesis), (2018).

[48] A. Peys, M. Peeters, A. Katsiki, L. Kriskova, H. Rahier, Y. Pontikes, Performance and Durability of Fe-Rich Inorganic Polymer Composites with Basalt Fibers, in: W.M. Kriven, N.P. Bansal, M. Kusnezoff, T. Ohji, Y. Zhou, K. Il Moon, J. Matyas, K. Shimamura, S. Kirihara, S. Gupta, J. Wang (Eds.), Proceedings of the 41st International Conference on Advanced Ceramics and Composites, John Wiley & Sons, Inc, Hoboken, NJ, USA, (2018), pp. 229–238.

[49] J.L. Provis, J.S.J. van Deventer, Alkali activated materials: State-of-the-art report, RILEM TC 224-AAM / John L. Provis, Jannie S.J. van Deventer, editors, Springer, Dordrecht, (2014).

[50] C.H. Fentiman, R.J. Mangabhai, K. Scrivener (Eds.), Calcium Aluminate Cements: Proceedings of a centenary conference, IHS BRE Press, (2008).

[51] H. Fryda, E. Charpentier, J.M. Bertino, Accelerated test for conversion of calcium aluminate cement concrete, in: C.H. Fentiman, R.J. Mangabhai, K. Scrivener (Eds.), Calcium Aluminate Cements: Proceedings of a centenary conference, IHS BRE Press, (2008).

[52] C. Parr, F. Simonin, B. Touzo, C. Wöhrmeyer, B. Valdelièvre, A. Namba, The impact of calcium aluminate cement hydration upon the properties of refractory castables: Technical report presented in TARJ meeting, Ako, Japan (2004).

[53] J. Bensted, Calcium aluminate cements: Structure and performance of cements (2002) 114–138.

[54] J. Bizzozero, K. Scrivener, Hydration and microstructure of rapid-strength binders based on OPC accelerated by early ettringite formation, in: C.H. Fentiman, R.J. Mangabhai, K. Scrivener (Eds.), Calcium aluminates: Proceedings of the international conference 2014, Palais des Papes, Avignon, France, 18-21 May 2014 / edited

by Charles Fentiman, Raman Mangabhai and Karen Scrivener, IHS, Bracknell, Berkshire, (2014).

[55] M.C. Alonso, J.L. García Calvo, A. Hidalgo, L. Fernández Luco, Development and application of low-pH concretes for structural purposes in geological repository systems, in: Geological Repository Systems for Safe Disposal of Spent Nuclear Fuels and Radioactive Waste, Elsevier, (2010), pp. 286–322.

[56] S. Ramírez, J. Cuevas, R. Vigil, S. Leguey, Hydrothermal alteration of "La Serrata" bentonite (Almeria, Spain) by alkaline solutions, Applied Clay Science 21 (2002) 257–269.

[57] A. Hidalgo, I. Llorente, C. Andrade, Physico-chemical characterization of some low pH concrete using silica fume and aluminous cement: Proceedings: Workshop on qualification of low pH cements for geological repository, Stockholm, Sweden (2003) 15–16.

[58] H. Rojo, A.C. Scheinost, B. Lothenbach, A. Laube, E. Wieland, J. Tits, Retention of selenium by calcium aluminate hydrate (AFm) phases under strongly-reducing radioactive waste repository conditions, Dalton transactions (Cambridge, England 2003) 47 (2018) 4209–4218.

[59] P. Swift, H. Kinoshita, N.C. Collier, C.A. Utton, Phosphate modified calcium aluminate cement for radioactive waste encapsulation, Advances in Applied Ceramics 112 (2013) 1–8.

[60] R.J. Collins, W. Gutt, Research on long-term properties of high alumina cement concrete, Magazine of Concrete Research 40 (1988) 195–208.

[61] H.G. Midgley, A. Midgley, The conversion of high alumina cement, Magazine of Concrete Research 27 (1975) 59–77.

[62] Concrete Society, Calcium aluminate cements in construction: A re-assessment (Technical report), (1997).

[63] D. Zhang, X. Cai, L. Hu, Effect of Curing Temperature on Hydration of Calcium Aluminate Cement–Calcium Sulfate–Limestone System, J. Mater. Civ. Eng. 30 (2018) 6018011.

[64] P.J. French, R.G. Montgomery, T.D. Robson, High concrete strength within the hour. Concrete Society, (1971), http://worldcat.org/issn/00105317.

[65] E. García Alcocel, P. Garcés, S. Chinchón, General study of alkaline hydrolysis in calcium aluminate cement mortars under a broad range

of experimental conditions, Cement and Concrete Research 30 (2000) 1689–1699.

[66] M. Collepardi, S. Monosi, P. Piccioli, The influence of pozzolanic materials on the mechanical stability of aluminous cement, Cement and Concrete Research 25 (1995) 961–968.

[67] A. Hidalgo, J.L. García, M.C. Alonso, L. Fernández, C. Andrade, Microstructure development in mixes of calcium aluminate cement with silica fume or fly ash, J Therm Anal Calorim 96 (2009) 335–345.

[68] M. Idrees, O. Ekincioglu, M.S. Sonyal, Hydration behavior of calcium aluminate cement mortars with mineral admixtures at different curing temperatures, Construction and Building Materials 285 (2021) 122839.

[69] F.P. Glasser, L. Zhang, Q. Zhou, Reactions of aluminate cements with calcium sulphate, in: R.J. Mangabhai, F.P. Glasser (Eds.), Proceedings of the international conference on calcium aluminate cement: IOM Communications, London, UK, (2001), pp. 551–564.

[70] H.F.W. Taylor, Cement chemistry, 2nd edition: Academic Press, (1990).

[71] Danielle van nes, Amorphous Calcium Aluminate Cement (ACA) is on of the latest developments in cement chemistry: Caltra Nederland B.V., Unpublished, (2021).

[72] Z. He, Y. Li, The Influence of Mayenite Employed as a Functional Component on Hydration Properties of Ordinary Portland Cement, Materials (Basel, Switzerland) 11 (2018).

[73] J. Bizzozero, C. Gosselin, K.L. Scrivener, Expansion mechanisms in calcium aluminate and sulfoaluminate systems with calcium sulfate, Cement and Concrete Research 56 (2014) 190–202.

[74] G. Le Saoût, B. Lothenbach, P. Taquet, H. Fryda, F. Winnefeld, Hydration of calcium aluminate cement blended with anhydrite, Advances in Cement Research 30 (2018) 24–36.

[75] A. Anderberg, Moisture properties of self-levelling flooring compounds: Division of Building Materials, LTH, Lund University (2004).

[76] C. Kedziora, Propriétés d'usage et mécanismes d'hydratation du système ternaire [Ciment Alumineux – Sulfate de Calcium – Laitier de Haut Fourneau] à haute teneur en sulfate de calcium De l'approche expérimentale à la modélisation: (Doctorate thesis),

Laboratoire de Génie Civil et d'Ingénierie Environnementale, INSA de Lyon, (2015).

[77] Y. Han, J. Xia, H. Chang, J. Xu, The Influence Mechanism of Ettringite Crystals and Microstructure Characteristics on the Strength of Calcium-Based Stabilized Soil, Materials (Basel, Switzerland) 14 (2021).

[78] M. Balonis, F.P. Glasser, The density of cement phases, Cement and Concrete Research 39 (2009) 733–739.

[79] B. Lee, G. Kim, J. Nam, K. Lee, G. Kim, S. Lee, K. Shin, T. Koyama, Influence of α-Calcium Sulfate Hemihydrate on Setting, Compressive Strength, and Shrinkage Strain of Cement Mortar, Materials (Basel, Switzerland) 12 (2019).

[80] T. Matschei, B. Lothenbach, F.P. Glasser, Thermodynamic properties of Portland cement hydrates in the system CaO–Al2O3–SiO2–CaSO4–CaCO3–H2O, Cement and Concrete Research 37 (2007) 1379–1410.

[81] J. Plank, C. Hirsch, Impact of zeta potential of early cement hydration phases on superplasticizer adsorption, Cement and Concrete Research 37 (2007) 537–542.

[82] H. Nguyen, P. Kinnunen, K. Gijbels, V. Carvelli, H. Sreenivasan, A.M. Kantola, V.-V. Telkki, W. Schroeyers, M. Illikainen, Ettringite-based binder from ladle slag and gypsum – The effect of citric acid on fresh and hardened state properties, Cement and Concrete Research 123 (2019) 105800.

[83] H. Nguyen, W. Kunther, K. Gijbels, P. Samyn, V. Carvelli, M. Illikainen, P. Kinnunen, On the retardation mechanisms of citric acid in ettringite-based binders, Cement and Concrete Research 140 (2021) 106315.

[84] E.G. Moffatt, M.D.A. Thomas, Durability of Rapid-Strength Concrete Produced with Ettringite-Based Binders, ACI Materials Journal 115 (2018).

[85] J. Bizzozero, K. Scrivener, Hydration and microstructure of rapid-strength binders based on OPC accelerated by early ettringite formation, in: C.H. Fentiman, R.J. Mangabhai, K. Scrivener (Eds.), Calcium aluminates: Proceedings of the international conference 2014, Palais des Papes, Avignon, France, 18-21 May 2014 / edited by Charles Fentiman, Raman Mangabhai and Karen Scrivener, IHS, Bracknell, Berkshire, (2014).

[86] D. Torréns-Martín, L. Fernández-Carrasco, M.T. Blanco-Varela, Conduction calorimetric studies of ternary binders based on

Portland cement, calcium aluminate cement and calcium sulphate, J Therm Anal Calorim 114 (2013) 799–807.

[87] J. Nehring, J. Neubauer, S. Berger, F. Goetz-Neunhoeffer, Acceleration of OPC by CAC in binary and ternary systems: The role of pore solution chemistry, Cement and Concrete Research 107 (2018) 264–274.

[88] A.C.A. Rego, F.A. Cardoso, R.G. Pileggi, Ternary system Portland cement-calcium aluminate cement-calcium sulfate applied to self-leveling mortar: a literature review, Cerâmica 67 (2021) 65–82.

[89] M. Burteaux, "Laitiers de haut fourneau," Techniques de l'Ingénieur. no. M 7 425 (1995).

[90] Y. Abzaev, A. Gnyrya, S. Korobkov, K. Gauss, A. Boyarintsev, S. Tomrachev, Thermodynamic modeling of Portland cement without mineral additives, J. Phys.: Conf. Ser. 1145 (2019) 12016.

[91] G. Van-Rompaey, Etude de la réactivité des ciments riches en laitier, à basse température et à temps court, sans ajout chloruré (Doctorate thesis): Université Libre de Bruxelles (2006).

[92] K. Scrivener, V. John, E. Gartner (Eds.), Eco-efficient cements: Potential, economically viable solutions for a low-CO2, cement-based materials industry, 2016.

[93] S. Sánchez Berriel, A. Favier, E. Rosa Domínguez, I.R. Sánchez Machado, U. Heierli, K. Scrivener, F. Martirena Hernández, G. Habert, Assessing the environmental and economic potential of Limestone Calcined Clay Cement in Cuba, Journal of Cleaner Production 124 (2016) 361–369.

[94] Y. Cancio Díaz, S. Sánchez Berriel, U. Heierli, A.R. Favier, I.R. Sánchez Machado, K.L. Scrivener, J.F. Martirena Hernández, G. Habert, Limestone calcined clay cement as a low-carbon solution to meet expanding cement demand in emerging economies, Development Engineering 2 (2017) 82–91.

[95] E.M.J. Berodier, Impact of the Supplementary Cementitious Materials on the kinetics and microstructuraldevelopment of cement hydration: (Doctorate thesis), École Polythechnique Fédérale de Lausanne, (2015).

[96] I. Mehdipour, K.H. Khayat, Effect of Supplementary Cementitious Material Content and Binder Dispersion on Packing Density and Compressive Strength of Sustainable Cement Paste: Technical report, ACI Materials Journal (2016) 361–369.

[97] M. Behim, M. Beddar, P. Clastres, Reactivity of Granulated Blast Furnace Slag, Slovak Journal of Civil Engineering 21 (2013) 7–14.

[98] P.T. Jones, D. Geysen, Y. Tielemans, S. van Passel, Y. Pontikes, B. Blanpain, M. Quaghebeur, N. Hoekstra, Enhanced Landfill Mining in view of multiple resource recovery: A critical review, Journal of Cleaner Production 55 (2013) 45–55.

[99] J. Krook, N. Svensson, M. Eklund, Landfill mining: a critical review of two decades of research, Waste management (New York, N.Y.) 32 (2012) 513–520.

[100] EU, Communication from the commission to the European parliament, the council, the European economic and social committee and the committee of the regions: Closing the loop - An EU action plan for the Circular Economy Brussels COM 614 final, (2015).

[101] M. Penpolcharoen, Utilization of secondary lead slag as construction material, Cement and Concrete Research 35 (2005) 1050–1055.

[102] C. Morrison, R. Hooper, K. Lardner, The use of ferro-silicate slag from ISF zinc production as a sand replacement in concrete, Cement and Concrete Research 33 (2003) 2085–2089.

[103] B. Gorai, R.K. Jana, Premchand, Characteristics and utilisation of copper slag—a review, Resources, Conservation and Recycling 39 (2003) 299–313.

[104] P. Asokan, M. Saxena, S.R. Asolekar, Hazardous jarosite use in developing non-hazardous product for engineering application, Journal of hazardous materials 137 (2006) 1589–1599.

[105] A. Wongsa, K. Boonserm, C. Waisurasingha, V. Sata, P. Chindaprasirt, Use of municipal solid waste incinerator (MSWI) bottom ash in high calcium fly ash geopolymer matrix, Journal of Cleaner Production 148 (2017) 49–59.

[106] K.S. Harchand, Vishwamittar, K. Chandra, Infrared and Mössbauer study of two Indian cements, Cement and Concrete Research 10 (1980) 243–252.

[107] F. Engström, Y. Pontikes, D. Geysen, P.T. Jones, B. Björkman, B. Blanpain, Review: Hot stage engineering to improve slag valorisation options, in: P.T. Jones, Y. Pontikes, J. Elsen, O. Cizer, L. Boehme, T. Van Gerven, D. Geysen, M. Go, B. Blanpain (Eds.), Slag Valorisation Sympossium: The transition to sustainable materials management, (2011), pp. 231–249.

[108] A.S. Brand, E.O. Fanijo, A Review of the Influence of Steel Furnace Slag Type on the Properties of Cementitious Composites, Applied Sciences 10 (2020) 8210.

[109] A.M. Joseph, R. Snellings, P. van den Heede, S. Matthys, N. de Belie, The Use of Municipal Solid Waste Incineration Ash in Various Building Materials: A Belgian Point of View, Materials (Basel, Switzerland) 11 (2018).

[110] Ž. Kamberović, N. Gajić, M. Korać, S. Jevtić, M. Sokić, J. Stojanović, Technologically Sustainable Route for Metals Valorization from Jarosite-PbAg Sludge, Minerals 11 (2021) 255.

[111] USGS National Minerals Information Center, Mineral Commodity Summaries 2018: Iron and Steel Slag, (2018), https://minerals.usgs.gov/minerals/pubs/commodity/iron_&_steel_slag/mcs-2018-fesla.pdf.

[112] A.A. Ramezanianpour, Cement Replacement Materials: Properties, Durability, Sustainability, 1st ed., Springer Berlin Heidelberg; Imprint: Springer, Berlin Heidelberg, (2014).

[113] A. Mancini, E. Wieland, G. Geng, R. Dähn, J. Skibsted, B. Wehrli, B. Lothenbach, Fe(III) uptake by calcium silicate hydrates, Applied Geochemistry 113 (2020) 104460.

[114] S. Onisei, A.P. Douvalis, A. Malfliet, A. Peys, Y. Pontikes, Inorganic polymers made of fayalite slag: On the microstructure and behavior of Fe, Journal of the American Ceramic Society 101 (2018) 2245–2257.

[115] A. Peys, A.P. Douvalis, C. Siakati, H. Rahier, B. Blanpain, Y. Pontikes, The influence of air and temperature on the reaction mechanism and molecular structure of Fe-silicate inorganic polymers, Journal of Non-Crystalline Solids 526 (2019) 119675.

[116] A. Peys, A.P. Douvalis, V. Hallet, H. Rahier, B. Blanpain, Y. Pontikes, Inorganic Polymers From CaO-FeOx-SiO2 Slag: The Start of Oxidation of Fe and the Formation of a Mixed Valence Binder, Front. Mater. 6 (2019).

[117] C. Siakati, A.P. Douvalis, P. Ziogas, A. Peys, Y. Pontikes, Impact of the solidification path of FeO x –SiO 2 slags on the resultant inorganic polymers, Journal of the American Ceramic Society 103 (2020) 2173–2184.

[118] C. Siakati, A.P. Douvalis, V. Hallet, A. Peys, Y. Pontikes, Influence of CaO/FeO ratio on the formation mechanism and

properties of alkali-activated Fe-rich slags, Cement and Concrete Research 146 (2021) 106466.

[119] C. Siakati, R. Macchieraldo, B. Kirchner, F. Tielens, A. Peys, D. Seveno, Y. Pontikes, Unraveling the nano-structure of a glassy CaO-FeO-SiO2 slag by molecular dynamics simulations, Journal of Non-Crystalline Solids 528 (2020) 119771.

[120] A. Peys, C.E. White, D. Olds, H. Rahier, B. Blanpain, Y. Pontikes, Molecular structure of CaO–FeO x –SiO 2 glassy slags and resultant inorganic polymer binders, Journal of the American Ceramic Society 101 (2018) 5846–5857.

[121] R.M. Cornell, U. Schwertmann, The iron oxides: Structure, properties, reactions, occurences and uses / R.M. Cornell, U. Schwertmann, 2nd ed., Wiley-VCH, Weinheim, Cambridge, (2003).

[122] G.E. Brown Jr., F. Farges, G. Calas, Chapter 9. X-RAY SCATTERING AND X-RAY SPECTROSCOPY STUDIES OF SILICATE MELTS, in: J.F. Stebbins, P.F. McMillan, D.B. Dingwell (Eds.), Structure, Dynamics, and Properties of Silicate Melts, De Gruyter, 1995, pp. 317–410.

[123] M. Wilke, F. Farges, P.-E. Petit, G.E. Brown, F. Martin, Oxidation state and coordination of Fe in minerals: An Fe K- XANES spectroscopic study, American Mineralogist 86 (2001) 714–730.

[124] A. Mancini, E. Wieland, G. Geng, B. Lothenbach, B. Wehrli, R. Dähn, Fe(II) interaction with cement phases: Method development, wet chemical studies and X-ray absorption spectroscopy, Journal of colloid and interface science 588 (2021) 692–704.

[125] C.N. Singman, Atomic volume and allotropy of the elements, J. Chem. Educ. 61 (1984) 137.

[126] S.J. Jaffer, C.M. Hansson, Chloride-induced corrosion products of steel in cracked-concrete subjected to different loading conditions, Cement and Concrete Research 39 (2009) 116–125.

[127] J. Rose, A. Bénard, S. El Mrabet, A. Masion, I. Moulin, V. Briois, L. Olivi, J.-Y. Bottero, Evolution of iron speciation during hydration of C4AF, Waste management (New York, N.Y.) 26 (2006) 720–724.

[128] Y. Tao, D. Wan, W. Zhang, F. Wang, S. Hu, Intrinsic reactivity and dissolution characteristics of tetracalcium aluminoferrite, Cement and Concrete Research 146 (2021) 106485.

[129] V. Lilkov, O. Petrov, Y. Tzvetanova, P. Savov, M. Kadiyski, Mössbauer, XRD, and Complex Thermal Analysis of the Hydration of Cement with Fly Ash, Journal of Spectroscopy 2013 (2013) 1–9.

[130] H.K. Choudhary, A.V. Anupama, R. Kumar, M.E. Panzi, S. Matteppanavar, B.N. Sherikar, B. Sahoo, Observation of phase transformations in cement during hydration, Construction and Building Materials 101 (2015) 122–129.

[131] G. Möschner, B. Lothenbach, J. Rose, A. Ulrich, R. Figi, R. Kretzschmar, Solubility of Fe–ettringite (Ca6[Fe(OH)6]2(SO4)3·26H2O), Geochimica et Cosmochimica Acta 72 (2008) 1–18.

[132] B.Z. Dilnesa, B. Lothenbach, G. Le Saout, G. Renaudin, A. Mesbah, Y. Filinchuk, A. Wichser, E. Wieland, Iron in carbonate containing AFm phases, Cement and Concrete Research 41 (2011) 311–323.

[133] J. Siramanont, B.J. Walder, L. Emsley, P. Bowen, Iron incorporation in synthetic precipitated calcium silicate hydrates, Cement and Concrete Research 142 (2021) 106365.

[134] K. Mei, X. Cheng, T. Gu, Y. Zheng, P. Gong, B. Li, C. Zhang, L. Zhang, B. Dai, Effects of Fe and Al ions during hydrogen sulphide (H2S)-induced corrosion of tetracalcium aluminoferrite (C4AF) and tricalcium aluminate (C3A), Journal of hazardous materials 403 (2021) 123928.

[135] K.S. Harchand, R. Kumar, K. Chandra, Vishwamittar, Mössbauer and X-ray investigations of some portland cements, Cement and Concrete Research 14 (1984) 170–176.

[136] M. Sharma, Vishwamittar, K.S. Harchand, D. Raj, Mössbauer and X-ray diffraction studies of two dry and hydrated portland cements and their clinker, Cement and Concrete Research 21 (1991) 484–488.

[137] M. Horgnies, J.J. Chen, C. Bouillon, Overview about the use of Fourier Transform Infrared spectroscopy to study cementitious materials, in: C.A. Brebbia, A.A. Mammoli, A. Klemm (Eds.), Materials Characterisation VI, WIT PressSouthampton, UK, (2013), pp. 251–262.

[138] C.M.B. Henderson, D. Taylor, Infrared spectra of aluminogermanate- and aluminate-sodalites and a re-examination of the relationship between T□O bond length, T□O□T angle and the position of the main i.r. absorption band for compounds with

framework structures, Spectrochimica Acta Part A: Molecular Spectroscopy 35 (1979) 929–935.

[139] V. Hallet, M.T. Pedersen, B. Lothenbach, F. Winnefeld, N. de Belie, Y. Pontikes, Hydration of blended cement with high volume iron-rich slag from non-ferrous metallurgy, Cement and Concrete Research 151 (2022) 106624.

[140] M.B. Haha, K. de Weerdt, B. Lothenbach, Quantification of the degree of reaction of fly ash, Cement and Concrete Research 40 (2010) 1620–1629.

[141] K. Nakagawa, I. Terashima, K. Asaga, M. Daimon, A study of hydration of amorphous calcium aluminate by selective dissolution analysis, Cement and Concrete Research 20 (1990) 655–661.

[142] A. Gholizadeh Vayghan, L. Horckmans, R. Snellings, A. Peys, P. Teck, J. Maier, B. Friedrich, K. Klejnowska, Use of Treated Non-Ferrous Metallurgical Slags as Supplementary Cementitious Materials in Cementitious Mixtures, Applied Sciences 11 (2021) 4028.

[143] S. Park, S.Y. Abate, H.K. Lee, H.-K. Kim, On the quantification of degrees of reaction and hydration of sodium silicate-activated slag cements, Mater Struct 53 (2020).

[144] Z. Wu, Y. Wei, S. Wang, J. Chen, Application of X-Ray Micro-CT for Quantifying Degree of Hydration of Slag-Blended Cement Paste, J. Mater. Civ. Eng. 32 (2020) 4020008.

[145] J. Środoń, Quantitative X-Ray Diffraction Analysis of Clay-Bearing Rocks from Random Preparations, Clays and Clay Minerals 49 (2001) 514–528.

[146] C.L. Honeybourne, An interpretation of the room temperature 57Fe - Mossbauer spectrum of Grey high alumina cement, Cement and Concrete Research 10 (1980) 35–40.

[147] S. Rai, S. Kurian, V.N. Dwivedi, S.S. Das, N.B. Singh, N.S. Gajbhiye, Mössbauer and calorimetric studies of portland cement hydration in the presence of black gram pulse, Hyperfine Interact 188 (2009) 19–24.

[148] Y. Feng, J. Kero, Q. Yang, Q. Chen, F. Engström, C. Samuelsson, C. Qi, Mechanical Activation of Granulated Copper Slag and Its Influence on Hydration Heat and Compressive Strength of Blended Cement, Materials (Basel, Switzerland) 12 (2019).

[149] H. Poellmann, H.-J. Kuzel, R. Wenda, Solid solution of ettringites part I: incorporation of OH− and CO32- in 3CaO.A12O3.32H2O, Cement and Concrete Research 20 (1990) 941–947.

[150] W. Wang, Y. Shao, H. Hou, M. Zhou, Synthesis and thermodynamic properties of arsenate and sulfate-arsenate ettringite structure phases, PloS one 12 (2017) e0182160.

[151] M.D. Jackson, G. Vola, D. Všianský, J.P. Oleson, B.E. Scheetz, C. Brandon, R.L. Hohlfelder, Cement Microstructures and Durability in Ancient Roman Seawater Concretes, in: J. Válek, J.J. Hughes, C.J.W.P. Groot (Eds.), Historic Mortars, Springer Netherlands, Dordrecht, (2012), pp. 49–76.

[152] A.E. Moore, H.F.W. Taylor, Crystal structure of ettringite, Acta Crystallogr B Struct Crystallogr Cryst Chem 26 (1970) 386–393.

[153] S.M. Clark, B. Colas, M. Kunz, S. Speziale, P.J.M. Monteiro, Effect of pressure on the crystal structure of ettringite, Cement and Concrete Research 38 (2008) 19–26.

[154] N. Maach, Etude experimentale de l'hydratation de sulfates de calcium et de mayenite (C12A7 et TEP) en suspension: Projet: Modelisation cinetique de l'hydratation des systemes cimentaires, Internal Technical Report, Kerneos Aluminate Technologies (2016) 1–88.

[155] J. Payá, M.V. Borrachero, J. Monzó, E. Peris-Mora, F. Amahjour, Enhanced conductivity measurement techniques for evaluation of fly ash pozzolanic activity, Cement and Concrete Research 31 (2001) 41–49.

[156] I. Kharchenco, V. Alekseev, Effect of ettringite morphology on the properties of expanding cement systems, E3S Web Conf. 110 (2019) 1037.

[157] M. Katsioti, P. Boura, S. Agatzini, P.E. Tsakiridis, P. Oustadakis, Use of jarosite/alunite precipitate as a substitute for gypsum in Portland cement, Cement and Concrete Composites 27 (2005) 3–9.

[158] T. Chen, J. Dutrizac, Jarofix: Addressing iron disposal in the zinc industry, The Journal of the Minerals, Metals & Materials Society 53 (2001) 32–35.

[159] N. Dave, A.K. Misra, A. Srivastava, S.K. Kaushik, Setting time and standard consistency of quaternary binders: The influence of cementitious material addition and mixing, International Journal of Sustainable Built Environment 6 (2017) 30–36.

[160] V. Hallet, N. de Belie, Y. Pontikes, The impact of slag fineness on the reactivity of blended cements with high-volume non-ferrous metallurgy slag, Construction and Building Materials 257 (2020) 119400.

[161] I. Fernandes, M.A.T.M. Broekmans, F. Noronha, Petrography and Geochemical Analysis for the Forensic Assessment of Concrete Damage, in: K. Ritz, L. Dawson, D. Miller (Eds.), Criminal and Environmental Soil Forensics, Springer Netherlands, Dordrecht, (2009), pp. 163–180.

[162] B. Chen, Study of an ettringite-based thermochemical energy storage for buildings: (Doctorate thesis) Thermics [physics.class-ph], Université de Lyon (2020).

[163] P. Feng, C. Miao, J.W. Bullard, Factors influencing the stability of AFm and AFt in the Ca-Al-S-O-H system at 25 °C, Journal of the American Ceramic Society 99 (2016) 1031–1041.

[164] D. Damidot, B. Lothenbach, D. Herfort, F.P. Glasser, Thermodynamics and cement science, Cement and Concrete Research 41 (2011) 679–695.

[165] M.U. Okoronkwo, F.P. Glasser, Stability of strätlingite in the CASH system, Mater Struct 49 (2016) 4305–4318.

[166] H.G. Midgley, P. Bhaskara Rao, Formation of stratlingite, 2CaO.SiO2.Al2O3.8H2O, in relation to the hydration of high alumina cement, Cement and Concrete Research 8 (1978) 169–172.

[167] Y. Xi, D.D. Siemer, B.E. Scheetz, Strength development, hydration reaction and pore structure of autoclaved slag cement with added silica fume, Cement and Concrete Research 27 (1997) 75–82.

[168] M.A. Chavda, H. Kinoshita, J.L. Provis, Modification of a calcium aluminate cement system to prevent conversion to cubic hydrates and minimise corrosion of encapsulated aluminium metal, in: 32nd Cement and Concrete Science Conference, Queen's University Belfast, (2012).

[169] A. Fernández-Jiménez, T. Vázquez, A. Palomo, Effect of Sodium Silicate on Calcium Aluminate Cement Hydration in Highly Alkaline Media: A Microstructural Characterization, Journal of the American Ceramic Society 94 (2011) 1297–1303.

[170] B.Z. Dilnesa, E. Wieland, B. Lothenbach, R. Dähn, K.L. Scrivener, Fe-containing phases in hydrated cements, Cement and Concrete Research 58 (2014) 45–55.

[171] J.F. Zapata, H.A. Colorado, M.A. Gomez, Effect of high temperature and additions of silica on the microstructure and properties of calcium aluminate cement pastes, Journal of Sustainable Cement-Based Materials 9 (2020) 323–349.

[172] P.A. Schroeder, Infrared Spectroscopy in Clay Science Schroeder, P.A., in: A.C. Rule, S. Guggenheim (Eds.), Teaching clay science, Clay Minerals Society, Aurora, CO, (2002), pp. 182–205.

[173] A. Cuesta, A.G. de La Torre, I. Santacruz, P. Trtik, J.C. da Silva, A. Diaz, M. Holler, M.A.G. Aranda, Chemistry and Mass Density of Aluminum Hydroxide Gel in Eco-Cements by Ptychographic X-ray Computed Tomography, The Journal of Physical Chemistry 121 (2017) 3044–3054.

[174] Y. Zhang, J. Chang, Microstructural evolution of aluminum hydroxide gel during the hydration of calcium sulfoaluminate under different alkali concentrations, Construction and Building Materials 180 (2018) 655–664.

[175] C. Phrompet, C. Sriwong, S. Maensiri, P. Chindaprasirt, C. Ruttanapun, Optical and dielectric properties of nano-sized tricalcium aluminate hexahydrate (C3AH6) cement, Construction and Building Materials 179 (2018) 57–65.

[176] N.C.M. Marty, S. Grangeon, F. Warmont, C. Lerouge, Alteration of nanocrystalline calcium silicate hydrate (C-S-H) at pH 9.2 and room temperature: a combined mineralogical and chemical study, Mineralogical Magazine 79 (2015) 437–458.

[177] G. Möschner, B. Lothenbach, F. Winnefeld, A. Ulrich, R. Figi, R. Kretzschmar, Solid solution between Al-ettringite and Fe-ettringite (Ca6[Al1−xFex(OH)6]2(SO4)3·26H2O), Cement and Concrete Research 39 (2009) 482–489.

[178] J.E. Rossen, K.L. Scrivener, Optimization of SEM-EDS to determine the C–A–S–H composition in matured cement paste samples, Materials Characterization 123 (2017) 294–306.

[179] J. Song, S.-Y. Jia, B. Yu, S.-H. Wu, X. Han, Formation of iron (hydr)oxides during the abiotic oxidation of Fe(II) in the presence of arsenate, Journal of hazardous materials 294 (2015) 70–79.

[180] C. Frandsen, B.A. Legg, L.R. Comolli, H. Zhang, B. Gilbert, E. Johnson, J.F. Banfield, Aggregation-induced growth and transformation of β-FeOOH nanorods to micron-sized α-Fe 2 O 3 spindles, CrystEngComm 16 (2014) 1451–1458.

[181] F. Bocher, A. Géhin, C. Ruby, J. Ghanbaja, M. Abdelmoula, J.-M.R. Génin, Coprecipitation of Fe(II–III) hydroxycarbonate green rust stabilised by phosphate adsorption, Solid State Sciences 6 (2004) 117–124.

[182] E. Bazilevskaya, Iron and aluminum hydroxide nanoparticles in the environment: From nano-scale to field processes: (Doctorate thesis), Soil and Science Biogeochemistry, The Pennsylvania State University (2009).

[183] S. Kanehira, S. Kanamori, K. Nagashima, T. Saeki, H. Visbal, T. Fukui, K. Hirao, Controllable hydrogen release via aluminum powder corrosion in calcium hydroxide solutions, Journal of Asian Ceramic Societies 1 (2013) 296–303.

[184] N. Karimian, S.G. Johnston, E.D. Burton, Iron and sulfur cycling in acid sulfate soil wetlands under dynamic redox conditions: A review, Chemosphere 197 (2018) 803–816.

[185] J.-M.R. Génin, S.J. Mills, A.G. Christy, O. Guérin, A.J. Herbillon, E. Kuzmann, G. Ona-Nguema, C. Ruby, C. Upadhyay, Mössbauerite, Fe 63+ O 4 (OH) 8 [CO 3]·3H 2 O, the fully oxidized 'green rust' mineral from Mont Saint-Michel Bay, France, Mineral. mag. 78 (2014) 447–465.

[186] A. de Roy, C. Forano, J.P. Besse, Layered Double Hydroxides: Synthesis and Post-Synthesis Modification, in: V. Rives (Ed.), Layered Double Hydroxides: Present and Future: Nova Science Publishers, Inc., (2006), pp. 1–39.

[187] T. Liang, Y. Nanru, Hydration products of calcium aluminoferrite in the presence of gypsum, Cement and Concrete Research 24 (1994) 150–158.

[188] M.D. Dyar, D.G. Agresti, M.W. Schaefer, C.A. Grant, E.C. Sklute, Mössbauer spectroscopy of Earth and planetary materials, Annual Review of Earth and Planetary Sciences 34 (2006) 83–125.

[189] M.D. Dyar, C.L. Perry, C.R. Rebbert, B.L. Dutrow, M.J. Holdaway, H.M. Lang, Mossbauer spectroscopy of synthetic and naturally occurring staurolite: American Mineralogist, 76 (1-2), 27-41, (1991), https://digitalcommons.lsu.edu/geo_pubs/742.

[190] M.D. Dyar, E.C. Sklute, O.N. Menzies, P.A. Bland, D. Lindsley, T. Glotch, M.D. Lane, M.W. Schaefer, B. Wopenka, R. Klima, J.L. Bishop, T. Hiroi, C. Pieters, J. Sunshine, Spectroscopic characteristics of synthetic olivine: An integrated multi-wavelength and multi-technique approach, American Mineralogist 94 (2009) 883–898.

[191] K. Kaewmanee, P. Krammart, T. Sumranwanich, P. Choktaweekarn, S. Tangtermsirikul, Effect of free lime content on properties of cement–fly ash mixtures, Construction and Building Materials 38 (2013) 829–836.

[192] M. De Schepper, L. Vernimmen, N. De Belie, K. De Buysser, I. Van Driessche, The assessment of clinker and cement regenerated from completely recyclable concrete, in: XIII ICCC International Congress on the Chemistry of Cement: Madrid, Spain, (2011).

[193] J. Purnomo, S. Sumarni, I.N. Saputro, Effect of citric acid on setting-time and compressive strength of concrete, IOP Conference Series: Materials Science and Engineering 578 (2019) 12077.

[194] M. Lanzón, P.A. García-Ruiz, Effect of citric acid on setting inhibition and mechanical properties of gypsum building plasters, Construction and Building Materials 28 (2012) 506–511.

[195] R. Salomão, V.C. Pandolfelli, Citric acid as anti-hydration additive for magnesia containing refractory castables, Ceramics International 37 (2011) 1839–1842.

[196] G.D. Stefanou, C. Larsinos, Influence of mixing water on the setting time of concrete, International Journal of Cement Composites and Lightweight Concrete 3 (1981) 45–48.

[197] V. Dodson, Time of Setting, Significance of Tests and Properties of Concrete and Concrete-Making Materials: STP 169C, ASTM, West Conshohocken, Pa., 83, (1994), https://www.concreteconstruction.net/.

[198] M. Juenger, M. Won, D. Fowler, C.W. Suh, A. Edson, Effects of supplementary cementing materials on the setting time and early strength of concrete: Materials Science, Engineering, University of Texas at Austin, (2008).

[199] M. Cyr, R. Pouhet, Resistance to alkali-aggregate reaction (AAR) of alkali-activated cement-based binders, in: Handbook of Alkali-Activated Cements, Mortars and Concretes, Elsevier, (2015), pp. 397–422.

[200] W. Guan, F. Ji, Q. Chen, P. Yan, L. Pei, Synthesis and Enhanced Phosphate Recovery Property of Porous Calcium Silicate Hydrate Using Polyethyleneglycol as Pore-Generation Agent, Materials (Basel, Switzerland) (2013) 2846–2861.

[201] I. Techer, D. Bartier, P. Boulvais, E. Tinseau, K. Suchorski, J. Cabrera, A. Dauzères, Tracing interactions between natural argillites and hyper-alkaline fluids from engineered cement paste and

concrete: Chemical and isotopic monitoring of a 15-years old deep-disposal analogue, Applied Geochemistry 27 (2012) 1384–1402.

[202] I. Garcia-Lodeiro, A. Palomo, A. Fernández-Jiménez, D.E. Macphee, Compatibility studies between N-A-S-H and C-A-S-H gels. Study in the ternary diagram Na2O–CaO–Al2O3–SiO2–H2O, Cement and Concrete Research 41 (2011) 923–931.

[203] F. Avet, E. Boehm-Courjault, K. Scrivener, Investigation of C-A-S-H composition, morphology and density in Limestone Calcined Clay Cement (LC3), Cement and Concrete Research 115 (2019) 70–79.

[204] F. Deschner, F. Winnefeld, B. Lothenbach, S. Seufert, P. Schwesig, S. Dittrich, F. Goetz-Neunhoeffer, J. Neubauer, Hydration of Portland cement with high replacement by siliceous fly ash, Cement and Concrete Research 42 (2012) 1389–1400.

[205] F. Ziegler, A.M. Scheidegger, C.A. Johnson, R. Dähn, E. Wieland, Sorption mechanisms of zinc to calcium silicate hydrate: X-ray absorption fine structure (XAFS) investigation, Environmental science & technology 35 (2001) 1550–1555.

[206] S.L. Poulsen, V. Kocaba, G. Le Saoût, H.J. Jakobsen, K.L. Scrivener, J. Skibsted, Improved quantification of alite and belite in anhydrous Portland cements by (29)Si MAS NMR: effects of paramagnetic ions, Solid state nuclear magnetic resonance 36 (2009) 32–44.

[207] E. Demoulian, C. Vernet, F. Hawthorn, P. Gourdin, Determination de la teneur en laitier dans les ciments par dissolutions sélectives: 7th International Congress on the chemistry of cement (1980) II, 111-151.

[208] P. CLOSE, H.M. SHEPHERD, C.H. DRUMMOND, Determination of Several Valences of Iron, Arsenic and Antimony, and Selenium in Glass, Journal of the American Ceramic Society 41 (1958) 455–460.

[209] NIST, Inorganic Crystal Structure Database (ICSD) Web Site, (2020), https://icsd.nist.gov/.

[210] E. Bill, 57Fe-Mössbauer Spectroscopy and Basic Interpretation of Mössbauer Parameters, in: Practical Approaches to Biological Inorganic Chemistry, Elsevier, (2013), pp. 109–130.

[211] Y. Yoshida, G. Langouche, Mössbauer Spectroscopy, Springer Berlin Heidelberg, Berlin, Heidelberg, (2013).